

DISS. ETH NO. 24810

**PALLADIUM ISOTOPE COSMOCHEMISTRY:  
CONSTRAINTS ON NEBULAR AND PARENT BODY  
PROCESSES FROM IRON METEORITES**

A thesis submitted to attain the degree of  
DOCTOR OF SCIENCES of ETH ZURICH  
(Dr. sc. ETH Zurich)

presented by  
PÄR KARL MATTIAS EK  
MSc in Earth Sciences, Göteborgs Universitet  
Born on August 11, 1988  
Citizen of Sweden

accepted on the recommendation of  
Prof. Dr. Mark Rehkämper  
Dr. Maria Lugaro  
Dr. Alison C. Hunt  
Prof. Dr. Maria Schönbachler

2018



# Contents

Abstract	v
Zusammenfassung	vii
<b>Chapter 1</b>	
<b>An introduction to cosmochemistry</b>	<b>1</b>
<b>1.1. A brief history of the universe</b>	<b>2</b>
1.1.1. The Big Bang and primordial nucleosynthesis	2
1.1.2. Stellar evolution and nucleosynthesis	3
1.1.3. Solar system evolution	6
1.1.4. Early Earth History	8
1.1.5. The Meteorite record	9
<b>1.2. Isotopic variations in meteorites</b>	<b>10</b>
1.2.1. The origin of mass-independent isotopic variations in the solar nebula	11
1.2.2. Parent body processes and mass-dependent isotopic fractionation	13
<b>1.3. Thesis outline</b>	<b>14</b>
<b>Chapter 2</b>	
<b>Initial separation of Pd and Pt from iron meteorites using ion exchange chromatography</b>	<b>17</b>
<b>2.1. Introduction</b>	<b>18</b>
<b>2.2. Methods</b>	<b>18</b>
2.2.1. Reagents and Materials	18
2.2.2. Sample preparation and dissolution	18
2.2.3. Ion exchange chromatography	19
<b>2.3. Results and discussion</b>	<b>19</b>
<b>2.4. Conclusion</b>	<b>20</b>

## **Chapter 3**

### **A new method for high-precision Palladium isotope analyses of iron meteorites and other metal samples 21**

#### **3.1. Introduction 22**

#### **3.2. Methods 25**

3.2.1. Reagents & Materials 25

3.2.2. Sample digestion 25

3.2.3. Ion-exchange procedure 25

3.2.4. Yields and procedural blanks 26

#### **3.3. Mass Spectrometry 27**

3.3.1. Instrumentation and data collection protocols 27

3.3.2. Interference correction and data reduction 27

#### **3.4. Results and Discussion 28**

3.4.1. Isobaric interferences 28

3.4.2. Molecular interferences 28

3.4.3. Reproducibility and accuracy 30

3.4.4. Cosmochemical implication for IAB and IVB iron meteorites 32

#### **3.5. Conclusions 35**

## **Chapter 4**

### **The Zr-Mo-Ru-Pd Correlation: Evidence for incomplete condensation around AGB stars and selective processing of dust in the solar nebula 37**

#### **4.1. Introduction 38**

#### **4.2. Samples 39**

#### **4.3. Methods 42**

4.3.1. Ion exchange separation of Pd and Pt 42

4.3.2. High precision Pd and Pt isotopic measurements 42

4.3.3. Element concentration analyses 43

#### **4.4. Results 43**

4.4.1. Palladium and Pt isotopic composition 43

4.4.2. Element ratios for Rh/Pd 45

#### **4.5. Discussion 45**

4.5.1. Sources of isotopic variation 45

4.5.2 Comparison to Mo and Ru nucleosynthetic variations 52

4.5.3 Origin of the Zr-Mo-Ru-Pd correlation and nucleosynthetic offsets in the solar system 52

#### **4.6. Conclusions 55**

<b>Chapter 5</b>	
Measurements of Palladium stable isotope ratio by double-spike multiple collector ICP-MS	57
<b>5.1. Introduction</b>	<b>58</b>
<b>5.2. Design and preparation of the Double spike</b>	<b>59</b>
<b>5.3. Materials and methods</b>	<b>61</b>
5.3.1. Chemicals and standard solutions	61
5.3.2. Samples	61
5.3.3. Sample digestion and separation procedure	61
5.3.4. Mass spectrometry	62
5.3.5. Data reduction	62
<b>5.4. Results and discussion</b>	<b>64</b>
5.4.1 Calibration of the double spike.	64
5.4.2. Reproducibility of double spike measurements.	64
5.4.3. Isobaric and molecular interferences	65
5.4.4. Modelling of mass-independent effects	67
5.4.5. Natural palladium stable isotope variations.	69
<b>5 Conclusions</b>	<b>72</b>
<b>Chapter 6</b>	
Conclusions	75
References	79
Appendix A	87
Appendix B	107
Acknowledgements	110
Curriculum vitae	113



# Abstract

Elements heavier than Fe were formed primarily by neutron capture nucleosynthesis in several generations of stars, before condensing into dust around stars or in the interstellar medium (ISM). Our solar system formed ~4.5 billion years ago from the gravitational collapse of a dense molecular cloud and inherited a proportion of these dust populations. A protoplanetary disk formed around our young sun, and selective dust processing led to small variations in the distribution of dust with distinct nucleosynthetic origins. This dust accreted into larger bodies, which preserved the nucleosynthetic signature of the accreted dust, and some of which underwent metal-silicate differentiation. Collisions between planetary bodies eventually led to the formation of the terrestrial planets. The Earth formed via several large impacts, the last being the giant Moon-forming impact, after which core formation ceased. Later, several smaller impactors added the final 0.5 % of the Earth's mass to the mantle.

In this thesis I determined the (i) mass-independent and (ii) mass-dependent Pd isotope compositions of a range of iron meteorites to address two fundamental questions about the early history of our solar system: 1) which processes led to the nucleosynthetic isotope variations observed for bulk planetary bodies in many refractory elements?, and 2) what processes operated during metal-silicate differentiation on Earth and other planetary bodies? Palladium, a platinum group element, is promising to address these questions. It has six naturally occurring isotopes originating from *p*-, *s*- and *r*-process nucleosynthesis, making it useful for studies on the origin of nucleosynthetic variations in planetary bodies. Additionally, Pd is a highly siderophile element that strongly partitions into the metal phase during metal-silicate differentiation and is more volatile than the other, generally refractory, platinum group elements. It has therefore great potential to provide information on the processes operating during core formation and solidification.

In order to address the outlined questions, a novel analytical method for high-precision Pd isotope analyses by MC-ICPMS was developed (Chapters 2 and 3). It includes a two-stage anion exchange method. The first anion exchange column allows for separation of both Pd and Pt from the same sample aliquot of an iron meteorite. Platinum isotopes were further purified and analysed in a companion study. Following the first separation step, Ru, forming isobaric interferences on Pd isotopes, is removed from the Pd fraction via volatilisation in HClO<sub>4</sub>. A second anion exchange column separates Pd from remaining matrix elements, chiefly Fe, Ni, and Mo. The final Pd fraction consistently yields Ru/Pd ratios of less than 0.0005, enabling accurate correction of isobaric interferences on <sup>102</sup>Pd and <sup>104</sup>Pd and ensuring high precision isotopic analyses by MC-ICPMS. The method yields an external reproducibility (2 standard deviations, SD) of 1.58 for  $\epsilon^{102}\text{Pd}$ , 0.26 for  $\epsilon^{104}\text{Pd}$ , 0.13 for  $\epsilon^{106}\text{Pd}$  and 0.27 for  $\epsilon^{110}\text{Pd}$  based on repeat mass-independent measurements of several iron meteorites.

Exploiting the new analytical technique, the mass-independent Pd isotope composition of 24 iron meteorites were determined to assess the processes leading to nucleosynthetic variations in planetary bodies (Chapter 4). Samples from the IAB, IIAB, IID, IIIAB, IVA, and IVB groups were analysed and show a wide range of Pd isotope compositions. The IID sample Carbo-J yields the largest deviations in  $\epsilon^{104}\text{Pd}$  ( $1.5 \pm 0.25$ ) and  $\epsilon^{110}\text{Pd}$  ( $0.8 \pm 0.16$ ) from the terrestrial composition observed for all analysed samples.

The variations between members of the same group agree well with the effects modelled for cosmic ray exposure. After correction for cosmic ray effects using Pt isotopes, four iron meteorite groups show nucleosynthetic signatures distinct from the terrestrial composition in the order IVA < IIIAB < IID ≤ IVB, while the IAB and IIAB groups display no resolvable offsets. The identified Pd isotope patterns are consistent with an s-process deficit, in accordance with observations from neighbouring elements (Zr, Mo and Ru). The Pd isotope variations are correlated with those for Mo and Ru isotopes. However, the observed slope does not fit with s-process model predictions and indicates a Pd abundance in the s-process component that is 4 times lower than predicted. My preferred explanation is that more volatile Pd condensed less readily into dust around AGB stars, relative to the more refractory Mo and Ru. The fraction of Pd that remained in the gas phase experienced extensive mixing with other material in the ISM and did not preserve its original nucleosynthetic signature. Furthermore, I propose that the origin of nucleosynthetic variations in planetary bodies is selective processing of the volatile element-enriched dust that condensed in the ISM relative to 'stardust', which predominately formed around AGB stars.

Metal-silicate differentiation and fractional crystallisation in a solidifying core can result in mass-dependent isotope fractionation, which can be used to determine the conditions prevailing during core formation. To this end, a new  $^{104}\text{Pd}$ - $^{108}\text{Pd}$  double spike procedure was developed and verified (Chapter 5). Repeat measurements of the NIST SRM 3138 Pd standard yielded an external reproducibility (2 SD) of  $\pm 0.01$  ‰ for  $\delta^{106/105}\text{Pd}$ . Furthermore, three measurements of two aliquots of Gibeon (IVA) are within uncertainty of one another ( $-0.108$  ‰  $\pm 0.025$ ), demonstrating that our procedure is capable of high precision Pd isotope measurements. Modelling shows that the mass-independent Pd isotope variation observed in iron meteorites can affect the accuracy of the double spike inversion if this is not taken into account. Analyses of five iron meteorites from four groups (IAB, IID, IVA and IVB) yield  $\delta^{106/105}\text{Pd}$  compositions in the range  $-0.55$  to  $-0.134$  ‰. These values are heavier than those of chondrites and ureilites ( $-0.192$  ‰  $\pm 0.05$ ; Creech et al., 2017a). The  $\delta^{106/105}\text{Pd}$  values increase with Ni content of the iron meteorite samples. This indicates that the isotopic variations may be caused by fractional crystallisation. However, further studies are needed for a thorough evaluation of the origin of the observed variations.



# Zusammenfassung

Elemente, schwerer als Fe, wurden hauptsächlich durch Neutroneneinfang in Sternen über mehrere Generationen gebildet, bevor sie in den Staub um die Sterne oder im interstellaren Medium (ISM) kondensierten. Unser Sonnensystem bildete sich vor 4,5 Milliarden Jahren aus dem Gravitationskollaps einer dichten Molekülwolke und erbte einen Anteil dieser Staubpopulationen. Eine protoplanetare Scheibe bildete sich um unsere junge Sonne und die selektive Zerstörung von Staub führte zu kleinen Variationen in der Verteilung von Staub unterschiedlichen nukleosynthetischen Ursprungs. Dieser Staub akkretierte zu größeren Körpern, welche die nukleosynthetische Signatur des angehäuften Staubes bewahrten. In einigen dieser Körper differenzierten sich anschließend Metalle und Silikate. Durch die Kollisionen dieser planetaren Körper formten sich schließlich die terrestrischen Planeten. Die Erde bildete sich aus mehreren großen Zusammenstößen, deren letzter großer Einschlag zur Mondentstehung führte und mit dem die Erdkernbildung einherginge. Die letzten 0,5% der Masse der Erde wurden dem Mantel später über mehrere kleinere Einschlagkörper zugeführt.

In dieser Arbeit habe ich die (i) massenunabhängigen und (ii) massenabhängigen Pd-Isotopenzusammensetzungen einer Reihe von Eisenmeteoriten untersucht um zwei grundlegende Fragen zur Frühgeschichte unseres Sonnensystems zu beantworten: 1) welche Prozesse führten zu nukleosynthetischen Isotopenvariationen, die in vielen refraktären Elementen für Gesamt-Planetare-Körper beobachtet werden, und 2) welche Prozesse wirkten während der Metall-Silikat-Differenzierung auf der Erde und anderen planetaren Körpern? Für die Beantwortung dieser Fragen ist Palladium, ein Platingruppenelement, vielversprechend. Es besitzt sechs natürlich vorkommende Isotope, aus der Nukleosynthese von *p*-, *s*- und *r*-Prozessen, die es erlauben die Entstehung von nukleosynthetischen Variationen in planetaren Körpern zu untersuchen. Zudem ist Pd ein hoch-siderophiles Element, das während der Metall-Silikat-Differenzierung nahezu ausschließlich in die Metallphase übergeht. Zudem ist es flüchtiger als die anderen refraktären Elemente der Platingruppe. Aufgrund dieser Eigenschaften bietet es großes Potenzial, Informationen zu den Prozessen, welche während der Kernbildung und -erstarrung wirkten, zu liefern.

Um die dargelegten Fragen beantworten zu können, wurde eine neuartige analytische Methode für hochpräzise Pd-Isotopenanalysen mit Hilfe von MC-ICPMS entwickelt (Kapitel 2 und 3). Die Methode beinhaltet eine zweistufige Säulentrennung mit Anionenaustauscherharz. Die erste Anionenaustauschersäule ermöglicht die Abtrennung von Pd und Pt aus dem gleichen Probenaliquot eines Eisenmeteoriten. Platinisotope wurden in einer Begleitstudie weiter aufgereinigt und analysiert. Nach dem ersten Trennschritt wird Ru, welches isobare Interferenzen auf den Pd-Isotopenmassen bildet, aus der Pd-Fraktion durch Verflüchtigung in HClO<sub>4</sub> entfernt. Eine zweite Anionenaustauschersäule trennt Pd von den restlichen Matrixelementen, hauptsächlich Fe, Ni und Mo, ab. Die finale Pd-Fraktion liefert ein konstantes Ru / Pd-Verhältnis von weniger als 0,0005, welches die akkurate Korrektur von isobaren Interferenzen auf <sup>102</sup>Pd und <sup>104</sup>Pd und hochpräzise Isotopenanalysen mit Hilfe von MC-ICPMS ermöglicht. Diese Methode liefert eine externe Reproduzierbarkeit (2 Standardabweichungen, SD) von 1,58 für  $\epsilon^{102}\text{Pd}$ , 0,26 für  $\epsilon^{104}\text{Pd}$ , 0,13 für  $\epsilon^{106}\text{Pd}$  und 0,27 für  $\epsilon^{110}\text{Pd}$ , basierend auf wiederholten massenunabhängigen Messungen mehrerer Eisenmeteorite.

Mit Hilfe der neuen Analysetechnik wurde die massenunabhängige Pd-Isotopenzusammensetzung von 24 Eisenmeteoriten bestimmt, um die Prozesse zu untersuchen, die zu nucleosynthetischen Variationen in planetaren Körpern führen (Kapitel 4). Proben aus den IAB-, IIAB-, IID-, IIIAB-, IVA- und IVB-Gruppen wurden analysiert und zeigen eine große Spannweite in ihren Pd-Isotopenzusammensetzungen. Die IID-Probe Carbo-J zeigt die größten Abweichungen aller analysierten Proben in  $\epsilon^{104}\text{Pd}$  ( $1,5 \pm 0,25$ ) und  $\epsilon^{110}\text{Pd}$  ( $0,8 \pm 0,16$ ) von der terrestrischen Zusammensetzung. Die Variationen zwischen Proben der gleichen Gruppe stimmen gut mit den Effekten überein, die für kosmische Bestrahlung modelliert wurden. Nach der Korrektur für kosmische Strahleneffekte mit Hilfe von Pt-Isotopen zeigen vier Eisenmeteorit-Gruppen nucleosynthetische Isotopensignaturen, welche sich von der terrestrischen Zusammensetzung in der Reihenfolge IVA < IIIAB < IID  $\leq$  IVB unterscheiden, während die IAB- und IIAB-Gruppen keine auflösbaren Abweichungen zeigen. Die identifizierten Pd-Isotopenmuster stimmen mit Beobachtungen von benachbarten Elementen (Zr, Mo und Ru) mit einem Defizit des s-Prozesses überein. Die Pd-Isotopenvariationen korrelieren mit Isotopenvariationen von Mo und Ru. Die beobachtete Steigung passt jedoch nicht zu den Vorhersagen des s-Prozessmodells und zeigt eine 4 mal niedrigere Pd-Häufigkeit im s-Prozesskomponent an, als vorhergesagt. Meine bevorzugte Erklärung ist, dass das flüchtigere Pd weniger leicht in den Staub um AGB-Sterne kondensiert, im relativen Vergleich zu den stärker refraktären Elementen Mo und Ru. Die Fraktion von Pd, die in der Gasphase verblieb, erfuhr eine extensive Vermischung mit anderem Material im ISM und bewahrte ihre ursprüngliche nucleosynthetische Signatur nicht. Des Weiteren gehe ich davon aus, dass es sich bei der Entstehung von nucleosynthetischen Variationen in planetaren Körpern um eine selektive Verarbeitung des mit flüchtigen Elementen angereicherten Staubs handelt, relativ zu "Sternenstaub". Der mit flüchtigen Elementen angereicherte Staub kondensierte im ISM, während sich „Sternenstaub“ überwiegend um AGB-Sterne bildete.

Metall-Silikat-Differenzierung und fraktionierte Kristallisation in einem erstarrenden Kern können zu einer massenabhängigen Isotopenfraktionierung führen, mit der sich die bei der Kernbildung herrschenden Bedingungen bestimmen lassen. Zu diesem Zweck wurde eine neue  $^{104}\text{Pd}$ - $^{108}\text{Pd}$  Double-Spike-Methode entwickelt und verifiziert (Kapitel 5). Wiederholmessungen des Standards NIST SRM 3138 Pd ergaben eine externe Reproduzierbarkeit (2 SD) von  $\pm 0,01$  ‰ für  $\delta^{106/105}\text{Pd}$ . Darüber hinaus überlappen drei Messungen zweier Aliquote von Gibeon (IVA) innerhalb der Unsicherheit ( $-0,108 \pm 0,025$ ). Dies zeigt, dass unser Verfahren hochpräzise Pd-Isotopenmessungen möglich macht. Eine Modellierung zeigt, dass die in Eisenmeteoriten beobachtete massenunabhängige Pd-Isotopenvariation die Genauigkeit der Double-Spike-Inversion beeinflussen kann, wenn dies nicht berücksichtigt wird. Analysen von fünf Eisenmeteoriten aus vier Gruppen (IAB, IID, IVA und IVB) ergeben  $\delta^{106/105}\text{Pd}$ -Zusammensetzungen im Bereich von -0,55 bis -0,134. Diese Werte sind schwerer als die von Chondriten und Uililiten ( $-0,192 \pm 0,05$ ; Creech et al., 2017a). Die  $\delta^{106/105}\text{Pd}$ -Werte nehmen mit dem Ni-Gehalt der Eisenmeteoritproben zu. Dies zeigt an, dass die Isotopenschwankungen durch fraktionierte Kristallisation verursacht werden können. Es sind jedoch zusätzliche Studien erforderlich, um den Ursprung der beobachteten Variationen gründlich beurteilen zu können.

# Chapter 1

An introduction to cosmochemistry

## Introduction

Astronomy, the study of celestial objects, is often considered to be the oldest of the natural sciences. Many of the earliest civilisations made careful observations of the stars and other objects in the night sky. These observations were the basis of the first calendars and used in celestial navigation. Today we commonly associate astronomy with astrophysics. In current terminology, the work presented in this thesis falls under the category of cosmochemistry, which is the study of the chemical composition of extra-terrestrial objects.

Two of the most fundamental questions in cosmochemistry are, 1) What processes governed the formation of the early solar system, and 2) how did the Earth and the other terrestrial planets form. In this thesis, I will address these questions using Pd isotope variations in meteorites. Palladium has several chemical properties that make it ideal to investigate these questions. Palladium has six stable natural isotopes,  $^{102}\text{Pd}$ ,  $^{104}\text{Pd}$ ,  $^{105}\text{Pd}$ ,  $^{106}\text{Pd}$ ,  $^{108}\text{Pd}$  and  $^{110}\text{Pd}$ , and one extinct radiogenic isotope,  $^{107}\text{Pd}$ , with a half-life of only 6.5 million years. When considering planet formation, and in particular core formation, it is useful to group the elements based on their chemical affinities for either metal or silicate phases during differentiation. Elements that preferentially enter the metal fraction are called 'siderophile', while elements that partition into silicates are termed 'lithophile'. Palladium is commonly referred to as a platinum group element (PGE) and a highly siderophile element (HSE), together with Rh, Ru, Ir, Pt, Re, and Os. These elements nearly completely partition into the metal phase during metal-silicate differentiation, such as core formation on Earth and other planetary bodies. Another important characteristic for studying the early solar system is the volatility of an element. Volatility, commonly defined by the half-mass condensation temperature ( $T_c$ ), plays an important role in the distribution of elements in solids formed in the early solar system (Palme et al., 1988). Vaporisation and incomplete condensation of volatile elements in the young solar nebula is an important mechanism for the fractionation of elements and isotopes seen in planetary bodies (Lodders et al., 2009). Palladium is regarded as main component element and has the lowest condensation temperature of all the HSE (1324 K; Lodders, 2003; Palme and O'Neill, 2014)

The following sections will provide an overview of the formation of the universe, our solar system, and the bodies within it, including Earth. This is followed by a more detailed description of the different types of isotopic variations recorded in meteorites, and what this can tell us about the early history of the solar system. The final section of the introduction presents an outline of the project presented in this thesis.

### 1.1. A brief history of the universe

#### 1.1.1. The Big Bang and primordial nucleosynthesis

The prevailing theory for the origin of the universe is the so-called Big Bang theory. The idea that the universe formed from a singularity was first proposed by Lemaître (1931) in the response to the observation that the universe is expanding (Hubble, 1929). The theory gained popularity since it could successfully explain the abundance of H and He in the universe (Alpher et al., 1948), and through the prediction and subsequent discovery of cosmic microwave background radiation (CMB; Alpher and Herman, 1948; Penzias and Wilson, 1965). The current theory states that the universe formed from the

rapid inflation of a gravitational singularity of infinite density, with the Big Bang commonly referring to the initial moment of inflation. Approximately 380 thousand years after the Big Bang the universe became transparent, which enabled photons to travel freely for the first time and which today is measured as the CMB radiation. Measurements of the CMB imply that the universe formed 13.8 billion years (Gy) ago (Hinshaw et al., 2013). The first stars and galaxies in the universe appeared few hundred million years (My) after the Big Bang (Bromm et al., 2009).

The current theory states that primordial nucleosynthesis, which occurred in the first 20 minutes after the Big Bang synthesised all the H, essentially all the He, and part of the Li in the universe today (e.g. Iocco et al., 2009), with all other elements subsequently produced by nucleosynthesis in stars (see following section). The exception is the remaining Li plus the B and Be in the universe, which cannot be synthesised in stars and are thought to form from spallation of C, N and O by galactic cosmic rays (GCR) in the interstellar medium.

### 1.1.2. Stellar evolution and nucleosynthesis

*Stellar evolution:* The interstellar medium (ISM), the region between stars in a galaxy, is comprised primarily of primordial H and He gas with minor amounts of C, N and O gas and dust produced by previous generations of stars. The stars forming today do so as the result of gravitational collapse in small fragments of giant molecular clouds, the densest regions of the ISM (Figure 1.1a). Most of the mass of the collapsing cloud will accumulate into a very hot and dense protostar surrounded by a flat circular disk of material called a protoplanetary disk. Planets can form in the protoplanetary disk (Figure 1.1b), and this process is described in the next section. The evolution of stars is strongly dependent on their mass (Woosley et al., 2002), commonly measured in solar masses ( $M_{\odot}$ ), i.e. the mass of the star relative to our Sun. Essentially all elements heavier than B are synthesised in stars, which is commonly referred to as stellar nucleosynthesis and was first proposed by Burbidge et al. (1957), to explain the



**Figure 1.1.** Left image: The 'Pillars of Creation'. These dense molecular clouds are located in the Eagle nebula. Gravitational instabilities may cause small fragments of such clouds to collapse, forming new stars. Image Credit: NASA, ESA/Hubble and the Hubble Heritage Team. Right image: A picture of a protoplanetary disk surrounding a young star. The gaps in the disk are likely the result of planets sweeping their orbits clear of dust. Image Credit: ALMA (ESO/NAOJ/NRAO)

abundance of elements in the solar system (Figure 1.2). Elements with masses between B and Fe are produced primarily by fusion reactions at the centre of stars, while most elements heavier than Fe are produced either by neutron capture processes or the so-called  $p$ -process. Once the temperature at the core of the protostar reaches  $\sim 10$  million K fusion of H atoms into He will begin, turning the star into a main sequence star. This hydrogen burning stage will power a star for  $\sim 90\%$  of its lifetime (Heger et al., 2014). When all the hydrogen has been exhausted in the core, He burning will begin. Given sufficient mass, the star will successively move through C-, Ne-, O- and Si- burning stages before ending up with a core consisting almost entirely of Fe. Iron is the heaviest element that can be produced by fusion as formation of heavier elements is endothermic and thus requires more energy than it releases. If the mass of the Fe core exceeds the Chandrasekhar limit, the star will collapse forming either a black hole or a neutron star. This can result in a supernovae explosion whereby the star will eject most of its mass. Only stars with a mass larger than  $10 M_{\odot}$  are large enough to synthesise Fe in their cores (Woosley et al., 2002). The asymptotic giant branch (AGB) phase is the final evolutionary stage of stars with a mass between  $1 - 10 M_{\odot}$  and it is characterised by thin shells of H and He burning on top of a core of C and O (Herwig, 2005). After this stage the stars will gradually cool and become white dwarfs.

*Nucleosynthesis of elements heavier than Fe:* Neutron capture adds a neutron to a nucleus, thus increasing the mass of an isotope while retaining its initial charge, e.g.,  $^{104}_{46}\text{Pd} + {}^1_0n \rightarrow ^{105}_{46}\text{Pd} + \gamma$ . Inevitably, this will lead to the production of unstable isotopes with half-life's ranging from seconds to days. These isotopes will undergo beta minus ( $\beta^-$ ) decay, turning a neutron into a proton, thereby creating an isotope of the neighbouring element, e.g.,  $^{104}_{45}\text{Rh} \rightarrow ^{104}_{46}\text{Pd} + {}^0_{-1}\beta$ . The s-process, or slow neutron capture process, is responsible for synthesising roughly half of the elements with a mass above

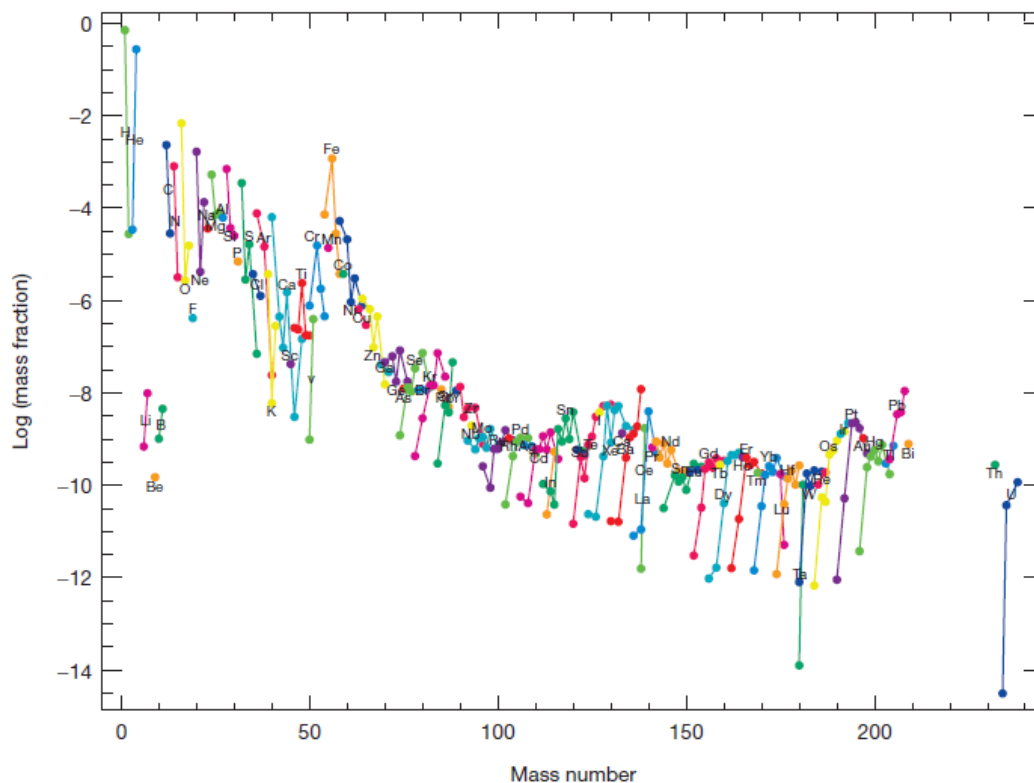


**Figure 1.2** A plot of the abundance of isotopes in the solar system against the mass number. Figure taken from Heger et al. (2014).

Fe e.g. Käppeler et al. (2011). Low neutron densities coupled with long timescales ensures that newly created unstable isotopes will have time to decay prior undergoing further neutron capture. Therefore, the *s*-process neutron capture path is close to the valley of beta stability (Figure 1.3b). Low mass (1 to 3  $M_{\odot}$ ) stars on the AGB phase of stellar evolution are believed to be the primary stellar site for nucleosynthesis of the *s*-process elements e.g. Arlandini et al. (1999). The relative production of *s*-process isotopes varies depending on stellar properties and the solar system is made up of a mixture of material from various generations of AGB stars (Busso et al., 1999; Zinner, 1998). Generalised models for the relative production of different elements and their isotopes exist, e.g. Arlandini et al. (1999) and Bisterzo et al. (2011), and these are generally in good agreement with solar system abundances.

The rapid neutron capture process, or *r*-process, is responsible for synthesising approximately half of the elements heavier than Fe (e.g. Thielemann et al., 2011). The *r*-process is characterised by short timescales and large neutron densities where unstable isotopes do not have time to decay between multiple successive neutron capture events. This forms isotopes deep into the neutron-rich regions outside the valley of beta stability (Figure 1.3b). Once the neutron flux has dissipated these undergo multiple steps of beta decay before they reach a stable isotope (Figure 1.3). Our solar system has

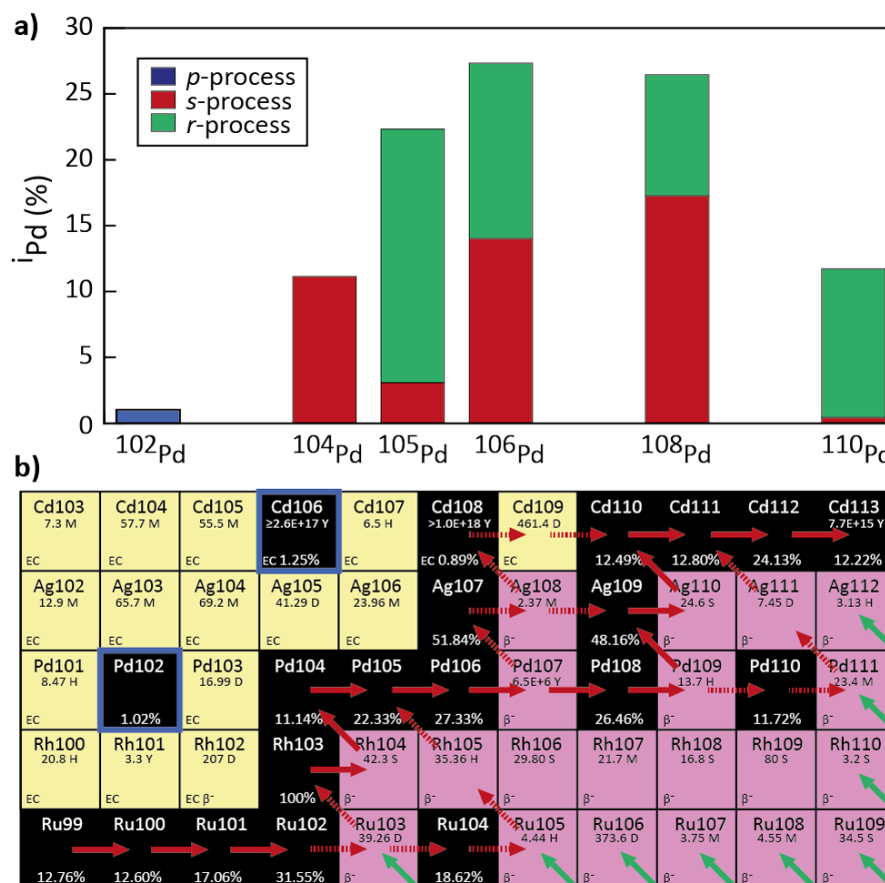


**Figure 1.3.** a) The abundance and nucleosynthetic origin of the six Pd isotopes. Based on the stellar production model from Arlandini et al. (1999). b) The chart of nuclides in the valley of stability surrounding Pd. Stable isotopes are highlighted in black. Proton rich isotopes that decay primarily by electron capture (EC) are shown in yellow, while neutron rich isotopes that undergo beta decay ( $\beta^-$ ) are shown in pink. The *s*-process path is highlighted with red arrows (dashed arrows represent minor contributions). The direction of the *r*-process contribution is shown as green arrows. Isotopes surrounded by blue squares are formed by the *p*-process.

contributions from at least two distinct *r*-processes. The first, weak *r*-process, is responsible for the production of the light elements ( $Z < 56$ ), while the second, main *r*-process, produces heavier elements (Wasserburg et al., 1996). Traditionally, the *r*-process has been linked to core collapse supernovae of massive ( $M_{\odot} > 10$ ) stars (e.g. Qian and Wasserburg, 2003). However, recently neutron star mergers have emerged as a favoured environment for production of *r*-process elements (e.g. Tsujimoto and Shigeyama, 2014). The first detection of gravitational waves from a neutron star merger in August 2017 by LIGO/Virgo provides strong evidence for the latter hypothesis (Côté et al., 2018).

The *p*-process is a collective term for the processes that synthesise proton rich isotopes that cannot be produced by neutron capture reactions (Figure 1.3b). The *p*-process is very ineffective and only contributes a small fraction of elements heavier than Fe, and as a result *p*-process isotopes generally have very low abundances compared to *s*- and *r*-process isotopes. They are also rare, with less than 35 *p*-process isotopes identified (Rauscher et al., 2013). Photodisintegration of heavy elements during Type II core collapse supernovae is thought to be responsible for at least a quarter of the *p*-process isotopes (Rayet et al., 1995) while at least half of the *p*-process isotopes are believed to have been synthesized in Type Ia supernovae of binary stars (Travaglio et al., 2011). However, the mechanisms and stellar environments that produce the *p*-process isotopes are poorly understood.

Palladium has one *p*-process isotope, the low abundance  $^{102}\text{Pd}$ , which cannot be reached by either the *s*-process or the *r*-process paths (Figure 1.3b). Palladium-104 is shielded from the *r*-process by  $^{104}\text{Ru}$  and is therefore a pure *s*-process isotope while the remaining isotopes ( $^{105}\text{Pd}$ ,  $^{106}\text{Pd}$ ,  $^{108}\text{Pd}$  and  $^{110}\text{Pd}$ ) have contributions from both the *s*-process and the *r*-process (Figure 1.3).

### 1.1.3. Solar system evolution

Our solar system is located in the Orion-Cygnus arm of the Milky Way galaxy. At present, it consists of four terrestrial planets (Mercury, Venus, Earth and Mars) and four giant gas planets (Jupiter, Saturn, Uranus and Neptune) that orbit around a central star (Figure 1.4). Many planets have one or several rocky moons orbiting them, the most famous being our own Moon. The asteroid belt lies between the orbits of Mars and Jupiter, and comprises a large collection of small (1 to 100s km in diameter) rocky bodies. Beyond the orbit of Neptune there are several dwarf planets, another belt of small rocky bodies called the Kuiper belt, and finally a large collection of comets defining the Oort cloud.

An improved version of the nebular hypothesis, originally proposed by Kant (1755), is the currently accepted model for the formation of our, and other, solar systems. It states that the formation of our solar system began with the gravitational collapse of a molecular cloud core. Conservation of angular momentum led to the formation of the solar nebula, a circular disk of gas and dust surrounding the early sun, as the cloud collapsed. Heating by radiation from the sun and by the release of gravitational energy from gas accreting onto the star resulted in a thermal gradient in the early solar nebula (Lewis, 1974). This led to the formation of the volatile-poor terrestrial planets in the inner disk, while the gas giants formed at greater radial distances where the temperature was lower, allowing volatile material to condense. The oldest materials in the solar system are refractory calcium aluminium-rich inclusions (CAI) that condensed 4568.22 My (Bouvier and Wadhwa, 2010) ago from a hot gas (Grossman, 1972), likely in a region close to the Sun. This age is commonly referred to as the age of the solar system, and



dating of events and material in the solar system are commonly made relative to CAI.

Terrestrial planet formation is thought to occur in several partially overlapping stages (Figure 1.5). The first stage began with coagulation of  $> 1 \mu\text{m}$  sized dust particles in the solar nebula to form millimetre- to centimetre-sized grains. In the second stage these grains coalesced into increasing larger objects until they reach 1 to 1,000 km in diameter objects called planetesimals, although the mechanisms for this growth are poorly understood (Chambers, 2014). The first planetesimals formed shortly after CAIs and continued to accrete until at least 4 My later (Dauphas and Chaussidon, 2011). Planetesimals grew into even larger bodies called planetary embryos (1,000 to 5,000's km in diameter) by accreting smaller bodies in their orbits around the sun (Dauphas and Chaussidon, 2011). Planetary embryos grew into planets ( $>10,000$  km in diameter) through giant impacts with other planetary embryos through a process called chaotic growth (Chambers, 2014). The decay of radiogenic isotopes, both short-lived and long-lived, and the energy generated from impacts meant that the interiors of many planetesimals and planetary embryos melted, differentiated, and formed iron-rich cores (Tonks and Melosh, 1992). Formation of planetary embryos began in the first few million years after CAI, concurrent with planetesimal formation, and lasted for 50-100 My (Dauphas and Chaussidon, 2011). The end result of this stage was the terrestrial planets, and a more detailed description of the evolution of Earth from this

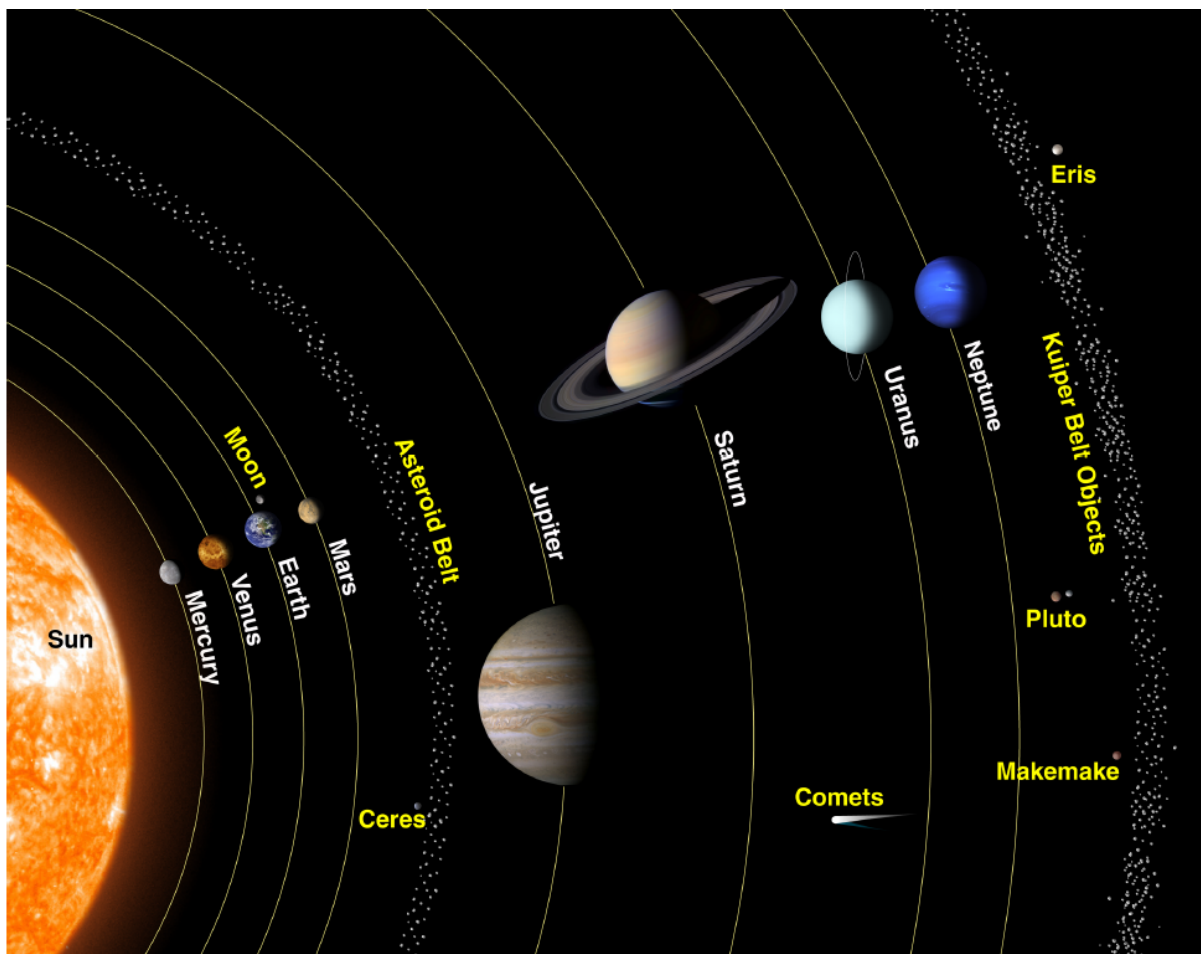


**Figure 1.4.** The relative position of the major bodies in the solar system. Bodies are not shown to scale. Closest to the sun are the four terrestrial planets (Mercury, Venus, Earth and Mars). Beyond Mars lie the four gas giants, Jupiter, Saturn, Uranus and Neptune. The asteroid belt is located between Mars and Jupiter, and the Kuiper Belt is found beyond Neptune. Also shown are four dwarf planets, Ceres, Pluto, Makemake and Eris. Image courtesy of NASA

stage onwards is given in the next section. The current favoured model for the formation of the gas giants is that they formed with rocky cores until they became large enough to gravitationally bind ice and gas from the disk (Levison et al., 2015). They must have formed before the gas dissipated from the solar nebula, which based on measurements of other protoplanetary disks is believed to have occurred within the first 10 My (Haisch et al., 2001).

#### 1.1.4. Early Earth History

The mass of the Earth, and other planets, is believed to have increased exponentially, with bodies acquiring most of their material early on. Halliday (2004) calculates the mean age of the Earth, i.e., the time by which it had acquired ~63 % of its current mass, to be  $4.550 \pm 0.003$  Gy or  $17 \pm 3$  My after the formation of CAIs. It is widely hypothesised that the Moon formed from a collision between Protoearth and an impacting Mars-sized planetary embryo (Cameron and Benz, 1991; Canup and Asphaug, 2001), although alternative models exist (Canup, 2012; Āuk and Stewart, 2012; Reufer et al., 2012). The Moon-forming collision is believed to represent the last major impact on Earth, contributing ~10 % of the mass of the Earth (Cameron and Benz, 1991; Canup and Asphaug, 2001) and bringing the total up to ~99.5 % of the present mass. There is a wide range of estimates for the timing of the Moon forming impact ranging from 10 to 120 My after the formation of CAIs (Halliday, 2014 and references therein). Core

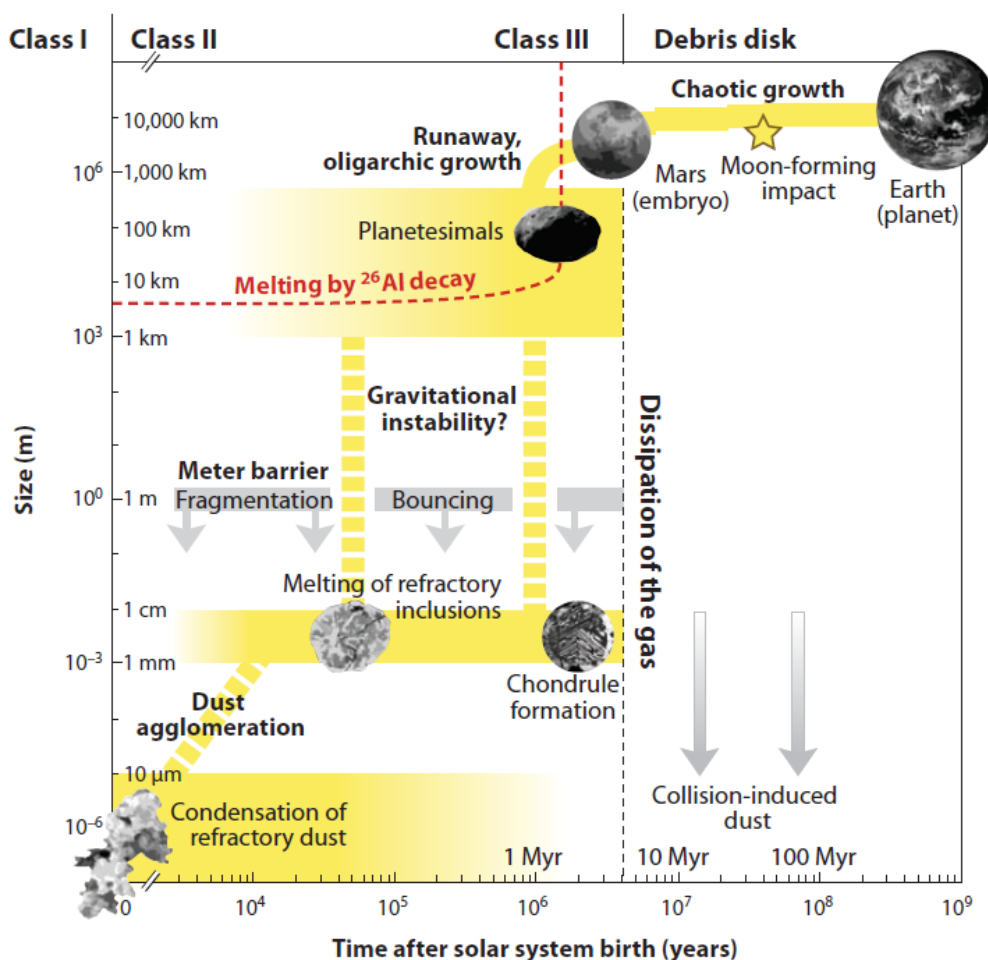


**Figure 1.5.** A summary of planet formation in the solar system. Starting with dust agglomeration to the formation of Earth. Image from Dauphas and Chaussidon (2011)

formation on Earth is expected to have occurred concurrent with accretion (Wetherill, 1990) as energy generated by giant impacts led to the formation of magma oceans (Benz and Cameron, 1990). After the Moon-forming impact the Earth cooled and core formation effectively ceased (Halliday, 2014). The final ~0.5 % of the Earth’s mass was added by impacts with smaller bodies (> 100 km) after the Moon-forming impact (Chou, 1978; Walker, 2009). These impacts were much too small to generate magma oceans and therefore the material added did not equilibrate with the core. This material, commonly referred to as the late veneer, can explain the absolute and relative concentration of HSEs in the bulk silicate earth (BSE; Figure 1.6), which cannot be easily reconciled with partitioning during core formation (Holzheid et al., 2000). The element abundance pattern of HSEs in the mantle suggests that the addition of chondritic material is responsible for the majority of the HSE in the BSE (Chou, 1978).

### 1.1.5. The Meteorite record

Much of the information we have about the chemical composition of solar system bodies other than the Earth comes from meteorites. Only a handful of samples have been collected in space and brought back to Earth, e.g., the Apollo sample return missions to the Moon. There are a few hundred meteorites from the Moon and Mars that were likely ejected by large impacts on these bodies. However, most of the meteorites in our collections are thought to originate from the asteroid belt. The asteroid belt is thought to comprise mainly fragments of planetesimals that failed to accrete onto bigger bodies, likely due to the presence of Jupiter. Collisions between asteroids can cause fragments of these bodies to enter unstable orbits and, as a result, they are ejected from the asteroid belt. Some of these asteroid fragments will move towards the Sun where there is a chance they will be captured by the gravitational field of the Earth.

Meteorites are classified based on their composition and textures and are categorised into chondrites and achondrites (Figure 1.7; Weisberg et al., 2006). Chondrites are undifferentiated meteorites which are thought to originate from parent bodies that did not melt, or possibly from the cool surface layers

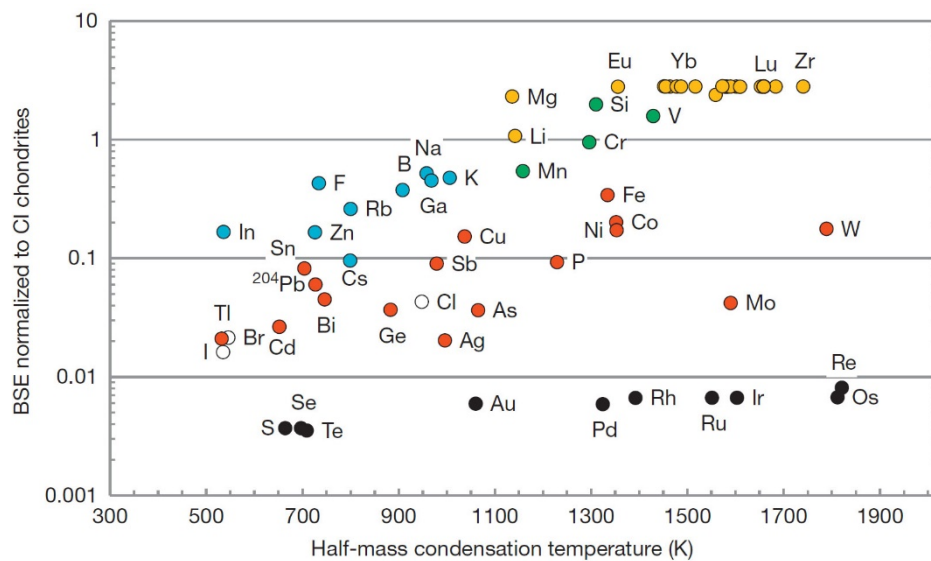


**Figure 1.6.** The estimated composition of the bulk silicate Earth relative to CI chondrite values (Anders and Grevesse (1989), ordered by  $T_c$  (Lodders (2003)). Yellow circles show lithophile elements, blue circles show volatile lithophile elements. Green circles show slightly siderophile elements, red circles show moderately siderophile elements and black circles shows highly siderophile and chalcophile elements that were strongly partitioned into the core. Open circles show halogens. Image from Halliday (2014).

of differentiated bodies (Elkins-Tanton et al., 2011). They are the most common type of meteorite and account for ~80 % of known specimens (Burbine et al., 2002). Achondrites are meteorites that have undergone various degrees of melting on their parent bodies (Weisberg et al., 2006). They account for the remaining ~20 % of identified meteorites (Burbine et al., 2002). Most achondrites are believed to originate from differentiated asteroids such as 4 Vesta (McSween et al., 2010), although a few are from the surface of the Moon and Mars. This study focuses on iron meteorites which account for 5 % of the meteorites collected (Burbine et al., 2002), although they represent a significant fraction of the mass of all collected meteorites. They comprise solid Fe and Ni (~< 20 wt% Ni) and most meteorites are believed to come from planetesimals that underwent metal-silicate differentiation due to large impacts and radiogenic heating by short-lived radioactive isotopes (Tonks and Melosh, 1992) In other words, they are believed to represent the metallic cores of differentiated planetesimals. The parent bodies of most the iron meteorites are believed to have accreted within the first ~ 0.5 My after CAI formation (Kruijer et al., 2014). Iron meteorites are divided into several different groups, where all members of a group are believed to have formed on the same parent body (Scott, 1972). Iron meteorites are enriched in the siderophile elements and are therefore ideal for studying the distribution of Pd isotopes in the early solar system.

Most meteorites available for scientific study are housed in collections at museums and scientific institutions. The samples analysed in this thesis were sourced from the meteorite collections at ETH Zürich, the Natural History Museum in London, the Smithsonian Institute in Washington D.C. and the Field Museum in Chicago.

## 1.2. Isotopic variations in meteorites

There are two types of isotopic variations found in geological materials: Mass-dependent and mass-independent variations. Mass-dependent Isotope variations are often associated with chemical exchange reactions, i.e., the partitioning of an element between different phases and are a function of isotope mass (Dauphas and Schauble, 2016). Isotopic variations uncorrelated to the isotopic mass are called mass-independent. Such isotopic variations are typically found in extra-terrestrial material and

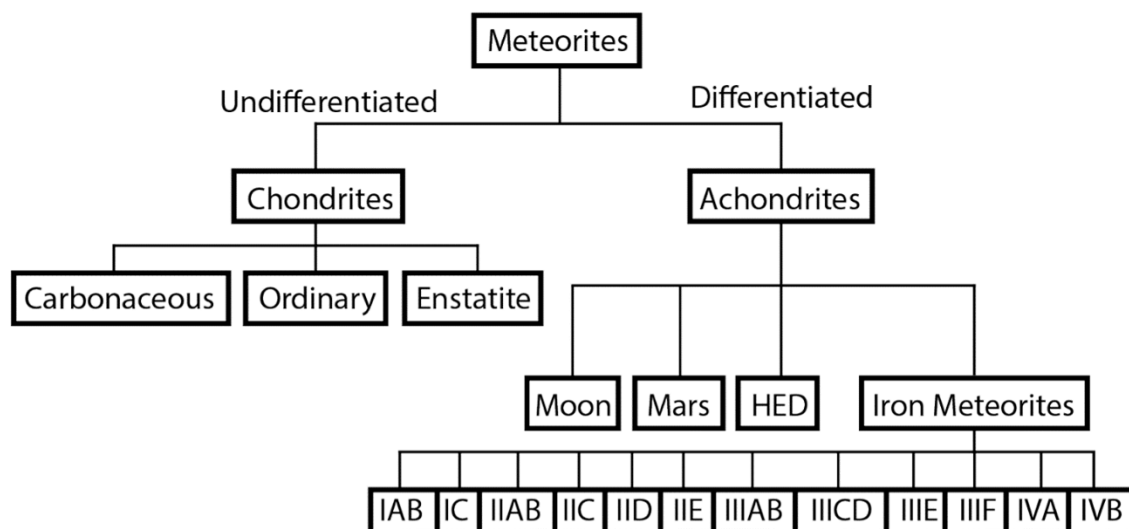


**Figure 1.7.** A simplified version of the classification of meteorites.

are related either to the heterogeneous distribution of nucleosynthetic material in the solar system or physical properties of isotopes other than mass. While both types of isotopic variation frequently occur together, they are generally studied separately as they require different analytical protocols. This thesis discusses both the mass-independent and mass-dependent isotope compositions of Pd in iron meteorites. In the following section the origin of these variations and their relevance to early solar system processes are briefly described.

### 1.2.1. The origin of mass-independent isotopic variations in the solar nebula

One important source of mass-independent isotopic variations is the heterogeneous distribution of dust in the solar nebula. There are two types of dust for the purposes of this study. Stardust, also referred to as presolar grains, formed in and around active stars and therefore retains a distinct nucleosynthetic composition (Zinner, 1998). The second type is dust that condensed from giant molecular clouds, containing gas from many different stellar sources, which will not carry a distinct isotope composition. Small variations in the distribution of stardust in the protoplanetary disk can generate planetary bodies with distinct nucleosynthetic signatures depending on their region of accretion. Nucleosynthetic isotope variations are reported as an isotopic ratio relative to the isotopic composition of the Earth, in parts per 10,000 ( $\epsilon$ ). Contributions to the isotopic variation of a sample by mass-dependent fractionation is commonly removed by internally normalising to a fixed isotopic ratio, using the exponential law (Russell et al., 1978). Excesses or deficits in the different nucleosynthetic endmembers will produce distinct isotopic patterns that can help identify the nucleosynthetic origin (Figure 1.8). Nucleosynthetic variations have been identified for a wide range of elements, including Pd (Mayer et al., 2015) and its

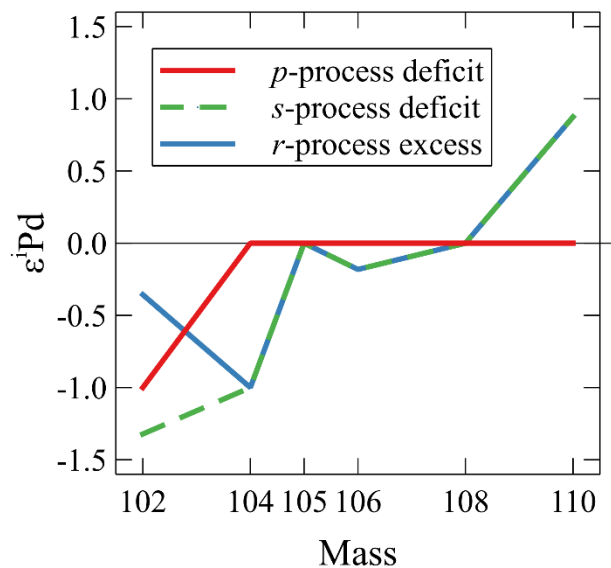


**Figure 1.8.** The nucleosynthetic pattern expected for mass-independent offsets in Pd, internally normalised to  $^{108}\text{Pd}/^{105}\text{Pd}$ . Red line shows a *p*-process deficit normalised to  $\epsilon^{102}\text{Pd} = -1$ . Dashed green line shows an *s*-process deficit and the blue line shows an *r*-process excess. Both lines are normalised to  $\epsilon^{104}\text{Pd} = -1$ . Note that the patterns for an *s*-process deficit and an *r*-process excess are identical except for  $\epsilon^{102}\text{Pd}$ . Based on the AGB stellar yields from Bisterzo et al. (2011).

neighbouring elements Zr (Akram et al., 2015), Mo (Burkhardt et al., 2014; Dauphas et al., 2002; Poole et al., 2017), and Ru (Chen et al., 2010; Dauphas et al., 2004; Fischer-Gödde et al., 2015; Fischer-Gödde and Kleine, 2017). However, for heavy elements ( $Z > 56$ ) either only very small nucleosynthetic variations were reported, e.g. Nd (Andreasen and Sharma, 2006; Burkhardt et al., 2016; Carlson et al., 2007) and W (Kruijer et al., 2013a; Qin et al., 2008; Wittig et al., 2013) or no such variations were observed, e.g. Hf (Sprung et al., 2010), Pt (Hunt et al., 2017a; Kruijer et al., 2013a) and Os (Walker, 2012; Yokoyama et al., 2007). No nucleosynthetic variations are reported for volatile elements, e.g. Cd (Kruijer et al., 2013b; Wombacher et al., 2008), Te (Fehr et al., 2005) and Zn (Chen et al., 2013). Palladium, which is more volatile than Zr, Mo and Ru and more refractory than Cd, Te and Zn can therefore provide valuable insight into the origin of

nucleosynthetic variations. A study of the Pd isotope composition of the IVB iron meteorite group by Mayer et al. (2015) found a smaller nucleosynthetic signature than that found in Mo and Ru. However, further studies of other iron meteorite groups are needed to determine whether Pd isotope variations are correlated with those of Mo and Ru.

A study of nucleosynthetic Ru variations for different meteorites found a correlation between the magnitude of the offset and the distance the parent body accreted from the sun (Figure 1.9; Fischer-Gödde and Kleine, 2017). Ruthenium isotopic variations can in turn be correlated with isotopic variations in Mo and Zr, and all three are characterised by a deficit in an s-process component (Akram et al., 2015; Dauphas et al., 2004; Fischer-Gödde et al., 2015; Poole et al., 2017). Several different theories have been put forward to explain the origin of nucleosynthetic variations in meteorites. One of the earliest theories proposed was that they represented a ‘cosmic chemical memory’ inherited from the ISM (Clayton, 1982). The modern consensus, however, favours that nucleosynthetic variations are formed from an initially well-mixed protoplanetary disk by processes in the early solar nebula. Grain sorting, either between different phases (Regelous et al., 2008) or by grain size (Dauphas et al., 2010) has been suggested as one possible process. However, such models struggle to explain the correlations observed in the nucleosynthetic signatures of multiple elements, owing to their affinities for different presolar grain types (Akram et al., 2015; Poole et al., 2017). Thermal processing of presolar material in the early solar nebula has also been put forward as a potential source of nucleosynthetic variations (Trinquier et al., 2009). Selective destruction of thermally more unstable components could lead to an enrichment in isotopically distinct presolar components. While this theory can explain many features of the nucleosynthetic variations, it struggles, in its present form, to explain why some heavy elements have nucleosynthetic variations while other do not. There is no single process currently proposed that can explain all the nucleosynthetic variations in the early solar nebula.

Nucleosynthetic variations are not the only type of mass-independent variations observed in meteorites. As meteoroids travel through space they are exposed to galactic cosmic rays (cosmic ray exposure; CRE) that can lead to significant mass-independent offsets (Leya and Masarik, 2013). As cosmic rays interact with the surface of the meteoroid, they produce secondary neutrons which, when

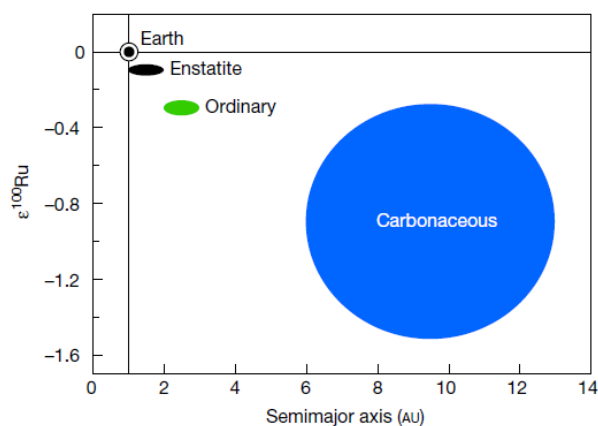


**Figure 1.9.** The nucleosynthetic offset in  $\epsilon^{100}\text{Ru}$  correlates with the distance from the sun the parent body is predicted to have formed. Figure from Fischer-Gödde and Kleine (2017)

they reach favourable energy levels, can lead to neutron capture within the meteoroid (Figure 1.10a). Unlike nucleosynthetic variations, which are identical for all meteorites from the same parent body, CRE will affect each meteorite differently. As a result, CRE can lead to significant isotopic variations between meteorites of the same group. Even pieces from a single meteorite sampled at different locations can show isotopic variations. Iron meteorites show the largest CRE effects due to their metal matrix (Leya and Masarik, 2013) and numerous studies have described CRE isotopic

variation in iron meteorites (Hunt et al., 2017a; Kruijjer et al., 2013a; Markowski et al., 2006; Wittig et al., 2013). The magnitude of isotopic offsets from CRE vary on a number of factors, including how long the meteoroid has been exposed in space, the position of a sample within the meteoroid, and the individual neutron cross sections of each isotope (Leya and Masarik, 2013). Additionally, the potential contribution to an isotope from the decay of CRE products from isotopes of other elements is an important factor. One such example is the contribution to  $^{104}\text{Pd}$  from the beta-decay of  $^{104}\text{Rh}$ , a product of neutron capture on  $^{103}\text{Rh}$ . The Rh/Pd ratio of a meteorite therefore becomes an important control on the CRE-induced isotopic variations seen in Pd (Figure 1.10b). Accounting for the contribution of CRE to the mass-independent signature of a meteorite is vital for studies of nucleosynthetic isotopic variations.

### 1.2.2. Parent body processes and mass-dependent isotopic fractionation

There are two types of mass-dependent isotope fractionation. Kinetic isotope fractionation occurs because lighter isotopes are ‘faster’ than heavier ones, meaning that when an element moves from one phase to another the second phase will initially be enriched in the light isotopes. The second type is called equilibrium fractionation and states that the heavy isotopes will be enriched in the phase with the stiffest bonds, which are characterised by the shortest bond length, highest oxidation and lowest coordination number (Schauble, 2004). Mass-dependent fractionation can occur in virtually all chemical exchange reactions, however, in this thesis we focus on those that occur during metal-silicate and metal-metal differentiation. Metal-silicate differentiation, such as core formation, is generally expected to enrich the silicate fraction in heavy isotopes while the metal fraction becomes enriched in light isotopes. This has been observed in nature where, for example, a study of the mass-dependent signature of Mo found that the terrestrial rocks and differentiated silicate meteorites have heavier isotopic compositions than iron meteorites (Burkhardt et al., 2014). Creech et al. (2017b) report that the present-day mantle has the same Pt isotope composition as iron meteorites and chondrites, which can be considered as analogues for the bulk composition of Earth, but that Archean samples (formed > 3.5 Gy ago) have a chondritic isotopic signature (Figure 1.11). This can be interpreted as evidence for isotopic fractionation during core formation followed by over-printing by material added during the late veneer. Both Mo and

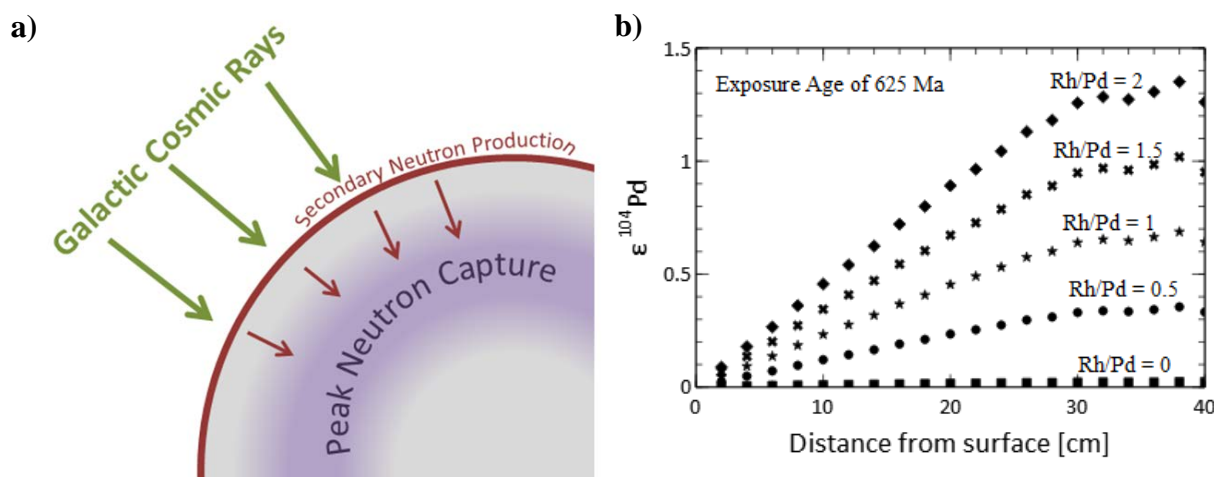


**Figure 1.10.** a) Schematic diagram showing the interaction of galactic cosmic rays with a meteoroid. As the cosmic rays interact with the meteoroid surface they produce secondary neutrons that at favourable energy levels result in neutron capture at depth inside the meteoroid. Figure from Kruijjer (2013) b) The offset in  $\epsilon^{104}\text{Pd}$  from cosmic ray exposure for a meteoroid with a 40 cm radius and different Rh/Pd ratios. Calculated using the equations from Leya and Masarik (2013)

Pt show a relatively homogenous mass-dependent signature among iron meteorites suggesting little isotopic fractionation takes place during the solidification of the core (Burkhardt et al., 2014; Creech et al., 2017b). In contrast, very large mass-dependent variations between different iron meteorites are found in Zn (Bridgestock et al., 2014) and Ru (Hopp et al., 2018). The former has been attributed to the formation of chromite, which preferentially sequesters light Zn isotopes as the core is solidifying (Bridgestock et al., 2014). The latter is explained as a result of liquid-solid metal fractionation (Hopp et al., 2016).

### 1.3. Thesis outline

The aim of this thesis is to assess the mass-independent and mass-dependent isotope variations of Pd in iron meteorites to better constrain 1) the origin of nucleosynthetic variations in the early solar system and 2) the processes that operate during metal-silicate differentiation and core solidification of planetary bodies. To achieve this, new methods for Pd purification and subsequent isotopic analysis by MC-ICPMS have been developed. The thesis can be divided into three parts:

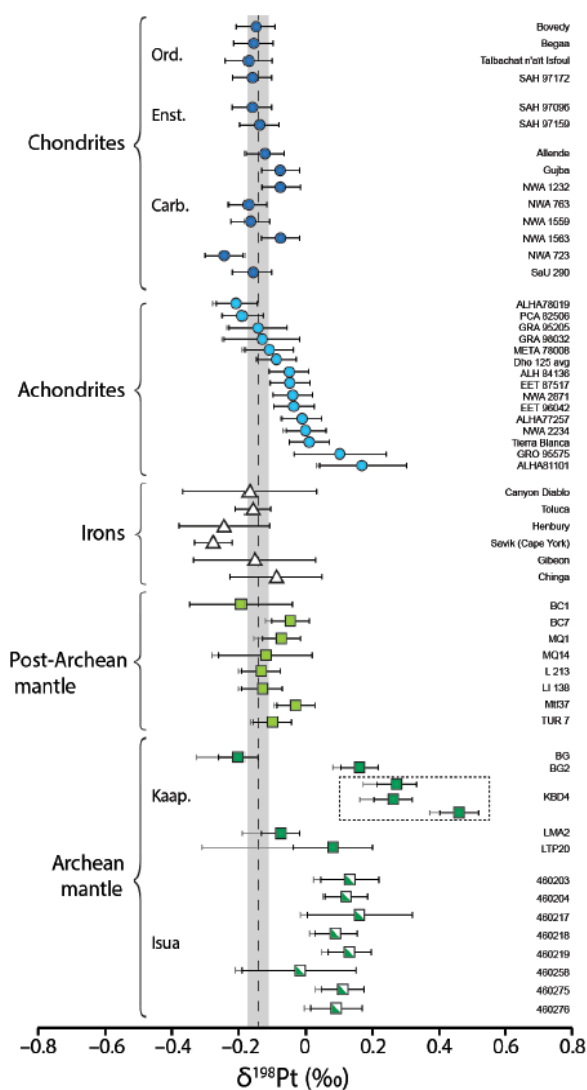


**Figure 1.11.** The stable isotope signature of  $\delta^{198}\text{Pt}$  for various terrestrial and extra-terrestrial rocks. Image from Creech et al. (2017b)

Chapters 2 and 3 describe a novel two-stage method for separation of Pd from an iron meteorite matrix. The first stage of our separation method, presented in Chapter 2, allows for the collection of both a Pd fraction and a Pt fraction from the same ion exchange column. This allows for direct comparison between isotopic variations in Pd and Pt without ambiguity. Chapter 3 describes the second stage of the separation method, where Ru is removed from the Pd fraction via volatilisation before a second ion exchange procedure is employed to remove the remaining matrix elements. The concentration of isobaric and molecular interferences in the final Pd fraction is consistently low enough to allow for accurate, high precision mass-independent and mass-dependent isotopic analysis, including the first accurate isotopic measurements of the low abundance  $^{102}\text{Pd}$  isotope. Chapter 3 also presents a method for high precision mass-independent isotopic analysis of Pd via MC-ICP-MS.

Chapter 4 presents the mass-independent Pd isotope composition of 24 iron meteorites from the IAB, IIAB, IID, IIIAB, IVA, and IVB groups. I evaluate the effects of cosmic ray exposure on Pd using the Pt isotope neutron dosimeter and



calculate the nucleosynthetic signature of each meteorite group. Several groups show resolvable nucleosynthetic offsets consistent with an *s*-process deficit that correlates with those found in Mo and Ru isotopes. However, the slope of the correlation does not match that predicted by stellar production models. I propose that this reflects incomplete condensation of Pd around AGB stars, relative to the more refractory Mo and Ru. Furthermore, I propose a new model for the origin of nucleosynthetic variations in the solar system based on selective processing of dust that condensed in the cold interstellar medium and ‘stardust’, dust that condensed around stars.

*Chapter 5* describes the development of a  $^{104}\text{Pd}$ – $^{108}\text{Pd}$  double spike for mass-dependent isotopic analysis of Pd. The calibrated spike is shown to be accurate for a wide range of sample-to-spike ratios. Repeat analyses of a synthetic iron meteorite doped with our Pd standard and processed using the method described in Chapters 1 and 2 show no resolvable offsets from the unprocessed standard. The mass-dependent Pd signature of five iron meteorites from the IAB, IID, IVA and IVB groups is presented. We see a range of  $\delta^{106/105}\text{Pd}$  signatures for the analysed iron meteorites that is generally heavier than that previously reported for chondrites. We present a preliminary discussion of the processes that may be responsible for the  $\delta^{106/105}\text{Pd}$  variation, based on our limited dataset.



# Chapter 2\*

## Initial separation of Pd and Pt from iron meteorites using ion exchange chromatography

\* a version of this chapter including further methods for Pt purification and isotopic analysis was published as: Hunt, A. C., Ek, M., Schönbacher, M. (2017) Separation of platinum from palladium and iridium in iron meteorites and accurate high precision analyses of platinum isotopes by multi-collector ICP-MS. *Geostandards and Geoanalytical Research* **216**, 82-95. The full manuscript is available as Appendix A

## 2.1. Introduction

In order to achieve high precision isotopic analyses, an element of interest must first be separated from the sample matrix. Palladium has isobaric interferences from Ru (on  $^{102}\text{Pd}$  and  $^{104}\text{Pd}$ ) and Cd (on  $^{106}\text{Pd}$ ,  $^{108}\text{Pd}$ , and  $^{110}\text{Pd}$ ) plus several potential molecular interferences (e.g.  $^{62}\text{Ni}^{40}\text{Ar}$ ,  $^{64}\text{Zn}^{40}\text{Ar}$ , and  $^{60}\text{Zr}^{16}\text{O}$ ) that can severely affect the accuracy of any isotopic measurements. The reader is referred to Chapter 3 for an in-depth discussion on the effects of isobaric and molecular interferences on isotopic determinations of Pd. Previous methods do not separate Pd sufficiently from potential interferences to allow accurate isotopic measurements of all Pd isotopes (Chu et al., 2015; Mayer et al., 2015; Rehkämper and Halliday, 1997). In this study, separation of Pd from the sample was achieved using a novel two-stage ion exchange chromatography procedure. The first stage is presented in this chapter and provides an initial separation of Pd from an iron meteorite matrix. This procedure was published as Hunt et al. (2017b; Appendix A). Significantly, this first stage in ion exchange procedure also allows for the collection of Pt isotopes. This is important because it enables offsets in Pt and Pd isotopes to be directly correlated, which is vital for the interpretation of nucleosynthetic versus CRE effects (Chapter 4). Further purification of Pd is achieved through a second stage, which is presented in Chapter 3.

## 2.2. Methods

### 2.2.1. Reagents and Materials

Throughout this study, all nitric ( $\text{HNO}_3$ ) and hydrochloric acids ( $\text{HCl}$ ) were twice distilled in Teflon stills and concentrated acids have molarities of  $\sim 14.2$  M and  $\sim 9.8$  M, respectively. Acid mixtures were titrated before use and diluted using MQ grade  $\text{H}_2\text{O}$  ( $>18.2$  M $\Omega$ .cm). Merck Millipore Bromine 99.9999 % SUPRAPUR<sup>®</sup> was used in the preparation of bromine-saturated solutions. Before use, the bromine solution was cleaned by repeatedly adding and decanting MQ water. Bromine saturated water (Br-water) was prepared and used within 24 hours of each ion exchange chemistry session.

BioRad<sup>™</sup> AG<sup>®</sup> 1-X8 (200 – 400 mesh, chloride form) resin was used for the ion exchange procedure. The resin was batched cleaned using 0.8 M  $\text{HNO}_3$  followed by 3 M  $\text{HNO}_3$ , concentrated  $\text{HNO}_3$ , 3 M  $\text{HNO}_3$ , 4 M  $\text{HCl}$ , concentrated  $\text{HCl}$  and finally 6 M  $\text{HCl}$ . The volume of acid used for each step was at least five times the volume of resin being cleaned.

### 2.2.2. Sample preparation and dissolution

All iron meteorites were abraded using silicon carbide paper to remove any weathering and fusion crust, and to polish any cut surfaces. A Buehler Isomet<sup>™</sup> low speed saw fitted with a CBN blade using ethanol as a cooling fluid was used to sub-sample larger pieces when necessary. Prior to sample dissolution samples were rinsed in ethanol in an ultrasonic bath for 5 minutes, followed by leaching in cold 2 M  $\text{HCl}$  for an additional 5 minutes. Samples were then digested in a 2:1 mixture of concentrated  $\text{HNO}_3$  and  $\text{HCl}$  using 8 ml of acid per gram of sample. Samples were refluxed for approximately 48 hours at 100 °C, during which time they were placed into an ultrasonic bath at least twice, before being taken to dryness. Samples were then redissolved in concentrated  $\text{HCl}$  overnight. The resulting solution was clear and free of undigested material.

### 2.2.3. Ion exchange chromatography

The first anion exchange procedure is based on that developed by Rehkämper and Halliday (1997; Method 1). A 0.3 g aliquot was taken from the digested mass for each column. Each aliquot was dried and then refluxed in a 2:1 mixture of concentrated HNO<sub>3</sub> and HCl at 100-110 °C for approximately 48 hours. The aliquots were dried again and redissolved in 10 ml 0.5 M HCl + 10 % Br-water and refluxed for ~48 hours at 100-110 °C.

A quartz glass column was loaded with 1.25 ml of AG1-X8 resin. The columns had an internal diameter of 6 mm and the resin was supported by a quartz wool bed. The resin was cleaned by subsequent washes of 0.8 M HNO<sub>3</sub> (20 ml), concentrated HCl (10 ml), and concentrated HNO<sub>3</sub> (25 ml) before being converted back to chloride form with 40 ml of 6 M HCl (Table 2.1). Prior to sample loading, the column was pre-conditioned with 8 ml of 0.5 M HCl + 10 % Br-water. The sample solution was loaded onto the column in 10 ml 0.5 M HCl + 10 % Br-water, which was followed by a 12 ml rinse of 1 M HCl + 10 % Br-water that eluted most of the Fe, Ni and Co from the column (Figure 2.1; Table 2.1). This was followed by 5.5 ml of 0.8 M HNO<sub>3</sub> + 10 % Br-water and 12 ml of concentrated HCl, which removed Zn, Cd, Ag and Ru from the column (Figure 2.1; Table 2.1). Palladium was eluted in five 2 ml steps of 8 M HNO<sub>3</sub> heated to 80 °C. This was followed by elution of Pt in 14 ml 13.5 M HNO<sub>3</sub> (Figure 2.1; Table 2.1). The Pd fraction was taken to dryness in preparation for the second stage of Pd purification, which is described in Chapter 3. The Pt cut was processed further as described in Hunt et al. (2017b; Appendix A).

### 2.3. Results and discussion

The Pd yields after the first column were typically 70-80 %, although could be as low as 50 % in meteorite samples. Significant tailing of its elution peak hampers the collection of Pd. Up to 20 % of the total Pd was eluted in the Pt fraction, and another ~8 % was frequently present in a 10 ml concentrated HNO<sub>3</sub> clean-up fraction collected after the elution of Pt (Figure 2.1). However, tests with synthetic meteorite samples (Fe and Ni powders doped with the NIST SRM 3138 Pd standard) frequently yielded better than 95 % Pd, suggesting that oxidation state plays an important role in determining the yield. The samples were therefore refluxed in aqua regia for ~48 hours before the first ion exchange column in an attempt to fully oxidise the sample.

**Table 2.1.** The separation procedure for the first ion exchange column.

Step	Acid	Volume	Elements eluted
<b>Resin cleaning</b>			
	0.8 M HNO <sub>3</sub>	20 ml	
	concentrated HCl	10 ml	Pd
	concentrated HNO <sub>3</sub>	25 ml	Pt, Pd and Ir
	6 M HCl	40 ml	
<b>Sample procedure</b>			
Precondition	0.5 M HCl + 10 % Br-water	8 ml	
Loading and matrix elution	0.5 M HCl + 10 % Br-water	10 ml	Fe, Ni, Co, Cr, W
Matrix elution	1 M HCl + 10 % Br-water	12 ml	Fe, Ni, Co, Cr, minor Ru elution.
Matrix elution	0.8 M HNO <sub>3</sub> + 10 % Br-water	5.5 ml	Zn, Cd; Limited elution of Ir.
Matrix elution	concentrated HCl	12 ml	Ag, Ru
Pd elution	8 M HNO <sub>3</sub> (80 – 90 °C)	10 ml	Pd with Ru and trace Fe, Ni, Cr
Pt elution	13.5 M HNO <sub>3</sub>	14 ml	Pt with Ir and trace Fe, Ni, Cr

Additionally, Rehkämper and Halliday (1997) used fire-assay to pre-concentrate the PGEs, which also removed most of the iron matrix. That technique is associated with high blanks and variable Pd yields (Gros et al., 2002; Rehkämper and Halliday, 1997; Ren et al., 2016) and therefore a hotplate digestion was used in this study, which is sufficient for complete dissolution of iron meteorites. As a result, the acid volumes for first steps on the column were increased to remove the larger concentration of matrix elements present. The loading acid was also changed to 0.5 M HCl + 10 % Br-water because lower HCl concentrations reduce the partition coefficient for Fe onto anion resin, while increasing the partition coefficients for Pd and Pt (Kraus and Nelson, 1956). This study utilised Br-water during the ion exchange procedure. Bromine-water acts to keep Ir oxidised during the chemical procedure (Rehkämper and Halliday, 1997), and its use here may be counter-intuitive. This is because Ir is eluted with Pt when Br-water is used, but Ir causes significant difficulties during the analysis of Pt isotopes (e.g. Hunt et al., 2017b; Kruijer et al., 2013a; Wittig et al., 2013). However, the use of Br-water was found to narrow the elution peak for Pd and to reduce tailing into the Pt fraction.

## 2.4. Conclusion

We present a method for initial separation of Pd and Pt from an iron meteorite matrix. The yield of Pd is 70 - 80 % however, the Pd fraction needs further purification before isotopic analysis. This is achieved with a second ion exchange procedure presented in Chapter 3.

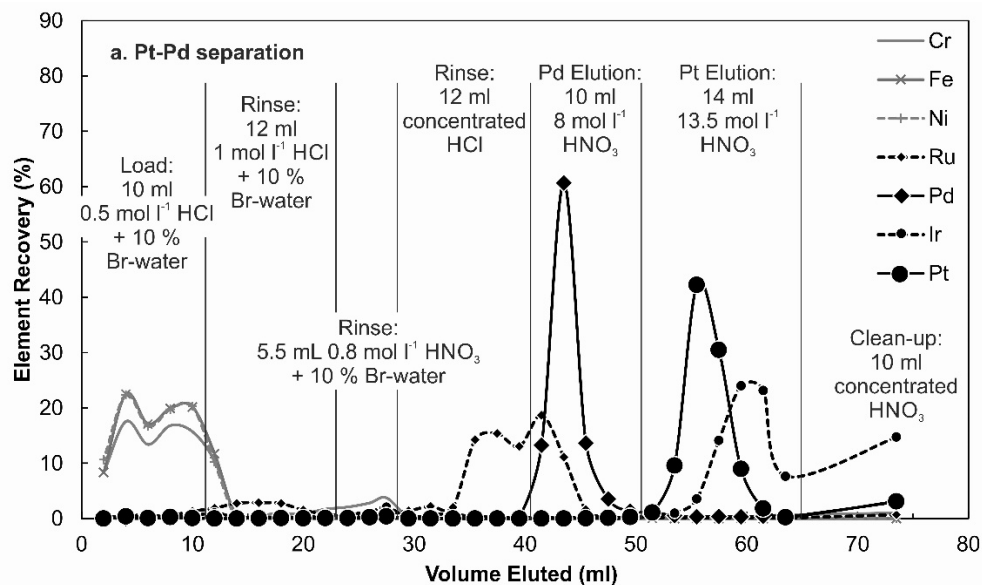


**Figure 2.1.** Elution curve for the first ion exchange procedure, showing the separation of Pd and Pt from a synthetic iron meteorite matrix. Image from Hunt et al. (2017b).

# Chapter 3\*

## A new method for high-precision Palladium isotope analyses of iron meteorites and other metal samples

\*a version of this chapter was published as: Ek, M., Hunt, A. C., Schönächler, M. (2017) A new method for high-precision Palladium isotope analyses of iron meteorites and other metal samples. *Journal of Analytical Atomic Spectrometry* **32**, 647-656.

## Abstract

This paper presents a new method for high precision Pd isotope analyses in iron meteorites. First Pd is separated from the sample matrix by a novel two-stage anion exchange procedure after which isotopic measurements are carried out using MC-ICPMS. Analyses of doped standard solutions show that isobaric interferences from Ru and Cd can be adequately corrected for  $Ru/Pd < 0.0005$  and  $Cd/Pd < 0.025$ . This is frequently achieved using the presented separation method. The purified Pd fraction after the ion exchange chromatography is also sufficiently devoid of Ni ( $Ni/Pd < 0.04$ ), Zr ( $Zr/Pd < 0.0002$ ), and Zn ( $Zn/Pd < 0.06$ ) for precise and accurate measurements because these elements produce molecular interferences on the masses of the Pd isotopes. An external reproducibility of 1.29 for  $\epsilon^{102}Pd$ , 0.22 for  $\epsilon^{104}Pd$ , 0.11 for  $\epsilon^{106}Pd$ , and 0.27 for  $\epsilon^{110}Pd$  is calculated based on the repeat analyses of five independently processed aliquots of the IAB iron meteorite Toluca. The method was verified by the analysis of three metals from IVB iron meteorites and the results show excellent agreement with previous data. The new method enables accurate analysis of all Pd isotopes, and in particular  $^{102}Pd$ , which is of major interest for cosmochemical applications.

## 3.1. Introduction

Palladium belongs to the main component elements that are predicted to condense from a gas of solar composition, together with elements such as, e.g., Fe and Ni. It is therefore considered moderately refractory (Lodders, 2003; Palme and O'Neill, 2014). Palladium is also a highly siderophile element (HSE) and together with the other HSE, strongly partitions into the metal fraction during metal-silicate differentiation, which leads to enrichments in iron meteorites and severe depletion in silicates and the Earth's mantle (e.g., Mann et al., 2012; Palme and O'Neill, 2014; Righter, 2011). Hence, Pd isotope variations could prove a useful and powerful tool for addressing a number of key questions outlined below.

First, in the recent years it has become obvious that many elements display small, but well resolvable, nucleosynthetic variations (0.1 per mil range) in meteorites compared to terrestrial samples. Meteorite parent bodies, Mars, and the Earth display unique isotope compositions for a range of elements, e.g. Cr, Ti, Ni, Zr and Mo (e.g., Akram et al., 2015; Steele et al., 2012; Trinquier et al., 2008; Trinquier et al., 2009). These variations stem from the heterogeneous distribution of presolar dust in the solar system carrying highly anomalous isotopic compositions that were synthesised in various stellar environments. They are extremely useful for meteorite provenance studies and provide important constraints on mixing processes in the early solar system. Iron meteorites are thought to represent the core of asteroids that formed, and were subsequently destroyed, throughout the solar system during the early stages of planet formation (Weisberg et al., 2006). Nucleosynthetic isotope variations in iron meteorites are reported for Ni, Ru, Mo, W and Pd (e.g., Burkhardt et al., 2011; Chen et al., 2010; Fischer-Gödde et al., 2015; Kruijer et al., 2013a; Mayer et al., 2015; Qin et al., 2008; Regelous et al., 2008; Wittig et al., 2013). Palladium is an ideal element to further investigate these variations because it features six stable isotopes that are produced in different stellar environments: one *p*-process isotope ( $^{102}Pd$ ), one *s*-process isotope ( $^{104}Pd$ ), one predominately *r*-process isotope ( $^{110}Pd$ ) and three isotopes ( $^{105}Pd, ^{106}Pd, ^{108}Pd$ ) that are a mixture between *s*- and *r*-process (Bisterzo et al., 2011). Accurate measurements of the *p*-process isotope  $^{102}Pd$  are necessary to differentiate between *s*-process and *r*-



process variations that would otherwise be indistinguishable in meteorites. A recent Pd isotope study investigating IVB iron meteorites (Mayer et al., 2015) reported that Pd nucleosynthetic isotope variations are smaller than those of Ru and Mo, and suggested that this reflects selective destruction of their carrier phases in the solar nebula. However, further high precision Pd isotope analyses for other iron meteorite groups are needed to better constrain this observation.

Moreover, meteorites are exposed to galactic cosmic rays (GCR) during their journeys in space. Modelling of GCR exposure for iron meteorites shows that significant isotopic shifts can be induced in many elements, including Pd (Leya and Masarik, 2013). Thus, it is important to quantify the GCR effects on Pd isotopes, because Pd isotope variations can be the result of both nucleosynthetic processes and exposure to GCR in space. Isotopic shifts are caused by the capture of secondary neutrons produced by nuclear reactions in meteorites due to the irradiation by GCR (e.g.  $^{104}_{46}\text{Pd} + \frac{1}{0}\text{n} \rightarrow ^{105}_{46}\text{Pd} + \gamma$ ). The magnitude of these reactions depends on several factors: (i) isotope-specific properties such as the neutron capture cross section; (ii) meteorite properties such as matrix composition, original depth of sample within the meteoroid and time of exposure to GCR; and (iii) epithermal burnout of other elements resulting in the production of unstable isotopes that decay to the isotopes of interest (e.g.,  $^{103}_{45}\text{Rh} + \frac{1}{0}\text{n} \rightarrow ^{104}_{45}\text{Rh} \rightarrow ^{104}_{46}\text{Pd} + \beta^-$ ). All Pd isotopes possess relatively small neutron capture cross sections resulting in small ( $\sim < 0.2 \epsilon$ ) isotopic shifts, even for samples with optimal sample depth and large exposure times. Nevertheless, epithermal burnout of  $^{103}\text{Rh}$  can lead to larger ( $> 1 \epsilon$ ) isotopic shifts in  $^{104}\text{Pd}$ , particularly due to the similar abundance of Rh and Pd in iron meteorites. Epithermal burnout of  $^{107,109}\text{Ag}$  also occurs but due to the low Ag/Pd ( $\sim < 1 \times 10^{-4}$ ) ratio in iron meteorites mean this reaction is negligible with current precision.

Another motivation to understand and quantify GCR effects in Pd isotopes is the Pd-Ag dating system (e.g. Schönbächler et al., 2008; Theis et al., 2013). This chronometer is based on the short-lived isotope  $^{107}\text{Pd}$ , which decays to  $^{107}\text{Ag}$  with a half-life of 6.5 Ma. Cosmogenic production of the short-lived isotope  $^{107}\text{Pd}$  could affect the accuracy of the Pd-Ag dating system (Leya and Masarik, 2013; Matthes et al., 2015). High precision Pd isotope analyses, together with the well-established Pt GCR neutron dosimeter, should enable a thorough evaluation of the GCR effects on Pd-Ag chronometry.

Finally, Pd isotopes are a potentially powerful tool to determine the origin of Pd and other HSE in the Earth. There are two end member scenarios to explain the origin of the HSE elements in the Earth's mantle. One proposes that the concentration of HSEs in the mantle reflects the addition of a so-called 'late veneer' to the Earth, post-core-formation (e.g., Chou, 1978; Walker, 2009). The second scenario states that the Pd (and other HSE) concentration of the mantle may be achieved during metal-silicate fractionation and core formation in a deep magma ocean, negating the need for a late veneer (Mann et al., 2012; Righter et al., 2008). The terrestrial nucleosynthetic signature relative to meteorites may provide constraints on the source of Pd in the Earth, particularly when correlated with other elements, e.g., Mo (Burkhardt et al., 2011) and Ru (Fischer-Gödde et al., 2015).

In order to achieve accurate high precision Pd isotope measurements, it is important that Pd is thoroughly separated from matrix elements, which can cause interferences and matrix effects during analysis. For example, Pd isotopes suffer from isobaric interferences from Ru and Cd isotopes (Table

3.1). While Cd abundances are low in iron meteorites, Ru can occur in concentrations similar to Pd (e.g., Hoashi et al., 1993). In particular, high precision measurements of the low abundance  $^{102}\text{Pd}$  (1.02 %) are hampered due to the high abundance of  $^{102}\text{Ru}$  (30 %), if Ru is not sufficiently removed prior to mass spectrometric analysis. Molecular interferences from matrix elements (i.e., Ni, Zn, Zr) can also affect the precision and accuracy of the isotopic analyses. Existing procedures for Pd separation from geological matrices are either aimed at abundance determination and do not sufficiently remove matrix elements to enable accurate high precision isotope analyses (Chu et al., 2015; Rehkämper and Halliday, 1997), or fail to efficiently separate Pd from Ru (Mayer et al., 2015).

Here we present a new method for high precision Pd isotope measurements involving a two-step ion exchange procedure to separate Pd from an iron meteorite matrix. Initial separation of Pd is achieved using a modified version of the ion exchange procedure of Rehkämper and Halliday (1997), described in further detail by Hunt et al. (2017b). This method allows the collection of both Pd and Pt from the same sample aliquot, enabling direct comparison with the well-established Pt neutron dosimeter. The Pd elution from the first ion exchange column requires further purification before isotopic measurements and a novel procedure to achieve this goal is presented here. First, Ru is removed from the Pd fraction by utilising its volatile nature. Then Pd is separated from the remaining matrix elements using an anion exchange column. This yields a final Pd fraction that is sufficiently devoid of matrix elements, including Ru, to allow for high precision isotopic measurements of all isotopes via multi-collector ICPMS (MC-ICPMS). The accuracy of our method was verified by processing one IAB, three IVB

**Table 3.1.** Collector configuration and isotopic abundances of the isotopes, isobaric interferences and major molecular interferences.

	101	102	104	105	106	107	108	110	111
<b>Collector configuration</b>									
Cup	L4	L3	L2	L1	C	H1	H2	H3	H4
Resistor ( $\Omega$ )	$10^{12}$	$10^{11}$	$10^{11}$	$10^{11}$	$10^{11}$	$10^{11}$	$10^{11}$	$10^{11}$	$10^{12}$
<b>Isotope abundances of Pd and isobaric elements (in %; Berglund and Wieser, 2011).</b>									
Ru	17.06	31.55	18.62						
Pd		1.02	11.14	22.33	27.33		26.46	11.72	
Cd					1.25		0.89	12.49	12.8
<b>Major molecular interferences and their isotopic abundance (in %; Berglund and Wieser, 2011).</b>									
M <sup>1</sup> H	$^{100}\text{Ru}$ (12.59)	$^{101}\text{Ru}$ (17.06)		$^{105}\text{Ru}$ (18.62)					
			$^{103}\text{Rh}$ (100)				$^{107}\text{Ag}$ (51.83)	$^{109}\text{Ag}$ (48.16)	
M <sup>40</sup> Ar	$^{61}\text{Ni}$ (1.14)	$^{62}\text{Ni}$ (3.63)	$^{64}\text{Ni}$ (0.93)						
			$^{64}\text{Zn}$ (49.17)		$^{66}\text{Zn}$ (27.73)	$^{68}\text{Zn}$ (4.04)	$^{68}\text{Zn}$ (18.45)	$^{70}\text{Zn}$ (0.61)	
M <sup>16</sup> O					$^{90}\text{Zr}$ (51.45)	$^{91}\text{Zr}$ (11.22)	$^{92}\text{Zr}$ (17.15)	$^{94}\text{Zr}$ (17.38)	
							$^{92}\text{Mo}$ (14.65)	$^{94}\text{Mo}$ (9.19)	$^{96}\text{Mo}$ (15.87)

iron meteorites and terrestrial standard solutions. Our new analytical method achieves the necessary precision and accuracy to enable the thorough evaluation of GCR effects and nucleosynthetic isotope variations in iron meteorites.

## **3.2. Methods**

### 3.2.1. Reagents & Materials

Hydrochloric (HCl) and nitric (HNO<sub>3</sub>) acids used in this study were twice distilled, while hydrofluoric (HF) acids used were once distilled in dedicated Savillex Teflon stills. The final concentration of these acids after distillation is ~9.6, ~13.9 and ~30 M for HCl, HNO<sub>3</sub> and HF respectively. Merck Suprapur® Perchloric (HClO<sub>4</sub>) acid (70%) and Merck Millipore Bromine Suprapur® (99.9999%) were used without further purification. Reagents were mixed using 18.4 MΩ.cm water supplied by a Millipore™ (MilliQ©) system. All acids and acid mixtures were titrated before use to ensure accurate molarities. BioRad AG1-X8 resin (200-400 mesh, chloride form) was utilised, and batched cleaned before use (Hunt et al., 2017b).

### 3.2.2. Sample digestion

The sample digestion procedure is described in Hunt et al. (2017b) and a short description of the procedure is given here. Prior to digestion and where necessary, the meteorite samples were sawn using a CBN blade operated with ethanol as a cooling fluid. Weathering and fusion crusts were removed using silicon carbide paper. Sample dissolution and ion exchange procedures were performed in laminar flow hoods in a clean laboratory environment. Prior to dissolution, samples were submerged in ethanol in an ultrasonic bath, followed by leaching in cold 2 M HCl for 5 minutes. Samples were dissolved in a 2:1 mixture of concentrated HNO<sub>3</sub> and HCl at 100 °C for 48 hours. They were then dried and re-dissolved in concentrated HCl at 100 °C for 48 hours, which yielded clear solutions of brown colour, indicating that they were fully dissolved.

### 3.2.3. Ion-exchange procedure

Palladium was purified in a two-stage ion exchange procedure. The first stage is adapted from Rehkämper and Halliday (1997) and described in detail by Hunt et al. (2017b). After acid digestion, up to 0.3 g of each sample was refluxed at 110 °C in a 2:1 mixture of concentrated HCl and HNO<sub>3</sub> (aqua regia) for ~48 hours before being evaporated to dryness. Next the samples were refluxed overnight (~18 hours) in 0.5 M HCl + 10 % Br<sub>2</sub>-water at 110 °C before being cooled to room temperature. Each aliquot was loaded onto a glass column with 1.25 ml of pre-cleaned BioRad AG1-X8 resin, which was preconditioned with 0.5 M HCl + 10 % Br<sub>2</sub>-water (Table 3.2). Loading was followed by the addition of 1 M HCl + 10% Br<sub>2</sub>-water, 0.8 M HNO<sub>3</sub> + 10 % Br<sub>2</sub>-water, and concentrated HCl to elute matrix elements including Fe, Ni and Ru (Table 3.2). Palladium was eluted from the column in 10 ml of hot (90 °C) 8 M HNO<sub>3</sub> and finally Pt was eluted in 14 ml of 13.5 M HNO<sub>3</sub>. The Pd fraction was taken to dryness in preparation for the Ru evaporation stage. The Pt fraction was further processed following the procedure described in Hunt et al. (2017b).

Ruthenium was removed from the Pd fraction via volatilisation. The Pd fraction from the first ion exchange column was refluxed in 2 ml aqua regia for 48 hours at 110 °C, after which the solution was allowed to cool before 0.3 ml HClO<sub>4</sub> was added. The solution was then dried down at 210 °C. This step was repeated twice to ensure maximum Ru loss before the second ion exchange column. Tests revealed

that evaporation of Ru after the second ion exchange column was much less efficient.

The second ion exchange column was designed to remove matrix elements (notably Fe, Mo, Ru, Ni, Zr) that remained in the Pd fraction after the first column. In preparation for the second column the Pd fractions were refluxed overnight (~18 hours) in 1 ml 4 M HF before being taken to dryness and again refluxed overnight in 1 ml of 4 M HF. Teflon columns (with an internal diameter of 5 mm) were loaded with 0.5 ml BioRad AG1-X8 resin and rinsed with 10 ml 0.8 M HNO<sub>3</sub>, 10 ml concentrated HCl, 10 ml HNO<sub>3</sub>, and finally 20 ml 6 M HCl, before being preconditioned with 8 ml 4 M HF (Table 3.2). The sample was loaded onto the column, and rinsed with 1 ml 4 M HF. Most non-transition metals have very low absorption in HF onto the anion resin and eluted directly (Faris, 1960; Schönbacher and Fehr, 2014). This was followed by 5 ml of 6 M HNO<sub>3</sub> to elute remaining Ru and Mo. Subsequently, 4 ml concentrated HCl was added to reduce tailing of Ru into the Pd fraction. Palladium was then eluted in 4 ml concentrated HCl followed by 6 ml 13.5 M HNO<sub>3</sub>. The final Pd fraction was generally devoid of elements that potentially form molecular interferences (see section 4.1-2) to enable accurate isotopic determination. This sequence of HCl and HNO<sub>3</sub> minimised the tailing of Pd that occurred otherwise. The Pd cuts were taken to dryness, then refluxed in 1 ml 5 M HNO<sub>3</sub> at 110 °C overnight before evaporation and preparation for isotopic analyses.

#### 3.2.4. Yields and procedural blanks

The yield from the first column was typically 70-80 %, based on Pd concentrations of iron meteorites from literature compared to the recovered Pd after the separation procedure. Yields for the second column were often > 70 %, although yields as low as 50% were observed. The total yield for both columns was generally > 50 %. In most cases the final Ru/Pd ratio of samples processed with the method outlined here was < 0.0005, however, on rare occasions samples with higher Ru/Pd ratios were observed. These samples were passed through the second column again to reduce their Ru/Pd ratio. Up to 20 % of the Ru loaded onto the second ion exchange column can be eluted in the Pd fraction. This

**Table 3.2.** Palladium ion exchange chromatography

First ion exchange procedure <sup>a</sup>			Second ion exchange procedure		
Resin Volume: 1.25 ml AG1-X8			Resin Volume: 0.5 ml AG1-X8		
Step	Acid	Volume	Step	Acid	Volume
Cleaning	0.8 M HNO <sub>3</sub>	20 ml	Cleaning	0.8 M HNO <sub>3</sub>	10 ml
	Concentrated HCl	10 ml		Concentrated HCl	10 ml
	Concentrated HNO <sub>3</sub>	25 ml		Concentrated HNO <sub>3</sub>	10 ml
	6 M HCl	40 ml		6 M HCl	20 ml
Preconditioning	0.5 M HCl + 10 % Br <sub>2</sub> <sup>b</sup>	8 ml	Preconditioning	4 M HF	8 ml
Sample loading	0.5 M HCl + 10 % Br <sub>2</sub> <sup>b</sup>	10 ml	Sample loading	4 M HF	1 ml
Rinse matrix	1 M HCl + 10 % Br <sub>2</sub> <sup>b</sup>	12 ml	Fe, Ni, Ru	4 M HF	1 ml
Rinse matrix	0.8 M HNO <sub>3</sub> + 10 % Br <sub>2</sub> <sup>b</sup>	5.5 ml	Ru, Mo	6 M HNO <sub>3</sub>	5 ml
Ru	Concentrated HCl	12 ml	Ru, Mo	Concentrated HCl	4 ml
Pd, Ru	8 M HNO <sub>3</sub> (80 – 90 °C) <sup>c</sup>	10 ml	Pd	Concentrated HCl	4 ml
Pt, Ir	13.5 M HNO <sub>3</sub>	14 ml	Pd (Ru)	13.5 M HNO <sub>3</sub>	6 ml

<sup>a</sup> From Hunt et al. (2017b). <sup>b</sup> As bromine saturated water. <sup>c</sup> Loaded in 5 steps of 2 ml

highlights the importance of the Ru volatilisation step, where 80 – 100 % of the Ru remaining after the first ion exchange column is lost. Cadmium concentrations are low in iron meteorites (< 20 ppb Rosman and Laeter, 1974) and negligible amounts of Cd (Cd/Pd ratios < 0.00001) were determined in the final Pd fraction. Procedural blanks for the ion exchange procedures were routinely collected and were always < 1.2 ng Pd per g sample. No blank correction was therefore necessary since typically > 300 ng of Pd was collected for each sample.

### **3.3. Mass Spectrometry**

#### 3.3.1. Instrumentation and data collection protocols

All measurements were carried out at ETH Zürich using a Thermo Fisher Scientific Neptune *Plus* MC-ICPMS operated in low resolution mode. Standard H-cones were used and samples were introduced into the plasma using a Cetac Aridus II desolvating system and a nebuliser with an uptake rate of 100  $\mu\text{l min}^{-1}$ . All Pd isotopes were measured simultaneously with  $10^{11} \Omega$  resistors, while also monitoring  $^{101}\text{Ru}$  and  $^{111}\text{Cd}$  using  $10^{12} \Omega$  resistors (Table 3.1). Before each sample/standard measurement an on-peak baseline (OPB) was measured using a solution containing an acid matrix identical to the subsequent sample/standard. Each OPB and standard/sample measurement consisted of a 30 s electronic baseline measurement followed by collection of 60 integrations (4.7 s each). A peak centre was also performed prior to each sample/standard analysis. Between measurements the sample introduction system was washed with 0.5 M  $\text{HNO}_3$  for ~20 min to reduce the background signal to below  $1/50^{\text{th}}$  of the original standard/sample signal. Samples were bracketed by measurements of the NIST SRM 3138 Pd standard solution at concentrations that were generally within 15% of the sample. All analyses were carried out in a 0.5 M  $\text{HNO}_3$  acid matrix, and solutions were diluted to achieve a signal of 5 to 7 V on  $^{105}\text{Pd}$ , typically 100  $\text{ng ml}^{-1}$  Pd, when possible. A single measurement typically consumed 1 ml (~100 ng of Pd) of solution and took 10 minutes to complete. The sensitivity of the instrument was between 240 and 340 V  $\text{ppm}^{-1}$  Pd. The concentrations of matrix elements in the sample solution were checked during each analytical session prior to sample analysis.

#### 3.3.2. Interference correction and data reduction.

Prior to the interference correction all analyses were background-corrected using the OPB collected before to each sample/standard analysis. Analyses were corrected for instrumental mass fractionation ( $\beta$ ) using the exponential law (Russell et al., 1978), and were internally normalised to  $^{108}\text{Pd}/^{105}\text{Pd} = 1.18899$  (Kelly and Wasserburg, 1978). Isobaric interferences from Ru ( $^{102}\text{Pd}$  and  $^{104}\text{Pd}$ ) and Cd ( $^{106}\text{Pd}$ ,  $^{108}\text{Pd}$ ,  $^{110}\text{Pd}$ ) were corrected using the following procedure. First, the  $\beta$  value for  $^{108}\text{Pd}/^{105}\text{Pd} = 1.18899$  was calculated using the measured intensities on mass 105 ( $^{105}\text{Pd}$ ) and mass 108 ( $^{108}\text{Pd} + ^{108}\text{Cd}$ ). The contribution on mass 108 from  $^{108}\text{Cd}$  was calculated using this  $\beta$  value and the measured intensity on mass 111 ( $^{111}\text{Cd}$ ) together with isotopic abundances of Cd from Rosman et al. (1980). The calculated  $^{108}\text{Cd}$  signal was then subtracted from the measured signal on mass 108 and a new  $\beta$  for  $^{108}\text{Pd}/^{105}\text{Pd}$  was calculated. This correction procedure was repeated until  $\beta$  converged. The final  $\beta$  value was then used to correct for  $^{106}\text{Cd}$  and  $^{110}\text{Cd}$  using  $^{111}\text{Cd}$  and for interferences from  $^{102}\text{Ru}$  and  $^{104}\text{Ru}$  using  $^{101}\text{Ru}$  as an interference monitor together with isotopic abundances from Huang and Masuda (1997). Results are reported relative to  $^{105}\text{Pd}$  in epsilon notation ( $\epsilon$ ), i.e., the deviation of the sample from the average of two bracketing NIST SRM 3138 Pd standards, given in parts per 10,000.

### 3.4. Results and Discussion

#### 3.4.1. Isobaric interferences

Isobaric interferences on Pd isotopes are caused by Ru and Cd isotopes (Table 3.1). Analysis of NIST SRM 3138 standard solutions doped with Ru and Cd (Table 3.4; Figure 3.1) demonstrate that Ru/Pd and Cd/Pd ratios of up to 0.001 and 0.025 (respectively) can be accurately corrected within our external reproducibility (discussed in section 4.3). Above these thresholds the correction breaks down and Ru is under-corrected, yielding positive values for  $\epsilon^{102}\text{Pd}$  and  $\epsilon^{104}\text{Pd}$  (Figure 3.1A), while Cd is over-corrected, generating negative values, most noticeably on  $\epsilon^{110}\text{Pd}$  (Figure 3.1B).

#### 3.4.2. Molecular interferences.

Molecular interferences from hydrides (Rh and Ag), argides (Ni and Zn) and oxides (Zr and Mo) can cause spectral interferences on several Pd isotopes (Table 3.1). Doped Pd standard solutions were analysed in order to constrain the level of these elements that can be tolerated in the final Pd fraction without jeopardizing the accuracy of the data.

Interferences from Ni (on  $^{101}\text{Ru}$ ,  $^{102}\text{Pd}$  and  $^{104}\text{Pd}$ ) and Zn (on  $^{104}\text{Pd}$  and  $^{106}\text{Pd}$ ) argides produce isotopic shifts outside of our external reproducibility at Ni/Pd > 0.04 and Zn/Pd > 0.06, (Table 3.3; Figure 3.1C). Samples processed through our ion exchange procedure rarely yielded Ni/Pd ratios above 0.005 and no sample was above the threshold ratio of 0.04. For Zn/Pd, ratios below 0.06 were consistently achieved after the ion exchange chemistry (Table 3.3; Figure 3.1D). Our analyses showed that the main source of Zn in our solutions was contamination during the final stages of sample preparation and it is therefore important to monitor the Zn/Pd ratio of samples before every analysis. Our doping tests revealed that production of  $^x\text{Zr}^{16}\text{O}$  depends on the instrumental settings and that ZrO/Zr ratios up to 0.2 can be produced. It is therefore vital to determine ZrO/Zr prior to each analytical session. Typically, the

**Table 3.3.** The upper limit of elemental ratios that allow for accurate interference correction

	$^{102}\text{Pd}$	$^{104}\text{Pd}$	$^{106}\text{Pd}$	$^{110}\text{Pd}$
Ru/Pd <sup>a</sup>	0.0005	0.0005		
Cd/Pd <sup>a</sup>			0.1	0.025
Ni/Pd	0.04	0.1		
Zn/Pd		0.06	0.1	
Zr/Pd <sup>b</sup>			0.0002	0.0005
Mo/Pd <sup>c</sup>				> 0.34 <sup>c</sup>
Rh/Pd <sup>c</sup>		> 0.5 <sup>c</sup>		
Ag/Pd <sup>c</sup>				> 0.28 <sup>c</sup>

<sup>a</sup> An interference correction is applied to correct for isobaric interferences from Ru and Cd. The correction yield erroneous Pd isotope data if concentrations exceeds indicated limits. <sup>b</sup> This ratio is dependent on the ZrO production during the analyses on the Neptune MC-ICPMS, which varies from session to session. Limits stated are for a ZrO/Zr value of 2%. <sup>c</sup> No isotopic shifts were detected for this ratio, which is at least 10 times larger than that in sample solutions.

instrument was calibrated to achieve ZrO/Zr ratios < 0.02. Zirconium/Pd ratios below 0.002 do not induce isotopic shifts outside of our external reproducibility, when ZrO/Zr = 0.02 (Table 3.3; Figure 3.1E). Generally, most samples yielded Zr/Pd ratios below 0.00015 after ion exchange chromatography, which is well below the threshold if the production of ZrO is minimised. No isotopic shifts were observed for Mo/Pd ratios below 0.34 (Table 3.3), while Mo/Pd in sample solutions after ion exchange chemistry is typically below 0.005. Additionally, standards with Pt/Pd ratios of up to 0.22 did not introduce resolvable isotopic shifts. This ratio is higher than the typical values obtained for iron meteorites after our ion exchange procedure. Rhenium and Ag can cause both isobaric interferences in the form of hydrides and tailing effects on adjacent isotopes (Table 3.1).

However, doping tests at up to  $\text{Ru/Pd} = 0.5$  and  $\text{Ag/Pd} = 0.28$  show no resolvable isotopic shifts. These levels are well above what is observed in samples ( $\text{Ru/Pd} < 0.01$ ,  $\text{Ag/Pd} < 0.0001$ ) after ion exchange chemistry. Samples with elemental ratios exceeding the stated thresholds (Table 3.3) were re-processed through the second ion exchange procedure to further purify the samples and achieve accurate results.

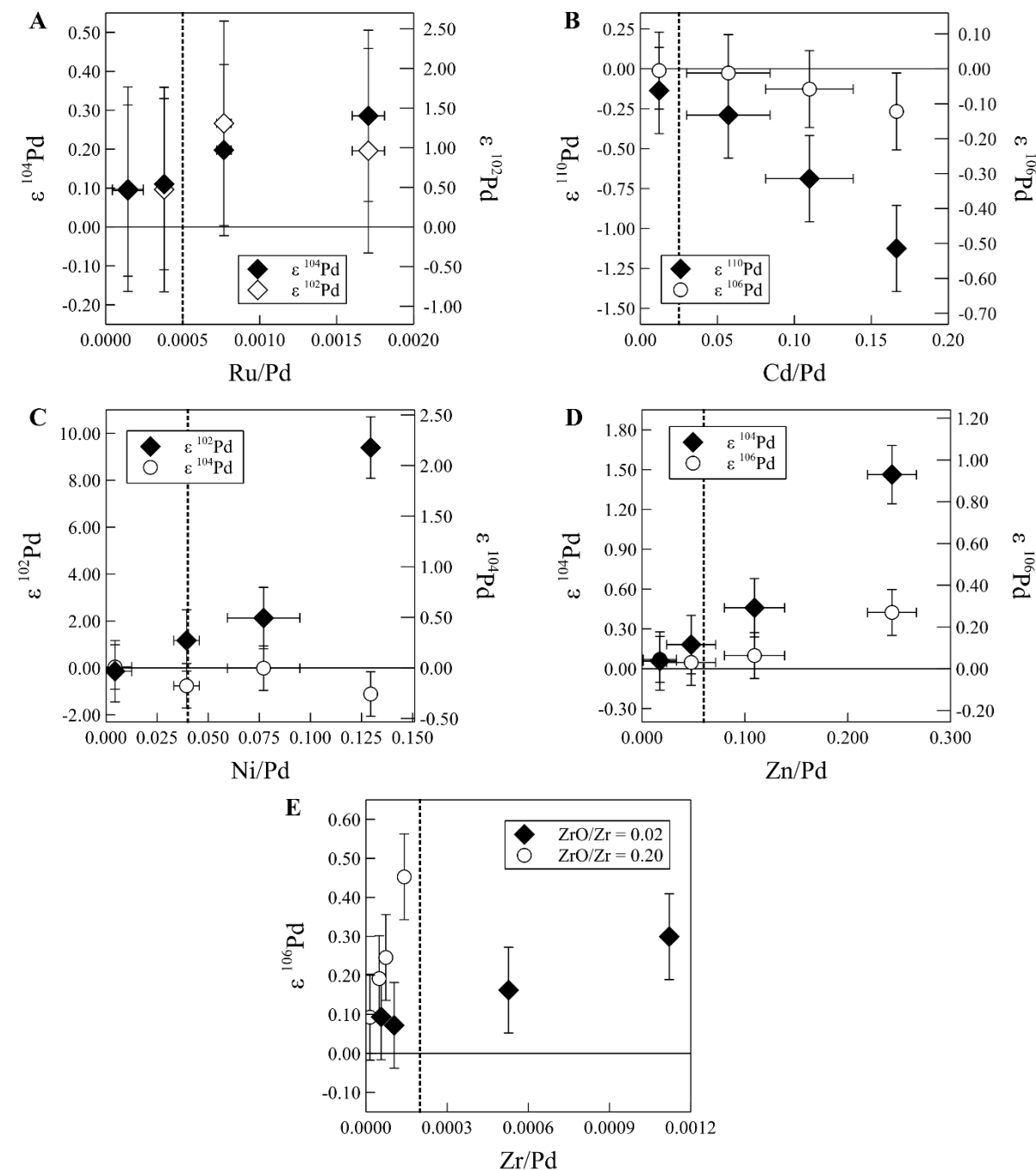


**Figure 3.1.** Palladium isotope compositions obtained for a 100ppb NIST SRM 3138 standard solution doped with Ru (A) and Cd (B), after interference correction, and varying amounts of Ni (C), Zn (D) and Zr (E). Data points shown are the mean of several analyses. Uncertainties of the isotopic data are reported as our 2 sd external reproducibility derived from Toluca, while, the uncertainty on the elemental ratios is given as the 2 sd of the analysed samples. The vertical dotted line represents the tolerance limit for each element. (A) Accurate corrections for the Ru isobaric interferences can be achieved for  $\text{Ru/Pd}$  below 0.0005. (B) Isobaric interferences from Cd can be accurately corrected for up to  $\text{Cd/Pd}$  ratios of 0.025. Ratios below (C)  $\text{Ni/Pd} = 0.04$ , (D)  $\text{Zn/Pd} = 0.06$ , (E)  $\text{Zr/Pd} = 0.0002$  (for  $\text{ZrO/Zr} = 0.02$ ), do not cause any resolvable isotopic shifts outside of our external reproducibility.

### 3.4.3. Reproducibility and accuracy

*Standard solutions:* The long-term average for a 100 ppb NIST SRM 3138 Pd standard solution analysed over the course of three years and 30 analytical sessions is  $^{102}\text{Pd}/^{105}\text{Pd} = 0.045392 \pm 5$ ,  $^{104}\text{Pd}/^{105}\text{Pd} = 0.496938 \pm 30$ ,  $^{106}\text{Pd}/^{105}\text{Pd} = 1.222805 \pm 48$ ,  $^{110}\text{Pd}/^{105}\text{Pd} = 0.526763 \pm 34$  (uncertainties are  $2\sigma$  standard deviations, 2 sd; Figure 3.2). The absolute values calculated from these ratios are within 0.03 % of those reported by Kelly and Wasserburg (1978), while the IUPAC recommended values (Berglund and Wieser, 2011; Shima et al., 1978) (after re-normalisation to  $^{108}\text{Pd}/^{105}\text{Pd} = 1.18899$ ) are within 0.22 %. The typical reproducibility (2 sd) of the Pd standard solution within an analytical session is 1.19 for  $\epsilon^{102}\text{Pd}$ , 0.17 for  $\epsilon^{104}\text{Pd}$ , 0.09 for  $\epsilon^{106}\text{Pd}$ , and 0.20 for  $\epsilon^{110}\text{Pd}$ . Three aliquots of NIST SRM 3138 doped with Fe, Ni, and Ru at levels present in iron meteorites were processed through our entire ion exchange procedure separately. Within uncertainty, the means of each aliquot overlap with each other and the mean of the entire data set yielded no resolvable differences from the unprocessed bracketing standard (Table 3.4). This verifies the accuracy of our data and demonstrates that (i) isotope fractionation did not occur during the ion exchange procedure beyond that corrected for using the internal normalisation procedure, and (ii) that all isobaric and molecular interferences were either accurately corrected for or absent in the analysed fractions.

*IAB iron meteorites:* Repeat measurements of five independently processed sample aliquots of the IAB iron meteorite Toluca (ETH meteorite collection) were performed to assess the sample reproducibility of our method for a sample with a natural matrix. The means of all aliquots overlap within uncertainty for all isotopes (Table 3.5; Figure 3.3) which indicates that there is no isotopic difference between the aliquots. The reproducibility calculated based on our entire Toluca data set ( $n=20$ ; 2 sd) is 1.29 for  $\epsilon^{102}\text{Pd}$ , 0.22 for  $\epsilon^{104}\text{Pd}$ , 0.11 for  $\epsilon^{106}\text{Pd}$ , and 0.27 for  $\epsilon^{110}\text{Pd}$  (Fig 3.3). These uncertainties are similar or slightly higher compared to those calculated from the doped synthetic solutions (Table 3.4), which we attribute to the more complex matrix of the natural samples. Since they were obtained on natural samples, we

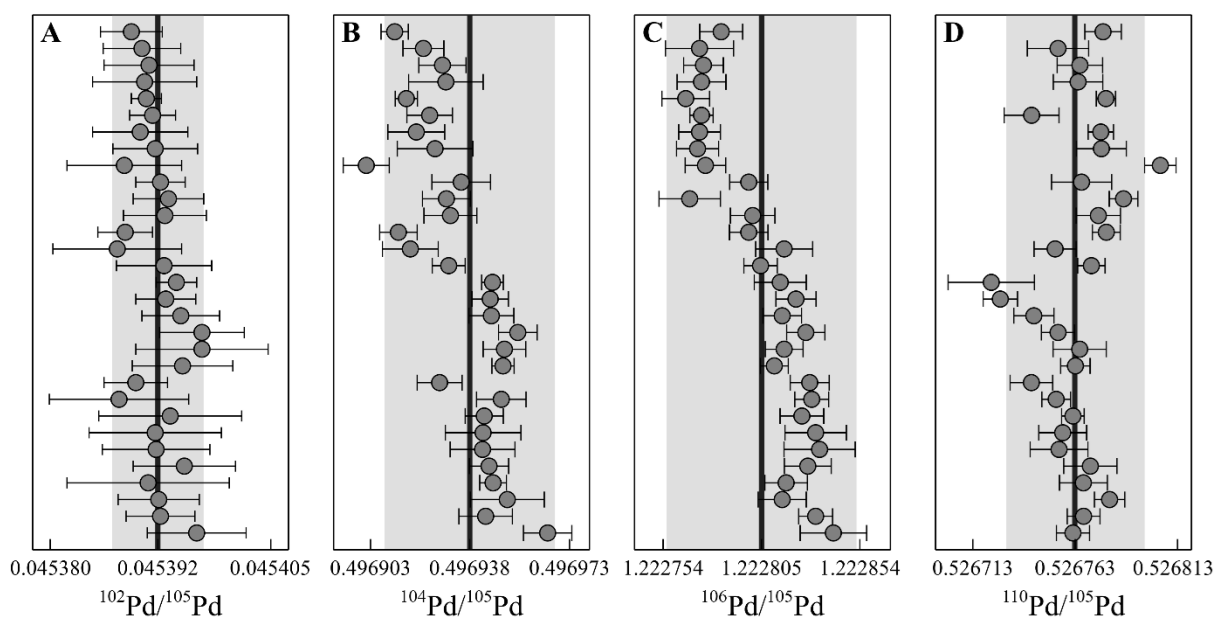


**Figure 3.2.** The average Pd isotope ratios of the NIST SRM 3138 Pd standard, internally normalised to  $^{108}\text{Pd}/^{105}\text{Pd}$ , for  $\sim 100$  ppb solutions obtained over 30 analytical sessions during the course of three years. Uncertainties represent the 2 sd within-session reproducibility, while the grey band represents the 2 sd long-term reproducibility based on all the session averages.



consider their uncertainty as a better approximation of the overall sample reproducibility and applied it for the inference tests described in section 3.4.1 and 3.4.2.

*IVB iron meteorites:* Three IVB iron meteorites (Hoba, BM 19030, 976, loaned by the Natural History Museum London; Santa Clara and Tawallah Valley, ETH collection), which were analysed in a previous Pd study (Mayer et al., 2015), were also processed to test the reproducibility and accuracy of our method. The  $\epsilon^{106}\text{Pd}$  values of these samples are all identical to the terrestrial value, within uncertainty (Figure 3.5C, Table 3.5). All IVB meteorites show a resolved  $\epsilon^{104}\text{Pd}$  deficit relative to the Earth (Figure 3.4B) and well-resolved excesses of similar magnitude in  $\epsilon^{110}\text{Pd}$  ( $\sim +0.6$ ; Figure 3.4D). Santa Clara is within uncertainty of the terrestrial value for  $\epsilon^{102}\text{Pd}$  while Hoba shows a very small negative offset compared to the terrestrial value (Figure 3.4A). Tawallah Valley shows a resolvable positive offset for  $\epsilon^{102}\text{Pd}$  that is not within uncertainty of the other two samples, however, this sample has a high Ni/Pd ratio ( $\sim 0.03$ ) that could affect accuracy at the given precision. The  $\epsilon^{104}\text{Pd}$ ,  $\epsilon^{106}\text{Pd}$  and  $\epsilon^{110}\text{Pd}$  values are in excellent agreement with those reported by Mayer et al. (2015; Figure 4) for the same meteorites, verifying the accuracy of our method. Mayer et al. (2015) observe large isotopic offsets for  $\epsilon^{102}\text{Pd}$  and

**Table 3.4.** Three aliquots of NIST SRM 3138 Pd Standard, doped with an iron meteorite matrix, independently processed through the new analytical procedure.

Sample Name <sup>a</sup>	Ru/Pd	$\epsilon^{102}\text{Pd}^b$	$\epsilon^{104}\text{Pd}^b$	$\epsilon^{106}\text{Pd}^b$	$\epsilon^{110}\text{Pd}^b$
NIST SRM 3138 Pd 1a	0.00013	$-0.18 \pm 0.37$	$-0.01 \pm 0.11$	$-0.03 \pm 0.06$	$-0.03 \pm 0.13$
NIST SRM 3138 Pd 1b	0.00013	$-0.25 \pm 0.40$	$0.06 \pm 0.12$	$-0.01 \pm 0.08$	$-0.03 \pm 0.11$
NIST SRM 3138 Pd 1c	0.00012	$0.55 \pm 0.34$	$0.03 \pm 0.11$	$0.03 \pm 0.08$	$0.07 \pm 0.11$
NIST SRM 3138 Pd 1d	0.00015	$1.16 \pm 0.41$	$-0.07 \pm 0.12$	$0.13 \pm 0.08$	$0.01 \pm 0.13$
NIST SRM 3138 Pd 1e	0.00016	$-1.07 \pm 0.36$	$-0.03 \pm 0.12$	$-0.03 \pm 0.07$	$-0.07 \pm 0.14$
NIST SRM 3138 Pd 1f	0.00018	$-0.26 \pm 0.43$	$-0.10 \pm 0.12$	$-0.03 \pm 0.08$	$-0.12 \pm 0.14$
NIST SRM 3138 Pd 1 Mean (n=6)	0.00014	$-0.01 \pm 0.63$	$-0.02 \pm 0.05$	$0.01 \pm 0.05$	$-0.03 \pm 0.05$
NIST SRM 3138 Pd 2a	0.00005	$1.58 \pm 0.35$	$0.12 \pm 0.13$	$-0.06 \pm 0.08$	$-0.09 \pm 0.11$
NIST SRM 3138 Pd 2b	0.00005	$0.40 \pm 0.55$	$-0.08 \pm 0.13$	$0.07 \pm 0.07$	$0.03 \pm 0.13$
NIST SRM 3138 Pd 2c	0.00004	$0.65 \pm 0.40$	$0.01 \pm 0.12$	$0.11 \pm 0.06$	$0.13 \pm 0.16$
NIST SRM 3138 Pd 2d	0.00003	$1.25 \pm 0.42$	$0.00 \pm 0.12$	$-0.03 \pm 0.08$	$-0.05 \pm 0.15$
NIST SRM 3138 Pd 2e	0.00003	$-0.37 \pm 0.36$	$0.02 \pm 0.16$	$-0.03 \pm 0.09$	$0.03 \pm 0.15$
NIST SRM 3138 Pd 2 Mean (n=5)	0.00004	$0.70 \pm 0.68$	$0.01 \pm 0.06$	$0.01 \pm 0.06$	$0.01 \pm 0.08$
NIST SRM 3138 Pd 3a	0.00010	$0.18 \pm 0.33$	$0.04 \pm 0.14$	$0.03 \pm 0.06$	$0.09 \pm 0.12$
NIST SRM 3138 Pd 3b	0.00011	$0.38 \pm 0.51$	$0.02 \pm 0.14$	$0.03 \pm 0.08$	$0.04 \pm 0.15$
NIST SRM 3138 Pd 3c	0.00009	$0.92 \pm 0.48$	$-0.10 \pm 0.12$	$-0.06 \pm 0.07$	$0.13 \pm 0.15$
NIST SRM 3138 Pd 3d	0.00010	$0.62 \pm 0.39$	$0.05 \pm 0.13$	$-0.07 \pm 0.09$	$0.17 \pm 0.12$
NIST SRM 3138 Pd 3 Mean (n=4)	0.00010	$0.53 \pm 0.32$	$0.00 \pm 0.07$	$-0.02 \pm 0.05$	$0.11 \pm 0.06$
NIST SRM 3138 Pd Mean <sup>c</sup> (n=15)		$0.37 \pm 1.42$	$0.00 \pm 0.12$	$0.00 \pm 0.12$	$0.02 \pm 0.17$

<sup>a</sup> Number after sample name denotes sample aliquot and letter indicated duplicate analyses of the sample aliquot. Each aliquot was processed separately through the entire separation procedure. <sup>b</sup> Uncertainties on the individual analyses are reported as the  $2\sigma$  standard errors (2 se) on the mean of the individual ratios obtained in a single analysis, while uncertainty on the mean of each aliquot is reported as the 2 se of the analyses. For means calculated based on analyses from multiple aliquots the uncertainty is reported as 2 sd. <sup>c</sup> Mean calculated based on the entire data set of that sample.

state that they reflect inaccurate correction of the isobaric  $^{102}\text{Ru}$  interferences due to high Ru/Pd ratios in their sample solutions after ion exchange procedure. Our data confirm their conclusion, because, in contrast to the previous work, our new analytical procedure yields low Ru/Pd ratios that are below the threshold at which the interference correction breaks down (Table 3.3, 3.4, 3.5). The IVB irons contain relatively high amounts of Ru (Ru/Pd > 2 Hoashi et al., 1993) and this also verifies the ability of our method to separate and/or correct for Ru interferences, even for samples with high Ru/Pd ratios.

### 3.4.4. Cosmochemical implication for IAB and IVB iron meteorites

The well-resolved deficits in  $\epsilon^{104}\text{Pd}$  ( $\sim -0.2$ ) and excess in  $\epsilon^{110}\text{Pd}$  (+0.6) for the three IVB meteorites most likely reflects the presence of a nucleosynthetic *s*-process deficit/*r*-process excess ( $^{104}\text{Pd}$  is an *s*-process

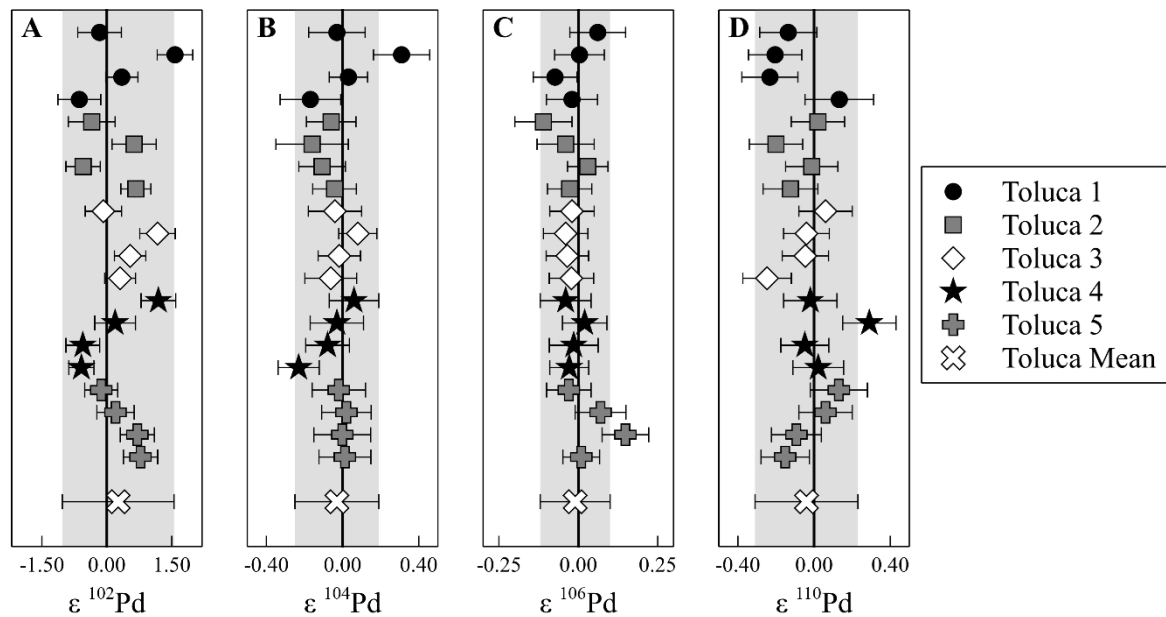


**Figure 3.3.** Repeat measurements of five independently processed aliquots of the IAB iron meteorite Toluca for  $\epsilon^{102}\text{Pd}$  (A),  $\epsilon^{104}\text{Pd}$  (B),  $\epsilon^{106}\text{Pd}$  (C) and  $\epsilon^{110}\text{Pd}$  (D). The shaded area and the uncertainty of Toluca Mean represents the 2 sd of the overall mean of Toluca, also taken as our external reproducibility. The uncertainty on the individual measurements of the five aliquots represents the 2 se internal uncertainty of each analysis. The overall mean for Toluca is within uncertainty of the terrestrial composition for all isotopes.

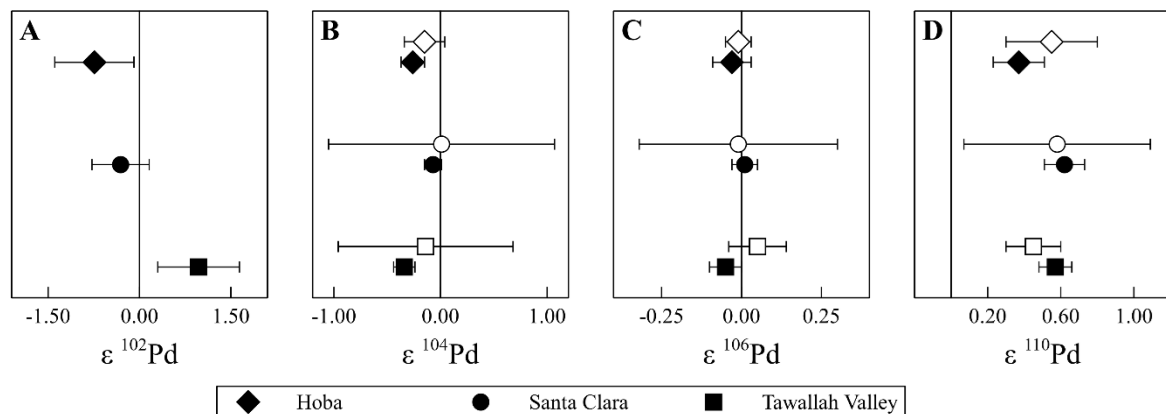


**Figure 3.4.** The mean Pd isotope compositions of three IVB iron meteorites (Hoba, Santa Clara, Tawallah Valley) from this study (filled symbols) compared to those from Mayer et al. (2015) (open symbols). Uncertainties for our values are given as the 2 se of several analyses, while the uncertainty of the data from Mayer et al. (2015) represent the 2 se internal uncertainty. The values from the two studies are in excellent agreement for  $\epsilon^{104}\text{Pd}$ ,  $\epsilon^{106}\text{Pd}$  and  $\epsilon^{110}\text{Pd}$ . The  $\epsilon^{102}\text{Pd}$  values from Mayer et al. (2015) are not shown because of large Ru interferences.

isotope and  $^{110}\text{Pd}$  is an  $r$ -process isotope) coupled with the effects of GCR. Both GCR and an  $s$ -process deficit/ $r$ -process excess will increase the  $\epsilon^{110}\text{Pd}$  ratio of a sample. The three IVB meteorite samples share a very similar GCR exposure history (Mayer et al., 2015), which resulted in this relatively constant positive offset. Similarly, the negative offsets in  $\epsilon^{104}\text{Pd}$  (Figure 3.5) are likely generated by a combination of GCR and nucleosynthetic effects, as discussed by Mayer et al. (2015). Studies of  $p$ -process isotopes of other elements such as Mo (Burkhardt et al., 2011) and Ru (Fischer-Gödde et al., 2015) allow an  $s$ -process deficit to be resolved from an  $r$ -process excess, however, the precision of our  $\epsilon^{102}\text{Pd}$  data is not sufficient to distinguish between an  $s$ -process deficit and an  $r$ -process excess without further investigation. Thus a more thorough evaluation of the GCR effects in our samples is needed to elucidate the details. Combining Pd with Pt isotope analyses obtained on the same sample aliquots will act as a neutron dosimeter, and allow for a decisive statement about the respective magnitude of the nucleosynthetic and GCR effects.

In contrast, the Pd isotope analyses for the IAB meteorite Toluca yield identical isotope compositions to the terrestrial standard. This indicates that our Toluca sample was not strongly exposed to GCR. This is in agreement with a study of the GCR exposure of the Toluca 1 aliquot by Hunt et al. (2018) using Pt isotopes. Moreover, the data also testify to the absence of nucleosynthetic variations in IAB meteorites, which confirms results from other elements, such as Mo (Burkhardt et al., 2011) and Ru (Fischer-Gödde et al., 2015).

**Table 3.5.** The Pd isotopic composition of 5 aliquots of Toluca and a single aliquot of Tawallah Valley, Santa Clara, and Hoba processed using the new analytical procedure

Sample Name <sup>a</sup>	Ru/Pd	$\epsilon^{102}\text{Pd}^b$	$\epsilon^{104}\text{Pd}^b$	$\epsilon^{106}\text{Pd}^b$	$\epsilon^{110}\text{Pd}^b$
Toluca 1a	0.00002	$-0.64 \pm 0.49$	$-0.17 \pm 0.16$	$-0.02 \pm 0.08$	$0.13 \pm 0.18$
Toluca 1b	0.00001	$0.34 \pm 0.37$	$0.03 \pm 0.10$	$-0.07 \pm 0.07$	$-0.23 \pm 0.15$
Toluca 1c	0.00001	$1.57 \pm 0.41$	$0.31 \pm 0.15$	$0.00 \pm 0.08$	$-0.20 \pm 0.14$
Toluca 1d	0.00071	$-0.17 \pm 0.50$	$-0.03 \pm 0.15$	$0.06 \pm 0.09$	$-0.14 \pm 0.15$
Toluca 1 (IAB) Mean (n=4)	0.00019	$0.28 \pm 0.95$	$0.04 \pm 0.20$	$-0.01 \pm 0.06$	$-0.11 \pm 0.17$
Toluca 2a	0.00003	$0.67 \pm 0.35$	$-0.04 \pm 0.11$	$-0.03 \pm 0.07$	$-0.12 \pm 0.14$
Toluca 2b	0.00002	$-0.55 \pm 0.40$	$-0.11 \pm 0.12$	$0.03 \pm 0.06$	$-0.01 \pm 0.14$
Toluca 2c	0.00002	$0.63 \pm 0.51$	$-0.16 \pm 0.19$	$-0.04 \pm 0.09$	$-0.20 \pm 0.14$
Toluca 2d	0.00003	$-0.35 \pm 0.54$	$-0.06 \pm 0.13$	$-0.11 \pm 0.09$	$0.02 \pm 0.14$
Toluca 2 (IAB) Mean (n=4)	0.00003	$0.10 \pm 0.65$	$-0.09 \pm 0.11$	$-0.04 \pm 0.06$	$-0.08 \pm 0.14$
Toluca 3a	0.00022	$0.31 \pm 0.36$	$-0.06 \pm 0.14$	$-0.02 \pm 0.07$	$-0.25 \pm 0.13$
Toluca 3b	0.00022	$0.54 \pm 0.36$	$-0.02 \pm 0.11$	$-0.03 \pm 0.07$	$-0.05 \pm 0.12$
Toluca 3c	0.0005	$1.17 \pm 0.41$	$0.08 \pm 0.10$	$-0.04 \pm 0.07$	$-0.04 \pm 0.12$
Toluca 3d	0.00051	$-0.08 \pm 0.42$	$-0.04 \pm 0.14$	$-0.02 \pm 0.07$	$0.06 \pm 0.14$
Toluca 3 (IAB) Mean (n=4)	0.00036	$0.49 \pm 0.65$	$-0.01 \pm 0.11$	$-0.03 \pm 0.06$	$-0.07 \pm 0.14$
Toluca 4a	0	$-0.59 \pm 0.29$	$-0.23 \pm 0.11$	$-0.03 \pm 0.06$	$0.02 \pm 0.13$
Toluca 4b	0	$-0.56 \pm 0.39$	$-0.08 \pm 0.11$	$-0.01 \pm 0.08$	$-0.05 \pm 0.13$
Toluca 4c	0	$0.19 \pm 0.47$	$-0.03 \pm 0.14$	$0.02 \pm 0.07$	$0.29 \pm 0.14$

*Continues on next page*

**Table 3.5. continued**

Sample Name <sup>a</sup>	Ru/Pd	$\epsilon^{102}\text{Pd}^b$	$\epsilon^{104}\text{Pd}^b$	$\epsilon^{106}\text{Pd}^b$	$\epsilon^{110}\text{Pd}^b$
Toluca 4d	0	1.19 ± 0.40	0.06 ± 0.13	-0.04 ± 0.08	-0.02 ± 0.14
Toluca 4 (IAB) Mean (n=4)	0	0.06 ± 0.83	-0.07 ± 0.12	-0.02 ± 0.06	0.06 ± 0.17
Toluca 5a	0.00006	0.78 ± 0.39	0.01 ± 0.14	0.01 ± 0.06	-0.15 ± 0.13
Toluca 5b	0.00006	0.70 ± 0.39	0.00 ± 0.15	0.15 ± 0.07	-0.09 ± 0.13
Toluca 5c	0.00007	0.20 ± 0.43	0.02 ± 0.13	0.07 ± 0.08	0.06 ± 0.14
Toluca 5d	0.00007	-0.13 ± 0.38	-0.02 ± 0.14	-0.03 ± 0.07	0.13 ± 0.15
Toluca 5 (IAB) Mean (n=4)	0.00007	0.39 ± 0.65	0.00 ± 0.11	0.05 ± 0.08	-0.01 ± 0.14
Toluca (IAB) Mean <sup>c</sup> (n=20)		0.26 ± 1.29	-0.03 ± 0.22	-0.01 ± 0.11	-0.04 ± 0.27
Tawallah Valley 1a	0.0002	-0.75 ± 0.49	-0.25 ± 0.17	0.04 ± 0.10	0.58 ± 0.20
Tawallah Valley 1b	0.00017	0.65 ± 0.53	-0.49 ± 0.14	-0.03 ± 0.08	0.55 ± 0.16
Tawallah Valley 1c	0.00017	1.92 ± 0.52	-0.49 ± 0.13	-0.01 ± 0.09	0.64 ± 0.17
Tawallah Valley 1d	0.00012	2.00 ± 0.42	-0.47 ± 0.12	-0.13 ± 0.08	0.49 ± 0.15
Tawallah Valley 1e	0.00013	0.81 ± 0.75	-0.50 ± 0.14	-0.08 ± 0.09	0.61 ± 0.16
Tawallah Valley 1f	0.00015	2.11 ± 0.44	-0.21 ± 0.17	-0.12 ± 0.09	0.50 ± 0.16
Tawallah Valley 1g	0.00014	1.31 ± 0.51	-0.21 ± 0.13	-0.11 ± 0.08	0.67 ± 0.15
Tawallah Valley 1h	0.00015	-0.30 ± 0.47	-0.30 ± 0.16	-0.06 ± 0.07	0.53 ± 0.14
Tawallah Valley 1i	0.00015	0.97 ± 0.40	-0.16 ± 0.10	0.07 ± 0.08	0.56 ± 0.13
Tawallah Valley (IVB) Mean (n=9)	0.00015	0.97 d ± 0.67	-0.34 ± 0.10	-0.05 ± 0.05	0.57 ± 0.09
Santa Clara 1a	0.00012	-0.92 ± 0.50	-0.25 ± 0.17	0.00 ± 0.11	0.55 ± 0.14
Santa Clara 1b	0.00009	-1.63 ± 0.58	-0.03 ± 0.17	0.02 ± 0.10	0.44 ± 0.18
Santa Clara 1c	0.00008	0.32 ± 0.40	-0.11 ± 0.11	0.01 ± 0.07	0.62 ± 0.11
Santa Clara 1d	0.00008	-0.07 ± 0.42	0.00 ± 0.13	-0.01 ± 0.07	0.83 ± 0.14
Santa Clara 1e	0.00008	0.30 ± 0.62	0.05 ± 0.12	-0.07 ± 0.07	0.81 ± 0.14
Santa Clara 1f	0.00008	-0.12 ± 0.43	-0.10 ± 0.13	0.02 ± 0.07	0.76 ± 0.16
Santa Clara 1g	0.00008	-0.09 ± 0.38	-0.12 ± 0.12	0.02 ± 0.08	0.47 ± 0.15
Santa Clara 1h	0.00009	-0.25 ± 0.36	0.02 ± 0.12	0.08 ± 0.07	0.47 ± 0.13
Santa Clara (IVB) Mean (n=8)	0.00009	-0.31 ± 0.47	-0.07 ± 0.08	0.01 ± 0.04	0.62 ± 0.11
Hoba 1a	0.00004	-1.17 ± 0.41	-0.32 ± 0.12	-0.02 ± 0.07	0.38 ± 0.15
Hoba 1b	0.00004	-0.68 ± 0.42	-0.37 ± 0.12	-0.04 ± 0.08	0.46 ± 0.17
Hoba 1c	0.00004	-0.35 ± 0.42	-0.21 ± 0.16	-0.01 ± 0.09	0.39 ± 0.14
Hoba 1d	0.00004	-0.77 ± 0.42	-0.16 ± 0.15	-0.06 ± 0.08	0.24 ± 0.17
Hoba (mean, n=4)	0.00004	-0.74 ± 0.65	-0.27 ± 0.11	-0.03 ± 0.06	0.37 ± 0.14

<sup>a</sup>Number after sample name denotes sample aliquot and letter indicated duplicate analyses of the sample aliquot. Each aliquot was processed separately through the entire separation procedure. <sup>b</sup>Uncertainties on the individual analyses are reported as the 2 $\sigma$  standard errors (2 se) on the mean of the individual ratios obtained in a single analysis. The 2 se uncertainty on the mean of an aliquot is calculated as the 2 sd of the aliquot or the 2 sd of the Toluca Mean (whichever is larger) divided by the square root of n. For means calculated based on analyses from multiple aliquots the uncertainty is reported as the 2 sd. <sup>c</sup>Mean calculated based on the entire data set of that sample. <sup>d</sup>Tawallah Valley has a high Ni/Pd ratio (~0.03) which may affect the accuracy of the  $\epsilon^{102}\text{Pd}$  data.

### **3.5. Conclusions**

We present a new analytical method for separating Pd from iron meteorites for high precision isotope analysis. Our separation procedure yields sample solutions with minimal amounts of Ru and other elements (e.g., Zn and Zr) that produce interferences during mass spectrometry. Following initial Pd separation from the iron meteorite matrix using anion exchange resin, Ru is volatilised and removed from the sample. A second anion exchange column is employed to remove remaining matrix elements including Ru. The new analytical procedure yields an external reproducibility (2 sd) of 1.29 for  $\epsilon^{102}\text{Pd}$ , 0.22 for  $\epsilon^{104}\text{Pd}$ , 0.11 for  $\epsilon^{106}\text{Pd}$ , and 0.27 for  $\epsilon^{110}\text{Pd}$  based on repeat analyses of five independently processed aliquots of the IAB iron meteorite Toluca. The method was also successfully applied to three IVB iron meteorites (Tawallah Valley, Santa Clara, and Hoba) and our Pd isotope data are in excellent agreement with those reported by Mayer et al. (2015) for the same meteorites. Our new procedure achieves separation of Ru from Pd to a high degree, which allows for the accurate determination of  $\epsilon^{102}\text{Pd}$ .

The Pd isotope compositions of the three IVB iron meteorites are consistent with the presence of a nucleosynthetic *s*-process deficit/*r*-process excess, while data for Toluca indicate that these effects are absent in IAB meteorites. Further work, however, is required for a thorough evaluation of GCR effects in IAB and IVB iron meteorites.

### **Acknowledgements**

This work was supported by the European Research Council under the European Union's Seventh Framework Programme (FP7/2007–2013)/ERC Grant agreement n°[279779]. We thank Caroline Smith and Deborah Cassey (Natural History Museum, London) for the loan of material used in this study. The authors would like to thank D. Cook, M. Fehr, R. Steele and T. Henshall for helpful discussions. We would also like to thank our editor H. Brewerton and two anonymous reviewers for their insightful and helpful comments.



# Chapter 4\*

The Zr-Mo-Ru-Pd Correlation: Evidence for incomplete condensation around AGB stars and selective processing of dust in the solar nebula

\* to be submitted to *Earth and Planetary Science Letters* as: Ek. M, Hunt, A. C., Schönächler, M.

## Abstract

Nucleosynthetic variations in bulk meteorites have been reported for a range of different elements, e.g., Cr, Zr, Mo, Ru, Pd and Ba. These variations are generally thought to result from selective processing of dust originating from a range of stellar sources in the solar nebula. Here we report mass-independent Pd isotope compositions for 24 iron meteorites from the IAB, IIAB, IID, IIIAB, IVA and IVB groups. Our external reproducibility (2 standard deviations), based on repeat measurements of several iron meteorites is 1.58 for  $\epsilon^{102}\text{Pd}$ , 0.26 for  $\epsilon^{104}\text{Pd}$ , 0.13 for  $\epsilon^{106}\text{Pd}$  and 0.27  $\epsilon^{110}\text{Pd}$ . There is considerable variation both within individual groups and between groups. The largest offsets are identified in  $\epsilon^{104}\text{Pd}$  ( $1.5 \pm 0.25$ ) and  $\epsilon^{110}\text{Pd}$  ( $0.8 \pm 0.16$ ) for the IID sample Carbo G. The within-group variation is consistent with cosmic ray exposure effects, inferred from Pt isotope measurements of the same samples. The nucleosynthetic isotope composition was calculated by correcting for cosmogenic effects. The largest nucleosynthetic offsets are found in  $\text{IVB} \geq \text{IID} > \text{IIIAB} > \text{IVA} > \text{IIAB} \geq \text{IAB}$ , with the IIAB and IAB iron meteorites within uncertainty of the terrestrial composition. The nucleosynthetic Pd isotope variations are consistent with an *s*-process deficit, in agreement with neighbouring elements, e.g. Zr, Mo and Ru. The offsets in Pd correlate well with those reported for Mo and Ru isotopes, however, the slope of the correlation is not consistent with an *s*-process component with solar abundances of these elements. The offsets in Pd are only 1/4 of the magnitude expected relative to the nucleosynthetic variations reported in Ru and Mo isotopes. We propose that Pd did not condense as readily around AGB stars as the more refractory Mo and Ru. Only a small fraction of elements synthesised within stars condense into ‘stardust’ around the star. Most material is injected into the interstellar medium as a gas, where it is homogenised and the nucleosynthetic signature is lost. Furthermore, we attribute variations in the early solar system to selective processing of dust that condensed in the interstellar medium relative to the stardust fraction.

## 4.1. Introduction

Our solar system formed from a fragment of a giant molecular cloud that collapsed due to gravitational instabilities. This molecular cloud comprised primarily gas with a small fraction ( $\gg 1\%$ ) of dust mixed in (Chambers, 2014). This dust was isotopically diverse and the product of many generations of stellar nucleosynthesis. After the formation of a protoplanetary disk surrounding the early Sun, dust in the disk accreted into growing bodies, eventually forming km-sized planetesimals, which collided to form the terrestrial planets. The presence of small nucleosynthetic isotope variations for a range of elements in bulk meteorites, relative to Earth, implies that the dust in the protoplanetary disk was not completely homogenised e.g., for Ca, Ti, Cr, Zr, Mo, Ru and Ba (Qin and Carlson, 2016, and references therein). It is generally believed that the molecular cloud was initially well-mixed and that processes occurring in the protoplanetary disk were responsible for un-mixing isotopically distinct nucleosynthetic components carried by presolar dust, resulting in the nucleosynthetic isotope variations observed. Physical sorting of grains, either by mineralogical type (Regelous et al., 2008) or size (Dauphas et al., 2010), was proposed as a possible mechanism for un-mixing isotopically distinct presolar dust in the early solar nebula. Another suggested mechanism is selective destruction of presolar grains by thermal processing in the protoplanetary disk (Akram et al., 2015; Trinquier et al., 2009). Aqueous alteration and other



parent body processes were also considered to selectively alter or destroy presolar grains (Yokoyama et al., 2011). It remains unclear which of these proposed mechanisms is the dominant process responsible for the nucleosynthetic variations observed in solar system material.

In this study we characterise the nucleosynthetic variation of Pd isotopes in iron meteorites to gain an improved understanding of the origin of these heterogeneities. Palladium is a main component element ( $T_c = 1324$  K; Lodders, 2003; Palme and O'Neill, 2014), with refractory neighbours that exhibit well-resolved nucleosynthetic isotope variations, e.g. Zr (Akram et al., 2015), Mo (Burkhardt et al., 2012; Dauphas et al., 2002; Poole et al., 2017) and Ru (Dauphas et al., 2004; Fischer-Gödde et al., 2015; Fischer-Gödde and Kleine, 2017). However, it is less volatile than Cd ( $T_c = 652$  K; Lodders, 2003) where no nucleosynthetic isotope variations have been observed (Kruijer et al., 2013b; Wombacher et al., 2008).

Palladium is highly siderophile and strongly partitions into metal during metal-silicate differentiation, together with the other platinum group elements (PGE). It has six stable isotopes produced in different stellar environments: one *p*-process isotope ( $^{102}\text{Pd}$ ), one pure *s*-process isotope ( $^{104}\text{Pd}$ ), one pure *r*-process isotope ( $^{110}\text{Pd}$ ) and three isotopes that are mixtures of *s*- and *r*-process components ( $^{105}\text{Pd}$ ,  $^{106}\text{Pd}$ ,  $^{108}\text{Pd}$ ), which renders Pd ideal for studies of nucleosynthetic variations. A previous investigation (Mayer et al., 2015) reported a nucleosynthetic offset, relative to the Earth, for the IVB iron meteorite group that was between 1/2 and 1/3 of that identified in neighbouring Mo and Ru isotopes based on *s*-process stellar production models and solar abundances. Here we present new Pd isotope data for 24 samples from six iron meteorite groups (IAB, IIAB, IID, IIIAB, IVA, and IVB) to better constrain the nucleosynthetic variations in Pd compared to the more refractory elements. In order to accurately determine the nucleosynthetic component, we evaluate possible contributions from cosmic ray exposure (CRE; Leya and Masarik, 2013) and nuclear field shift effects (NFS; Fujii et al., 2006) to the mass-independent isotope composition of these samples.

## 4.2. Samples

A total of 24 meteorites from the IAB, IIAB, IID, IIIAB, IVA and IVB iron meteorite classes were selected for Pd isotope analyses (Table 4.1). Platinum isotope data were also collected from the same sample aliquots and are published in Hunt et al. (2017a; 2017b; 2018), except new Pt isotope data for the IVB iron meteorites Tlacotepec and Hoba, and the IID iron meteorite Rodeo. Four samples from the IID Carbo were analysed to evaluate the effects of CRE. These samples were taken from a cross section through Carbo and the CRE magnitude of each sample, inferred from offsets in  $\epsilon^{182}\text{W}/^{184}\text{W}$  and  $^3\text{He}$  concentration (Markowski et al., 2006), increases in the order Carbo J > Carbo G > Carbo Y > Carbo A. Sampling locations are adjacent to those of Markowski et al. (2006).

When necessary samples were sawn using a CBN blade using ethanol as a cooling fluid. Weathering, fusion crusts and saw marks were removed using silicon carbide paper. Prior to dissolution samples were rinsed with ethanol and leached in 2 M HCl as outlined in Hunt et al. (2017b; Chapter 2).

**Table 4.1.** Palladium isotope composition of iron meteorites analysed in this study.

Group	Sample <sup>a</sup>	Collection	$\epsilon^{196}\text{Pt}^b$	Rh/Pd <sup>c</sup>	n <sup>d</sup>	$\epsilon^{102}\text{Pd}^e$	$\epsilon^{104}\text{Pd}^e$	$\epsilon^{106}\text{Pd}^e$	$\epsilon^{110}\text{Pd}^e$
IAB	Caddo County	ETH	-0.01 ± 0.09 <sup>2</sup>		4	0.48 ± 0.96	0.09 ± 0.13	-0.02 ± 0.06	-0.06 ± 0.14
	Canyon Diablo	ETH	0.00 ± 0.09 <sup>2</sup>	0.48 <sup>1</sup>	3	0.21 ± 0.91	-0.09 ± 0.15	0.00 ± 0.07	-0.05 ± 0.16
	Cranbourne	ETH	0.13 ± 0.09 <sup>2</sup>	0.44 <sup>1</sup>	4	-0.10 ± 0.79	0.16 ± 0.13	0.06 ± 0.08	-0.11 ± 0.14
	Edmonton KY	USNM 1413			2	0.57 ± 1.12	0.12 ± 0.18	0.04 ± 0.09	-0.01 ± 0.19
	Magura	ETH	0.11 ± 0.09 <sup>2</sup>	0.59 <sup>1</sup>	3	-0.11 ± 0.91	-0.04 ± 0.15	0.04 ± 0.07	-0.01 ± 0.16
	Odessa	ETH	0.56 ± 0.09 <sup>2</sup>	0.35 <sup>1</sup>	2	0.17 ± 1.12	0.45 ± 0.18	0.17 ± 0.09	0.10 ± 0.19
	Toluca 1a <sup>f</sup>	ETH	0.00 ± 0.09 <sup>3</sup>		4	0.28 ± 0.95	0.04 ± 0.20	-0.01 ± 0.06	-0.11 ± 0.17
	Toluca 2a <sup>f</sup>	ETH	0.14 ± 0.09 <sup>3</sup>		4	0.10 ± 0.64	-0.09 ± 0.05	-0.04 ± 0.06	-0.08 ± 0.10
	Toluca 2b <sup>f</sup>				4	0.48 ± 0.52	-0.01 ± 0.06	-0.03 ± 0.01	-0.07 ± 0.13
	Toluca 2c <sup>f</sup>				4	0.06 ± 0.83	-0.07 ± 0.12	-0.01 ± 0.03	0.06 ± 0.15
IIAB	Toluca 2d <sup>f</sup>			4	0.39 ± 0.43	0.00 ± 0.02	0.05 ± 0.08	0.05 ± 0.08	-0.01 ± 0.13
	Toluca Mean <sup>f</sup>		0.07 ± 0.09 <sup>1</sup>	0.23 <sup>1</sup>	20	0.26 ± 0.35	-0.03 ± 0.06	-0.01 ± 0.03	-0.04 ± 0.06
	North Chile	ETH	0.18 ± 0.07 <sup>3</sup>	1.48 <sup>1</sup>	2	-0.02 ± 1.12	0.22 ± 0.18	0.02 ± 0.09	0.22 ± 0.19
	Sikhote Alin	NHM, BM 1992, M38	0.21 ± 0.07 <sup>3</sup>	0.86 <sup>2</sup>	2	1.18 ± 1.12	0.28 ± 0.18	0.01 ± 0.09	0.24 ± 0.19
	Coahuila	NHM, BM 54242	0.01 ± 0.07 <sup>3</sup>	1.56 <sup>2</sup>	3	0.30 ± 0.91	-0.12 ± 0.15	-0.05 ± 0.07	0.05 ± 0.16
	Rodeo	FMNH, ME 590#3	0.03 ± 0.09 <sup>1</sup>	0.55 <sup>1</sup>	5	0.03 ± 0.71	-0.56 ± 0.12	-0.08 ± 0.06	0.32 ± 0.12
	Carbo A	ETH	0.68 ± 0.09 <sup>3</sup>		3	0.04 ± 0.91	0.82 ± 0.15	0.12 ± 0.07	0.76 ± 0.16
	Carbo J	ETH	0.88 ± 0.09 <sup>3</sup>		3	-0.04 ± 0.91	1.50 ± 0.15	0.19 ± 0.07	0.80 ± 0.16
	Carbo Y	ETH	0.63 ± 0.09 <sup>3</sup>	0.81 <sup>1</sup>	3	0.64 ± 0.91	0.85 ± 0.15	0.08 ± 0.07	0.68 ± 0.16
	Carbo G	ETH	0.87 ± 0.09 <sup>3</sup>	0.90 <sup>1</sup>	3	0.43 ± 0.91	1.28 ± 0.15	0.18 ± 0.07	0.76 ± 0.16
IIIAB	Boxhole	NHM, BM 1938, 406	0.25 ± 0.07 <sup>3</sup>	0.74 <sup>2</sup>	4	0.63 ± 0.79	0.40 ± 0.19	0.01 ± 0.07	0.28 ± 0.14
	Thunda	NHM, BM 2005, M269	0.03 ± 0.07 <sup>3</sup>		1	-1.30 ± 1.58	-0.29 ± 0.26	-0.03 ± 0.13	0.01 ± 0.27
	Cape York	ETH	0.05 ± 0.07 <sup>3</sup>	0.59 <sup>2</sup>	1	-1.52 ± 1.58	-0.28 ± 0.26	0.01 ± 0.13	0.42 ± 0.27

*Continues on next page*

**Table 4.1. continued**

Group	Sample <sup>a</sup>	Collection	$\epsilon^{196}\text{Pt}^b$	Rh/Pd <sup>c</sup>	n <sup>d</sup>	$\epsilon^{102}\text{Pd}^e$	$\epsilon^{104}\text{Pd}^e$	$\epsilon^{106}\text{Pd}^e$	$\epsilon^{110}\text{Pd}^e$
IVA	Gibeon 1a	ETH	0.03 ± 0.09 <sup>3</sup>		4	0.44 ± 0.79	-0.13 ± 0.13	-0.04 ± 0.06	0.04 ± 0.16
	Gibeon 2a	ETH			4	-0.15 ± 0.79	-0.07 ± 0.16	0.07 ± 0.11	0.10 ± 0.14
	Gibeon 2b				4	0.34 ± 0.79	-0.23 ± 0.17	-0.04 ± 0.06	0.20 ± 0.32
	Gibeon 2c				4	-0.14 ± 1.34	-0.09 ± 0.16	-0.05 ± 0.06	0.22 ± 0.14
	Gibeon 2d				4	-0.14 ± 1.34	-0.09 ± 0.16	-0.05 ± 0.06	0.22 ± 0.14
IVB	Gibeon Mean	ETH	0.03 ± 0.09 <sup>3</sup>	0.35 <sup>2</sup>	14	0.12 ± 0.40	-0.13 ± 0.07	-0.02 ± 0.04	0.14 ± 0.09
	Muonionalusta	ETH	0.14 ± 0.09 <sup>1</sup>		6	0.06 ± 0.90	-0.19 ± 0.13	-0.03 ± 0.09	0.06 ± 0.12
IVB	Tawallah Valley <sup>f</sup>	ETH	0.24 ± 0.07 <sup>4</sup>		9	0.97 ± 0.67	-0.34 ± 0.10	-0.05 ± 0.05	0.57 ± 0.09
	Santa Clara <sup>f</sup>	ETH	0.38 ± 0.06 <sup>4</sup>		8	-0.31 ± 0.56	-0.07 ± 0.09	0.01 ± 0.05	0.62 ± 0.11
	Tlacotepec <sup>f</sup>	NHM, BM1959, 913	0.79 ± 0.07 <sup>1</sup>		3	-0.77 ± 0.91	0.94 ± 0.15	0.11 ± 0.07	0.77 ± 0.16
	Hobaf <sup>f</sup>	NHM, BM 1930, 976	0.19 ± 0.07 <sup>1</sup>		4	-0.74 ± 0.79	-0.26 ± 0.13	-0.03 ± 0.06	0.37 ± 0.14

<sup>a</sup> Numbers in sample names indicate different dissolutions. Letters after number indicate aliquot of dissolution. <sup>b</sup> Platinum from this <sup>1</sup> study, <sup>2</sup> Hunt et al. (2018), <sup>3</sup> Hunt et al. (2017a), <sup>4</sup> Hunt et al. (2017b). <sup>c</sup> Rh/Pd ratios from <sup>1</sup> this study or <sup>2</sup> Ryan et al. (1990) and Hoashi et al. (1993). <sup>d</sup> Number of analyses. <sup>e</sup> Palladium isotope data are internally normalised to <sup>108</sup>Pd/<sup>105</sup>Pd using the exponential law. Uncertainties were calculated using the method outlined in section 4.3.1. <sup>f</sup> Palladium data from Ek et al. (2017). Uncertainties updated using the method described in section 3.1.

## 4. 3. Methods

### 4.3.1 Ion exchange separation of Pd and Pt

Samples were dissolved according to the method described by Hunt et al. (2017b; Chapter 2) and Pd was purified using a two stage ion exchange procedure described in Hunt et al. (2017b; Chapter 2) and Ek et al. (2017; Chapter 3). After sample dissolution, Pd was separated from matrix elements using a modified version of the ion exchange procedure by Rehkämper and Halliday (1997). At this stage, a Pt fraction was also collected and processed further give reference. Palladium was further purified as described in Ek et al. (2017; Chapter 3) and summarised in the following. First, Ru was removed from the Pd fraction via volatilisation in an aqua regia and perchloric acid mixture (Ek et al., 2017; Chapter 3). A second ion exchange procedure then separated Pd from the remaining matrix elements (e.g. Fe, Zr, Zn, Mo), and resulted in a Pd fraction that was sufficiently devoid of matrix elements for accurate determination of the isotopic composition (Ek et al., 2017; Chapter 3). The concentration of Pd in the meteorites analysed here is between 2 – 9 ppm, while Pd blanks were routinely less than 1.2 ng g<sup>-1</sup> (Ek et al., 2017; Chapter 3).

### 4.3.2. High precision Pd and Pt isotopic measurements

Palladium and Pt were separated from the same sample aliquot using the method outlined in Hunt et al. (2017b; Chapter 2) and Ek et al. (2017; Chapter 3). All Pd and Pt isotope measurements were performed at ETH Zürich using a Thermo Scientific Neptune *Plus* multi collector-inductively coupled plasma mass spectrometer (MC-ICPMS) coupled with a Cetac Aridus II desolvating introduction system and standard H cones. Results are reported in epsilon notation ( $\epsilon$ ), i.e. the deviation of the sample from the average of the bracketing NIST SRM 3138 Pd standards, given in parts per 10 000. Palladium isotope determinations follow the procedure of Ek et al. (2017; Chapter 3). Samples were bracketed by the NIST SRM 3138 Pd standard matched to within 15 % of the sample concentration. Sample solutions were diluted to ~100 ng ml<sup>-1</sup> Pd to achieve an ion beam intensity of 5 to 7 × 10<sup>-11</sup> A for <sup>105</sup>Pd. All ratios were internally normalised to <sup>108</sup>Pd/<sup>105</sup>Pd = 1.18899, <sup>110</sup>Pd/<sup>105</sup>Pd = 0.52692 or <sup>108</sup>Pd/<sup>106</sup>Pd = 0.97238 (Kelly and Wasserburg, 1978) using the exponential law. All data presented, unless otherwise noted, are normalised to <sup>108</sup>Pd/<sup>105</sup>Pd and given relative to <sup>105</sup>Pd. Data normalised to <sup>108</sup>Pd/<sup>106</sup>Pd are reported relative to <sup>106</sup>Pd.

To obtain a robust estimate of the external reproducibility of our Pd data, they were evaluated using the equations outlined in Steele et al. (2012) and are based on the entire Pd isotope dataset presented here and in Ek et al. (2017; Chapter 3). For every sample that was analysed four or more times (n≥4), the deviation of each analysis from that sample's mean was calculated. The deviations for multiple samples were then combined and the external reproducibility was determined by calculating the 2 SD based on these deviations using following equation:

$$2 SD_{external} = 2\sqrt{k^{-1} \sum d^2} \quad (1)$$

where  $2 SD_{external}$  is the external reproducibility,  $d$  is the deviation from zero, and  $k$  is the number of degrees of freedom (total number of analyses minus the number of samples). Estimating the precision using the entire data set, instead of repeat measurements of the same sample, has the advantage that it takes into account the entire range of matrix elements that remained in the analysed sample solutions,

in addition to variations in instrument performance between different sessions. measurements of five independently processed aliquots of the IAB iron meteorite Toluca (Ek et al., 2017; Chapter 3). This confirms (i) that all the Toluca aliquots have identical isotopic compositions and (ii) that the analytical method does not produce resolvable isotopic offsets in multiple aliquots of the same sample. The external reproducibility calculated above was therefore used when calculating the uncertainty of the data presented in this study. For samples where  $n < 4$  the uncertainty is reported as 2 standard errors (2 SE) calculated as follows:

$$2 SE_{sample} = 2 SD_{external} / \sqrt{n_{sample}} \quad (2)$$

where  $2 SE_{sample}$  is the uncertainty of the sample and  $n_{sample}$  is the number of analyses of the sample.

For samples where  $n \geq 4$  the uncertainty is calculated using the following equation:

$$2 SE_{sample} = \max(2 SD_{external}, 2 SD_{sample}) / \sqrt{n_{sample}} \quad (3)$$

where  $2 SD_{sample}$  is the 2 SD calculated based on the individual analyses of the sample and the *max* function selects the largest value,  $2 SD_{external}$  or  $2 SD_{sample}$ . For samples with  $< 4$  analyses, the standard deviation calculated from any given sample ( $2 SD_{sample}$ ) will not be representative of the true SD because of the low number of analyses (Dixon and Massey, 1950). When  $n \geq 4$  the  $2 SD_{sample}$  will begin to approach the true SD. However, there is still a large uncertainty associated with any SD calculated for small sample populations (Dixon and Massey, 1950) and to avoid under-estimating the uncertainty, the external reproducibility is used as a lower limit when calculating the sample uncertainty.

Platinum isotope determinations followed the method outlined by Hunt et al. (2017b; Appendix A). Data were corrected for instrumental mass bias using the exponential law, and were internally normalized to  $^{198}\text{Pt}/^{195}\text{Pt} = 0.2145$  (Kruijer et al., 2013a). Sample solutions were diluted to give ion beam intensities of between  $\sim 2 \times 10^{-10}$  and  $4 \times 10^{-10}$  A for  $^{194}\text{Pt}$ . Samples were measured relative to the NIST SRM 3140 Pt reference material and data are presented in the epsilon notation, relative to  $^{195}\text{Pt}$ . The 2 SD external precision determined using repeat analyses of the IAB iron meteorite North Chile (our in-house standard) is used as the Pt isotope uncertainty. Five aliquots of North Chile, passed through column chemistry independently, yield a precision of 0.49 for  $\epsilon^{192}\text{Pt}$ , 0.17 for  $\epsilon^{194}\text{Pt}$  and 0.07 for  $\epsilon^{196}\text{Pt}$  ( $n=9$ ; Hunt et al., 2017a) for ion beam intensities of  $4 \times 10^{-10}$  A.

#### 4.3.3. Element concentration analyses

A 20 mg aliquot of sample was prepared for Rh/Pd measurements following the procedure described in the Supplementary Material. Elemental abundances were measured on a Thermo Scientific Element XR. Analyses were calibrated against synthetic standards and repeat analyses of two aliquots of the meteorite Odessa indicate a precision for the Rh/Pd ratio of better than 8 % (2 RSD). Blanks are less than 1 ng for Rh and Pd, and hence negligible.

## **4.4. Results**

### 4.4.1. Palladium and Pt isotopic composition

The Pd isotope compositions (Table 4.1; Figure 4.1) reveal that the maximum offsets relative to the terrestrial standard decrease in the order  $\epsilon^{104}\text{Pd} > \epsilon^{110}\text{Pd} > \epsilon^{106}\text{Pd} > \epsilon^{102}\text{Pd}$ . Several groups show isotopic

variations between their members, most notably the IAB and IVB irons. Data for the Toluca (IAB), Tawallah Valley (IVB), Hoba (IVB), Santa Clara (IVB), and Tlacotepec (IVB) were previously presented in Ek et al. (2017; Chapter 3).

The Pd isotope compositions of all IAB samples except Odessa are within uncertainty of the bracketing standard (Figure 4.1). Odessa shows resolvable offsets in  $\epsilon^{104}\text{Pd}$  and  $\epsilon^{106}\text{Pd}$  of  $0.48 \pm 0.16$  and  $0.17 \pm 0.09$  respectively. Of the three IIAB samples, North Chile and Sikhote Alin show resolvable offsets relative to the bracketing standard in  $\epsilon^{104}\text{Pd}$  and  $\epsilon^{110}\text{Pd}$  of  $\sim 0.25 \pm 0.20$  for both ratios. The IIDs display variations in all isotope ratios except  $^{102}\text{Pd}$ . Rodeo is characterised by negative offsets in  $\epsilon^{104}\text{Pd}$  ( $-0.56 \pm 0.12$ ) and  $\epsilon^{106}\text{Pd}$  ( $-0.08 \pm 0.06$ ) and a positive offset in  $\epsilon^{110}\text{Pd}$  ( $0.32 \pm 0.12$ ). Carbo A and Carbo Y yield a positive  $\epsilon^{104}\text{Pd}$  of  $\sim 0.83 \pm 0.15$  while Carbo J and Carbo G have a larger  $\epsilon^{104}\text{Pd}$  of  $\sim 1.4 \pm 0.25$ . All Carbo samples show positive offsets in  $\epsilon^{106}\text{Pd}$  and  $\epsilon^{110}\text{Pd}$  of  $\sim 0.15 \pm 0.10$  and  $0.75 \pm 0.20$ , respectively. Carbo A and Y (the least exposed Carbo samples) have significantly lower  $\epsilon^{104}\text{Pd}$  values than those of Carbo G and J, while the other Pd isotope ratios are within uncertainty for all samples. Rodeo has a  $\epsilon^{196}\text{Pt}$  value of  $0.03 \pm 0.09$ , indicating that it is unexposed to cosmic rays. The IIIAB irons Thunda and Cape York display negative  $\epsilon^{104}\text{Pd}$  values of  $-0.29 \pm 0.26$ , while Boxhole has a positive  $\epsilon^{104}\text{Pd}$  of  $0.40 \pm 0.19$ . Boxhole and Cape York have positive  $\epsilon^{110}\text{Pd}$  offsets ( $\sim 0.40 \pm 0.30$ ) that are resolved from the bracketing standard

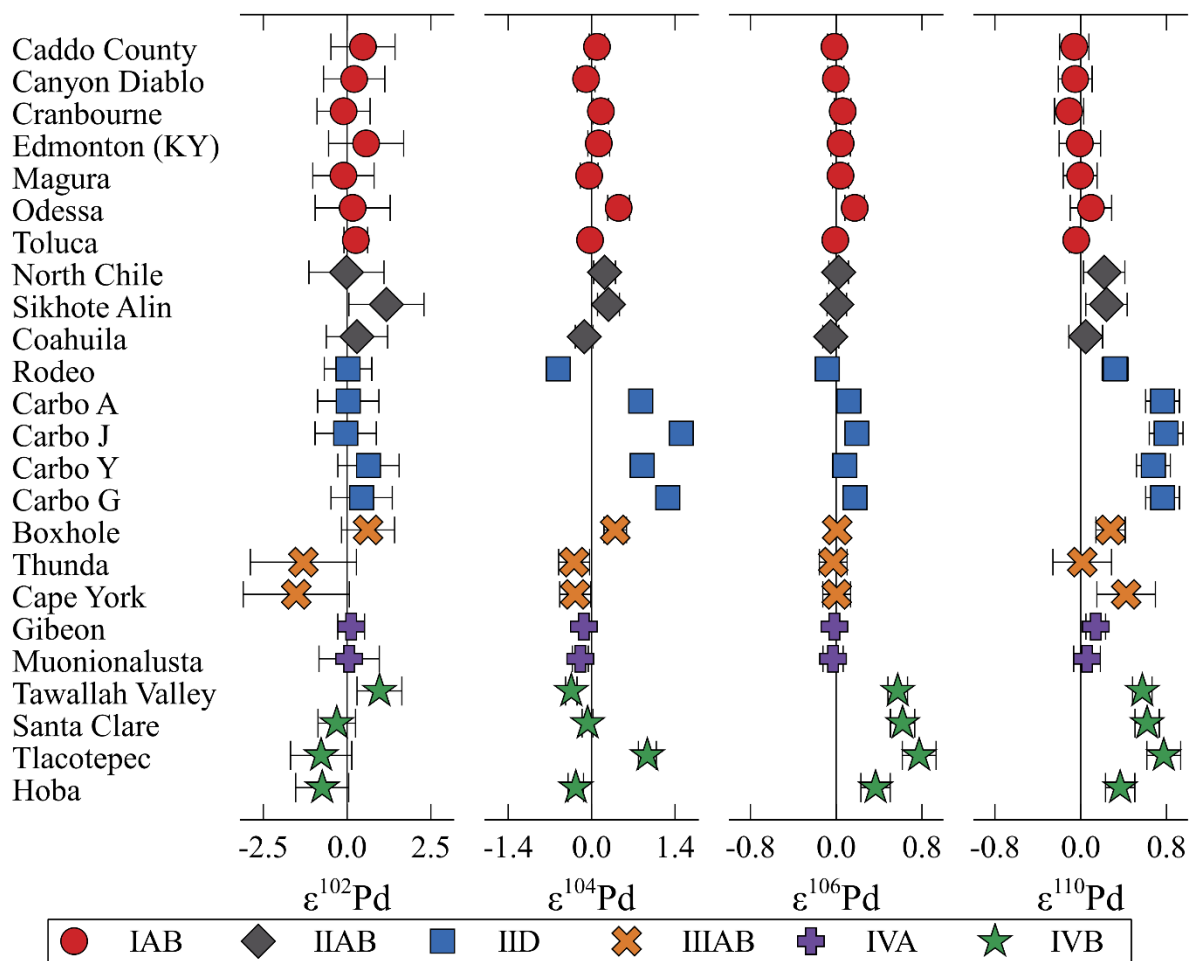


**Figure 4.1.** Palladium stable isotopic composition of iron meteorites from the IAB, IIAB, IID, IIIAB, IVA and IVB groups. All epsilon values are reported relative to  $^{105}\text{Pd}$  and were internally normalised to  $^{108}\text{Pd}/^{105}\text{Pd}$ . The largest offsets are found in  $\epsilon^{104}\text{Pd}$  and  $\epsilon^{110}\text{Pd}$  in meteorites from the IID and IVB groups, however considerable isotopic variations within the groups occur.

but within uncertainty of Thunda ( $0.01 \pm 0.27 \epsilon$ ). The two samples display a negative  $\epsilon^{104}\text{Pd}$  of  $\sim -0.19 \pm 0.13$ , while Gibeon has a small positive offset in  $\epsilon^{110}\text{Pd}$  of  $0.14 \pm 0.09$ . Of the four IVB samples only Tawallah Valley is resolvable from the bracketing standard, and the other IVB samples, for  $\epsilon^{102}\text{Pd}$  ( $0.97 \pm 0.67$ ). As discussed in Ek et al. (2017) this is likely due to the elevated Ni/Pd ratio of that sample, which has affected the accuracy of the  $\epsilon^{102}\text{Pd}$  data. Tawallah Valley and Hoba have negative variations in  $\epsilon^{104}\text{Pd}$  ( $-0.5 \pm 0.15$ ), Tlacotepec has a large positive  $\epsilon^{104}\text{Pd}$  offset ( $0.95 \pm 0.15$ ), and Santa Clara is unresolvable from the bracketing standard. Tlacotepec has a resolvable offset in  $\epsilon^{106}\text{Pd}$  ( $0.11 \pm 0.07$ ) while the remaining samples are indistinguishable, within uncertainty, from the bracketing standard for  $\epsilon^{106}\text{Pd}$ . All IVB samples yield positive values of  $\sim 0.6 \pm 0.3$  for  $\epsilon^{110}\text{Pd}$ . Hoba and Tlacotepec have  $\epsilon^{196}\text{Pt}$  values of  $0.19 \pm 0.07$  and  $0.79 \pm 0.07$ , respectively, in good agreement with values from previous studies (Kruijer et al., 2013a).

#### 4.4.2. Element ratios for Rh/Pd

The Rh/Pd ratios measured for the IAB samples range between 0.35 to 0.59 (Table 4.1), which is within the range reported by Ryan et al. (1990) and Hoashi et al. (1993). The Rh/Pd ratios for North Chile (IIAB) and Sikhote Alin (IIAB) are 1.48 and 0.86 (Table 4.1) respectively, which is also within the range previously determined for the IIAB (Hoashi et al., 1993; Ryan et al., 1990). All IVBs have Rh/Pd ratios between 0.52 and 0.62, in good agreement with those reported by Walker et al. (2008). The IID Rodeo has an Rh/Pd ratio of 0.55 while Carbo Y and Carbo G yield Rh/Pd ratios of 0.81 and 0.90, respectively.

### **4.5. Discussion**

#### 4.5.1. Sources of Pd isotope variations

The significant mass-independent variation in the Pd isotope composition (Table 4.1; Figure 4.1) reported here could have several causes. First, they could represent nuclear field shift effects (NFS), that can arise due to differences in the shape and size of isotope nuclei, and can occur during chemical exchange reactions (Bigeleisen, 1996). Second, secondary neutron capture due to CRE as meteoroids are traveling through space has been determined as the source of within-group Pd isotopic variations for the IVB by Mayer et al. (2015).. Finally, the observed variations could represent nucleosynthetic offsets, which are thought to be linked to isotopic heterogeneity in the early protoplanetary disk. In this scenario, meteorites within the same group are expected to have identical mass-independent isotope composition because they originate from the same parent body. Our data reveal isotopic heterogeneity within individual meteorite groups and this suggests that, besides potential nucleosynthetic effects in Pd, the other mass-independent processes must also contribute to the observed variations and they are discussed in the following.

#### *Nuclear field shift*

Due to differences in the nuclear size and shape of isotopes, particularly between odd and even mass isotopes, mass-independent fractionation can occur during chemical exchange reactions. First proposed by Bigeleisen (1996) to explain the mass-independent fractionation of U isotopes during exchange reactions, nuclear field shift (NFS) effects have been described for a wide range of elements (Fujii et al., 2009). The largest offsets usually occur in the odd isotopes because they often have a smaller nuclear charge radii than adjacent isotopes (Bigeleisen, 1996). A study of W isotopes showed mean offset of

$-0.14 \pm 0.08$  for  $\epsilon^{183\text{W}/184\text{W}}$ , internally normalised to  $^{186\text{W}/184\text{W}}$ , from repeat measurements of a metal alloy which was attributed to NFS effects (Cook and Schönbacher, 2016). Those authors determined that NFS offsets arose from the ion exchange procedure to purify W. Nuclear field shift effects could therefore vary for each aliquot that is processed through ion exchange chemistry, resulting in varying offsets for meteorites from the same group. Additionally, multiple aliquots of the same sample may also show variable Pd isotope signatures. The relative offset for each isotope can be modelled based on the nuclear charge radii using the equation presented in Fujii et al. (2006). The largest effect in Pd is expected on  $^{105}\text{Pd}$ , the sole odd isotope (Figure 4.2a). This effect would propagate on to all Pd isotope ratios when  $^{105}\text{Pd}$  is used for internal normalisation, and would result in positive offsets on  $\epsilon^{102}\text{Pd}$ ,  $\epsilon^{104}\text{Pd}$ , and  $\epsilon^{106}\text{Pd}$  and a negative offset in  $\epsilon^{110}\text{Pd}$  (Figure 4.2a). A more suitable normalisation for detecting NFS effects is  $^{108}\text{Pd}/^{106}\text{Pd}$  where a large negative offset in  $\epsilon^{105}\text{Pd}$  is expected (Figure 4.2a). All three aliquots of the NIST SRM 3138 Pd standard processed through the ion exchange procedure are within uncertainty of one another and show no offsets, within uncertainty, relative to the unprocessed bracketing standards (Ek et al., 2017; Chapter 2). Hence, we see no evidence of NFS effects. However, the yield for the processed standard is higher (>90%) than that generally achieved for meteorite samples (50-70%; Ek et al., 2017) and therefore it is possible that they are not fractionated to the degree where NFS effects would become apparent. The IAB irons show the smallest nucleosynthetic offsets of all the

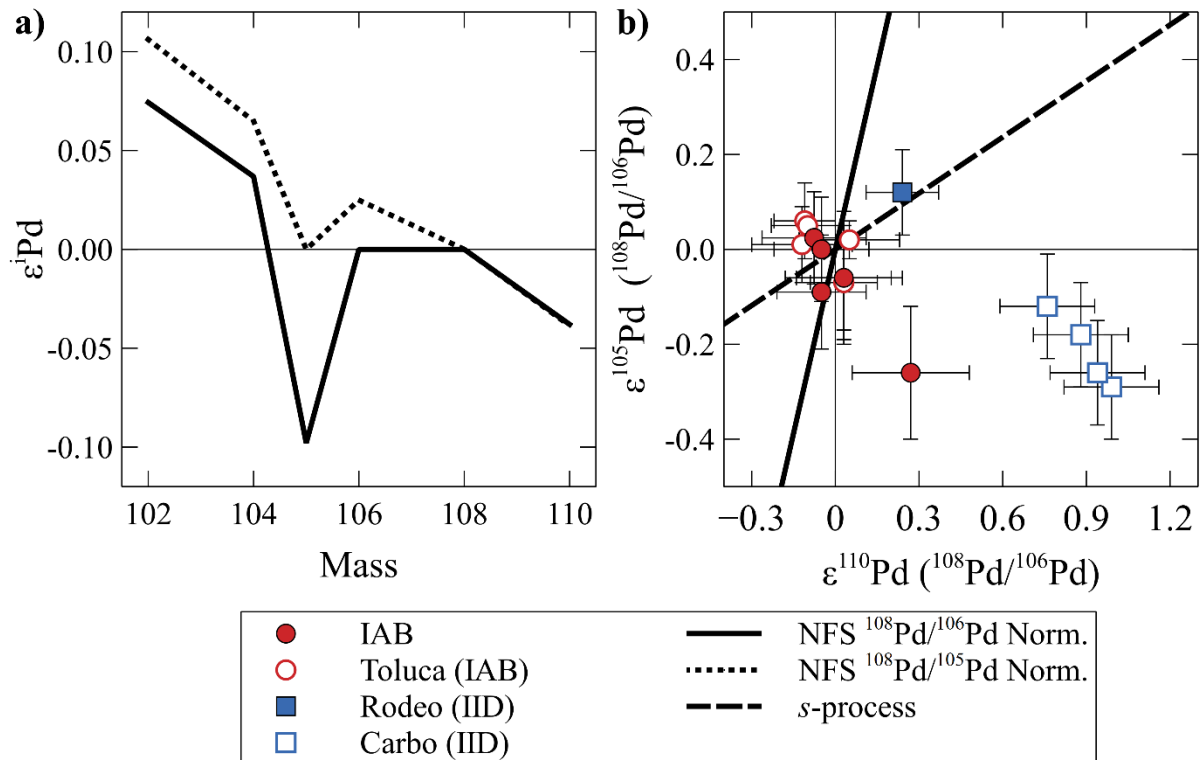


**Figure 4.2.** a) The nucleosynthetic offsets predicted from nuclear field shift calculated using the equations from Fujii et al. (2009) using the charge radii from Angeli and Marinova (2013). Short dashed line and solid line shows the NFS effects internally normalised to  $^{108}\text{Pd}/^{105}\text{Pd}$  and  $^{108}\text{Pd}/^{106}\text{Pd}$ , respectively. b)  $\epsilon^{105}\text{Pd}$  against  $\epsilon^{110}\text{Pd}$  for five aliquots of Toluca (IAB; Red hollow circles), the other IAB meteorites (Full red circles), Rodeo (IID; Full red square) and four aliquots of Carbo (IID; Hollow blue squares) sampled at different locations within the meteorite. All aliquots of the same sample were individually processed through chemistry. The black line shows the predicted nuclear field shift trend, the dashed line shows the s-process deficit trend calculated using the model by Bisterzo et al. (2011). All values were internally normalised to  $^{108}\text{Pd}/^{106}\text{Pd}$  and shown relative to  $^{106}\text{Pd}$ .



iron groups in other elements including, e.g. Mo and Ru (Fischer-Gödde and Kleine, 2017; Poole et al., 2017), and therefore they are the ideal samples to look for NFS effects. With one exception, all IAB samples, including the five individual aliquots of Toluca, are within uncertainty of the bracketing standard (Figure 4.2b). Odessa is clearly resolvable from the other IAB meteorites, however, it does not fall on the predicted NFS trend suggesting the offset is not caused by such effects. Similarly, the isotopic heterogeneities in the IID group between Rodeo and the four samples of Carbo (IID) are not consistent with the NFS trend. These within-group variations are, as will be discussed in detail in the next section, better explained by CRE effects. We therefore find no evidence for NFS effects on Pd isotopes in our data, and can exclude this process when interpreting variations in the iron meteorites.

#### *Cosmic ray exposure*

Mass-independent isotope variation can occur from exposure to galactic cosmic rays as a meteoroid travels through space. Cosmic ray exposure leads to the production of secondary neutrons upon interaction with a meteoroid. When these secondary neutrons reach the epithermal to thermal energy range (0.025 eV to 10 keV), neutron capture reactions begin to occur (Leya and Masarik, 2013). The magnitude of isotopic offsets caused by CRE depends on several different factors. First, each isotope has a distinct neutron capture cross section and susceptibility to neutron capture at certain energies (Leya and Masarik, 2013). Second, contributions from the decay of unstable isotopes produced by CRE on isotopes of other elements can lead to significant increases in the stable daughter isotopes. Within-group variations due to CRE have been observed for a range of different elements, e.g., Mo, Ru, Pd, W, Os and Pt (Fischer-Gödde et al., 2015; Hunt et al., 2017a; Kruijjer et al., 2013a; Markowski et al., 2006; Mayer et al., 2015; Wittig et al., 2013; Worsham et al., 2017).

Here we use  $\epsilon^{196}\text{Pt}$  as a neutron dosimeter to assess the CRE effects on Pd isotopes. Platinum isotopes are a well-established neutron dosimeter with well-resolved CRE offsets. In addition, they also lack nucleosynthetic isotope variations, which renders the data interpretation straight forward (Hunt et al., 2017a; Kruijjer et al., 2013a; Wittig et al., 2013). For Pd, the reaction  $^{103}\text{Rh}(n,\beta)^{104}\text{Pd}$  is important because of the large difference in relative abundance of  $^{103}\text{Rh}$  and  $^{104}\text{Pd}$  (100 % vs. 11 %), particularly as both elements occur at similar abundances in iron meteorites (Hoashi et al., 1993; Ryan et al., 1990). Hence, higher Rh/Pd ratios lead to larger CRE effects on  $\epsilon^{104}\text{Pd}$ . Modelling predicts that production of  $^{104}\text{Pd}$  from Pd alone is very low (0.1  $\epsilon^{104}\text{Pd}$  per 1  $\epsilon^{196}\text{Pt}$  Leya and Masarik, 2013), while the production from  $^{103}\text{Rh}$  is much larger (3.5  $\epsilon^{104}\text{Pd}$  per 1  $\epsilon^{196}\text{Pt}$  when Rh/Pd = 1). Third, sample-specific properties such chemical composition, exposure time, pre-atmospheric radius and sample depth within the meteoroid all contribute to the expected CRE offsets (Leya and Masarik, 2013). This implies that meteorites from the same group, and even samples from different depths within the same meteorite, will display different isotopic offsets.

All Pt and Pd isotope data in this study were determined on the same sample aliquot and they thus can be compared without ambiguity. The CRE effects in each group were assessed by fitting a linear regression for each Pd isotope ratio against  $\epsilon^{196}\text{Pt}$ . The slope of the regression represents the  $\epsilon^i\text{Pd}$  offset for every 1  $\epsilon^{196}\text{Pt}$  offset due to CRE effects and the y-axis intercept is the nucleosynthetic Pd composition. Regressions for the IAB, IID and IVB groups all yield well-defined slopes, while the slopes for the IIAB, IIIAB, and IVA irons show very large uncertainties because of the narrow spread of  $\epsilon^{196}\text{Pt}$

values ( $\Delta \epsilon^{196}\text{Pt} < 0.3$ ; Table 4.2), i.e. all samples within these groups had similar levels of CRE. The latter slopes are therefore of limited use and are omitted from the discussion.

No variations in  $\epsilon^{102}\text{Pd}$  were identified and this suggests that  $\epsilon^{102}\text{Pd}$  is not affected by CRE, at our current level of precision (Figure 4.3a). For the  $\epsilon^{104}\text{Pd}$ -  $\epsilon^{196}\text{Pt}$  isotope space, the regression must include the variable Rh/Pd ratios of the samples (Leya and Masarik, 2013). For samples where no Rh/Pd ratios were available, a value was estimated based on other samples in the same group (Table 4.1). The  $\epsilon^{196}\text{Pt}$  value of each sample was then normalised to the Rh/Pd ratio of the sample, using the following equation:

$$\epsilon^{196}\text{Pt}_{\text{Rh/Pd normalised}} = \epsilon^{196}\text{Pt} \times \frac{(\text{Rh/Pd})_{\text{sample}}}{(\text{Rh/Pd})_{\text{median}}} \quad (4)$$

After applying this formula, the best-fit line for each group was obtained and the resulting slopes were re-normalised to Rh/Pd = 1 for ease of comparison (Table 4.2). The slopes of the  $\epsilon^{104}\text{Pd}$  -  $\epsilon^{196}\text{Pt}$  correlations for the IAB, IID and the IVB irons are within uncertainty of each other ( $\sim 2.6 \pm 1.3$  for Rh/Pd = 1; Figure 4.3b). The regression for  $\epsilon^{106}\text{Pd}$  against  $\epsilon^{196}\text{Pt}$  yields consistent slopes across all three groups of  $\sim 0.30 \pm 0.15$  (Table 4.2; Figure 4.3c). The IID and IVB irons define slopes of  $\sim 0.55 \pm 0.30$  in the  $\epsilon^{110}\text{Pd}$  -  $\epsilon^{196}\text{Pt}$  diagram (Figure 4.3d), while the IABs have a shallower slope of  $0.26 \pm 0.38$ . However, all three slopes are within uncertainty of each other (Table 4.2; Figure 4.3d).

Overall, the consistency of the  $\epsilon^{104}\text{Pd}$ ,  $\epsilon^{106}\text{Pd}$  and  $\epsilon^{110}\text{Pd}$  variations against  $\epsilon^{196}\text{Pt}$  for the different groups strongly suggests CRE as the source of within-group Pd isotope variations (Figure 4.3). These variations also agree well with the modelled CRE effects by Leya and Masarik (2013; Table 4.2; Figure 4.3), providing further support of this conclusion. This is also supported by CRE models where an offset of

**Table 4.2.** Linear regressions of  $\epsilon^i\text{Pd}$  against  $\epsilon^{196}\text{Pt}$ .

Group	$\Delta \epsilon^{196}\text{Pt}^a$	$\epsilon^{102}\text{Pd}$	$\epsilon^{102}\text{Pd}$	$\epsilon^{102}\text{Pd}$	$\epsilon^{104}\text{Pd}$	$\epsilon^{104}\text{Pd}$	$\epsilon^{104}\text{Pd}$
		Unexposed <sup>b</sup>	Intercept <sup>c</sup>	Slope <sup>c</sup>	Unexposed <sup>b</sup>	Intercept <sup>c,d</sup>	Slope <sup>c,d</sup>
IAB	$0.57 \pm 0.18$	$0.20 \pm 0.26$	$0.24 \pm 0.35$	$-0.42 \pm 2.22$	$0.01 \pm 0.12$	$-0.05 \pm 0.08$	$2.56 \pm 1.17$
IIAB	$0.20 \pm 0.14$	$0.46 \pm 0.60$	$0.18 \pm 1.00$	$2.36 \pm 6.78$	$-0.12 \pm 0.15$	$-0.15 \pm 0.25$	$1.75 \pm 1.41$
IID	$0.85 \pm 0.18$	$0.20 \pm 0.38$	$0.04 \pm 0.88$	$0.26 \pm 1.35$	$-0.56 \pm 0.12$	$-0.65 \pm 0.24$	$2.74 \pm 0.42$
IIIAB	$0.22 \pm 0.14$	$-0.05 \pm 0.97$	$-1.89 \pm 1.55$	$10.12 \pm 8.16$	$-0.29 \pm 0.26$	$-0.42 \pm 0.28$	$4.44 \pm 2.36$
IVA	$0.11 \pm 0.18$	$0.11 \pm 0.37$	$0.14 \pm 0.58$	$-0.57 \pm 9.37$	$-0.13 \pm 0.07$	$-0.11 \pm 0.12$	$-1.63 \pm 4.56$
IVB	$0.60 \pm 0.14$	$-0.52 \pm 0.41$	$-0.42 \pm 0.90$	$-0.22 \pm 1.96$		$-0.66 \pm 0.22$	$3.29 \pm 0.85$
CRE Model <sup>e</sup>				0.12			3.59
	$\Delta \epsilon^{196}\text{Pt}^a$	$\epsilon^{106}\text{Pd}$	$\epsilon^{106}\text{Pd}$	$\epsilon^{106}\text{Pd}$	$\epsilon^{110}\text{Pd}$	$\epsilon^{110}\text{Pd}$	$\epsilon^{110}\text{Pd}$
		Unexposed <sup>b</sup>	Intercept <sup>c</sup>	Slope <sup>c</sup>	Unexposed <sup>b</sup>	Intercept <sup>c</sup>	Slope <sup>c</sup>
IAB	$0.57 \pm 0.18$	$-0.01 \pm 0.02$	$-0.02 \pm 0.03$	$0.36 \pm 0.19$	$-0.05 \pm 0.05$	$-0.07 \pm 0.06$	$0.26 \pm 0.38$
IIAB	$0.20 \pm 0.14$	$-0.05 \pm 0.07$	$-0.05 \pm 0.08$	$0.35 \pm 0.57$	$0.05 \pm 0.16$	$0.03 \pm 0.19$	$1.01 \pm 1.25$
IID	$0.85 \pm 0.18$	$-0.08 \pm 0.06$	$-0.10 \pm 0.07$	$0.32 \pm 0.10$	$0.32 \pm 0.12$	$0.31 \pm 0.13$	$0.57 \pm 0.21$
IIIAB	$0.22 \pm 0.14$	$-0.01 \pm 0.09$	$-0.02 \pm 0.12$	$0.12 \pm 0.59$	$0.22 \pm 0.19$	$0.16 \pm 0.25$	$0.54 \pm 1.23$
IVA	$0.11 \pm 0.18$	$-0.02 \pm 0.04$	$-0.01 \pm 0.06$	$-0.12 \pm 0.97$	$0.14 \pm 0.09$	$0.16 \pm 0.15$	$-0.77 \pm 1.74$
IVB	$0.60 \pm 0.14$		$-0.09 \pm 0.06$	$0.26 \pm 0.15$		$0.39 \pm 0.13$	$0.53 \pm 0.32$
CRE Model <sup>e</sup>				0.35			0.31

<sup>a</sup> The difference between the smallest and largest  $\epsilon^{196}\text{Pt}$  values reported for samples within the group <sup>b</sup> The weighted mean of samples with  $\epsilon^{196}\text{Pt}$  values less than 1.3 for  $\epsilon^{102}\text{Pd}$ , 0.03 for  $\epsilon^{104}\text{Pd}$ , 0.08 for  $\epsilon^{106}\text{Pd}$  and 0.11 for  $\epsilon^{110}\text{Pd}$ . <sup>c</sup> Regressions calculated using the equation from York et al. (2004). <sup>d</sup> Normalised to Rh/Pd = 1. <sup>e</sup> From Leya and Masarik (2013).

only  $0.12 \epsilon^{102}\text{Pd}$  per  $1 \epsilon^{196}\text{Pt}$  is expected (Leya and Masarik, 2013), which is well below our current uncertainty for  $\epsilon^{102}\text{Pd}$ .

#### Calculating the nucleosynthetic Pd isotope composition

To determine the nucleosynthetic isotope composition of a group requires either samples with no CRE contribution, or alternatively a method for correction of CRE effects. In reality, all analysed samples may have experienced some exposure to CRE and a tolerance limit for what is considered negligible relative to the analytical uncertainties needs to be defined. For this study the tolerance limits, i.e. the maximum

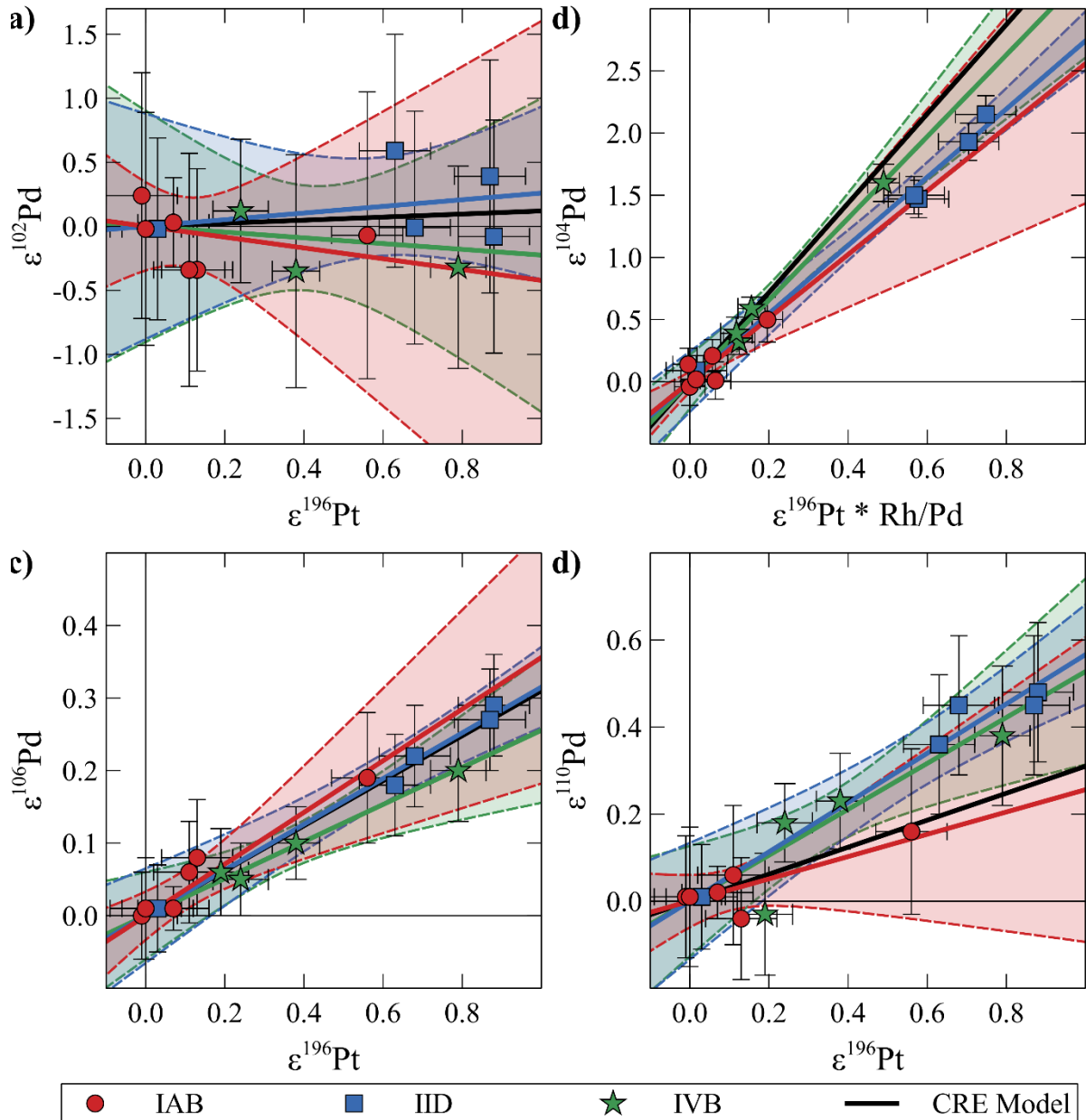


**Figure 4.3.** Regressions of  $\epsilon^{102}\text{Pd}$  (a),  $\epsilon^{106}\text{Pd}$  (c), and  $\epsilon^{110}\text{Pd}$  (d) against  $\epsilon^{196}\text{Pt}$  for the IAB (Red), IID (Blue) and IVB (Green) groups. b) Regressions of  $\epsilon^{104}\text{Pd}$  against  $\epsilon^{196}\text{Pt}$  multiplied by the Rh/Pd ratio of the sample, to account for varied CRE contributions from  $^{103}\text{Rh}(n,\beta)^{104}\text{Pd}$ , for the same three groups. Individual samples and the slope of the regression have been normalised to the intercept for each isotope/group such that the slopes can be compared directly unambiguously. The black line shows the modelled CRE trend for each isotope by Leya and Masarik (2013). The slope of the regressions for  $\epsilon^{102}\text{Pd}$ ,  $\epsilon^{104}\text{Pd}$ ,  $\epsilon^{106}\text{Pd}$  and  $\epsilon^{110}\text{Pd}$  all overlap for all three groups and agrees well with the modelled slope.

$\epsilon^{196}\text{Pt}$  value where a sample can be considered unexposed, are 0.03 for  $\epsilon^{104}\text{Pd}$  ( $\text{Rh}/\text{Pd} = 1$ ), 0.08 for  $\epsilon^{106}\text{Pd}$  and 0.1 for  $\epsilon^{110}\text{Pd}$ . These numbers represent the typical  $\epsilon^{196}\text{Pt}$  value where the Pd isotope composition of samples (Table 4.1) falls outside the uncertainty of the regression intercept, i.e. the unexposed Pd isotope composition (Table 4.2). The lack of covariation between  $\epsilon^{102}\text{Pd}$  and  $\epsilon^{196}\text{Pt}$  implies that all  $\epsilon^{102}\text{Pd}$  data in this study can be considered unexposed. Given the uncertainty on  $\epsilon^{196}\text{Pt}$  these tolerance limits are somewhat arbitrary and can only be considered useful in this particular study. Unexposed values are preferentially selected over calculated intercepts to determine the nucleosynthetic composition of each group (Table 4.3). If more than one sample falls below the  $\epsilon^{196}\text{Pt}$  limits stated above a weighted mean is used to calculate the unexposed composition. All groups with the exception of the IVB have at least one sample with a  $\epsilon^{196}\text{Pt}$  value that falls below the limits stated above.

All groups apart from the IAB irons show nucleosynthetic effects that are distinct from the isotopic composition of the terrestrial standard in the order  $\text{IVB} \geq \text{IID} > \text{IIIAB} > \text{IVA} > \text{IIAB} \geq \text{IAB} = \text{Earth}$  (Figure 4.4). The largest offsets are identified for the IVBs in  $\epsilon^{104}\text{Pd}$  ( $-0.66 \pm 0.22$ ) and  $\epsilon^{110}\text{Pd}$  ( $0.29 \pm 0.13$ ). The negative shifts in  $\epsilon^{104}\text{Pd}$  and  $\epsilon^{106}\text{Pd}$ , with concomitant positive values in  $\epsilon^{110}\text{Pd}$ , are in good agreement with *s*-process deficit/*r*-process excess variations predicted from *s*-process stellar yields (Bisterzo et al., 2011; Figure 4.4). Two different approaches were used to account for the over production (+ 21.6 %) of  $^{104}\text{Pd}$ , relative to the solar abundance, in this model. First, all the yields were renormalized to a solar abundance for  $^{104}\text{Pd}$ , keeping the relative abundance of each isotope the same. The second approach was to set  $^{104}\text{Pd}$  to the solar abundance without changing the yields of the other isotopes. Our data fit better to the *s*-process trend using the first approach (Figure 4.4), suggesting that there may be a systematic inaccuracy in the recommended Maxwellian-averages cross sections (MACS) for Pd isotopes (taken from Cornelis et al., 1983; Macklin and Winters, 1981). Renewed measurements of the MACS for all the Pd isotopes might help resolve this issue.

The *p*-process-only isotope  $^{102}\text{Pd}$  can be used to distinguish between an *s*-process deficit and an *r*-process excess signature. However, the uncertainty associated with  $\epsilon^{102}\text{Pd}$  renders it difficult to draw decisive conclusions. Nevertheless, although all groups apart from the IID are consistent with either an *s*-deficit or an *r*-excess, the IID are consistent with an *s*-process deficit only (Figure 4.4b). This indicates that variations in our new Pd isotope data reflect a relative deficit in the *s*-process component, in agreement with studies of Ru and Mo isotopes (Burkhardt et al., 2011; Fischer-Gödde et al., 2015; Fischer-Gödde and Kleine, 2017; Poole et al., 2017).

**Table 4.3.** The average nucleosynthetic Pd isotope composition of iron meteorite groups.

Group	$\epsilon^{102}\text{Pd}$	$\epsilon^{104}\text{Pd}$	$\epsilon^{106}\text{Pd}$	$\epsilon^{110}\text{Pd}$
IAB	$0.20 \pm 0.26^a$	$0.01 \pm 0.12^a$	$-0.01 \pm 0.02^a$	$-0.05 \pm 0.05^a$
IIAB	$0.46 \pm 0.60^a$	$-0.12 \pm 0.15^a$	$-0.05 \pm 0.07^a$	$0.05 \pm 0.16^a$
IID	$0.20 \pm 0.38^a$	$-0.56 \pm 0.12^a$	$-0.08 \pm 0.06^a$	$0.32 \pm 0.12^a$
IIIAB	$-0.05 \pm 0.97^a$	$-0.29 \pm 0.26^a$	$-0.01 \pm 0.09^a$	$0.22 \pm 0.19^a$
IVA	$0.11 \pm 0.37^a$	$-0.13 \pm 0.07^a$	$-0.02 \pm 0.04^a$	$0.14 \pm 0.09^a$
IVB	$-0.52 \pm 0.41^a$	$-0.66 \pm 0.22^b$	$-0.09 \pm 0.06^b$	$0.39 \pm 0.13^b$

<sup>a</sup> Calculated from unexposed samples as described in section 4.1.3. <sup>b</sup> Calculated via regression against  $\epsilon^{196}\text{Pt}$  (Table 2).

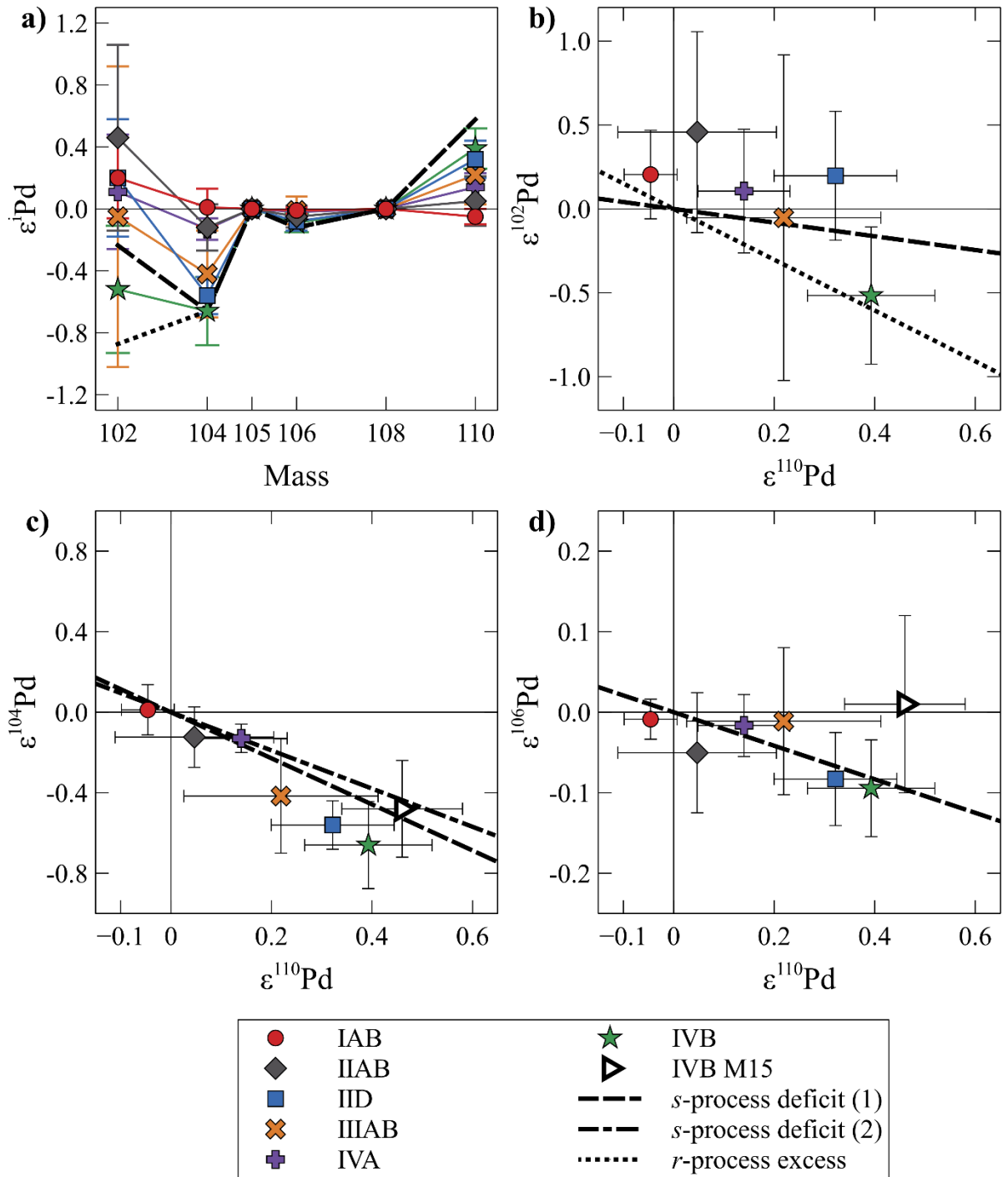


**Figure 4.4.** a) The preferred nucleosynthetic signature of the IAB, IIAB, IID, IVA, and IVB groups from Table 3. Dashed line shows a modelled  $s$ -process deficit, from Bisterzo et al. (2011), normalised to the IVB  $\epsilon^{104}\text{Pd}$  value. Short dashed line shows a modelled  $r$ -process excess, calculated from  $r$ -process residual from Bisterzo et al. (2011), again normalised to  $\epsilon^{104}\text{Pd}$  of the IVB group.  $\epsilon^{102}\text{Pd}$  (b),  $\epsilon^{104}\text{Pd}$  (c) and  $\epsilon^{106}\text{Pd}$  (d) against  $\epsilon^{110}\text{Pd}$  normalised to  $\epsilon^{108}\text{Pd}/\epsilon^{105}\text{Pd}$  for the IAB (Red circles), IIAB (Grey diamonds), IID (Blue squares), IIIAB (Orange crosses), IVA (Purple plusses), and IVB (Green stars) groups after correction for CRE. Also shown in c) and d) are the Pd data from Mayer et al. (2015; M15; White triangles). Long dashed and dash dot lines shows a  $s$ -process deficit mixing line using the model by Bisterzo et al. (2011) accounting for the  $^{104}\text{Pd}$  overproduction using approach 1 and 2 as described in section 6.1, respectively. Short dash line shows the  $r$ -process excess missing line calculated from the residual of Bisterzo et al. (2011). All isotopes shows a good agreement with the trend predicted  $s$ -process mixing lines. The results favour a  $s$ -process deficit over an  $r$ -process excess based on  $\epsilon^{102}\text{Pd}$ .

The nucleosynthetic isotope composition obtained here for the IVB group is within uncertainty of that presented by Mayer et al. (2015) for  $\epsilon^{104}\text{Pd}$ ,  $\epsilon^{106}\text{Pd}$  and  $\epsilon^{110}\text{Pd}$  (Figure 4.4). All samples in the IVB group show considerable CRE effects and both studies determined the nucleosynthetic composition using a regression against a neutron dosimeter ( $\epsilon^{196}\text{Pt}$ , this study;  $\epsilon^{192}\text{Pt}$ , Mayer et al., 2015) analysed using the same sample aliquot. The excellent agreement between the two studies illustrates that the nucleosynthetic Pd composition can be consistently calculated for exposed samples using Pt isotope neutron dosimeters.

#### 4.5.2 Comparison to Mo and Ru nucleosynthetic variations

The neighbouring elements Ru and Mo show a well-documented correlation between their nucleosynthetic offsets in different meteorite groups, which is consistent with a deficit in the *s*-process isotopes relative to Earth, as defined by SiC grains and stellar *s*-process production models (e.g. Dauphas et al., 2004; Fischer-Gödde et al., 2015; Poole et al., 2017). Palladium lies in the same mass range as Mo and Ru and here we show that the Mo-Ru correlation extends to Pd (Figure 4.5). However, unlike the slope of the Mo-Ru correlation, the slope of the (Mo-Ru)-Pd correlation cannot be explained by *s*-process stellar production models assuming solar abundances of Mo, Ru and Pd (Figure 4.5). A linear regression of  $\epsilon^{96}\text{Mo}$  against  $\epsilon^{110}\text{Pd}$  (Figure 4.5a) yields a slope of  $-1.8 \pm 0.6$ , while stellar production models predict a much shallower slope of about  $-0.4$  with solar abundances of Mo and Pd (Figure 4.5a). The same is true for  $\epsilon^{110}\text{Pd}$  versus  $\epsilon^{100}\text{Ru}$ , which yields a slope of  $-2.5 \pm 0.8$ , while stellar models predict a slope of approximately  $-0.75$  (Figure 4.5b). To recreate the slope of the (Mo-Ru)-Pd correlation using the stellar production models the abundance of Pd needs to be reduced by a factor of  $\sim 4$  compared to its solar abundance.

Additionally, recent studies provided evidence for two distinct suites of meteorites based on Mo isotope data (Budde et al., 2016; Kruijer et al., 2017; Poole et al., 2017). The first suite encompasses the IAB, IC, IIAB, IIE, IIIAB, IIIE and IVA iron meteorites, and the second suite includes the IIC, IID, IIF and the IVB iron meteorites (Kruijer et al., 2017; Poole et al., 2017). While both groups are characterised by *s*-process deficits, the latter group also shows evidence for an additional *r*-process component relative to the first group. While our Pd data is consistent with an *s*-process deficit, we are unable to identify more than one suite of such deficits in our data. However, this does not preclude their existence given the relatively large uncertainty on  $\epsilon^{102}\text{Pd}$  compared to the expected nucleosynthetic offsets.

Worsham et al. (2017) report that the IAB subgroups sHH and sHL display distinct Mo isotope compositions compared to the main group (MG) and sLL, sLM and sLH subgroups. In this study, we measured samples from the MG (Canyon Diablo, Cranbourne, Magura, Odessa), sLM (Edmonton KY), sLL (Toluca) and one ungrouped meteorite (Caddo County). All the analysed subgroups show an identical Pd isotopic composition that is indistinguishable from the bracketing standard, in accordance with the results of Worsham et al. (2017).

#### 4.5.3 Origin of the Zr-Mo-Ru-Pd correlation and nucleosynthetic offsets in the solar system

The correlation between Mo and Ru can be explained by a mixing trend between the bulk solar system isotope composition and an *s*-process component (Dauphas et al., 2004). Furthermore, Akram et al. (2015) showed that the Mo isotope variations also correlate with those in Zr, and that the latter also

reflect the heterogeneous distribution of an *s*-process component in the solar system. The magnitude of the Zr, Mo and Ru isotope variations relative to each other are explained by the admixture of a pure *s*-process component based on AGB yields from e.g. Bisterzo et al. (2011). However, such a model predicts larger than observed Pd isotope offsets (i.e. a shallower slope in Figure 4.5). Mayer et al. (2015) suggested that the diminished Pd isotope offsets were due to selective destruction of the *s*-process Pd carrier phase relative to that of the more refractory elements Mo and Ru in the early solar nebula. Here we propose an alternative hypothesis for the origin of the reduced Pd offsets relative to those of Zr, Mo and Ru isotopes, namely that it reflects incomplete condensation of elements around AGB stars.

Modelling of dust formation in AGB stellar environments suggests that the majority of the elements produced by these stars are returned to the interstellar medium (ISM) in the gas phase, with only a small dust fraction (Ferrarotti and Gail, 2006). Therefore, only a small fraction of the dust in the ISM is stardust (or presolar grains) which retains a signature unique to the stellar environment in which it formed. The majority of dust in the ISM grows from a well-mixed gas phase in dense molecular clouds as separate dust grains or as dust coatings onto existing grains (e.g. Draine, 2009). As a consequence, this dust inherits an isotopic composition akin to the bulk ISM. It has been shown that refractory

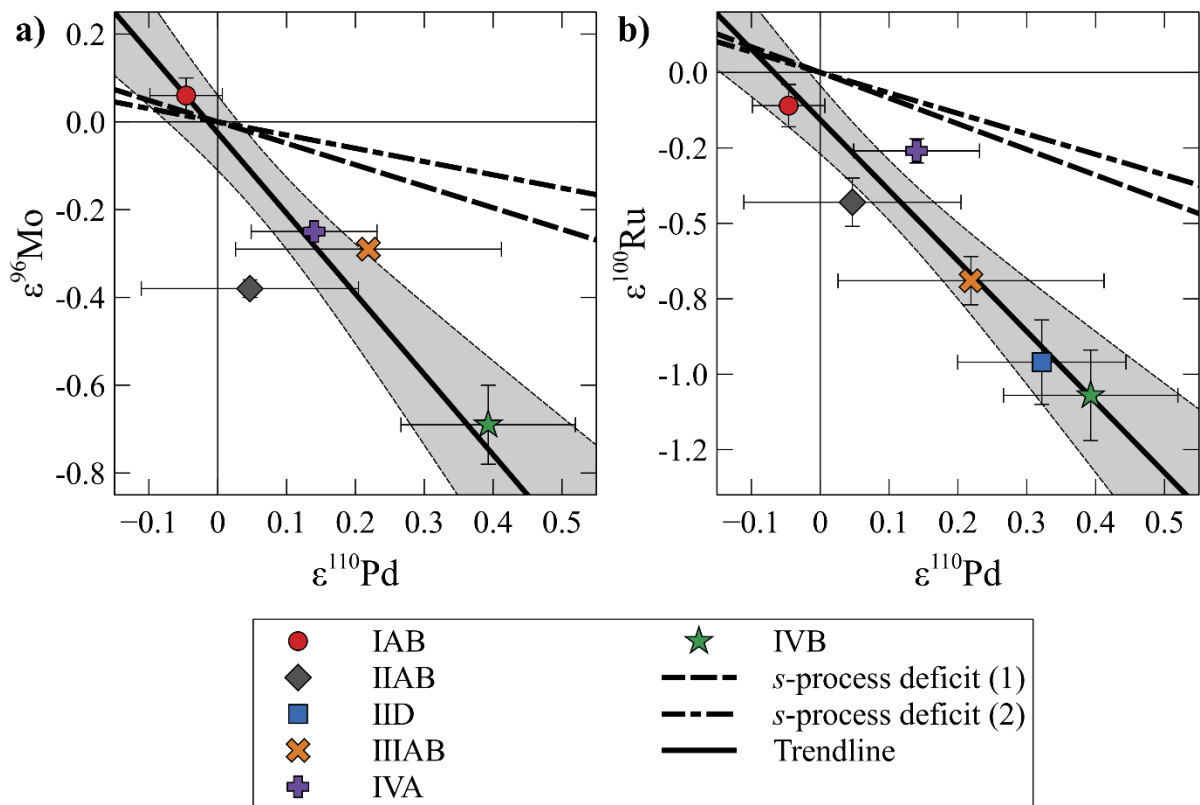


**Figure 4.5.** The correlation of  $\epsilon^{96}\text{Mo}$  (a; Poole et al., 2017) and  $\epsilon^{100}\text{Ru}$  (b; Fischer-Gödde et al., 2015; Fischer-Gödde and Kleine, 2017) against  $\epsilon^{110}\text{Pd}$  for the IAB (Red circles), IIAB (Charcoal diamonds), IID (Blue squares), IIIAB (Orange crosses), IVA (Purple plusses), and IVB (Green stars). The dashed and dash dot line show a modelled *s*-process mixing trend based on solar abundances of Mo, Ru and Pd using *s*-process yields from Bisterzo et al. (2011) accounting for overproduction of isotopes using approach 1 and 2 as described in section 3.1, respectively. Solid line shows the best fit trend and the surrounding shaded area shows the uncertainty envelope calculated using York et al. (2004). Palladium shows good correlation between the offsets found in  $\epsilon^{96}\text{Mo}$  and  $\epsilon^{100}\text{Ru}$  however, the correlation cannot be explained by the modelled *s*-process mixing line. The best fit trend is best explained by a *s*-process mixing line consisting of a factor of 4 more Mo and Ru than Pd.

elements are favourably incorporated into SiC grains (Lodders and Fegley, 1997), suggesting that the trace element composition of stardust is related to the condensation temperature of elements. Given that Zr, Mo and Ru are more refractory than Pd, they should more readily condense into the dust formed around the AGB stars. This results in a larger concentration of Zr, Mo and Ru in the stardust compared to Pd. Therefore the slope of the Zr-Mo-Ru-Pd correlation found in meteorites is inherited from the AGB stardust.

An additional process is needed to explain the heterogeneous distribution of the AGB stardust in the solar nebula, which gives rise to the nucleosynthetic variations observed between different planetary bodies. The Earth is the most *s*-process enriched material known to-date for Zr (Akram et al., 2015), Mo (Burkhardt et al., 2011; Dauphas et al., 2002; Poole et al., 2017) and Ru (Chen et al., 2010; Dauphas et al., 2004; Fischer-Gödde et al., 2015; Fischer-Gödde and Kleine, 2017), and this requires the removal of *p*- and *r*- process material from the terrestrial building blocks (Akram et al., 2015). Studies of Zr, Mo and Ru isotopes showed that the magnitude of the *s*-process deficit increases with the distance from the Sun at which the parent body is inferred to have formed (Akram et al., 2015; Burkhardt et al., 2011; Fischer-Gödde and Kleine, 2017). It has been proposed that the *p*- and *r*-process carrier phases are more susceptible to thermal processing than the *s*-process carrier phases, leading to the destruction of the former in regions closer to the Sun (Akram et al., 2015; Poole et al., 2017). However, modelling predicts that the majority of stardust originated from AGB stars, with supernovae material comprising only a small fraction (Zhukovska et al., 2008). This agrees with the inferred origins of presolar grains preserved in chondrites (Hoppe and Zinner, 2000). A recent study estimates the total stardust fraction in our solar system to ~3% based on the abundance of presolar grains in chondritic meteorites (Hoppe et al., 2017). Therefore, the majority of the *p*- and *r*-process mass of the solar system condensed from the well-mixed ISM gas phase with only a minute fraction of stardust retaining the original nucleosynthetic signature. As a result, a very large fraction of the available *p*- and *r*-process stardust would have to be destroyed to produce the observed *s*-process deficits. Another possible way to recreate the nucleosynthetic variations in the early solar system is by selective destruction of ISM-grown dust coatings which would increase the relative abundance of stardust, predominately carrying an *s*-process signature, in regions closer to the sun. Thermal processing is a possible mechanism given that the ISM-grown dust rims formed in the relatively cold ISM and are therefore likely to be more susceptible to thermal processing than stardust that formed at much higher temperatures. The lower abundance of nucleosynthetic Pd (relative to Zr, Mo and Ru) was inherited from the stardust, negating the need for selective destruction the Pd *s*-process carrier in the solar nebula as proposed by Mayer et al. (2015).

The model described above would predict that elements that are more volatile than Pd should have even smaller, or lack altogether, nucleosynthetic offsets. This is supported by limited studies on Zn (Chen et al., 2013), Cd (Kruijjer et al., 2013b; Wombacher et al., 2008) and Te (Fehr et al., 2005), which have half-mass condensation temperatures between 730 and 600 K (Lodders, 2003), where no nucleosynthetic offsets were reported. Small nucleosynthetic offsets, relative to Zr, Mo and Ru, have been reported for Nd (Andreasen and Sharma, 2006; Burkhardt et al., 2016; Carlson et al., 2007) and W (Kruijjer et al., 2013a; Qin et al., 2008; Wittig et al., 2013) while no nucleosynthetic offsets in even heavier elements Pt (Hunt et al., 2018; Hunt et al., 2017a; Kruijjer et al., 2013b; Kruijjer et al., 2014;



Peters et al., 2015; Wittig et al., 2013), and Os (Reisberg et al., 2009; Walker, 2012; Yokoyama et al., 2007). Many of these elements are highly refractory and therefore incomplete condensation around AGB stars cannot explain the reduced or lack of nucleosynthetic offsets observed in these elements. The production of elements heavier than Ba ( $Z \geq 56$ ) in AGB stars decreases, relative to Zr, Mo, Ru and Pd, as a function of the initial metallicity of the star (Figure 4.6; Cristallo et al., 2011; Cristallo et al., 2009; Cristallo et al., 2015; Karakas and Lugaro, 2016). Meanwhile several studies suggest that dust production increases as a function of metallicity (Ferrarotti and Gail, 2006; Lewis et al., 2013) and Lugaro et al. (2018) recently argued that the majority of the mainstream SiC grains, which make up a majority of presolar grains, originated from AGB stars with metallicities twice that of our sun. The bulk solar system *s*-process component resembles that of an AGB star with a metallicity roughly half that of our sun (Gallino et al., 1998). If the majority of stardust in the solar nebula formed in AGB stars with supersolar metallicities then the concentration of heavy elements in stardust, relative to Zr, Mo, Ru and Pd, would be much lower than the bulk solar system *s*-process component. This can explain why we see much smaller nucleosynthetic offsets in heavy elements than what is predicted by a variation in the bulk

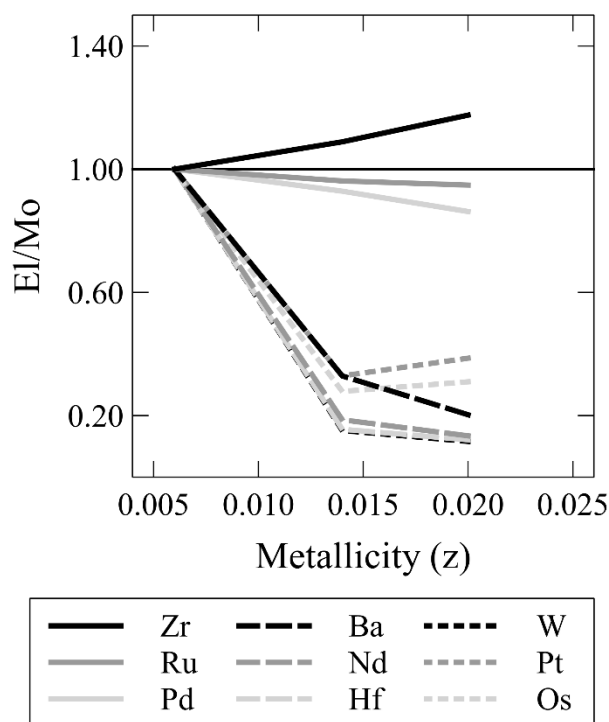


**Figure 4.6.** The *s*-process yield of Zr, Pd, Ru and Cd (solid lines) and Ba, Nd, Hf, W, Pt and Os (dashed lines), normalised to Mo, as a function of the metallicity for an AGB star of 3 solar masses taken from the FRUITY database (Cristallo et al., 2011; Cristallo et al., 2009; Cristallo et al., 2015). All  $E_i/M_o$  yields are have been further normalised to model of an AGB star with a metallicity of  $z = 0.006$ , which approximately resembles the solar system *s*-process component (Gallino et al., 1998). The production of heavy *s*-process elements (dashed lines) decreases as a function of metallicity relative to Zr, Mo, Ru, and Pd.

solar system *s*-process component. A dilution effect has previously been proposed to explain the lack of nucleosynthetic variations in heavy elements (Akram et al., 2013; Burkhardt et al., 2012; Hunt et al., 2017a). It is unclear if this alone can explain why for example nucleosynthetic offsets are found in W but not neighbouring Os isotopes due to uncertainties in the yields of current nucleosynthetic models. It is possible that other factors such as the mean residency time of different dust phases in the ISM could play a role. Overall, the stardust model presented above shows great promise in explaining not only the origin of the Zr-Mo-Ru-Pd correlation but also in explaining the small nucleosynthetic variation, or lack thereof, reported for more volatile and heavier elements.

#### 4.6. Conclusions

We analysed 24 iron meteorites from 6 groups and observe a wide range of Pd isotope compositions. The variations within individual groups correlate well with the effects predicted for cosmic ray exposure. After correction for cosmic ray effects, the iron meteorite groups show underlying offsets which vary from IAB < IIAB < IVA < IIIAB < IID <

IVB, where both the IABs and IIABs are within uncertainty of the terrestrial standard. These offsets are in agreement with an *s*-process deficit and show an excellent correlation with variations previously reported in Mo and Ru. However, the slope of the correlation does not match that of an *s*-process component with solar abundances of these elements. The nucleosynthetic offsets in Pd require only  $\sim 1/4$  of the *s*-process deficit compared to those in Mo and Ru.

We suggest that this relationship stems from dust formation around AGB stars where Pd, a moderately volatile element, is not expected to condense as readily as the more refractory elements, e.g. Zr, Mo and Ru. The origin of nucleosynthetic variations in the solar system is attributed to selective processing between a 'stardust' fraction that is dominated by dust formed around AGB stars, and dust, which formed in the interstellar medium and contains solar-like isotope abundances. We suggest thermal destruction of the latter in regions close to the proto-sun acted to enrich the *s*-process-dominated stardust fraction, and resulted in the observed correlation in nucleosynthetic variations between Zr, Mo, Ru and Pd. This model can also explain the lack of nucleosynthetic offsets in volatile elements, e.g. Zn, Cd, and Te, as these elements not condense around these stars. The small or absent nucleosynthetic offsets in heavy elements ( $Z > 56$ ) could be due to the decreased production of these elements in AGB stars with high metallicities, an environment that favours stardust production.

### **Acknowledgements**

This work was supported by the European Research Council under the European Union's Seventh Framework Programme (FP7/2007–2013)/ERC Grant agreement no. [279779]. We wish to thank David Farsky and David Cook for their assistance in acquiring the Rh/Pd ratios used in this study. Additionally, we thank Caroline Smith and Deborah Cassey (Natural History Museum, London), Julie Hoskin (Smithsonian Institute) and Philipp Heck (Field Museum) for the loan of meteorite materials used in this study. The manuscript was greatly improved by comments from Mark Rehkämper and Maria Lugaro.

# Chapter 5

Measurements of Palladium stable isotope ratio by double-spike multiple collector ICP-MS.

## Abstract

Palladium mass-dependent isotopic variations in iron meteorites have the potential to trace processes that operate during metal-silicate differentiation or fractional crystallisation in asteroidal and planetary cores. Here we present a  $^{104}\text{Pd}$ - $^{108}\text{Pd}$  double spike for precise mass-dependent Pd isotopic analysis using MC-ICP-MS. Our double spike approach produces accurate data for sample-to-spike ratios between 0.4 and 3.5. Doping tests show that the concentration of isobaric and molecular interferences in the Pd fraction, after purification through a two stage ion exchange procedure, is consistently below the limit where the accuracy of the double spike inversion is affected. The long-term reproducibility (2 SD) of the NIST SRM 3138 Pd standard is 0.001 % for  $\delta^{106/105}\text{Pd}$ , and three analyses of two separate aliquots of the IVA iron meteorite Gibeon yield a  $\delta^{106/105}\text{Pd}$  value of  $-0.108 \pm 0.025$ . Analysis of five iron meteorites from the IAB, IID, IVA and IVB groups show a range of  $\delta^{106/105}\text{Pd}$  values. The lightest composition is found in the IAB iron Cranbourne, which overlaps within uncertainty with the previously reported value for chondrites ( $-0.192 \text{‰} \pm 0.050$ ; Creech et al., 2017b). The heaviest Pd isotope compositions are seen in the two IVB samples Tlacotepec ( $-0.055 \text{‰} \pm 0.15$ ) and Hoba ( $-0.062 \text{‰} \pm 0.015$ ).

The correlation of  $\delta^{106/105}\text{Pd}$  with Ni content suggests that Pd isotopes in the core are fractionated via crystallization fractionation. However, more detailed studies are needed to further corroborate this hypothesis.

## 5.1. Introduction

Mass-dependent, also called stable, isotope variations of siderophile elements can provide valuable information on the condition and processes that occur during planet formation. The difference in the oxidation state and bonding environment between metal and silicate typically favour fractionation of heavy isotopes into the silicate fraction during metal-silicate differentiation (Schauble, 2004). Experiments at temperature and pressures relevant for planet formation identified isotopic fractionation for several siderophile elements, e.g. Zn (Mahan et al., 2017) and Mo (Hin et al., 2013). This has been corroborated by recent studies on terrestrial and extra-terrestrial samples, which showed that some differentiated silicate rocks display an enrichment in heavy isotopes for Mo (Burkhardt et al., 2014) and Pt (Creech et al., 2017b). This has been interpreted as a signature of core formation. The mass-dependent isotope composition of siderophile elements can also provide insight into mechanisms operating during the crystallisation of planetary cores. Considerable isotopic variation has been found in iron meteorites for Fe (Williams et al., 2006), Cu (Chen et al., 2016; Williams and Archer, 2011), and Zn (Bridgestock et al., 2014) and was interpreted as isotopic fractionation during fractional crystallisation. Noteworthy is that that no isotopic variation was observed in iron meteorites for Mo (Burkhardt et al., 2014) and Pt (Creech et al., 2017b) suggesting that not all elements are affected. Results from Pd isotopes indicate no variation between the present day crust and chondrites (Creech et al., 2017a), much like Mo (Burkhardt et al., 2014) and Pt (Creech et al., 2017b). However, stable isotope data for Pd in iron meteorites are absent. Such Pd data for iron meteorites could therefore help to further constrain the crystallisation history of planetary cores.

Palladium is a member of the platinum group elements (PGE) and has with six naturally occurring isotopes,  $^{102}\text{Pd}$ ,  $^{104}\text{Pd}$ ,  $^{105}\text{Pd}$ ,  $^{106}\text{Pd}$ ,  $^{108}\text{Pd}$  and  $^{110}\text{Pd}$  (Table 1). It is a strongly siderophile element although it has a metal-silicate partition coefficient (D) an order of magnitude lower ( $\sim 10,000 \log D_{\text{metal/silicate}}$ ) than

the other PGEs (e.g. Pt = 320,000  $D_{\text{metal/silicate}}$ ; Mann et al. 2012). It is also the most volatile of the PGEs with a 50 % condensation temperature of 1324 K (Lodders, 2003), compared to e.g. Pt (1408 K).

Here we present a new method for high precision measurements of the mass-dependent isotope composition of Pd in iron meteorites by multi-collector inductively coupled plasma mass spectrometry (MC-ICP-MS). A Pd double spike procedure was developed to correct for mass-dependent isotope fractionation occurring during chemical separation or isotopic analysis. Nucleosynthetic and CRE related mass-independent offsets are known for Pd in iron meteorites (Chapter 4) and we evaluate the importance of using the mass-independent Pd isotope composition in the double spike inversion. The stable Pd isotope composition of five iron meteorites from different groups were measured and compared to the results from other siderophile elements.

## 5.2. Design and preparation of the double spike

Mass-dependent isotope fractionation can occur during ion exchange chromatography, particularly with low yields, and during isotopic analysis by MC-ICP-MS. For mass-independent isotopic studies, this fractionation can be corrected for by internal normalisation. However, this will also remove any natural mass-dependent signature following the applied fractionation law. Thus, mass-dependent studies need a way to distinguish between the natural mass-dependent fractionation ( $\alpha$ ) and the instrumental and lab-induced ( $\beta$ ) mass-dependent fractionation. This can be done by using the double spike technique,

**Table 5.1.** Collector configuration and isotopic abundances of Pd isotopes, plus isobaric interferences and major molecular interferences.

	99	101	104	106	108	110	111	112
<b>Collector configuration</b>								
Cup	L4	L2	L2	C	H1	H2	H3	H4
Resistor ( $\Omega$ )	$10^{12}$	$10^{12}$	$10^{11}$	$10^{11}$	$10^{11}$	$10^{11}$	$10^{11}$	$10^{11}$
<b>Isotope abundances of Pd and isobaric interferences (in %; Berglund and Wieser, 2011).</b>								
Ru	12.76	17.06	18.62					
Pd			11.14	27.33	26.46	11.72		
Cd				1.25	0.89	12.49	12.8	24.13
Sn								0.97
<b>Major molecular interferences and their isotopic abundances (in %; Berglund and Wieser, 2011).</b>								
M <sup>1</sup> H	<sup>98</sup> Ru (1.87)	<sup>100</sup> Ru (12.59)	<sup>103</sup> Rh (100)		<sup>107</sup> Ag (51.83)	<sup>109</sup> Ag (48.16)		
M <sup>40</sup> Ar	<sup>58</sup> Fe (0.28) <sup>58</sup> Ni (68.07)	<sup>61</sup> Ni (1.14)	<sup>64</sup> Ni (0.93) <sup>64</sup> Zn (49.17)	<sup>66</sup> Zn (27.73)	<sup>68</sup> Zn (18.45)	<sup>70</sup> Zn (0.61)		
M <sup>16</sup> O			<sup>90</sup> Zr (51.45)	<sup>92</sup> Zr (17.15)	<sup>94</sup> Zr (17.38)	<sup>96</sup> Zr (2.80)		
				<sup>92</sup> Mo (14.65)	<sup>94</sup> Mo (9.19)	<sup>96</sup> Mo (15.87)	<sup>97</sup> Mo (9.60)	

where a double spike, a mixture of two enriched isotope tracers, is added to the sample of interest. This allows the natural fractionation to be calculated independently of the instrumental fractionation (Dodson, 1963). The double spike inversion solves for three unknowns; the natural fractionation ( $\alpha$ ), the instrumental fractionation ( $\beta$ ) and the sample-to-spike ratio ( $Q$ ) of the sample and spike mixture. To solve for these unknowns four isotopes are required (e.g. Dodson, 1970). Palladium has six isotopes and so several different double spike schemes are available. There are different factors to consider when choosing which isotopes to spike and to use in the inversion. The first is the uncertainty introduced by the double spike inversion itself. Rudge et al. (2009) compiled a list of the optimal double spikes and inversions for all elements with four or more isotopes without taking into account analytical or other sources of uncertainty, such as isobaric and molecular interferences. The Pd double spike inversion that introduces in the least uncertainty according to Rudge et al. (2009) utilises  $^{102}\text{Pd}$ ,  $^{104}\text{Pd}$ ,  $^{108}\text{Pd}$  and  $^{110}\text{Pd}$ , with  $^{102}\text{Pd}$  and  $^{108}\text{Pd}$  being spiked. However, while this inversion provides the smallest uncertainty for the natural fractionation, the low abundance of  $^{102}\text{Pd}$  results in a larger analytical uncertainty, and this isotope also requires a significant correction for the isobaric inference of  $^{102}\text{Ru}$  (Ek et al., 2017), making it less suitable for use in the double spike inversion. Additionally, including  $^{105}\text{Pd}$  in the double spike inversion may induce problems due to nuclear field shift effects. These can arise from the ion exchange procedure for Pd purification, and are the strongest on the odd isotopes (Fujii et al., 2009). However, no NFS effects were identified in iron meteorites (Chapter 4). In this study, we have chosen a  $^{104}\text{Pd}$ ,  $^{106}\text{Pd}$ ,  $^{108}\text{Pd}$  and  $^{110}\text{Pd}$  double spike routine with a  $^{104}\text{Pd}$ - $^{108}\text{Pd}$  spike mixture. While the isotopes used in this inversion have minor isobaric interferences from Ru ( $^{104}\text{Ru}$ ) and Cd ( $^{106}\text{Cd}$ ,  $^{108}\text{Cd}$ ,  $^{110}\text{Cd}$ ), the Ru/Pd and Cd/Pd ratios of the final sample solutions after ion exchange procedure are expected to be sufficiently low to ensure accurate corrections of these interferences (Ek et al., 2017; Chapter 3). The optimal sample to spike mixture for this double spike is  $\sim 1:1$  (Figure 5.1).

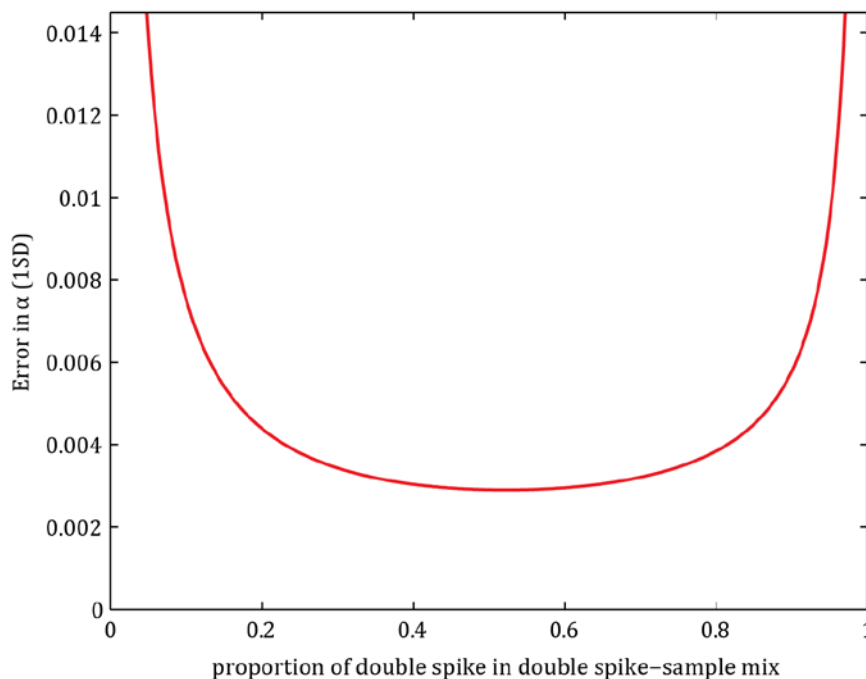


**Figure 5.1.** The error on  $\alpha$  when using a  $^{104}\text{Pd}$ - $^{106}\text{Pd}$ - $^{108}\text{Pd}$ - $^{110}\text{Pd}$  double spike inversion as a function of the double spike to sample ratio, shown for a 1:1 mixture of a  $^{104}\text{Pd}$ - $^{108}\text{Pd}$  double spike. Image generated using the double spike toolbox (Rudge et al., 2009).

### 5.3. Materials and methods

#### 5.3.1. Chemicals and standard solutions

All nitric and hydrochloric acids used in this study were twice distilled in Teflon stills, while hydrofluoric acids were distilled once in Teflon stills. Merck Suprapur® HClO<sub>4</sub> (70%) and Merck Millipore Bromine Suprapur® (99.999%) were used without further purification. All H<sub>2</sub>O (18.2 MΩ cm) was purified using a Merck Millipore Milli-Q™ system. Acids and samples were stored in pre-cleaned Teflon containers. Additionally, acids and acid mixtures were routinely titrated to ensure accurate molarities. A BioRad™ AG® 1-X8 resin (200-400 mesh, chloride form) was used throughout the chemical procedure and was batch cleaned before use as described in Hunt et al. (2017b; Chapter 2).

#### 5.3.2. Samples

Three Fe-Ni powders doped with NIST SRM 3138, the bracketing standard used in this study, were prepared with different sample-to-spike ratios to test the accuracy of the method. Iron, Ni, and Pd were mixed in proportions similar to those found in IVB iron meteorites. Additionally, six samples from five different iron meteorites were analysed. Cranbourne (IAB), Carbo G (IID), and two aliquots of Gibeon (IVA) were acquired from the ETH meteorite collection. The two remaining iron meteorites, Hoba (IVB; BM1959, 913) and Tlacotepec (IVB; BM1930, 976) were acquired from the Natural History Museum in London. All the iron meteorites analysed here were previously studied for mass-independent Pd isotope ratio variations (Chapter 4).

#### 5.3.3. Sample digestion and separation procedure

Samples were dissolved using the method described in Hunt et al. (2017b; Chapter 2), and repeated here in brief. Where necessary meteorites were subsampled using a CBN blade cooled with ethanol. Saw marks, fusion crust and weathered areas were removed using silicon carbide paper. Prior to dissolution samples were rinsed in ethanol, after which they were leached in cold 2M HCl for 5 minutes. All samples were dissolved in a mixture of two parts concentrated HNO<sub>3</sub> to one part concentrated HCl. After being refluxed for two days at 100 °C, samples were dried and re-dissolved in concentrated HCl. After refluxing at 100 °C for another 24 hours all samples were fully dissolved. At this stage, an aliquot of the solution was taken for mass-dependent isotope analysis. The aliquot was carefully weighed and the <sup>104</sup>Pd-<sup>108</sup>Pd double spike mixture was added to achieve a natural Pd to Pd double spike ratio of 1. The amount of spike added was based on Pd concentration data available in literature (Campbell and Humayun, 2005; Hoashi et al., 1993). The solution was evaporated to dryness and refluxed in a 2:1 mixture of concentrated HCl to HNO<sub>3</sub> at 110 °C for 48 hours in preparation for the ion exchange procedure (Hunt et al., 2017b).

A two-stage ion exchange procedure was used to separate Pd from the metal matrix. The first stage is described in Hunt et al. (2017b; Chapter 2) and is outlined below. Sample solutions were taken to dryness then redissolved in 0.5 M HCl + 10 % Br<sub>2</sub>-water and refluxed overnight at 110 °C. The samples were cooled to room temperature before being loaded onto a glass column preloaded with 1.25 ml of BioRad™ AG® 1-X8 resin. Matrix elements were eluted from the column in subsequent washes of 1 M HCl + 10 % Br<sub>2</sub>-water, 0.8 M HNO<sub>3</sub> + 10 % Br<sub>2</sub>-water, and concentrated HCl. Palladium was then eluted from the column with hot (~80 °C) 8 M HNO<sub>3</sub>. The column also allows for the collection of Pt in 13.5 M HNO<sub>3</sub> immediately after the Pd elution. The Pd fraction was dried in preparation for the second stage of

Pd purification. The Pt fraction can be purified using the method described in Hunt et al. (2017b).

The second stage of Pd purification is described in Ek et al. (2017; Chapter 3) and is summarised below. The Pd fraction from the first stage was redissolved in a 2 ml 3:1 mixture of HCl to HNO<sub>3</sub> and refluxed for 48 hours at 110 °C. The solution was cooled to room temperature before 0.3 ml of HClO<sub>4</sub> was added. This mixture was evaporated at 210 °C, which removes up to 99 % of the remaining Ru. To maximise the Ru loss this step was repeated twice. In preparation for the second ion exchange procedure the solution was refluxed in 1 ml 4 M HF for 48 hours at 110 °C. After cooling to room temperature this solution was loaded into a Teflon column packed with 0.5 ml of BioRad™ AG® 1-X8 resin, followed by a wash of another 1 ml of 4 M HF. This elutes most of the non-transition metals from the resin. A 5 ml wash of 6 M HNO<sub>3</sub> followed by 4 ml of concentrated HCl elutes any remaining Mo and Ru from the column. Palladium is subsequently eluted in a further 4 ml of concentrated HCl, followed by 6 ml of 13.5 M HNO<sub>3</sub>. The Pd fraction was dried and redissolved in 5 M HNO<sub>3</sub> in preparation for isotopic analysis. The final Pd fraction was sufficiently devoid of potential isobaric and molecular interferences for accurate mass-independent (Ek et al., 2017; Chapter 3) and mass-dependent isotopic analysis (See section 5.4.3)

#### 5.3.4. Mass spectrometry

Palladium isotope measurements were carried out at ETH Zürich using a Thermo Scientific Neptune Plus MC-ICP-MS equipped with standard H cones and operated in low resolution mode. A Cetac Aridus II desolvating system equipped with a 100 µl min<sup>-1</sup> Savillex nebuliser was used for sample introduction and all solutions analysed in this study had an acid matrix consisting of 0.5 M HNO<sub>3</sub>. The instrument was tuned to minimise the ZrO production (>1%), which resulted in a typical sensitivity of 500-600 V ppm<sup>-1</sup> for Pd. Prior to each standard/sample measurement an on peak baseline (OPB) was performed consisting of a 30 s electronic baseline measurement and 60 cycles with 4.2s integrations. The sample/standard measurement routine begins with a 30 s electronic baseline measurement, then a peak centre routine, which was followed by analysis of the concentration of potential molecular interferences (Table 5.1). This was conducted by cycling through <sup>107</sup>Ag, <sup>60</sup>Ni, <sup>66</sup>Zn, <sup>90</sup>Zr, <sup>95</sup>Mo and <sup>103</sup>Rh in a dedicated measurement routine, measuring one cycle for each mass. Finally, a static measurement with 60 cycles of 4.2s integrations was performed. This protocol determined the four Pd isotopes used in double spike inversion plus <sup>111</sup>Cd and <sup>112</sup>Cd. These were measured using 10<sup>11</sup>Ω resistors. Ruthenium-99 and <sup>101</sup>Ru were also measured simultaneously using 10<sup>12</sup>Ω resistors (Table 5.1). All samples were bracketed against a NIST SRM 3138 Pd standard solution with double spike added to achieve a concentration and standard to spike ratio within 10% of the sample. Samples and standards were diluted to achieve a ~12 V signal on <sup>106</sup>Pd, which allowed solutions with up to a 1:2 sample-to-spike ratio to be safely analysed before exceeding the 50 V ion beam signal limit on <sup>108</sup>Pd. The concentration of standard and sample solutions was typically 75 ppb Pd. In total, the measurement routine consumed 1 ml of solution or ~75 ng Pd. A ~20 minute wash of the introduction system with 0.5 M HNO<sub>3</sub> was performed between each isotopic measurement routine to reduce the background signal to less than 1/200<sup>th</sup> of the preceding solution. Blanks processed through the entire ion exchange procedure contain less than 1 ng Pd in the final Pd fraction.

#### 5.3.5. Data reduction

Data reduction took place offline using the geometric double spike inversion approach of Siebert et al.



(2001). The double spike inversion requires four input parameters to solve for the three unknowns, the natural fractionation ( $\alpha$ ), instrumental fractionation ( $\beta$ ), and sample-to-spike ratio (Q). 1) The measured composition of our sample- double spike mixture. 2) The isotope composition of the Pd double spike (Table 5.2), 3) The atomic mass ratios for Pd (Table 5.2), taken from Meija et al. (2016). 4) The ‘natural’ composition of the sample relative to which  $\alpha$  is determined. The true composition of the sample therefore has to lie on the same mass-fractionation line as the natural Pd isotope composition. For standards the long-term average of repeat mass-independent measurements of the NIST SRM 3138 Pd standard determined by Ek et al. (2017; Chapter 3; Table 5.3) was used as the natural composition. For extra-terrestrial samples the natural isotope composition can be calculated using the  $\epsilon^{iPd}$  values presented in Chapter 4 and Appendix B, using the following equation:

$$R^{i/108}Pd_{sample} = \left( \frac{\epsilon^{iPd}}{10,000} + 1 \right) / \left( \frac{\epsilon^{108Pd}}{10,000} + 1 \right) \times R^{i/108}Pd_{SRM} \quad (1)$$

where  $R^{i/108}Pd_{sample}$  and  $R^{i/108}Pd_{SRM}$  is the isotope ratio of the sample and NIST SRM 3138 (Table 5.2), respectively. Each input parameter is given for the same three isotope ratios (Table 5.2), in this case  $^{104}Pd/^{108}Pd$ ,  $^{106}Pd/^{108}Pd$  and  $^{110}Pd/^{108}Pd$ .

The raw data were background corrected by subtraction of the OBP collected prior to each measurement. Data were also corrected for isobaric interferences from Ru and Cd. To do this, an estimate of the  $\beta$  value is needed. A first estimate was determined by carrying out the double spike inversion without interference correction. The resulting  $\beta$  value was then used to calculate, and subtract, the contribution from Ru to  $^{104}Pd$ , and Cd to  $^{106}Pd$ ,  $^{108}Pd$  and  $^{110}Pd$ , based on the  $^{101}Ru$  and  $^{111}Cd$  signal intensities (described in Ek et al., 2017; Chapter 3). The interference corrected values were then used to calculate a new  $\beta$  value. After 2 iterations of this procedure the  $\beta$  value typically converged. Mass-dependent Pd isotope data are reported as  $\delta^{106/105}Pd$  for comparison with other Pd stable isotope studies (Creech et al., 2017a). The  $\delta^{106/105}Pd$  signature of each sample can be calculated using the following equation:

$$\delta^{106/105}Pd_{sample} = \left( (m_{106}/m_{105})^{(\alpha_{sample} - \alpha_{meanSRM})} - 1 \right) * 1000 \quad (3)$$

Where  $m_{106}$  and  $m_{105}$  are the atomic masses of  $^{106}Pd$  and  $^{105}Pd$  and  $\alpha_{sample}$  and  $\alpha_{meanSRM}$  is the natural fractionation of the sample and the average natural fractionation of the bracketing standards, respectively.

**Table 5.2.** Standard input of the double spike inversion

	$^{104}Pd/^{108}Pd$	$^{106}Pd/^{108}Pd$	$^{110}Pd/^{108}Pd$
Spike composition	1.05906(5)	0.01811(10)	0.00570(5)
Mass ratios <sup>b</sup>	0.962931	0.981461	1.018547
NIST SRM 3138 composition <sup>c</sup>	0.417951	1.028438	0.443035

<sup>a</sup> Numbers in the brackets represent 2 SD uncertainties on the last decimal. <sup>b</sup> Calculated using the atomic masses given in Meija et al. (2016). <sup>c</sup> From Ek et al. (2017; Chapter 3)

## 5.4. Results and discussion

### 5.4.1. Calibration of the double spike.

The  $^{104}\text{Pd}$  and  $^{108}\text{Pd}$  enriched tracers were obtained from Oak Ridge National Laboratory, USA, as 10 mg metal granulate. After careful weighing, each spike was transferred to a Teflon beaker and ~4 ml (4 g) of 5 M  $\text{HNO}_3$  was added. The spikes were refluxed for ~72 hours at 110 °C before being transferred to Teflon bottles and diluted to ~100 mg/g Pd in a 2 M  $\text{HNO}_3$  acid matrix. These single isotope spike solutions were combined in equal proportions, which is the optimal ratio for minimising the  $\alpha$  uncertainty (Figure 5.1; Rudge et al., 2009), to create the double spike. The composition of the  $^{104}\text{Pd}$ - $^{108}\text{Pd}$  double spike was determined following the steps below.

- 1) First a 100 ppb NIST SRM 3138 Pd solution doped with 50 ppb NIST SRM 978a Ag was analysed via MC-ICP-MS.
- 2) Then a solution mixture containing 50 ppb Pd spike and 50 ppb Ag standard was analysed.
- 3) Step one and two were repeated three times.
- 4) The  $^{107}\text{Ag}/^{109}\text{Ag}$  ratio for each NIST SRM 3138 solution was corrected for instrumental fractionation using  $^{106}\text{Pd}/^{105}\text{Pd} = 1.22277$  (Kelly and Wasserburg, 1978). A mean  $^{107}\text{Ag}/^{109}\text{Ag}$  ratio was then calculated based on all NIST SRM 3138 standards. Importantly, no memory effects were observed on  $^{105}\text{Pd}$  or  $^{106}\text{Pd}$  after the introduction of the spike. However,  $^{108}\text{Pd}$  and  $^{104}\text{Pd}$  showed a memory effect after introduction of the spike.
- 5) The composition of each spike measurement was corrected for instrumental fractionation using  $^{107}\text{Ag}/^{109}\text{Ag}$  internally normalised to the mean of the standard solution calculated above.

The mean spike composition was calculated to be  $1.05906 \pm 0.00005$ ,  $0.01811 \pm 0.00010$ , and  $0.00570 \pm 0.00005$  for  $^{104}\text{Pd}/^{108}\text{Pd}$ ,  $^{106}\text{Pd}/^{108}\text{Pd}$  and  $^{110}\text{Pd}/^{108}\text{Pd}$  (Table 5.2), respectively. This spike composition was validated by measuring six different NIST SRM 3138 Pd and spike mixtures ranging from sample-to-spike ratios of ~0.4 to ~3.5 (Figure 5.2a). All different sample-to-spike ratios yielded identical  $\delta^{106/105}\text{Pd}$  compositions, indicating that the composition of the double spike was correctly determined. The concentration of the double spike was ascertained relative to a 10 mg piece of Alfa Aesar Palladium wire (99.99+ % Pd) dissolved at ETH. The concentration of the double spike is  $3.850 \pm 0.001$  ppm.

### 5.4.2 Reproducibility of double spike measurements.

The typical internal precision (2 standard errors; SE) of a single measurement is ~0.004 ‰ for  $\delta^{106/105}\text{Pd}$ . The mean value for  $\delta^{106/105}\text{Pd}$  obtained from 226 individual NIST SRM 3128 Pd standard measurements, spanning 10 analytical sessions over a 6 months period (Figure 5.5a), is  $-0.037 \text{ ‰} \pm 0.027$  (2 SD). The mean offset from zero likely reflects the difference between the true composition of our standard and the internally normalised composition we use as input for the double spike inversion. The session-to-session variation is likely the effect of differences in the tuning settings for the MC-ICP-MS between sessions that results in non-exponential mass fractionation effects. Therefore, the reproducibility of method is best assessed by first normalising each measurement by the mean of the analytical session (Figure 5.3b). With this approach, the reproducibility of the standard solutions is  $\pm 0.01 \text{ ‰}$  (2 SD) for  $\delta^{106/105}\text{Pd}$ .

Three Fe Ni powders doped with NIST SRM 3138 Pd and our Pd double spike were processed through the ion exchange procedure to verify that no isotopic fractionation occurs that cannot be corrected by the double spike inversion. The three solutions contain different sample-to-spike ratios between 0.9 to 1.1 and the mean of 16 analyses yields a  $\delta^{106/105}\text{Pd}$  value of  $0.002 \pm 0.005$  (2 SD; Figure 5.2b; Table 5.3), which is within uncertainty of the unprocessed bracketing standards. This suggests that the new analytical method produces accurate and precise data.

#### 5.4.3. Isobaric and molecular interferences

The effect on the accuracy of the double spike procedure was tested in the presence of isobaric and/or molecular interferences on the four Pd isotopes used (Table 5.1). Isobaric interferences from Ru ( $^{104}\text{Ru}$ ) and Cd ( $^{106}\text{Cd}$ ,  $^{108}\text{Cd}$ ,  $^{110}\text{Cd}$ ) are corrected using the signal intensity of  $^{101}\text{Ru}$  and  $^{111}\text{Cd}$  as described in section 3.4. This correction breaks down at Ru/Pd and Cd/Pd ratios above  $\sim 0.0005$  (Figure 5.4a), which is almost two orders of magnitude higher than those observed in the samples analysed in this study. Nickel and Zn argides can cause spectral interferences on  $^{101}\text{Ru}$ ,  $^{104}\text{Pd}$ ,  $^{106}\text{Pd}$ ,  $^{108}\text{Pd}$ , and  $^{110}\text{Pd}$ . We

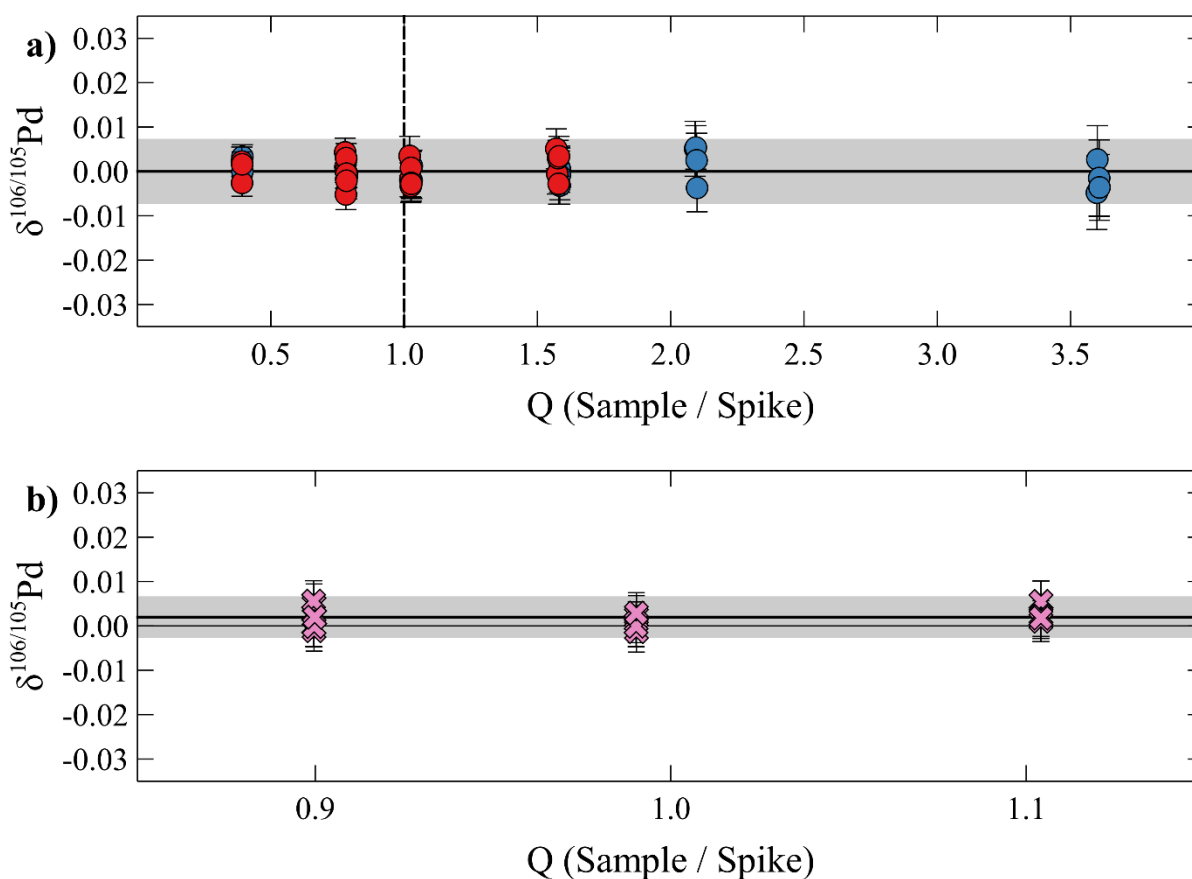


**Figure 5.2.** a) The  $\delta^{106/105}\text{Pd}$  composition for different sample-to-spike ratios of NIST SRM 3138 and our Pd double spike between  $\sim 0.4$  and  $\sim 3.5$ , measured on two separate sessions (Red and Blue). The values have been normalised to the mean  $\delta^{106/105}\text{Pd}$  of all standard solutions measured during each session. The uncertainty on each data point is reported as the 2 SE internal uncertainty for each measurement. The grey band represent the 2 SD reproducibility of all measurements included in the figure. No variation is observed for the different sample-to-spike ratios. b) Repeat measurements of three Fe and Ni powders doped with NIST SRM 3138, and varying amounts of our Pd double spike. The grey band represents the 2 SD reproducibility of all the individual measurements. The uncertainty on each data point is reported as the 2 SE internal uncertainty for each measurement. There is no variation for different sample-to-spike ratios and the mean overlaps with zero.

analysed solutions doped with Ni/Pd and Zn/Pd ratios up to  $\sim 0.01$  that did not produce resolvable offsets in  $\delta^{106/105}\text{Pd}$ . The maximum Ni/Pd ratio observed in a sample is  $\sim 0.0005$  while the highest Zn/Pd ratio was 0.007 (Figure 5.4b). Molybdenum oxides can cause spectral interferences on  $^{108}\text{Pd}$ ,  $^{110}\text{Pd}$  and  $^{111}\text{Cd}$ , however, no shift in  $\delta^{106/105}\text{Pd}$  was observed for a Mo/Pd ratio of  $\sim 0.01$ , which is a factor of 2 higher than found in samples (Figure 5.4c). Production of ZrO was found to be highly dependent on MC-ICP-MS tune settings (Ek et al., 2017). The instrument was therefore tuned to achieve a ZrO/Zr ratio lower than 0.01. At Zr/Pd ratios (ZrO/Zr = 0.005) above  $\sim 0.0005$  a small offset in  $\delta^{106/105}\text{Pd}$  is observed (Figure 5.4c). Sample solutions consistently yielded Zr/Pd ratios an order of magnitude below this limit. Finally, no offsets caused by molecular interferences from Rh ( $^{104}\text{Pd}$ ) and Ag ( $^{108}\text{Pd}$ ,  $^{110}\text{Pd}$ ) were observed at Rh/Pd and Ag/Pd ratios of 0.01 and 0.04, respectively (Figure 5.4d). This is at least 3 orders of magnitude higher than the ratio of these elements observed in the purified sample solutions. This confirms that the ion exchange procedure effectively removes these elements prior to isotopic analysis enabling high precision Pd isotope composition measurements. However, Zn and Zr contamination can occur during sample preparation (Ek et al., 2017), e.g., from accidental contact with gloves (Garçon et al., 2017), and it is therefore important to monitor the Zn/Pd and Zr/Pd ratio of the solutions in every analytical session.

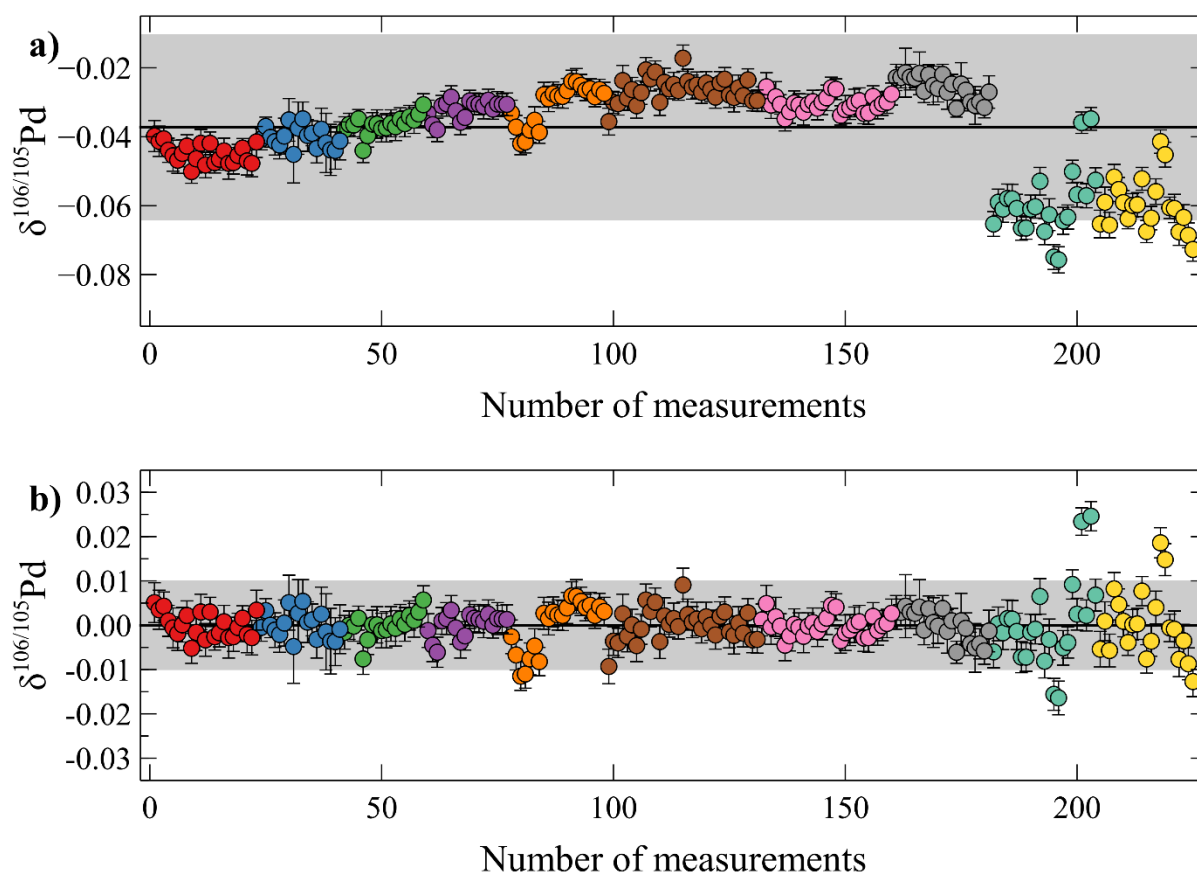


**Figure 5.3.** a) The absolute  $\delta^{106/105}\text{Pd}$  value for 226 individual measurements of the NIST SRM 3138Pd solution over 10 different analytical sessions. b) The  $\delta^{106/105}\text{Pd}$  of individual measurements normalised to the mean of the each analytical session. Symbol colours represents different analytical sessions. Grey band shows the reproducibility (2 SD) and are 0.027 and 0.01 for  $\delta^{106/105}\text{Pd}$  in (a) and (b) respectively.

#### 5.4.4. Modelling of mass-independent effects

For samples with mass-independent offsets using the composition of the NIST SRM 3138 standard as the ‘natural’ composition in the double spike inversion is incorrect and the actual mass-independent composition of the samples needs to be used (e.g. Galer, 1999). The double spike inversion requires that the ‘natural’ composition utilised in the inversion lies on an exponential mass fractionation line relative to the true composition of the sample. Using incorrect ‘natural’ composition will affect the accuracy of the double spike inversion, most notably on  $\alpha$ . To assess how mass-independent offsets affect the accuracy of the inversion we modelled the effects from nucleosynthetic and cosmic ray mass-independent offsets using the procedure outline below:

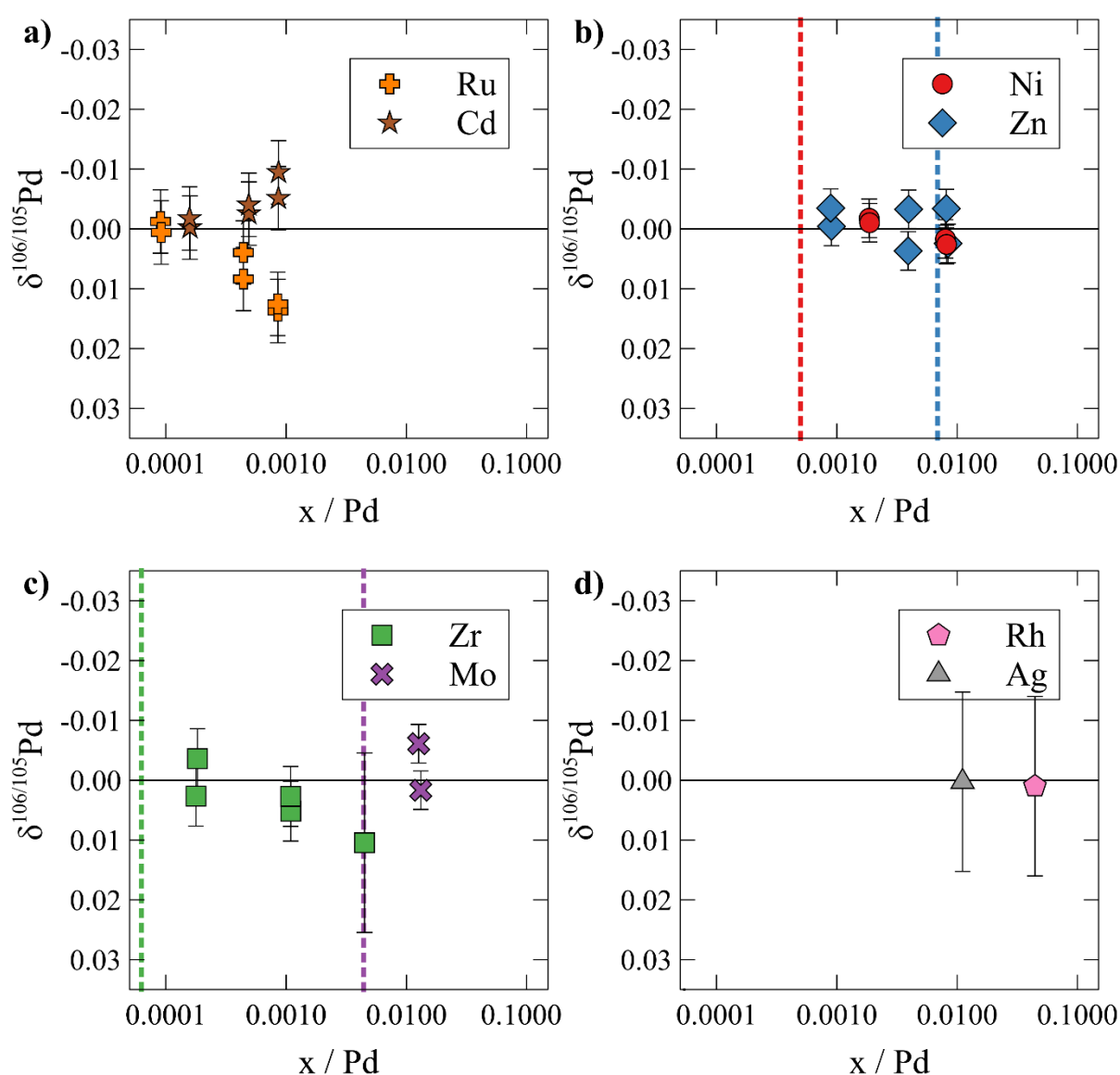


**Figure 5.4.** The  $\delta^{106/105}\text{Pd}$  values of NIST SRM 3138 standard solutions doped with (a) elements that can cause isobaric interferences (Ru and Cd) and molecular interferences from (b) argides (Ni and Zn), (c) oxides (Zr and Mo) and (d) hydrides (Rh and Ag). All data points show individual measurements normalised to two bracketing NIST SRM 3138 standard solutions. The uncertainty on each data point represents the reproducibility (2SD) of the analytical session in which they were measured. Vertical dashed lines, matched to symbol colours, show the maximum  $x / \text{Pd}$  ratio found in sample solutions. If no vertical line is shown then the  $x / \text{Pd}$  ratio falls below the limit of the figure. No offsets in  $\delta^{106/105}\text{Pd}$  are observed at the concentration of isobaric or molecular interferences present in our sample solutions.

1) The ‘true’ composition of a mass-independent offset was calculated based on the NIST SRM 3138 Pd composition (Table 5.2). For the nucleosynthetic test this was done by subtracting an *s*-process component, calculated using the *s*-process yields from Bisterzo et al. (2011), from the NIST SRM 3138 composition. For the CRE test the true composition was calculated using the equations from Leya and Masarik (2013) varying depth in an iron meteorite with a radius of 60 cm and an exposure age of 625 Ma, using NIST SRM 3138 composition as the starting Pd composition.

2) The ‘measured’ composition was calculated by adding the composition of the spike (Table 5.2) to the ‘true’ composition from step 1 in a one to one ratio.

3) Using the double spike inversion  $\alpha$  was calculated using the measured composition from step 2 and the NIST SRM 3138 composition as the ‘natural’ composition.

4) This time  $\alpha$  was calculated using the using the ‘true’ composition from step 1 after that composition has been internally normalised to a fixed ratio. This internally normalised composition is the composition that would be determined by mass-independent isotopic analysis. All possible normalisations ratios for Pd ( $^{104,106,108}\text{Pd}/^{105}\text{Pd}$ ,  $^{104,108,110}\text{Pd}/^{106}\text{Pd}$ ,  $^{104,110}\text{Pd}/^{108}\text{Pd}$ ,  $^{104}\text{Pd}/^{110}\text{Pd}$ ), excluding  $^{102}\text{Pd}$ , were tested this try. The ratio was normalised to the composition of NIST SRM 3138.

The ‘measured’ composition tested did not include any natural fractionation and therefore  $\alpha$  should be 0 if the inversion is accurate, thus no offset is seen in  $\delta^{106/105}\text{Pd}$ . Any deviation from zero for  $\delta^{106/105}\text{Pd}$  is therefore due to a bias induced by the incorrect ‘natural’ composition in the double spike inversion. The offset in  $\delta^{106/105}\text{Pd}$  for these various ‘natural’ compositions for the two types of mass-independent offsets are presented below. Only the results for the  $^{108}\text{Pd}/^{105}\text{Pd}$  and  $^{110}\text{Pd}/^{105}\text{Pd}$  internally normalised compositions are discussed because former is the commonly used internal normalisation while the latter is the normalisation with the smallest offsets in  $\delta^{106/105}\text{Pd}$ .

Nucleosynthetic variations in the form of varying degrees of an *s*-process deficit are reported for several iron meteorite groups (Chapter 4). We modelled an *s*-process deficit up to 0.1‰ which is about twice that required to form the largest nucleosynthetic Pd offset reported for iron meteorites (Chapter 4). For the inversion using NIST SRM 3138 we see  $\delta^{106/105}\text{Pd}$  offsets outside of our long-term reproducibility ( $\pm 0.01$  ‰) for a  $\sim 0.06$  ‰ *s*-process deficit (Figure 5.5a). This roughly corresponds to the *s*-process deficit seen in the IVB and IID iron meteorites (Chapter 4). ). Inversions using the  $^{110}\text{Pd}/^{105}\text{Pd}$  normalisation scheme showed the smallest bias in  $\delta^{106/105}\text{Pd}$  ( $< 0.002$  ‰ for a 0.1 ‰ *s*-process deficit), which is not resolvable within our long-term reproducibility.

The Rh/Pd ratio is important when evaluating the mass-independent effects from CRE because  $^{104}\text{Pd}$  receives a significant CRE contribution from the reaction  $^{103}_{45}\text{Rh} + \frac{1}{0}n \rightarrow ^{104}_{45}\text{Rh} \rightarrow ^{104}_{46}\text{Pd} + \frac{0}{-1}\beta$  (Chapter 4). For the inversion using the NIST SRM 3138 ‘natural’ composition only a very small, not resolvable effect ( $< 0.0001$  ‰) in  $\delta^{106/105}\text{Pd}$  was modelled for a Rh/Pd ratio of 0. For an Rh/Pd ratio of 1, however, the offset is larger ( $\sim 0.012$  ‰) than our long-term reproducibility ( $\pm 0.01$  ‰) Several iron meteorites show CRE effects that result in equivalent offsets in  $^{104}\text{Pd}$  (Chapter 4). Both  $^{108}\text{Pd}/^{105}\text{Pd}$  and  $^{110}\text{Pd}/^{105}\text{Pd}$  internally normalised natural compositions show small ( $< 0.002$  ‰) biases in the  $\delta^{106/105}\text{Pd}$ , independent of the Rh/Pd ratio.

The results highlight the importance of using the natural mass-independent isotope composition of a sample instead of the terrestrial composition in the double spike inversion for high precision studies of mass-dependent Pd isotope variations in meteorites. Therefore, here the mass-independent isotope composition of each analysed sample was used in the double spike inversion. They were measured on the same sample aliquot as the double spike analyses for all meteorites apart from Gibeon. The Gibeon sample was sampled adjacent to the one used for the mass-independent study.

#### 5.4.5. Natural palladium stable isotope variations.

All five analysed meteorites show well resolved mass-dependent variations in  $\delta^{106/105}\text{Pd}$  (Table 5.3; Figure 5.6), relative to NIST SRM 3138. The IAB iron meteorite Cranbourne displays the lightest  $\delta^{106/105}\text{Pd}$  value ( $-0.134\text{‰} \pm 0.015$ ). Two analyses of a single aliquot of Carbo G (IID) are in excellent agreement with each other ( $0.087\text{‰} \pm 0.020$  and  $0.085\text{‰} \pm 0.015$ ). The same is true for three analyses of two separate aliquots of Gibeon (IVA), with different sample-to-spike ratios (Table 5.3), which all overlap within uncertainty and yield a  $\delta^{106/105}\text{Pd}$  mean of  $-0.010\text{‰} \pm 0.020$ . Hoba (IVB) and Tlacotepec (IVB) have, within uncertainty, the same  $\delta^{106/105}\text{Pd}$  values, which is the heaviest of the samples studied here

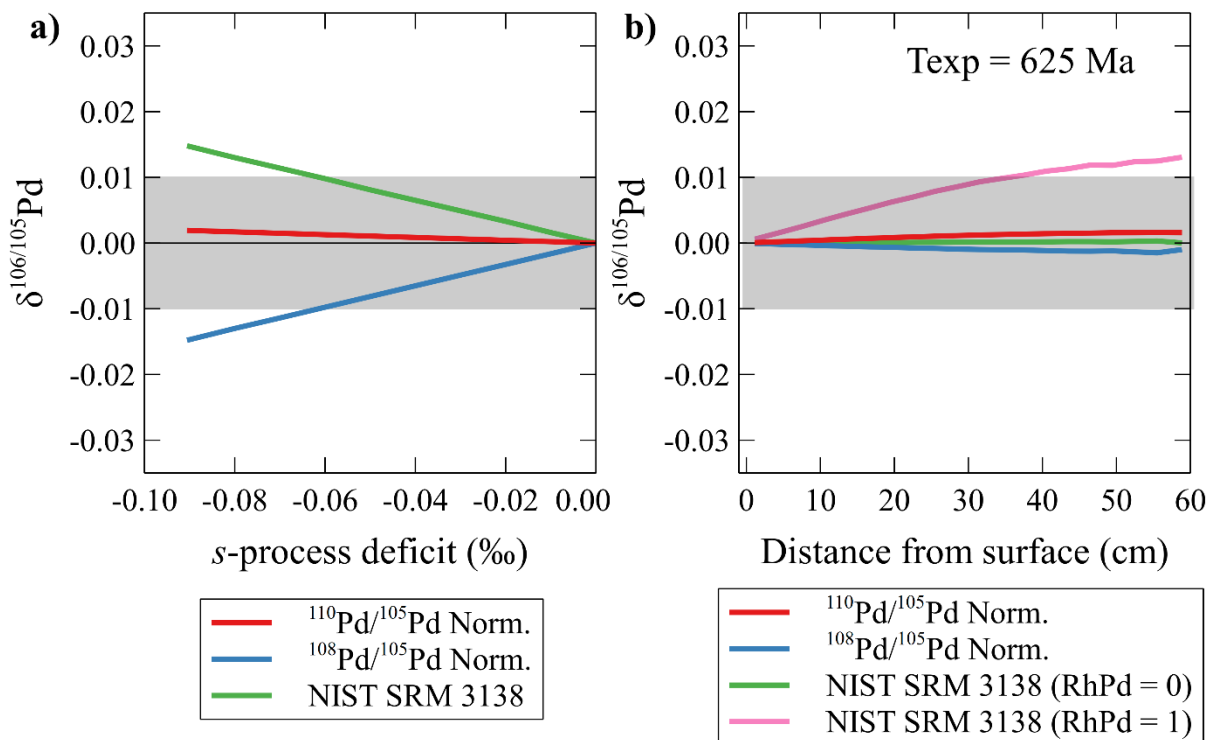


**Figure 5.5.** Modelled effects on  $\delta^{106/105}\text{Pd}$  accuracy for (a) nucleosynthetic and (b) CRE mass-independent offsets using the NIST SRM 3138 composition,  $^{108}\text{Pd}/^{105}\text{Pd}$  internally normalised and  $^{110}\text{Pd}/^{105}\text{Pd}$  internally normalised compositions during the double spike inversion. The grey band shows the long-term reproducibility of the NIST SRM 3138 standard (Figure 5.5.3b). a) The error in  $\delta^{106/105}\text{Pd}$  for varying amounts of an *s*-process deficit, calculated using yields from Bisterzo et al. (2011). Inversions featuring the terrestrial and  $^{108}\text{Pd}/^{110}\text{Pd}$  internally normalised natural compositions show  $\delta^{106/105}\text{Pd}$  offsets outside of our reproducibility for an *s*-process deficit of  $\sim 0.06\text{‰}$ , corresponding to that seen in the IID and IVB. The inversion for a  $^{110}\text{Pd}/^{105}\text{Pd}$  normalised composition does not show a resolvable offset to  $\delta^{106/105}\text{Pd}$  ( $< 0.002\text{‰}$ ). b) The error to  $\delta^{106/105}\text{Pd}$  modelled for different depths in a 120 cm diameter iron meteoroid with an exposure age of 625 Ma based on the CRE model by Leya and Masarik (2013). No resolvable offsets ( $> 0.002\text{‰}$ ) in  $\delta^{106/105}\text{Pd}$  are observed for either of the internally normalised compositions, independent of the Rh/Pd ratio. The same is true for the NIST SRM 3138 composition for a Rh/Pd ratio of 0. For a NIST SRM 3138 composition with a Rh/Pd Ratio of 1 the maximum offset to  $\delta^{106/105}\text{Pd}$  increases to  $\sim 0.012\text{‰}$ .

(-0.059 ‰ ± 0.015). Compared to the previous Pd data (Creech et al., 2017a; Figure 5.6) the isotopic composition of the analysed iron meteorites is heavier than that of chondrites (-0.192 ‰ ± 0.050) and ureilites (-0.197 ‰ ± 0.065), but are within uncertainty of the terrestrial crust (-0.191 ‰ ± 0.162). With such few samples the origin of the  $\delta^{106/105}\text{Pd}$  variation cannot be thoroughly evaluated. However, some insight can be gained by comparison to mass-dependent isotope studies of other elements.

**Table 5.3.** The Pd isotope composition of NIST SRM 3138 Pd standard and iron meteorite samples.

Sample <sup>a</sup>	n <sup>b</sup>	$\alpha^{c,d}$	Q <sup>e</sup>	$\delta^{106/105}\text{Pd}^d$	$^{104}\text{Pd}/^{108}\text{Pd}$	$^{106}\text{Pd}/^{108}\text{Pd}$	$^{110}\text{Pd}/^{108}\text{Pd}$
<b>Processed standards<sup>d</sup></b>							
NIST SRM 3138 1a		0.0006(05)	1.10	0.006 ± 0.005			
NIST SRM 3138 1b		0.0006(05)	1.10	0.006 ± 0.005			
NIST SRM 3138 1c		0.0001(05)	1.10	0.001 ± 0.005			
NIST SRM 3138 1d		0.0002(05)	1.10	0.002 ± 0.005			
NIST SRM 3138 1e		0.0002(05)	1.10	0.002 ± 0.005			
Mean	5	0.0003(05)		0.003 ± 0.004			
NIST SRM 3138 2a		0.0002(05)	0.99	0.002 ± 0.005			
NIST SRM 3138 2b		-0.0001(05)	0.99	-0.001 ± 0.005			
NIST SRM 3138 2c		0.0001(05)	0.99	0.001 ± 0.005			
NIST SRM 3138 2d		0.0000(05)	0.99	0.000 ± 0.005			
NIST SRM 3138 2e		0.0003(05)	0.99	0.003 ± 0.005			
Mean	5	0.0001(04)		0.001 ± 0.003			
NIST SRM 3138 3a		0.0005(05)	0.90	0.005 ± 0.005			
NIST SRM 3138 3b		0.0006(05)	0.90	0.006 ± 0.005			
NIST SRM 3138 3c		0.0000(05)	0.90	0.000 ± 0.005			
NIST SRM 3138 3d		-0.0001(05)	0.90	-0.001 ± 0.005			
NIST SRM 3138 3e		0.0000(05)	0.90	0.000 ± 0.005			
NIST SRM 3138 3f		0.0002(21)	0.90	0.002 ± 0.020			
Mean	6	0.0002(06)		0.002 ± 0.006			
Overall Mean	16	0.0002(05)		0.002 ± 0.005			
<b>Iron meteorites</b>							
Cranbourne		-0.0142(16)	1.18	-0.134 ± 0.015	0.417954	1.028440	0.443032
Carbo G a		-0.0091(21)	0.85	-0.087 ± 0.020	0.418030	1.028488	0.443055
Carbo G b		-0.0090(16)	0.85	-0.085 ± 0.015	0.418030	1.028488	0.443055
Gibeon 1a		-0.0110(21)	0.60	-0.104 ± 0.020	0.417950	1.028442	0.443039
Gibeon 1b		-0.0114(16)	0.60	-0.108 ± 0.015	0.417950	1.028442	0.443039
Gibeon 2a		-0.0120(21)	0.73	-0.113 ± 0.020	0.417950	1.028442	0.443039
Hoba		-0.0065(16)	1.04	-0.062 ± 0.015	0.417952	1.028450	0.443045
Tlacotepec		-0.0058(16)	0.98	-0.055 ± 0.015	0.418016	1.028481	0.443056

<sup>a</sup> Numbers indicate aliquots that have been processed separately while letters represent repeat measurements of the same solution. <sup>b</sup> Number of analyses included in mean. <sup>c</sup> Natural fractionation factor for each sample. Number in brackets indicate uncertainty of the last decimals. <sup>d</sup> Uncertainties on individual measurements are reported as the 2 SD daily reproducibility of the bracketing standards. Uncertainties of means represents 2 SD. <sup>e</sup> The sample-to-spike ratio of the measured solution. <sup>f</sup> The natural composition of the sample used in the double spike inversion. Calculated from the  $^{110}\text{Pd}/^{105}\text{Pd}$  internally normalised mass-independent signature (Appendix B) as described in section 5.3.5. For NIST SRM 3138 the long term average of NIST SRM 3138 from the mass-independent study was used (Table 5.2)



The large variation in stable Zn isotope compositions observed within different iron meteorite groups has been linked to the segregation of chromite, which preferentially sequesters light Zn isotopes from the melt (Bridgestock et al., 2014). However, it is not clear whether Pd is present in chromite or other accessory phases in iron meteorites and if this could explain the variation observed in  $\delta^{106/105}\text{Pd}$ . Preliminary results on the mass-dependent Ru isotope composition of iron meteorites also show large within group variations that have been linked to isotope fractionation between liquid and solid metal during crystallisation of the metal core (Hopp et al., 2016). If liquid-solid metal fractionation fractionated Pd isotopes we should see large within group variations. Nickel concentration can be used to trace fractional crystallisation in a solidifying core (Scott, 1972), and we see a correlation between the  $\delta^{106/105}\text{Pd}$  signature of iron meteorites and their Ni content (Figure 5.7a). However, we have only measured two meteorites from the same group (Tlacotepec and Hoba) and these do not show any variation in their  $\delta^{106/105}\text{Pd}$  signature (Figure 5.6), but this is far from conclusive. A study on a range of meteorites spanning a crystallisation sequence from the same group is needed to thoroughly evaluate liquid-solid metal fractional crystallisation as the origin of the observed  $\delta^{106/105}\text{Pd}$  variations.

However, the range of Ni concentrations found within groups are relatively narrow and therefore Ni commonly used for geochemical classification of iron meteorites (Scott and Wasson, 1975). The correlation between Ni and  $\delta^{106/105}\text{Pd}$  may therefore be more indicative of processes that govern the overall abundance of Ni in the core. Partitioning of Ni during metal-silicate differentiation varies depending pressure and temperature of the magma ocean (Li and Agee, 2001), and this suggests that  $\delta^{106/105}\text{Pd}$  could be a useful tracer of conditions during core formation. Iron meteorite parent bodies are

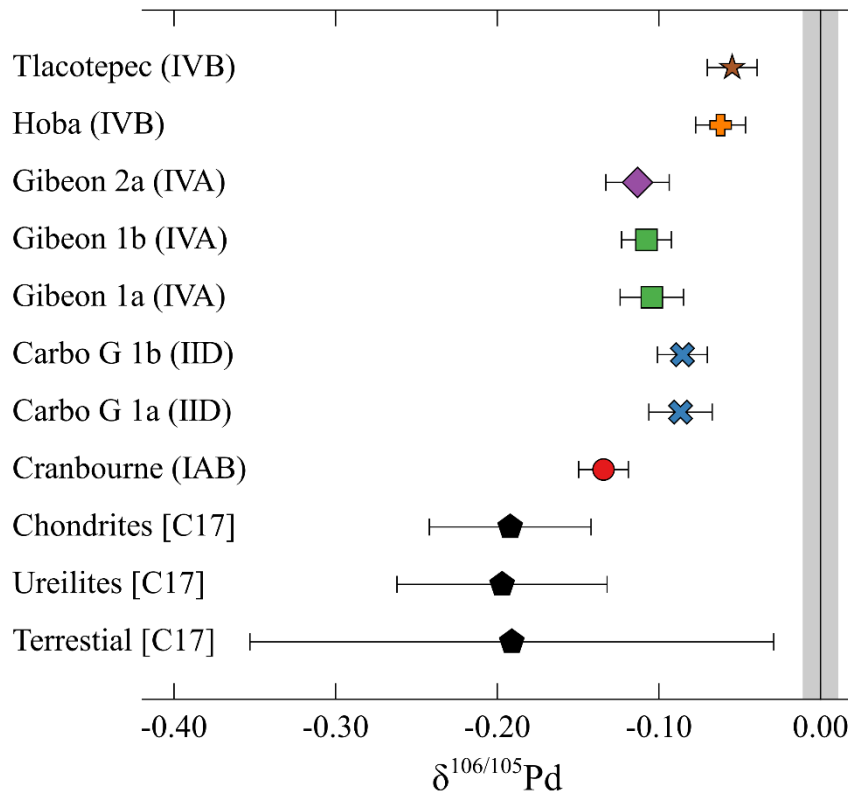


**Figure 5.6.** The variation in  $\delta^{106/105}\text{Pd}$  data for the iron meteorites analysed in this study. The grey shaded area shows the 2 SD long-term reproducibility of our bracketing standards. Data for chondrites, ureilites and terrestrial samples (labelled C17) are taken from Creech et al. (2017a).

interpreted to form at low pressures in small, similarly sized parent bodies (Goldstein and Short, 1967), which is not expected to result in a wide range of fractionation between the different iron meteorite parent bodies. Additionally, no mass-dependent variation is observed in Mo (Burkhardt et al., 2014) or Pt (Creech et al., 2017b) for iron meteorites despite differentiated silicate rocks showing evidence of isotopic fractionation during core-formation. Given that Pd is much more siderophile than Mo, this suggests that the metal fraction would not preserve a core-formation signature. Furthermore, metal-silicate differentiation is expected to enrich the metal phase in light isotopes (Schauble, 2004) and this is the opposite of what is observed here (Figure 5.6), assuming an initial Pd isotopic composition of chondrites.

Interestingly, the  $\delta^{106/105}\text{Pd}$  data also correlates with the mass-independent nucleosynthetic composition calculated for each group (Figure 5.7; Chapter 4) suggesting that the  $\delta^{106/105}\text{Pd}$  composition might be related to nebular processes. Isotopic condensation during evaporation/condensation is expected to enrich the heavy isotopes in the solid phase. The low concentrations of volatile elements in the IVB irons has led to the proposal that they accreted at high temperatures (Kelly and Larimer, 1977). This may explain why the IVBs have the heaviest  $\delta^{106/105}\text{Pd}$  value, and suggests there may a volatility control on Pd stable isotope fractionation in the solar system. However, processes including fractional crystallisation must be thoroughly evaluated before this hypothesis can be explored further.

## 5. Conclusions

This study reports the development of a new  $^{104}\text{Pd}$ - $^{108}\text{Pd}$  double spike procedure for precise measurements of mass-dependent Pd isotope compositions by MC-ICP-MS. Analyses of standard solutions with varying amounts of spike show that the results remains accurate for a wide range of

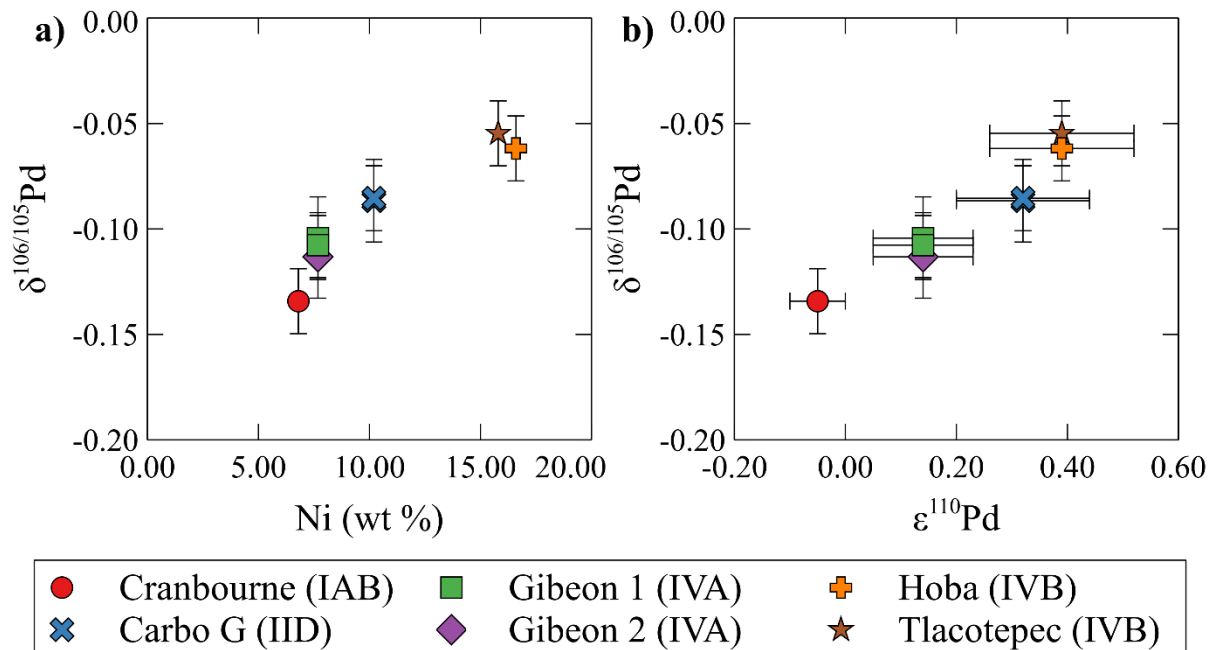


**Figure 5.7.** a) New  $\delta^{106/105}\text{Pd}$  data plotted against Ni content from Hoashi et al. (1993) and references therein. There is a positive correlation between the Ni content and the  $\delta^{106/105}\text{Pd}$  for the different meteorites. b) The  $\delta^{106/105}\text{Pd}$  data against the nucleosynthetic composition for each group from Chapter 4.  $\delta^{106/105}\text{Pd}$  and the nucleosynthetic isotope composition show a positive correlation.

sample-to-spike ratios (0.4 to 3.5). Doping tests demonstrate that samples prepared using the Pd separation procedure from Hunt et al. (2017; Chapter 2) and Ek et al. (2017; Chapter 3) yield consistently low concentrations of elements that generate isobaric (Ru and Cd) and molecular (Ni, Zn, Zr, Mo, Rh, Ag) interferences such that the accuracy of isotopic analysis is guaranteed. The long-term reproducibility of a NIST SRM 3138 Pd standard solution is  $\pm 0.01$  ‰ for  $\delta^{106/105}\text{Pd}$  (2 SD), enabling high precision measurements. Three analyses of two separately processed aliquots of the IVA Gibeon are within uncertainty of another ( $-0.108$  ‰  $\pm 0.025$ ). Modeling shows that accounting for mass-independent Pd isotope variation in the double spike procedure is mandatory for accurate results, given the magnitude of the mass-independent variations previously reported in iron meteorites (Chapter 4).

Analyses of five iron meteorites from four groups (IAB, IID, IVA, IVB) yield  $\delta^{106/105}\text{Pd}$  data ranging from -0.134 to -0.055. They are generally enriched in heavier isotopes compared to chondrites and ureilites ( $-0.192$  ‰  $\pm 0.050$ ; Creech et al., 2017b), except for the IAB iron Cranbourne ( $-0.134$  ‰  $\pm 0.015$ ). The mass-dependent isotope fractionation of iron meteorites relative to chondrites may be the effect of fractional crystallization, but requires further studies.

### **Acknowledgements**

This work was supported by the European Research Council under the European Union's Seventh Framework Programme (FP7/2007–2013)/ERC Grant agreement no. [279779].



# Chapter 6

## Conclusions

The aim of this thesis was to use the Pd isotopic composition of iron meteorites to assess (1) the origin of nucleosynthetic variations in bulk meteorites and (2) the processes operating during metal-silicate differentiation of planetary bodies. The first step towards high precision isotope studies is to separate the element of interest from the matrix and elements that cause isobaric and molecular interferences. In this thesis I present a novel two-stage ion exchange method that consistently yields a purified Pd fraction that allows for accurate, high precision mass-independent and mass-dependent Pd isotopic measurements of iron meteorites. The first ion exchange procedure separates Pd from the main matrix; however Ru, Mo and traces of Fe and Ni remain in the Pd fraction. This ion exchange procedure also allows for the collection of Pt, which was used in a companion study allowing direct comparison between the Pd and Pt isotope compositions of a single sample aliquot. Ruthenium is removed from the first Pd fraction via volatilisation in HClO<sub>4</sub> before a second ion exchange procedure removed the remaining matrix elements. The final Pd fraction consistently yields a Ru/Pd ratio of less than 0.0005, enabling accurate isotope measurements of <sup>102</sup>Pd.

In Chapter 4, I investigate the origin of nucleosynthetic variations in the solar system by measuring the mass-independent Pd isotope composition of 24 meteorites from the IAB, IIAB, IID, IIIAB, IVA and IVB iron meteorite groups. Based on repeat measurements of several iron meteorites, I deduced an external reproducibility (2 sd) of 1.58 for  $\epsilon^{102}\text{Pd}$ , 0.26 for  $\epsilon^{104}\text{Pd}$ , 0.13 for  $\epsilon^{106}\text{Pd}$  and 0.27 for  $\epsilon^{110}\text{Pd}$ . There is a wide range of Pd isotope compositions where the largest offsets from the terrestrial composition are identified in Carbo J (IID) with  $\sim 1.4$  and  $\sim 0.8$  for  $\epsilon^{104}\text{Pd}$  and  $\epsilon^{110}\text{Pd}$ , respectively. The variations within a meteorite group correlate with the mass-independent Pt isotope composition, a proxy for cosmic ray exposure effects. After correction for cosmic ray effects four iron meteorite groups have nucleosynthetic signatures that can be resolved from the terrestrial composition (IVA < IIIAB < IID  $\leq$  IVB), and that are consistent with an *s*-process deficit. The nucleosynthetic Pd data correlate with those of Mo and Ru; however, the slope of the correlation is not consistent with *s*-process production models. The observed slope suggests that the *s*-process components contained only 1/4<sup>th</sup> of the Pd suggested by *s*-process production models relative to Mo and Ru. Palladium is more volatile than both Mo and Ru, and I propose that this leads to less Pd condensing around AGB stars, relative to the more refractory Mo and Ru. The material that does not condense around the star is injected into the interstellar medium, where it is homogenised with other stellar material, losing its unique nucleosynthetic signature in the process. Selective processing of dust that condensed in the interstellar medium, containing roughly solar isotopic abundances, relative to 'stardust', dust grains formed around stars with unique nucleosynthetic compositions, led to the formation of nucleosynthetic offsets in the early solar system. This model predicts the lack of nucleosynthetic variations in even more volatile elements and can also, in part, explain the small or absent nucleosynthetic offsets for heavy elements.

To study the processes that operated during metal-silicate differentiation on planetary bodies in the early solar system I developed a <sup>104</sup>Pd-<sup>108</sup>Pd double spike. Once calibrated our spike remains accurate for sample-to-spike ratios ranging from 0.4 to 3.5. The long-term reproducibility of  $\delta^{106/105}\text{Pd}$  for a NIST SRM 3138 Pd standard solution is  $\pm 0.01$  ‰. Three analysis, from two individually processed sample aliquots of Gibeon (IVA) yield a  $\delta^{106/105}\text{Pd}$  composition of  $-0.108$  ‰  $\pm 0.025$ . Five metal samples from the IAB, IID, IVA and IVB groups were analysed as part of this project. They show a range of  $\delta^{106/105}\text{Pd}$

compositions, varying from -0.134 ‰ for the IAB Cranbourne to  $\sim$ -0.060 ‰ for the IVBs Tlacotepec and Hoba. All but Cranbourne (IAB) have a  $\delta^{106/105}\text{Pd}$  value that is heavier than that reported for chondrites ( $-0.192 \text{ ‰} \pm 0.050$ ; Creech et al., 2017b). Ascertaining the origin of the detected  $\delta^{106/105}\text{Pd}$  variation is difficult due to the limited number of samples analysed. Perhaps the most likely origin is fractional crystallisation during solidification of the core, however, further studies are needed to thoroughly evaluate the merits of this claim.

In summary, Pd isotope data show a range of both mass-independent and mass-dependent variations in iron meteorites. I demonstrate that the volatile nature of Pd relative to Mo and Ru makes Pd isotopes a useful tracer to constrain diverse processes occurring in the early solar system. Furthermore, the highly siderophile nature of Pd implies it is an ideal tracer of processes occurring during planet formation and differentiation. Further studies on the mass-dependent Pd isotope composition of meteorites should be able to constrain the process resulting in the  $\delta^{106/105}\text{Pd}$  variations observed in this thesis.





# References

- Akram, W., Schönbächler, M., Bisterzo, S. and Gallino, R. (2015) Zirconium isotope evidence for the heterogeneous distribution of s-process materials in the solar system. *Geochimica et Cosmochimica Acta* **165**, 484-500.
- Alpher, R.A., Bethe, H. and Gamow, G. (1948) The origin of chemical elements. *Physical Review* **73**, 803-804.
- Alpher, R.A. and Herman, R. (1948) Evolution of the universe. *Nature* **162**, 774-775.
- Anders, E. and Grevesse, N. (1989) Abundances of the elements: Meteoritic and solar. *Geochimica et Cosmochimica Acta* **53**, 197-214.
- Andreasen, R. and Sharma, M. (2006) Solar nebula heterogeneity in p-process samarium and neodymium isotopes. *Science* **314**, 806-809.
- Arlandini, C., Käppeler, F., Wisshak, K., Gallino, R., Lugaro, M., Busso, M. and Straniero, O. (1999) Neutron capture in low-mass asymptotic giant branch stars: Cross sections and abundance signatures. *The Astrophysical Journal* **525**, 886-900.
- Benz, W. and Cameron, A. (1990) Terrestrial effects of the Giant Impact. *Origin of the Earth*, 61-67.
- Berglund, M. and Wieser, M.E. (2011) Isotopic compositions of the elements 2009 (IUPAC Technical Report). *Pure and Applied Chemistry* **83**, 397-410.
- Bisterzo, S., Gallino, R., Straniero, O., Cristallo, S. and Käppeler, F. (2011) The s-process in low-metallicity stars – II. Interpretation of high-resolution spectroscopic observations with asymptotic giant branch models. *Monthly Notices of the Royal Astronomical Society* **418**, 284-319.
- Bouvier, A. and Wadhwa, M. (2010) The age of the Solar System redefined by the oldest Pb-Pb age of a meteoritic inclusion. *Nature Geoscience* **3**, 637-641.
- Bridgestock, L.J., Williams, H., Rehkämper, M., Larner, F., Giscard, M.D., Hammond, S., Coles, B., Andreasen, R., Wood, B.J., Theis, K.J., Smith, C.L., Benedix, G.K. and Schönbächler, M. (2014) Unlocking the zinc isotope systematics of iron meteorites. *Earth and Planetary Science Letters* **400**, 153-164.
- Bromm, V., Yoshida, N., Hernquist, L. and McKee, C.F. (2009) The formation of the first stars and galaxies. *Nature* **459**, 49-54.
- Burbidge, E.M., Burbidge, G.R., Fowler, W.A. and Hoyle, F. (1957) Synthesis of the elements in stars. *Reviews of Modern Physics* **29**, 547-650.
- Burbine, T.H., McCoy, T.J., Meibom, A., Gladman, B. and Keil, K. (2002) 'Meteoritic parent bodies: Their number and identification', in Bottke Jr., W.F., Cellino, A., Paolicchi, P., Binzel, R.P. (Eds.), *Asteroids III*, University of Arizona Press, Tucson, pp. 653-667.
- Burkhardt, C., Borg, L.E., Brennecka, G.A., Shollenberger, Q.R., Dauphas, N. and Kleine, T. (2016) A nucleosynthetic origin for the Earth's anomalous <sup>142</sup>Nd composition. *Nature* **537**, 394-398.

- Burkhardt, C., Hin, R.C., Kleine, T. and Bourdon, B. (2014) Evidence for Mo isotope fractionation in the solar nebula and during planetary differentiation. *Earth and Planetary Science Letters* **391**, 201-211.
- Burkhardt, C., Kleine, T., Oberli, F., Pack, A., Bourdon, B. and Wieler, R. (2011) Molybdenum isotope anomalies in meteorites: Constraints on solar nebula evolution and origin of the Earth. *Earth and Planetary Science Letters* **312**, 390-400.
- Busso, M., Gallino, R. and Wasserburg, G.J. (1999) Nucleosynthesis in asymptotic giant branch stars: Relevance for galactic enrichment and solar system formation. *Annual Review of Astronomy and Astrophysics* **37**, 239-309.
- Cameron, A.G.W. and Benz, W. (1991) The origin of the moon and the single impact hypothesis IV. *Icarus* **92**, 204-216.
- Canup, R.M. (2012) Forming a Moon with an Earth-like composition via a giant impact. *Science* **338**, 1052-1055.
- Canup, R.M. and Asphaug, E. (2001) Origin of the Moon in a giant impact near the end of the Earth's formation. *Nature* **412**, 708.
- Carlson, R.W., Boyet, M. and Horan, M. (2007) Chondrite barium, neodymium, and samarium isotopic heterogeneity and early earth differentiation. *Science* **316**, 1175-1178.
- Chambers, J.E. (2014) 'Planet formation', in Holland, H.D., Turekian, K.K. (Eds.), *Treatise on Geochemistry*, 2<sup>nd</sup> ed., Elsevier, Oxford, pp. 55-72.
- Chen, H., Nguyen, B.M. and Moynier, F. (2013) Zinc isotopic composition of iron meteorites: Absence of isotopic anomalies and origin of the volatile element depletion. *Meteoritics & Planetary Science* **48**, 2441-2450.
- Chen, J.H., Papanastassiou, D.A. and Wasserburg, G.J. (2010) Ruthenium endemic isotope effects in chondrites and differentiated meteorites. *Geochimica et Cosmochimica Acta* **74**, 3851-3862.
- Chou, C.-L. (1978) Fractionation of siderophile elements in the Earth's upper mantle, *8th Lunar and Planetary Science Conference*, Houston, pp. 219-230.
- Chu, Z., Yan, Y., Chen, Z., Guo, J., Yang, Y., Li, C. and Zhang, Y. (2015) A comprehensive method for precise determination of re, os, ir, ru, pt, pd concentrations and os isotopic compositions in geological samples. *Geostandards and Geoanalytical Research* **39**, 151-169.
- Clayton, D. (1982) Cosmic chemical memory: A new astronomy. *Quarterly Journal of the Royal Astronomical Society* **23**, 174-212.
- Côté, B., Fryer, C.L., Belczynski, K., Korobkin, O., Chruślińska, M., Vassh, N., Mumpower, M.R., Lippuner, J., Sprouse, T.M. and Surman, R. (2018) The origin of *r*-process elements in the milky way. *The Astrophysical Journal* **855**, 99-108.
- Creech, J., Moynier, F. and Bizzarro, M. (2017a) Tracing metal–silicate segregation and late veneer in the Earth and the ureilite parent body with palladium stable isotopes. *Geochimica et Cosmochimica Acta* **216**, 28-41.
- Creech, J.B., Baker, J.A., Handler, M.R., Lorand, J.P., Storey, M., Wainwright, A.N., Luguet, A., Moynier, F. and Bizzarro, M. (2017b) Late accretion history of the terrestrial planets inferred from platinum stable isotopes. *Geochemical Perspectives Letters* **3**, 94-104.

- Ćuk, M. and Stewart, S.T. (2012) Making the Moon from a fast-spinning Earth: a giant impact followed by resonant despinning. *Science* **338**, 1047-1052.
- Dauphas, N. and Chaussidon, M. (2011) A Perspective from extinct radionuclides on a young stellar object: The sun and its accretion disk. *Annual Review of Earth and Planetary Sciences* **39**, 351-386.
- Dauphas, N., Davis, A.M., Marty, B. and Reisberg, L. (2004) The cosmic molybdenum–ruthenium isotope correlation. *Earth and Planetary Science Letters* **226**, 465-475.
- Dauphas, N., Marty, B. and Reisberg, L. (2002) Molybdenum evidence for inherited planetary scale isotope heterogeneity of the protosolar nebula. *The Astrophysical Journal* **565**, 640-644.
- Dauphas, N., Remusat, L., Chen, J.H., Roskosz, M., Papanastassiou, D.A., Stodolna, J., Guan, Y., Ma, C. and Eiler, J.M. (2010) Neutron-rich chromium isotope anomalies in supernova nanoparticles. *The Astrophysical Journal* **720**, 1577-1591.
- Dauphas, N. and Schauble, E.A. (2016) Mass fractionation laws, mass-independent effects, and isotopic anomalies. *Annual Review of Earth and Planetary Sciences* **44**, 709-783.
- Elkins-Tanton, L.T., Weiss, B.P. and Zuber, M.T. (2011) Chondrites as samples of differentiated planetesimals. *Earth and Planetary Science Letters* **305**, 1-10.
- Faris, J.P. (1960) Adsorption of the elements from hydrofluoric acid by anion exchange. *Analytical Chemistry* **32**, 520-522.
- Fehr, M.A., Rehkämper, M., Halliday, A.N., Wiechert, U., Hattendorf, B., Günther, D., Ono, S., Eigenbrode, J.L. and Rumble, D. (2005) Tellurium isotopic composition of the early solar system—A search for effects resulting from stellar nucleosynthesis,  $^{126}\text{Sn}$  decay, and mass-independent fractionation. *Geochimica et Cosmochimica Acta* **69**, 5099-5112.
- Fischer-Gödde, M., Burkhardt, C., Kruijer, T.S. and Kleine, T. (2015) Ru isotope heterogeneity in the solar protoplanetary disk. *Geochimica et Cosmochimica Acta* **168**, 151-171.
- Fischer-Gödde, M. and Kleine, T. (2017) Ruthenium isotopic evidence for an inner Solar System origin of the late veneer. *Nature* **541**, 525-527.
- Gros, M., Lorand, J.-P. and Luguët, A. (2002) Analysis of platinum group elements and gold in geological materials using NiS fire assay and Te coprecipitation; the NiS dissolution step revisited. *Chemical Geology* **185**, 179-190.
- Grossman, L. (1972) Condensation in the primitive solar nebula. *Geochimica et Cosmochimica Acta* **36**, 597-619.
- Haisch, K.E.J., Lada, E.A. and Lada, C.J. (2001) Disk frequencies and lifetimes in young clusters. *The Astrophysical Journal Letters* **553**, L153-L156.
- Halliday, A.N. (2004) Mixing, volatile loss and compositional change during impact-driven accretion of the Earth. *Nature* **427**, 505-509.
- Halliday, A.N. (2014) 'The origin and earliest history of the earth', in Holland, H.D., Turekian, K.K. (Eds.), *Treatise on Geochemistry*, 2<sup>nd</sup> ed., Elsevier, Oxford, pp. 149-211.
- Heger, A., Fröhlich, C. and Truran, J.W. (2014) 'Origin of the elements', in Holland, H.D., Turekian, K.K. (Eds.), *Treatise on Geochemistry*, 2<sup>nd</sup> ed., Elsevier, Oxford, pp. 1-14.
- Herwig, F. (2005) Evolution of asymptotic giant branch stars. *Annual Review of Astronomy and Astrophysics* **43**, 435-479.

- Hinshaw, G., Larson, D., Komatsu, E., Spergel, D.N., Bennett, C.L., Dunkley, J., Nolte, M.R., Halpern, M., Hill, R.S., Odegard, N., Page, L., Smith, K.M., Weiland, J.L., Gold, B., Jarosik, N., Kogut, A., Limon, M., Meyer, S.S., Tucker, G.S., Wollack, E. and Wright, E.L. (2013) Nine-year wilkinson microwave anisotropy probe (WMAP) observations: Cosmological parameter results. *The Astrophysical Journal Supplement Series* **208**, 19-43.
- Hoashi, M., Brooks, R.R. and Reeves, R.D. (1993) Palladium, platinum and ruthenium in iron meteorites and their taxonomic significance. *Chemical Geology* **106**, 207-218.
- Holzheid, A., Sylvester, P., O'Neill, H.S.C., Rubie, D. and Palme, H. (2000) Evidence for a late chondritic veneer in the Earth's mantle from high-pressure partitioning of palladium and platinum. *Nature* **406**, 396-399.
- Hopp, T., Fischer-Gödde, M. and Kleine, T. (2018) Ruthenium isotope fractionation in protoplanetary cores. *Geochimica et Cosmochimica Acta* **223**, 75-89.
- Huang, M. and Masuda, A. (1997) Measurement of the atomic weight of ruthenium by negative thermal ionization mass spectrometry. *Analytical Chemistry* **69**, 1135-1139.
- Hubble, E. (1929) A relation between distance and radial velocity among extra-galactic nebulae. *Proceedings of the National Academy of Sciences* **15**, 168-173.
- Hunt, A.C., Cook, D.L., Lichtenberg, T., Reger, P.M., Ek, M., Golabek, G.J. and Schönbächler, M. (2018) Late metal-silicate separation on the IAB parent asteroid: Constraints from combined W and Pt isotopes and thermal modelling. *Earth and Planetary Science Letters* **482**, 490-500.
- Hunt, A.C., Ek, M. and Schönbächler, M. (2017a) Platinum isotopes in iron meteorites: Galactic cosmic ray effects and nucleosynthetic homogeneity in the *p*-process isotope <sup>190</sup>Pt and the other platinum isotopes. *Geochimica et Cosmochimica Acta* **216**, 82-95.
- Hunt, A.C., Ek, M. and Schönbächler, M. (2017b) Separation of platinum from palladium and iridium in iron meteorites and accurate high-precision determination of platinum isotopes by multi-collector ICP-MS. *Geostandards and Geoanalytical Research* **41**, 633-647.
- Iocco, F., Mangano, G., Miele, G., Pisanti, O. and Serpico, P.D. (2009) Primordial nucleosynthesis: From precision cosmology to fundamental physics. *Physics Reports* **472**, 1-76.
- Kant, I. (1755) *Allgemeine Naturgeschichte und Theorie des Himmels oder Versuch von der Verfassung und dem mechanischen Ursprunge des ganzen Weltgebäudes nach Newtonischen Grundsätzen abgehandelt*, Johan Friederich Petersen, Königsberg und Leipzig.
- Käppeler, F., Gallino, R., Bisterzo, S. and Aoki, W. (2011) The s-process: Nuclear physics, stellar models, and observations. *Reviews of Modern Physics* **83**, 157-193.
- Kelly, W. and Wasserburg, G. (1978) Evidence for the existence of Pd-107 in the early solar system. *Geophysical Research Letters* **5**, 1079-1082.
- Kraus, K.A. and Nelson, F. (1956) Anion exchange studies of the fission products, *Proceedings of International Conference on Peaceful Use of Atomic Energy*, pp. 113-125.
- Kruijer, T.S., Fischer-Gödde, M., Kleine, T., Sprung, P., Leya, I. and Wieler, R. (2013a) Neutron capture on Pt isotopes in iron meteorites and the Hf-W chronology of core formation in planetesimals. *Earth and Planetary Science Letters* **361**, 162-172.
- Kruijer, T.S., Sprung, P., Kleine, T., Leya, I. and Wieler, R. (2013b) The abundance and isotopic composition of Cd in iron meteorites. *Meteoritics & Planetary Science* **48**, 2597-2607.

- Kruijer, T.S., Touboul, M., Fischer-Gödde, M., Bermingham, K.R., Walker, R.J. and Kleine, T. (2014) Protracted core formation and rapid accretion of protoplanets. *Science* **344**, 1150-1154.
- Lemaître, G. (1931) The beginning of the world from the point of view of quantum theory. *Nature* **127**, 706.
- Levison, H.F., Kretke, K.A. and Duncan, M.J. (2015) Growing the gas-giant planets by the gradual accumulation of pebbles. *Nature* **524**, 322-324.
- Lewis, J.S. (1974) The temperature gradient in the solar nebula. *Science* **186**, 440-443.
- Leya, I. and Masarik, J. (2013) Thermal neutron capture effects in radioactive and stable nuclide systems. *Meteoritics & Planetary Science* **48**, 665-685.
- Lodders, K. (2003) Solar system abundances and condensation temperatures of the elements. *The Astrophysical Journal* **591**, 1220-1247.
- Lodders, K., Palme, H. and Gail, H.-P. (2009) Abundances of the elements in the Solar System, in: Trümper, J.E. (Ed.), *Solar System. Springer Verlag, Berlin, Heidelberg, New York*, pp. 560-598.
- Mann, U., Frost, D.J., Rubie, D.C., Becker, H. and Audétat, A. (2012) Partitioning of Ru, Rh, Pd, Re, Ir and Pt between liquid metal and silicate at high pressures and high temperatures- Implications for the origin of highly siderophile element concentrations in the Earth's mantle. *Geochimica et Cosmochimica Acta* **84**, 593-613.
- Markowski, A., Leya, I., Quitté, G., Ammon, K., Halliday, A.N. and Wieler, R. (2006) Correlated helium-3 and tungsten isotopes in iron meteorites: Quantitative cosmogenic corrections and planetesimal formation times. *Earth and Planetary Science Letters* **250**, 104-115.
- Matthes, M., Fischer-Gödde, M., Kruijer, T.S., Leya, I. and Kleine, T. (2015) Pd-Ag chronometry of iron meteorites: Correction of neutron capture-effects and application to the cooling history of differentiated protoplanets. *Geochimica et Cosmochimica Acta* **169**, 45-62.
- Mayer, B., Wittig, N., Humayun, M. and Leya, I. (2015) Palladium isotopic evidence for nucleosynthetic and cosmogenic isotope anomalies in iron meteorites. *The Astrophysical Journal* **809**, 180-187.
- McSween, H.Y., Mittlefehldt, D.W., Beck, A.W., Mayne, R.G. and McCoy, T.J. (2010) 'HED meteorites and their relationship to the geology of Vesta and the Dawn mission', in Russel, C., Raymond, C. (Eds.), *The Dawn Mission to Minor Planets 4 Vesta and 1 Ceres*. Springer, pp. 141-174.
- Palme, H., Larimer, J. and Lipschutz, M. (1988) 'Moderately volatile elements', in Kerridge, J.F., Matthews, M.S. (Eds.), *Meteorites and the early solar system*, University of Arizona Press, Tuscon, pp. 436-461.
- Palme, H. and O'Neill, H.S.C. (2014) Cosmochemical estimates of mantle composition. *Treatise on geochemistry* **2**, 1-38.
- Penzias, A.A. and Wilson, R.W. (1965) A measurement of excess antenna temperature at 4080 Mc/s. *The Astrophysical Journal* **142**, 419-421.
- Poole, G.M., Rehkämper, M., Coles, B.J., Goldberg, T. and Smith, C.L. (2017) Nucleosynthetic molybdenum isotope anomalies in iron meteorites – new evidence for thermal processing of solar nebula material. *Earth and Planetary Science Letters* **473**, 215-226.
- Qian, Y.Z. and Wasserburg, G.J. (2003) Stellar sources for heavy r-process nuclei. *The Astrophysical Journal* **588**, 1099-1109.

- Qin, L., Dauphas, N., Wadhwa, M., Markowski, A., Gallino, R., Janney, P., E. and Bouman, C. (2008) Tungsten nuclear anomalies in planetesimal cores. *The Astrophysical Journal* **674**, 1234-1241.
- Rauscher, T., Dauphas, N., Dillmann, I., Fröhlich, C., Zs, F. and Gy, G. (2013) Constraining the astrophysical origin of the *p*-nuclei through nuclear physics and meteoritic data. *Reports on Progress in Physics* **76**, 066201.
- Rayet, M., Arnould, M., Hashimoto, M., Prantzos, N. and Nomoto, K. (1995) The *p*-process in Type II supernovae. *Astronomy and Astrophysics* **298**, 517-527.
- Regelous, M., Elliott, T. and Coath, C.D. (2008) Nickel isotope heterogeneity in the early Solar System. *Earth and Planetary Science Letters* **272**, 330-338.
- Rehkämper, M. and Halliday, A.N. (1997) Development and application of new ion-exchange techniques for the separation of the platinum group and other siderophile elements from geological samples. *Talanta* **44**, 663-672.
- Ren, M., Sun, Y., Wang, C.Y. and Sun, S. (2016) Determination of platinum-group elements in geological samples by isotope dilution-inductively coupled plasma-mass spectrometry combined with sulfide fire assay preconcentration. *Geostandards and Geoanalytical Research* **40**, 67-83.
- Reufer, A., Meier, M.M., Benz, W. and Wieler, R. (2012) A hit-and-run giant impact scenario. *Icarus* **221**, 296-299.
- Righter, K. (2011) Prediction of metal–silicate partition coefficients for siderophile elements: An update and assessment of PT conditions for metal–silicate equilibrium during accretion of the Earth. *Earth and Planetary Science Letters* **304**, 158-167.
- Righter, K., Humayun, M. and Danielson, L. (2008) Partitioning of palladium at high pressures and temperatures during core formation. *Nature Geoscience* **1**, 321-323.
- Rosman, K.J.R., Barnes, I.L., Moore, L.J. and Gramlich, J.W. (1980) Isotope composition of Cd, Ca and Mg in the Brownfield chondrite. *Geochemical Journal* **14**, 269-277.
- Rosman, K.J.R. and Laeter, J.R.D. (1974) The abundance of cadmium and zinc in meteorites. *Geochimica et Cosmochimica Acta* **38**, 1665-1677.
- Russell, W.A., Papanastassiou, D.A. and Tombrello, T.A. (1978) Ca isotope fractionation on the Earth and other solar system materials. *Geochimica et Cosmochimica Acta* **42**, 1075-1090.
- Schauble, E.A. (2004) Applying stable isotope fractionation theory to new systems. *Reviews in Mineralogy and Geochemistry* **55**, 65-111.
- Schönbächler, M., Carlson, R.W., Horan, M.F., Mock, T.D. and Hauri, E.H. (2008) Silver isotope variations in chondrites: Volatile depletion and the initial <sup>107</sup>Pd abundance of the solar system. *Geochimica et Cosmochimica Acta* **72**, 5330-5341.
- Schönbächler, M. and Fehr, M.A. (2014) '15.7-Basics of ion exchange chromatography for selected geological applications' in Holland, H.D., Turekian, K.K. (Ed.), *Treatise on Geochemistry*, 2<sup>nd</sup> ed., Elsevier, Oxford, pp. 123-146.
- Scott, E.D. (1972) Chemical fractionation in iron meteorites and its interpretation. *Geochimica et Cosmochimica Acta* **36**, 1205-1236.
- Shima, M., Rees, C.E. and Thode, H.G. (1978) The isotopic composition and atomic weight of palladium. *Canadian Journal of Physics* **56**, 1333-1339.

- Sprung, P., Scherer, E.E., Upadhyay, D., Leya, I. and Mezger, K. (2010) Non-nucleosynthetic heterogeneity in non-radiogenic stable Hf isotopes: Implications for early solar system chronology. *Earth and Planetary Science Letters* **295**, 1-11.
- Steele, R.C.J., Coath, C.D., Regelous, M., Russell, S. and Elliott, T. (2012) Neutron-poor nickel isotope anomalies in meteorites. *The Astrophysical Journal* **758**, 59-80.
- Theis, K.J., Schönbächler, M., Benedix, G.K., Rehkämper, M., Andreasen, R. and Davies, C. (2013) Palladium–silver chronology of IAB iron meteorites. *Earth and Planetary Science Letters* **361**, 402-411.
- Thielemann, F.K., Arcones, A., Käppeli, R., Liebendörfer, M., Rauscher, T., Winteler, C., Fröhlich, C., Dillmann, I., Fischer, T., Martinez-Pinedo, G., Langanke, K., Farouqi, K., Kratz, K.L., Panov, I. and Korneev, I.K. (2011) What are the astrophysical sites for the *r*-process and the production of heavy elements? *Progress in Particle and Nuclear Physics* **66**, 346-353.
- Tonks, B.W. and Melosh, J.H. (1992) Core formation by giant impacts. *Icarus* **100**, 326-346.
- Travaglio, C., Röpke, F.K., Gallino, R. and Hillebrandt, W. (2011) Type Ia supernovae as sites of the *p*-process: Two-dimensional models coupled to nucleosynthesis. *The Astrophysical Journal* **739**, 93.
- Trinquier, A., Birck, J.L., Allègre, C.J., Göpel, C. and Ulfbeck, D. (2008) <sup>53</sup>Mn–<sup>53</sup>Cr systematics of the early Solar System revisited. *Geochimica et Cosmochimica Acta* **72**, 5146-5163.
- Trinquier, A., Elliott, T., Ulfbeck, D., Coath, C., Krot, A.N. and Bizzarro, M. (2009) Origin of nucleosynthetic isotope heterogeneity in the solar protoplanetary disk. *Science* **324**, 374-376.
- Tsujiimoto, T. and Shigeyama, T. (2014) Enrichment history of *r*-process elements shaped by a merger of neutron star pairs. *Astronomy & Astrophysics* **565**, L5.
- Walker, R.J. (2009) Highly siderophile elements in the Earth, Moon and Mars: Update and implications for planetary accretion and differentiation. *Chemie der Erde - Geochemistry* **69**, 101-125.
- Walker, R.J. (2012) Evidence for homogeneous distribution of osmium in the protosolar nebula. *Earth and Planetary Science Letters* **351**, 36-44.
- Wasserburg, G.J., Busso, M. and Gallino, R. (1996) Abundances of actinides and short-lived nonactinides in the interstellar medium: Diverse supernova sources for the *r*-processes. *The Astrophysical Journal Letters* **466**, L109.
- Weisberg, M.K., McCoy, T.J. and Krot, A.N. (2006) 'Systematics and evaluation of meteorite classification', in Lauretta, D.S., McSween Jr, H.Y. (Eds.), *Meteorites and the early solar system II*, Arizona Press, Tuscon, pp. 19-52.
- Wetherill, G.W. (1990) Formation of the Earth. *Annual Review of Earth and Planetary Sciences* **18**, 205-256.
- Wittig, N., Humayun, M., Brandon, A.D., Huang, S. and Leya, I. (2013) Coupled W–Os–Pt isotope systematics in IVB iron meteorites: In situ neutron dosimetry for W isotope chronology. *Earth and Planetary Science Letters* **361**, 152-161.
- Wombacher, F., Rehkämper, M., Mezger, K., Bischoff, A. and Münker, C. (2008) Cadmium stable isotope cosmochemistry. *Geochimica et Cosmochimica Acta* **72**, 646-667.
- Woosley, S.E., Heger, A. and Weaver, T.A. (2002) The evolution and explosion of massive stars. *Reviews of Modern Physics* **74**, 1015-1071.

- Yokoyama, T., Rai, V.K., Alexander, C.M.D., Lewis, R.S., Carlson, R.W., Shirey, S.B., Thiemens, M.H. and Walker, R.J. (2007) Osmium isotope evidence for uniform distribution of *s*- and *r*-process components in the early solar system. *Earth and Planetary Science Letters* **259**, 567-580.
- Zinner, E. (1998) Stellar nucleosynthesis and the isotopic composition of presolar grains from primitive meteorites. *Annual Review of Earth and Planetary Sciences* **26**, 147-188.



# Appendix A\*

Separation of platinum from palladium and iridium in iron meteorites and accurate high precision analyses of platinum isotopes by multi-collector ICP-MS.

\*A version of this chapter was published as: Hunt, A. C., Ek, M., Schönbacher, M. (2017) Separation of platinum from palladium and iridium in iron meteorites and accurate high precision analyses of platinum isotopes by multi-collector ICP-MS. *Geostandards and Geoanalytical Research* **216**, 82-95.

## Abstract

This study presents a new analytical method for the isolation of Pt from iron meteorites. The method also allows for the separation of Pd from the same sample aliquot. The separation entails a two-stage anion exchange procedure. In the first stage, Pt and Pd are separated from each other, and from major matrix constituents including Fe and Ni. In the second stage, Ir is reduced with ascorbic acid and eluted from the column before Pt collection. Platinum yields for the total procedure are typically 50 – 70 %. After purification, high precision Pt isotope analyses are performed by multi-collector ICP-MS. The reproducibility of the new method is assessed using the IAB iron meteorite North Chile. Replicate analyses of multiple digestions of this material yield a reproducibility of 0.73 for  $\epsilon^{192}\text{Pt}$ , 0.15 for  $\epsilon^{194}\text{Pt}$  and 0.09 for  $\epsilon^{196}\text{Pt}$  (2 standard deviations). The Pt SRM 3140 standard was passed through the analytical procedure and yields an isotopic composition that is identical to the unprocessed Pt standard. This indicates that the new technique is accurate within the limit of the stated uncertainties. Data for three iron meteorites support that Pt isotope variations in these samples are due to exposure to galactic cosmic rays in space.

## A.1. Introduction

Platinum is a platinum group element (PGE; also Ru, Rh, Pd, Os and Ir) with six isotopes ( $^{190}\text{Pt}$ ,  $^{192}\text{Pt}$ ,  $^{194}\text{Pt}$ ,  $^{195}\text{Pt}$ ,  $^{196}\text{Pt}$  and  $^{198}\text{Pt}$ ; Table 1). It principally occurs as  $\text{Pt}^0$ ,  $\text{Pt}^{2+}$  and  $\text{Pt}^{4+}$  in the Earth, but can also exist in a range of other oxidation states (Cotton et al., 1999). It is refractory, with a 50 % condensation temperature of 1408 K (Lodders 2003). In common with all PGEs, Pt is highly siderophile, and therefore strongly partitioned into the metal phase during core formation.

The applications of Pt isotopes are potentially very diverse. Mass-dependent isotope analyses may help to constrain terrestrial core formation and the late addition of extra-terrestrial materials to the Earth's mantle (Creech et al., 2017). Moreover, stable Pt isotope techniques may also be applied as a redox tracer in marine environments, as environmental monitors of vehicle emissions (Creech et al., 2013), and also to medical applications, where Pt-based compounds with various oxidation states are used as chemotherapy drugs (Cotton et al., 1999).

In this study, however, we focus on the improvement of analytical techniques for mass-independent Pt isotope analyses, although our new separation technique may also be relevant for mass-dependent isotope analyses. Mass-independent Pt isotope analyses are a novel tool of increasing importance in cosmochemistry. This is because recently, Pt isotopes were established as a powerful neutron-capture dosimeter (Leya and Masarik 2013). Neutron capture reactions in meteorites are a result of exposure to galactic cosmic rays (GCR) in space, and can modify isotope ratios. Cosmogenic noble gases have

**Table A.1. Relative abundances, nucleosynthetic production sites, and major interferences for Pt isotopes.**

Isotope	$^{190}\text{Pt}$	$^{192}\text{Pt}$	$^{194}\text{Pt}$	$^{195}\text{Pt}$	$^{196}\text{Pt}$	$^{198}\text{Pt}$
Relative abundance (%) <sup>a</sup>	0.012	0.782	32.86	33.78	25.21	7.356
Nucleosynthetic production sites and % of contribution <sup>b</sup>	<i>p</i> - (100.0)	<i>s</i> - (87.1)	<i>r</i> - (93.4)	<i>r</i> - (97.4)	<i>r</i> - (86.8)	<i>r</i> - (100.0)
Major isobaric interferences and relative abundances (%) <sup>c</sup>	$^{190}\text{Os}$ (26.26)	$^{192}\text{Os}$ (40.78)	$^{193}\text{Ir}$ (62.7)		$^{196}\text{Hg}$ (0.15)	$^{198}\text{Hg}$ (9.97)
		$^{191}\text{Ir}$ (37.3)				

<sup>a</sup> Platinum abundances are taken from Wolff Briche et al., (2002). <sup>b</sup> *s*- and *r*-process contributions to Pt isotopes are taken from Bisterzo et al., (2011). <sup>c</sup> Ir, Os and Hg abundances from Berglund and Wieser (2011).

traditionally been used to correct for GCR effects (e.g., Markowski et al., 2006), but their production occurs mainly at energies > 1 Me (Leya et al., 2000) and near the surface of meteoroids. Neutron capture occurs in the epithermal to thermal energy ranges (0.025 eV- 10 keV) and its effects are greater deeper in the meteoroid. Neutron capture affects Pt and isotopes important for short-lived dating systems (i.e.,  $^{182}\text{Hf}$ - $^{182}\text{W}$  and  $^{107}\text{Pd}$ - $^{107}\text{Ag}$ ; Masarik 1997, Leya and Masarik 2013). This indicates that Pt isotopes are important dosimeters for quantifying neutron capture effects on other isotopes (Kruijjer et al., 2013, Kruijjer et al., 2014, Matthes et al., 2015, Wittig et al., 2013). For example, the short-lived  $^{182}\text{Hf}$ - $^{182}\text{W}$  decay system is an important chronometer to constrain the timing of metal-silicate separation in the early solar system. However, the W isotope data are affected by both the ingrowth of radiogenic  $^{182}\text{W}$  and exposure to GCR (e.g., Kleine et al., 2005, Markowski et al., 2006). Platinum isotopes can be applied to monitor and correct for GCR-induced W isotope shifts, such that reliable  $^{182}\text{Hf}$ - $^{182}\text{W}$  ages are obtained (Kruijjer et al., 2013, Kruijjer et al., 2014, Wittig et al., 2013). In this approach, 'pre-GCR exposure' W isotope ratios are determined by empirical correlation of GCR-induced offsets in W and Pt isotopes, thereby allowing the determination of precise and accurate metal-silicate separation ages. Additionally, Pt isotopes can be used for the correction of neutron capture-induced effects to various elements (e.g., Ru and Pd) to allow for the accurate assessment of nucleosynthetic isotope variations (Ek et al., 2017, Fischer-Gödde et al., 2015, Fischer-Gödde and Kleine 2017, Mayer et al., 2015).

Additionally, Pt isotopes can help to determine the nucleosynthetic sources of solar system materials and the potential heterogeneous distribution of material from these sources in our solar system. Elements heavier than Fe, including Pt, are mainly produced by neutron capture reactions (*s*- and *r*-processes; Table 1) that take place during the final stages of a stars' lifetime. Since Pt isotopes are produced by different nucleosynthetic processes (Table 1), they are useful for assessing the mechanisms that affected the delivery and distribution of these nuclides in our solar system. This includes (i) the heterogeneous injection of new material and inefficient mixing during the early evolution of our solar system (Dauphas et al., 2004, Vanhala and Boss 2002), and (ii) processing of presolar dust carrying unique nucleosynthetic signatures in the protoplanetary disk (Akram et al., 2015, Burkhardt et al., 2012, Mayer et al., 2015, Trinquier et al., 2009). Previous Pt isotope studies indicate *s*- and *r*-process homogeneity between different iron meteorite groups, within analytical uncertainty (Kruijjer et al., 2013, Kruijjer et al., 2014, Peters et al., 2015, Wittig et al., 2013). This corresponds well to studies of other heavy nuclides such as Hf and Os (Sprung et al., 2010, Walker 2012). However, lighter nuclides such as Pd, Ru and Zr show nucleosynthetic isotope variations (Akram et al., 2013, Akram et al., 2015, Fischer-Gödde et al., 2015, Fischer-Gödde and Kleine 2017, Mayer et al., 2015), potentially suggesting a decoupling of stellar sources between these two groups of elements (i.e., Akram et al., 2013). Moreover, the low-abundance isotope  $^{190}\text{Pt}$  is a *p*-process, or proton-rich, isotope. These form in supernova environments and can yield information on the addition of supernovae components to the solar system (Table 1). To date, however, very few published data exist for  $^{190}\text{Pt}$  (Peters et al., 2015).

For GCR and nucleosynthetic studies, the combined determination of Pt isotopes with those of other elements, such as Pd, on the same sample aliquot is very beneficial. For example, these combined analyses are crucial to determine whether the nucleosynthetic decoupling of light and heavy nuclides is a true feature and not an artefact due to local sample heterogeneity. Similarly, because GCR effects vary with sample depth, correlated Pd and Pt isotope analyses from the same sample aliquot are vital for the

interpretation of neutron capture in meteorites (Ek et al., 2017, Mayer et al., 2015). Only correlated data allow for discrimination between GCR and nucleosynthetic contributions to Pd isotopes in iron meteorites. Additionally, analysing Pt and Pd on the same aliquot of a meteorite consumes less of these precious materials.

To be useful, a separation scheme must isolate Pt from Ir nearly quantitatively, because Ir isotopes can tail onto Pt during mass spectrometry (Kruijer et al., 2013, Peters et al., 2015, Wittig et al., 2013). Furthermore, Ir isotopes can generate isobaric interferences on Pt isotopes in the form of hydrides. It is also vital to eliminate isobaric interferences from Os isotopes. In particular, the high relative abundances of  $^{191}\text{Ir}$  (37.3 %),  $^{190}\text{Os}$  and  $^{192}\text{Os}$  (26.26 and 40.78 %, respectively; Table 1) render accurate and precise measurements of  $^{190}\text{Pt}$  and  $^{192}\text{Pt}$  impossible if these elements are not removed to an appropriate level.

Current methods for Pt purification either are not optimised for the collection of both Pt and Pd (Creech et al., 2014, Kruijer et al., 2013, Peters et al., 2015, Wittig et al., 2013), or do not purify Pt from Ir well enough for accurate isotopic analysis (Rehkamper and Halliday 1997). Here we present a new analytical method that allows the extraction of both Pt and Pd from iron meteorites. The further Pd purification and the determination of high precision Pd isotope data by multi-collector inductively-coupled plasma mass spectrometry (MC-ICP-MS) are described in a companion study (Ek et al., 2017). Here, we focus on Pt isotope analyses and the separation of Pt from Pd, Ir and Os in preparation for measurement by MC-ICP-MS. The accuracy and precision of our method is verified using IIAB and IVB iron meteorites and a synthetic standard.

## **A.2. Methods**

### A.2.1. Reagents and materials

During the course of this study, double Teflon-distilled hydrochloric (HCl) and nitric ( $\text{HNO}_3$ ) acids were used. Concentrated HCl is  $\sim 9.8 \text{ mol l}^{-1}$ , while concentrated  $\text{HNO}_3$  is  $\sim 14.2 \text{ mol l}^{-1}$ . Acids were routinely titrated before use. All  $\text{H}_2\text{O}$  used was MQ grade ( $\geq 18.2 \text{ M}\Omega\cdot\text{cm}$ ). Saturated bromine solutions ('bromine water') were prepared using Merck Millipore Bromine 99.9999 % SUPRAPUR<sup>®</sup>. The bromine solution was first cleaned by repeatedly adding and decanting MQ  $\text{H}_2\text{O}$ , before producing the final saturated bromine-water solution. The Br-water solution was freshly mixed prior to each ion exchange chemistry and used within 24 hours. Ascorbic acid ( $\text{C}_6\text{H}_8\text{O}_6$ ) from Sigma Aldrich as FLUKA L-ascorbic acid powder (TraceSELECT<sup>®</sup>), hydrogen peroxide ( $\text{H}_2\text{O}_2$ ; 30% Suprapur<sup>®</sup>) from Merck Millipore, perchloric acid (70% Suprapur<sup>®</sup>) from Merck Millipore and FLUKA analytical grade ethanol absolut ( $\leq 99.8 \%$ ) from Sigma Aldrich were also used.

All anion exchange procedures utilised Biorad AG<sup>®</sup> 1-X8 (200 – 400 mesh, chloride form). The resin was batch cleaned with 5x the resin volume of  $0.8 \text{ mol l}^{-1} \text{ HNO}_3$ , followed by the same quantities of  $3 \text{ mol l}^{-1} \text{ HNO}_3$ , concentrated  $\text{HNO}_3$ ,  $3 \text{ mol l}^{-1} \text{ HNO}_3$ , MQ,  $4 \text{ mol l}^{-1} \text{ HCl}$ , concentrated HCl, and finally  $6 \text{ mol l}^{-1} \text{ HCl}$ .

### A.2.2. Geological materials

Two IVB iron meteorites (Santa Clara and Tawallah Valley), plus North Chile (IIAB, our in-house reference material) were analysed. All samples were taken from the meteorite collection housed at ETH Zürich. Iron meteorites were prepared using a CBN blade fitted to a Buehler Isomet<sup>™</sup> low speed saw, operated with ethanol as the cooling fluid. Samples were then abraded with silicon carbide paper to remove any

remaining weathering and fusion crust, and to polish cut surfaces. The new analytical technique was also tested with Fe-Ni powders (Alfa Aesar, Puratronic® 99.999 %) doped with additional elements to match an iron meteorite composition, including Pt, Ir and Pd (30  $\mu\text{g g}^{-1}$  each). The synthetic iron meteorites had initial Ir/Pt ratios of 1.0, which models the most extreme ratios expected in iron meteorites (Campbell and Humayun 2005).

#### A.2.3. Sample digestion

All materials were digested in pre-cleaned Savillex™ Teflon beakers in Class 10 (iso 4) laminar flow hoods within a Class 1000 (iso 6) clean laboratory environment. Once in the clean laboratory environment, samples were placed in ethanol in the ultrasonic bath for 5 minutes, before leaching for 5 minutes in cold 2 mol l<sup>-1</sup> HCl prior to weighing and digestion. Samples were digested in a 2:1 mix of concentrated HNO<sub>3</sub> and HCl (~8 ml g<sup>-1</sup> of sample), and refluxed on the hotplate for ~48 hours at 100 °C. They were treated in an ultrasonic bath at least twice during this period. Once dried, all samples were taken up in concentrated HCl and refluxed overnight. At this stage the solution was clear, indicating that no undigested sample material remained in the beaker.

#### A.2.4. Ion exchange chromatography

*Pt-Pd separation (first ion exchange column).* The first anion exchange chemistry (Pt-Pd separation) is based on method 1 of Rehkamper and Halliday (1997). Up to 0.3 g of sample per column was taken from the digested mass. Each aliquot was refluxed in a 2:1 mix of concentrated HNO<sub>3</sub> and HCl for ~ 48 hours at 100-110 °C. Next, the samples were dried and taken up in 10 ml 0.5 mol l<sup>-1</sup> HCl + 10 % Br-water. Bromine water is an oxidant that is used throughout the early stages of the first procedure to keep Ir in its oxidised (Ir<sup>+4</sup>) state (Rehkamper and Halliday 1997). Samples were refluxed in this mixture overnight at 100-110 °C, and treated in the ultrasonic bath at least once during this period.

Quartz glass columns with an internal diameter of 6 mm were used during this study. The resin was supported by quartz glass wool (5- 30  $\mu\text{m}$  fibre thickness). Columns were loaded with 1.25 ml of pre-cleaned AG1-X8 resin. The resin was further cleaned on the column before the separation procedure was carried out (steps 1-4, Table 2). Prior to the anion separation procedure the samples were removed from the hotplate and allowed to cool. The resin was pre-conditioned with 8 ml 0.5 mol l<sup>-1</sup> HCl + 10 % Br-water. The samples were then loaded, followed by 12 ml 1 mol l<sup>-1</sup> HCl + 10 % Br-water, and 5.5 ml of 0.8 mol l<sup>-1</sup> HNO<sub>3</sub> + 10 % Br-water (Fig. 1a). Next, concentrated HCl was added to remove as much Ru as possible before Pd elution. Palladium was subsequently eluted in 10 ml of 8 mol l<sup>-1</sup> HNO<sub>3</sub>. This step was loaded in five 2 ml increments and performed using acid heated to 80 – 90 °C to aid efficient Pd elution (Rehkamper and Halliday 1997). Finally, Pt was removed from the column in 14 ml of 13.5 mol l<sup>-1</sup> HNO<sub>3</sub>. A clean-up fraction consisting of 10 ml of concentrated HNO<sub>3</sub> was collected to verify whether Pt and Pd were fully eluted. The Pd fraction was then further processed for high precision Pd isotope analyses according to Ek et al., (2017), while the Pt elution was purified to remove Ir and Os, as described below.

*Pt-Ir separation.* Two methods for Pt-Ir separation are presented. For both methods, Pt fractions from the first column were evaporated, re-dissolved in a 2:1 mixture of concentrated HNO<sub>3</sub> and HCl (1.5 ml) and refluxed for 48 hours at 100 °C. Samples were then dried down, taken up in 2.5 ml 1 mol l<sup>-1</sup> HCl and refluxed overnight at 120 °C. Pre-cleaned AG1-X8 resin (1 ml) was loaded into the columns and cleaned again (Steps 1-4, Table 3).

*Pt-Ir separation: Method 1 (ascorbic acid).* Iridium was reduced by adding ascorbic acid before loading the sample onto the column. Prior to loading onto the columns, the samples were removed from the hotplate and allowed to cool before being diluted to 5 ml 0.5 mol l<sup>-1</sup> HCl – 0.1 mol l<sup>-1</sup> ascorbic acid. Samples were shaken thoroughly and allowed to stand for ~ 30 minutes before loading. During this time the columns were preconditioned with 8 ml 0.5 mol l<sup>-1</sup> HCl. The sample was then loaded onto the resin and matrix elements were eluted with 10 ml of 0.5 mol l<sup>-1</sup> HCl. Iridium was then stripped from the column using 20 ml 2 mol l<sup>-1</sup> HCl. Finally, Pt was eluted in 30 ml of 13.5 mol l<sup>-1</sup> HNO<sub>3</sub> (Table 3; Fig. 1b).

*Pt-Ir separation: Method 2 (hydrogen peroxide).* The breakdown of H<sub>2</sub>O<sub>2</sub> to O<sub>2</sub> can act as a weak reducing agent (e.g., Song and Zhang 2008), and this was utilised to reduce Ir in method 2 (Table 3; Fig. 1c). The samples were diluted to 5 ml 0.5 mol l<sup>-1</sup> HCl and the columns were preconditioned with 8 ml 0.5 mol l<sup>-1</sup> HCl. After sample loading, the columns were rinsed with 10 ml 0.5 mol l<sup>-1</sup> HCl, and 20 ml 0.5 mol l<sup>-1</sup> HCl – 1 % H<sub>2</sub>O<sub>2</sub> to reduce the Ir. Iridium was subsequently eluted in 2 mol l<sup>-1</sup> HCl. Finally, as in method 1, Pt was collected in 30 ml of 13.5 mol l<sup>-1</sup> HNO<sub>3</sub>. Depending on the initial Ir/Pt ratio of the sample, the ion exchange column (method one or two) was repeated to achieve the required separation of these elements.

Total procedural blanks for the entire chemical separation procedure were typically in the range 0.1 – 0.3 ng of Pt per 0.3 g sample, and are therefore negligible (Pt in samples, 6.6 – 9.0 µg per 0.3 g of iron meteorite sample; Campbell and Humayun 2005, Wasson et al., 2007). The blank contribution to Pd after the first column is 0.05 – 0.4 ng of Pd per 0.3 g sample.

#### A.2.5 Preparation for Mass Spectrometry

*Isotopic Analysis.* After Ir is adequately separated from Pt, remaining Os is removed from the sample to achieve accurate isotopic data. This was accomplished through volatilisation of Os by repeated drying with HClO<sub>4</sub> (Kruijer et al., 2013, Peters et al., 2015). To this end, Pt fractions were dried and then taken up in 0.5 ml of 2:1 HNO<sub>3</sub> and HCl. Samples were refluxed overnight at 100 °C and then cooled. Next, 50 µl HClO<sub>4</sub> was added to each beaker and the samples were dried. During drying the temperature was increased incrementally to ~ 205 °C, and held there until all HClO<sub>4</sub> was evaporated. This procedure was

**Table A.2.** Platinum-Palladium separation procedure (first column procedure).

Step		Acid	Volume (ml)	Elements eluted
1.	Resin cleaning	0.8 mol l <sup>-1</sup> HNO <sub>3</sub>	20	
2.	Resin cleaning	concentrated HCl	10	Pd
3.	Resin cleaning	concentrated HNO <sub>3</sub>	25	Pt, Pd and Ir
4.	Reconversion of resin to chloride form	6 mol l <sup>-1</sup> HCl	40	
5.	Precondition	0.5 mol l <sup>-1</sup> HCl + 10 % Br-water	8	
6.	Loading and matrix elution	0.5 mol l <sup>-1</sup> HCl + 10 % Br-water	10	Fe, Ni, Co, Cr, W
7.	Matrix elution	1 mol l <sup>-1</sup> HCl + 10 % Br-water	12	Fe, Ni, Co, Cr, minor Ru elution.
8.	Matrix elution	0.8 mol l <sup>-1</sup> HNO <sub>3</sub> + 10 % Br-water	5.5	Zn, Cd. Limited elution of Ir.
9.	Matrix elution	concentrated HCl	12	Ag, Ru
10.	Pd elution	8 mol l <sup>-1</sup> HNO <sub>3</sub> (80 – 90 °C)	10	Pd with Ru and trace Fe, Ni, Cr.
11.	Pt elution	13.5 mol l <sup>-1</sup> HNO <sub>3</sub>	14	Pt with Ir and trace Fe, Ni, Cr.

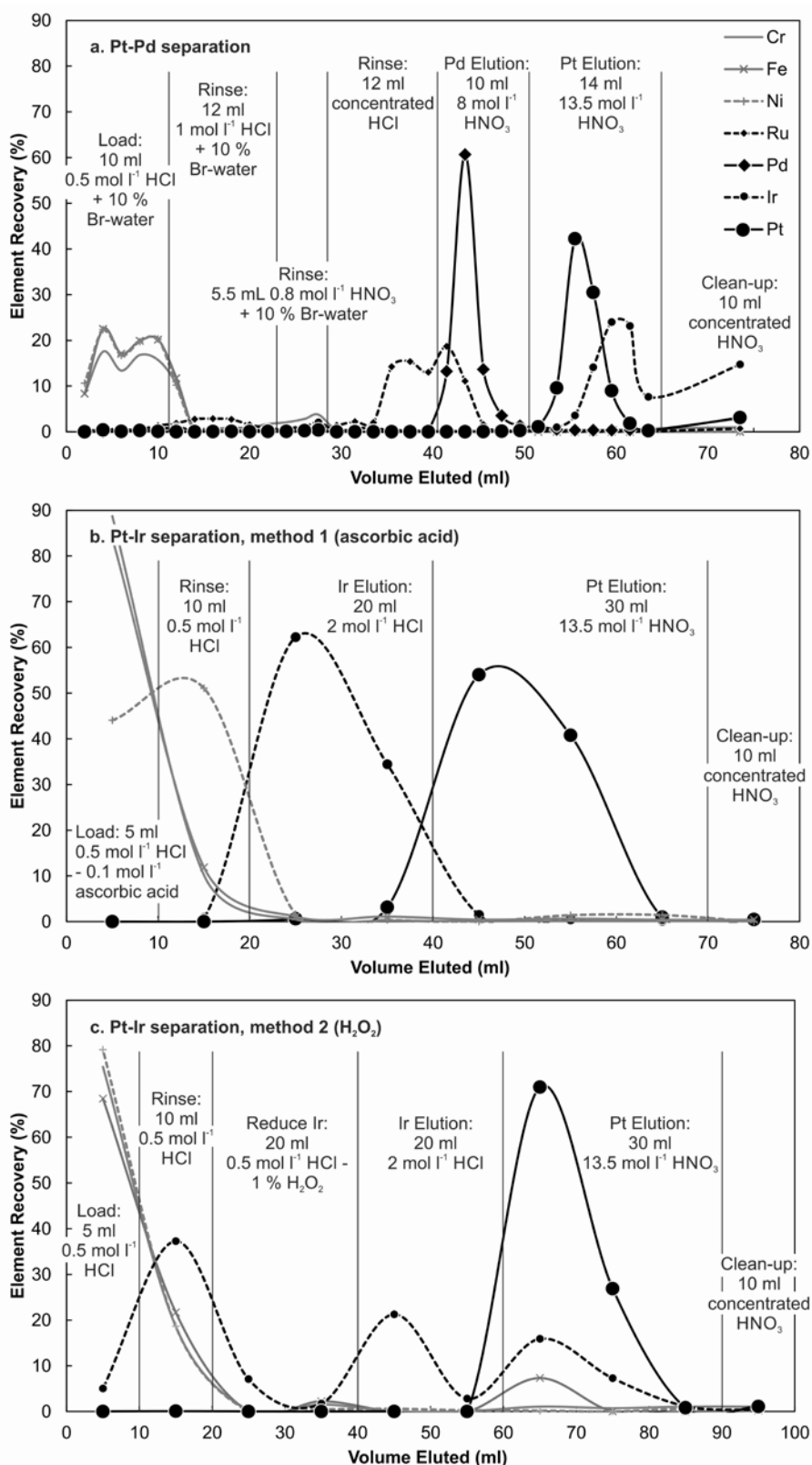


**Figure A.1.** Elution curves for (a) the Pt-Pd separation, (b) the Ir-Pt separation procedure utilising ascorbic acid as a reducing agent (method 1), and (c) the Ir-Pt separation procedure using H<sub>2</sub>O<sub>2</sub> as a reducing agent (method 2). Elution curves were produced using a synthetic sample with a composition based on an iron meteorite. The starting Ir/Pt ratio for the Pt-Pd separation was 1.0. Both Ir-Pt separation procedures used a starting composition with an Ir/Pt ratio of 0.77, which is based on the Pt fraction eluted during the Pt-Pd separation.

repeated until the desired Os/Pt was reached, typically 3- 4 times. After treatment with HClO<sub>4</sub>, the sample was refluxed overnight in 0.5 ml of 2:1 HNO<sub>3</sub> and HCl and then dried, before being briefly re-dissolved in 0.5 ml of 5 mol l<sup>-1</sup> HNO<sub>3</sub> and dried again. Finally, samples were taken up in 5 mol l<sup>-1</sup> HNO<sub>3</sub> and diluted to 0.5 mol l<sup>-1</sup> HNO<sub>3</sub> before isotopic analysis.

*Concentration Analysis.* Samples for concentration analyses were dried down after column chemistry. They were then refluxed and dried with 0.5 ml aqua regia, followed by 0.5 ml HNO<sub>3</sub>. Finally, samples were taken up in 5 mol l<sup>-1</sup> HNO<sub>3</sub> and refluxed overnight, before being diluted to 0.5 mol l<sup>-1</sup> HNO<sub>3</sub> for analysis.

#### A.2.6 Mass spectrometry

*Isotopic Analysis.* Platinum isotope analyses were performed at ETH Zürich using a Thermo Scientific Neptune Plus fitted with a Cetac Aridus II desolvating nebuliser and standard H cones. The machine was operated in low-resolution mode. All Pt isotopes were collected simultaneously, along with <sup>188</sup>Os and <sup>200</sup>Hg to apply corrections for isobaric interferences, and <sup>191</sup>Ir in order to assess Ir tailing effects onto Pt isotopes (Table 4). Two 10<sup>12</sup> Ω resistors were employed for collecting <sup>188</sup>Os and <sup>190</sup>Pt. All other isotopes were collected with 10<sup>11</sup> Ω resistors.

Detector gain was measured daily before each analytical session. An on-peak baseline (OPB) was collected before each measurement. The OPB was measured as a reference, but was not subtracted during the data reduction described here (see discussion below). For samples and standards, each measurement included a peak centre and a 30 s electronic baseline before 60 integrations of 8.4 s. Samples were bracketed by the NIST SRM 3140 Pt standard solution, and the concentration of sample and bracketing standard was matched to better than 10 %. Between each sample and standard, 0.5 mol l<sup>-1</sup> HNO<sub>3</sub> was introduced to reduce the Pt background of the sample introduction system.

Samples and standards were diluted to give a ~2 x 10<sup>-10</sup> A ion beam for <sup>194</sup>Pt. This equates to ~300 ng g<sup>-1</sup> Pt and indicates a sensitivity of ~200 V µg g<sup>-1</sup> for Pt. Each analysis consumed 0.9 – 1.2 ml of solution using a nebuliser with an uptake rate of ~100 µl min<sup>-1</sup>, therefore requiring ~300 ng Pt per analysis.

**Table A.3.** Platinum-Iridium separation procedures (methods 1 and 2; second column procedure).

Step		Acid	Volume (ml)	Elements eluted
1.	Resin cleaning	0.8 mol l <sup>-1</sup> HNO <sub>3</sub>	20	
2.	Resin cleaning	concentrated HCl	10	Pd
3.	Resin cleaning	concentrated HNO <sub>3</sub>	25	Pt, Pd and Ir
4.	Reconversion of resin to chloride form	6 mol l <sup>-1</sup> HCl	40	
<b>Method 1</b>				
5.	Precondition	0.5 mol l <sup>-1</sup> HCl	8	
6.	Load	0.5 mol l <sup>-1</sup> HCl – 0.1 mol l <sup>-1</sup> ascorbic acid	5	Fe, Ni
7.	Rinse	0.5 mol l <sup>-1</sup> HCl	10	Cr, Ni, Fe
8.	Ir elution	2 mol l <sup>-1</sup> HCl	20	Ir
9.	Pt elution	13.5 mol l <sup>-1</sup> HNO <sub>3</sub>	30	Pt with minor Ir
<b>Method 2</b>				
5.	Precondition	0.5 mol l <sup>-1</sup> HCl	8	
6.	Load	0.5 mol l <sup>-1</sup> HCl	5	Fe, Ni
7.	Rinse	0.5 mol l <sup>-1</sup> HCl	10	Cr, Ni, Fe
8.	Reduce Ir	0.5 mol l <sup>-1</sup> HCl – 1 % H <sub>2</sub> O <sub>2</sub>	20	
9.	Ir elution	2 mol l <sup>-1</sup> HCl	20	Ir
10.	Pt elution	13.5 mol l <sup>-1</sup> HNO <sub>3</sub>	30	Pt with minor Ir



Analyses were corrected for instrumental mass bias using the exponential law, and were internally normalized to  $^{198}\text{Pt}/^{195}\text{Pt}$  ('8/5') = 0.2145 (Kruijer et al., 2013). Mercury interferences were first corrected on  $^{198}\text{Pt}$  using  $^{200}\text{Hg}/^{198}\text{Hg} = 2.31695$  (Berglund and Wieser 2011). The corrected  $^{198}\text{Pt}$  was then used for the internal normalisation and interference corrections. Mercury-196 was also stripped off  $^{196}\text{Pt}$ . The Os interference on  $^{192}\text{Pt}$  was corrected using  $^{188}\text{Os}/^{192}\text{Os} = 0.32467$  (Berglund and Wieser 2011). Finally, a  $2\sigma$  rejection criteria was applied to the 60 corrected cycles. All data are presented in the epsilon notation (i.e.,  $\epsilon^{191}\text{Pt}/^{195}\text{Pt}$  = deviation in parts per 10,000 from the average of the two bracketing standards).

*Concentration Analysis.* Eluates from the column calibration were analysed using either a Thermo Scientific Element XR (Pt-Pd separation, Ir-Pt separation method 2) or a Perkin Elmer Elan DRC-e ICP quadrupole mass spectrometer (Ir-Pt separation method 1) at ETH Zürich. The Thermo Scientific Element XR was operated with standard H cones and a wet plasma introduction system. Platinum group elements were analysed in low resolution mode; other elements (including Cr, Fe and Ni) were measured in medium resolution. The Perkin Elmer Elan DRC-e ICP was operated using a Scott spray chamber. In both cases, analyses were standardised using synthetic solutions. The reproducibility of both techniques is better than 5 % (2 RSD).

### A.3. Results and Discussion

#### A.3.1. Ion Exchange chemistry

*Pt-Pd separation.* The first ion exchange column separated Pt and Pd from each other and removed the majority of matrix elements (Fig. 1a; Table 2). Platinum yields from iron meteorites after this column were variable and ranged from 50 to 90 %, but were typically 70 – 90 %. Low yields were a result of early Pt elution into the Pd fraction, or Pt not adsorbing to the resin during loading. We routinely collected an additional clean-up fraction of 10 ml concentrated  $\text{HNO}_3$  at the end of the column procedure and these fractions contained only 1 % of the Pt load. Yields for Pd from iron meteorites after the first column were usually  $\sim 70$ - 80 %, but could be as low as 50 %. Palladium often showed peak tailing into the Pt elution, which reduced the Pd yields. Up to 20 % of the Pd was eluted with Pt, and a further 8 % was routinely present in the clean-up fraction. Tests with synthetic meteorites (Fe and Ni powders doped with PGE standards) always yielded close to 100 % for both Pt and Pd. This suggests that the oxidation state of both Pt and Pd before the column chemistry is important for the yield. Therefore, samples were refluxed in inverse aqua regia for  $\sim 48$  hours before each column stage to try fully oxidise these elements and ensure that Pt and Pd were adsorbed to the resin during loading.

The volumes of the sample loading and first elution steps (steps 6 – 7, Table 2) are greater than those suggested by Rehkemper and Halliday (1997). Those authors utilised a sulfide fire-assay technique to pre-concentrate the PGEs, which removes the majority of the Fe matrix. This technique, however, results in relatively high blanks and variable yields for both Pt and Pd (Gros et al., 2002, Rehkemper and Halliday 1997, Ren et al., 2016), Furthermore, iron meteorites can be readily dissolved using a hotplate digestion, and therefore that method was chosen for this study. As a result more matrix elements were loaded on to our columns, and larger acid volumes were necessary to remove these elements (Table 2).

**Table A.4.** Cup configuration used for Pt isotope measurements on the Neptune *Plus*.

Cup	L4	L3	L2	L1	C	H1	H2	H3	H4
Isotope	$^{188}\text{Os}$	$^{190}\text{Pt}$	$^{191}\text{Ir}$	$^{192}\text{Pt}$	$^{194}\text{Pt}$	$^{195}\text{Pt}$	$^{196}\text{Pt}$	$^{198}\text{Pt}$	$^{200}\text{Hg}$
Resistor	$10^{12}$	$10^{12}$	$10^{11}$	$10^{11}$	$10^{11}$	$10^{11}$	$10^{11}$	$10^{11}$	$10^{11}$

Additionally, the samples were loaded in 10 ml 0.5 mol l<sup>-1</sup> HCl – 10 % Br<sub>2</sub> (instead of 5 – 10 ml 1.0 mol l<sup>-1</sup> HCl – 10 % Br<sub>2</sub>; Rehkamper and Halliday 1997) because the partition coefficient for Fe on strong anion exchange resin decreases with decreasing HCl concentration, while those for Pt and Pd increase (Kraus and Nelson 1956). Hence, lowering the acid concentration improves the separation of these elements.

Iridium and Pt were not well separated after this first stage of ion exchange chemistry. Iridium elution in the Pt fraction was ~60- 80 % of the total Ir (with Ir/Pt ranging from ~0.2 to 0.8). The poor separation of Ir from Pt is partly due to the use of bromine water. Bromine water acts to keep Ir oxidised, and thus retained by the column until rinsed with concentrated HNO<sub>3</sub> (Rehkamper and Halliday 1997). Without the use of bromine water the fraction of Ir eluted with Pt is ~ 10 % lower. Bromine water, however, aids in the elution of Pd by narrowing the Pd elution peak and reducing some of the tailing problems associated with this element, increasing the Pd yield by up to 10 %.

*Pt-Ir separation.* For the further purification of Pt from Ir, a second ion exchange column was developed. Accurate Pt isotope analyses by MC-ICP-MS rely on low Ir contents in the analysed Pt fraction. This is achieved by utilising the weak affinity of Ir<sup>3+</sup> for strong anion resin (Kraus and Nelson 1956). Once Ir<sup>4+</sup> has been reduced to Ir<sup>3+</sup>, it can be efficiently eluted from the column with HCl before Pt (Anbar et al., 1997, Pearson and Woodland 2000). Sulfurous acid and ascorbic acid were used previously for Ir reduction (Anbar et al., 1997, Wittig et al., 2013). We tested ascorbic acid (method 1; Fig. 1b) and H<sub>2</sub>O<sub>2</sub> (method 2; Fig. 1c). Iridium elution in the Pt fraction can be decreased to between 2- 15 % of the total Ir using ascorbic acid as a reducing agent, and ~25 % when using H<sub>2</sub>O<sub>2</sub>. These results indicate that ascorbic acid is the more effective reducing agent, while in both cases, 70- 100 % of the Pt is retained. Yields for Pt for the full ion exchange column are 50 – 70 %. In both method 1 and method 2 the column is rinsed with 0.5 mol l<sup>-1</sup> HCl after the sample is loaded, which elutes remaining matrix elements to the extent that they are absent or insignificant during MC-ICP-MS analysis. Method 1 (ascorbic reduction) was chosen as our primary technique because of the better Ir separation. Therefore, all samples and standards for isotope analysis were processed following this procedure.

*Os volatilisation.* Osmium is near-quantitatively removed during the two-stage ion exchange procedure. However, a final stage of evaporation in a mixture of inverse aqua regia and perchloric acid at ≥180 °C was necessary to allow precise ε<sup>192</sup>Pt measurements. This procedure was typically repeated 3 – 4 times until <sup>188</sup>Os/<sup>195</sup>Pt < 3 x 10<sup>-5</sup> (see discussion of this value below). An additional benefit of drying the samples in HClO<sub>4</sub> is the destruction of organic molecules. These result from the use of (i) high molarity HNO<sub>3</sub>, which can attack and release the organics from the resin (e.g., Schönbacher and Fehr 2014); and (ii) ascorbic acid.

### A.3.2. High Precision Pt isotope measurements

*Interfering elements and corrections.* Doping tests were performed to determine the level of interfering elements that can be tolerated for accurate and precise analyses. Osmium is a significant interference in the measurement of ε<sup>192</sup>Pt and must be removed so that <sup>188</sup>Os/<sup>195</sup>Pt < 3 x 10<sup>-5</sup> (Fig. 2). Below this level, doping tests show that an accurate correction for the isobaric interference from <sup>192</sup>Os on <sup>192</sup>Pt is possible. For a <sup>188</sup>Os/<sup>195</sup>Pt ratio of 3 x 10<sup>-5</sup>, the correction to ε<sup>192</sup>Pt is ~41 ε. The <sup>188</sup>Os/<sup>195</sup>Pt ratio of the IVB iron meteorites after the chemical separation procedure was always significantly lower and required Os corrections to ε<sup>192</sup>Pt in the range of 1.3 – 3.1 ε.

Mercury was not detected above the background level in any sample, although Hg can be present in the Ar gas used by the mass spectrometer (e.g., Thirlwall 2002). A minor correction for Hg was applied by peak-stripping during the data reduction process (correction to  $\epsilon^{196}\text{Pt} < 0.02$ ; see the 'Mass Spectrometry section'). In addition, an OPB was measured before each analysis of a sample or bracketing standard to subtract background Hg. Data were processed both with and without the subtraction of this OPB. This correction did not result in an improvement to ratios where Hg interferences were present, because background Hg levels were extremely low ( $^{200}\text{Hg} < 0.1$  mV). At the same time, background Os is negligible but small variations in the OPB measurements resulted in inaccuracies to the Os correction applied to  $^{192}\text{Pt}$  when the OPB was subtracted. The subtraction of the OPB increased the scatter (2 SD) of  $\epsilon^{192}\text{Pt}$  from  $\sim 0.75$  to  $\sim 0.90$  for the bracketing standard Pt SRM 3140. For this reason, the data presented here were not corrected with the OPB.

Tailing from Ir isotopes onto Pt isotopes also presents a significant challenge during Pt isotope analysis. This is because the high-abundance isotopes  $^{191}\text{Ir}$  (37.3 %) and  $^{193}\text{Ir}$  (62.7 %) produce tailing on the adjacent  $^{192}\text{Pt}$  peak (0.78 %) (Kruijer et al., 2013, Peters et al., 2015, Wittig et al., 2013). This results in a perceived excess of  $^{192}\text{Pt}$ . To a lesser degree, this effect is also present on  $^{194}\text{Pt}$  (32.86 %). Additionally, Ir can generate hydride interferences on Pt isotopes, which is less of a concern for this study because the samples were analysed with a desolvating nebuliser. Tests using Pt standard solutions doped with various amounts of Ir demonstrate the combined effect of Ir tailing and hydride formation on  $\epsilon^{192}\text{Pt}$  (Fig. 3). For  $^{191}\text{Ir}/^{195}\text{Pt}$  ratios of 0.28 or more, excesses of at least 1  $\epsilon$  can be induced on  $\epsilon^{192}\text{Pt}$ . Furthermore, the addition of Ir suppresses the Pt signal. To ensure that no corrections for Ir tailing were necessary, samples were passed through the second ion exchange column until a  $^{191}\text{Ir}/^{195}\text{Pt}$  ratio of  $< 0.2$  (equivalent to an Ir/Pt ratio of  $< 0.13$ ) was achieved. For samples with initial elemental Ir/Pt ratios of  $< 0.5$ , this was usually achieved after a single column pass. After two repeats, all samples displayed  $^{191}\text{Ir}/^{195}\text{Pt}$  ratios  $< 0.2$ , and usually lower than 0.1. However, care must be taken as the magnitude of Ir tailing can vary between analytical sessions with instrument settings. Pressure in the back-end of the mass spectrometer should

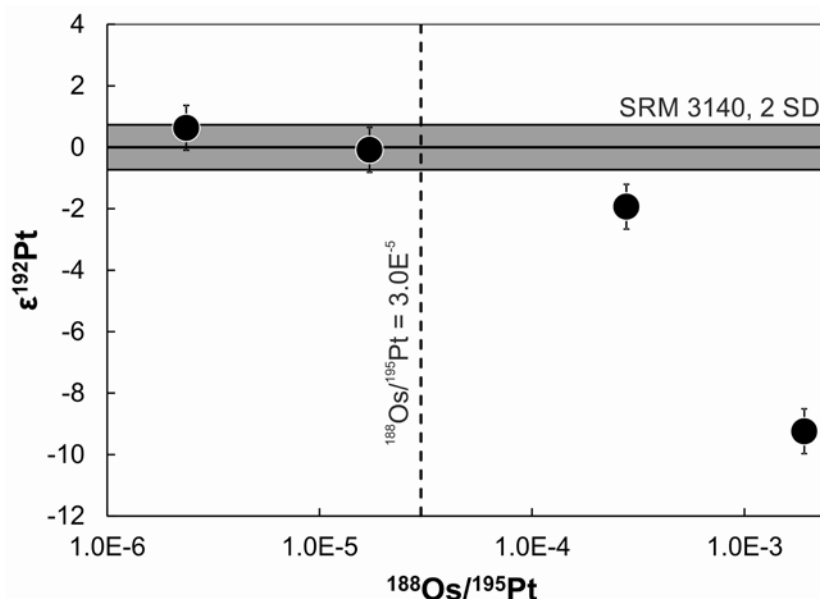


**Figure A.2.** The  $^{188}\text{Os}/^{195}\text{Pt}$  ratios relative to  $\epsilon^{192}\text{Pt}$  for standard solutions doped with Os. Platinum ratios are corrected for Os interferences. The results indicate that the  $^{188}\text{Os}/^{195}\text{Pt}$  ratio must be below  $3 \times 10^{-5}$  to obtain accurate Pt isotope data. Grey bar represents the 2 SD daily uncertainty of the Pt bracketing NIST SRM 3140 standard. Individual measurement uncertainties are based on the 2 SD obtained from repeat analyses of North Chile (in-house standard; Table 5).

also be monitored carefully and additional doping tests performed as necessary, particularly for samples that are close to the  $^{191}\text{Ir}/^{195}\text{Pt}$  threshold.

Other major molecular interferences on Pt isotopes in iron meteorites may arise from W ( $\text{WC}^+$ ,  $\text{WN}^+$ ,  $\text{WO}^+$ ) or Au ( $\text{AuH}^+$ ). Our new ion exchange procedure essentially completely removes these elements. Occasionally, trace levels of W were detected in the samples ( $^{183}\text{W}/^{195}\text{Pt}$  up to a maximum of 0.0003). However, W doping tests up to a  $^{183}\text{W}/^{195}\text{Pt}$  ratio of 0.0035 exhibited no offsets to any Pt isotope ratios. Iron and Ni are present at background levels in samples and are important to monitor. Nickel doping tests were conducted as part of this study and indicate that at high levels of Ni ( $^{60}\text{Ni}/^{195}\text{Pt} > 0.067$ ), a deficit of -0.6 on  $\epsilon^{192}\text{Pt}$  can be induced. However, this effect is not significant for our current study, where the  $^{60}\text{Ni}/^{195}\text{Pt}$  ratio was  $< 0.024$  in all samples analysed.

*Reproducibility and accuracy of Pt isotope measurements.* The typical daily 2 standard deviation (2 SD) reproducibility of the bracketing Pt standard SRM 3140 is  $\sim 0.75$  for  $\epsilon^{192}\text{Pt}$ , and 0.05 – 0.07 for both  $\epsilon^{194}\text{Pt}$  and  $\epsilon^{196}\text{Pt}$ . A more robust assessment of our reproducibility is given by repeated analysis of the IAB iron meteorite North Chile, which is used as an in-house reference material. Approximately 3 g of this sample was dissolved and four 0.3 g aliquots were independently passed through our chemical separation procedure. Nineteen measurements of this standard were performed over the course of six analytical sessions (Table 5 and Fig. 4). As this is a natural, non-terrestrial material, Pt isotope ratios are not expected to be within uncertainty of 0 (see discussion below), however, North Chile can be used to assess the reproducibility of our technique. The external reproducibility (2 SD) obtained for all four aliquots indicates the uncertainty of our analyses is 0.73 for  $\epsilon^{192}\text{Pt}$ , 0.15 for  $\epsilon^{194}\text{Pt}$  and 0.09 for  $\epsilon^{196}\text{Pt}$  (n=19). The 2 SD reproducibility for a single aliquot (North Chile A) analysed over five sessions is better, yielding 0.67 for  $\epsilon^{192}\text{Pt}$ , 0.06 for  $\epsilon^{194}\text{Pt}$  and 0.04 for  $\epsilon^{196}\text{Pt}$  (n=10). These data show that replicate analyses of samples processed through the entire analytical procedure yield a larger scatter (2 SD), particularly on  $\epsilon^{194}\text{Pt}$ , compared to replicate analyses of a single sample solution. This is likely due to the small, but variable, amount of matrix elements that remains in the purified sample solution after the ion exchange

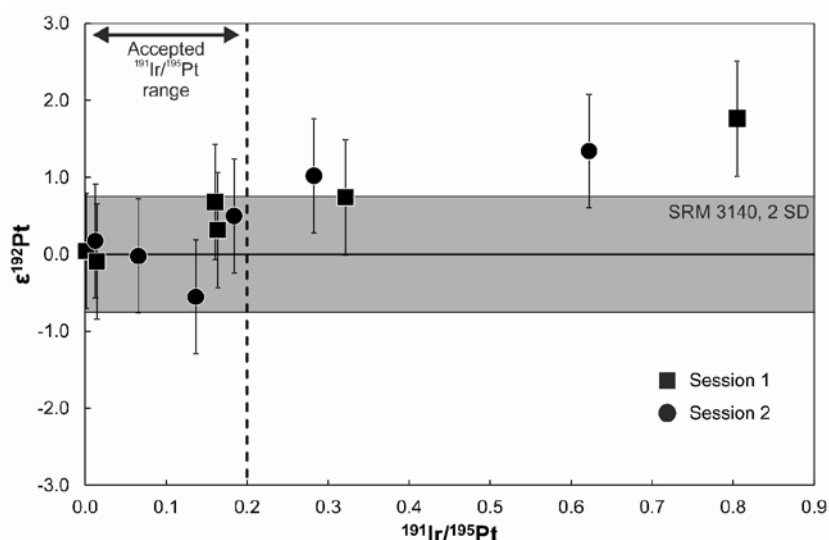


**Figure A.3.** The  $^{191}\text{Ir}/^{195}\text{Pt}$  ratios relative to  $\epsilon^{192}\text{Pt}$  for standard solutions doped with Ir. Iridium causes tailing on Pt isotopes. The results from two analytical sessions indicate that these effects are negligible for samples with  $^{191}\text{Ir}/^{195}\text{Pt}$  ratios of  $< 0.2$ . After processing through our new ion exchange procedure, natural samples analysed as part of this study showed very low  $^{191}\text{Ir}/^{195}\text{Pt}$  ratios of between 0.01 and 0.06. The grey bar represents the 2 SD daily uncertainty of the bracketing NIST SRM 3140 Pt standard. Individual measurement uncertainties are as in Fig. 2.

chemistry. Matrix elements remaining in Pt fractions for iron meteorites can include Ni (1- 8 ng per sample), Pd (up to 40 ng) and Fe (1- 5 ng per sample). Minor organic interferences may also remain from the use of ascorbic acid and from the ion exchange resin. Values for the overall uncertainty on  $\epsilon^{194}\text{Pt}$  and  $\epsilon^{196}\text{Pt}$  are similar to previous studies when comparing analyses with similar signal sizes (Kruijer et al., 2013, Kruijer et al., 2014, Wittig et al., 2013), although our reproducibility for  $\epsilon^{192}\text{Pt}$  is significantly improved compared to Kruijer et al., (2013, 2014) due to the lack of an Ir tailing correction required in our study.

To test the accuracy of our method, iron-nickel powders were doped with Pt SRM 3140 and passed through our column procedure. This yielded results that are within uncertainty of 0 for all ratios (Table 6; Fig. 4), indicating our new technique is accurate within the limits of our uncertainties. Additionally, the Pt reference material IRMM-010 was analysed relative the SRM 3140 standard solution (Table 6; Fig. 4). The results were identical within uncertainty to the SRM 3140 standard solution for all ratios ( $0.01 \pm 0.85$  for  $\epsilon^{192}\text{Pt}$ ,  $0.01 \pm 0.06$  for  $\epsilon^{194}\text{Pt}$  and  $0.00 \pm 0.05$  for  $\epsilon^{196}\text{Pt}$ ; uncertainties are 2 SD,  $n=10$ ).

Although the chemical purification procedure described here can also be used for the analysis of  $^{190}\text{Pt}$  (0.012 %), a different MC-ICP-MS set-up is necessary to perform those challenging measurements. Therefore, results for  $\epsilon^{190}\text{Pt}$  are not discussed further in this contribution.

**Table A.5.** Platinum isotope data for the North Chile meteorite.

	Yield <sup>a</sup>	$\epsilon^{192}\text{Pt}$	2 SE <sup>b</sup>	$\epsilon^{194}\text{Pt}$	2 SE <sup>b</sup>	$\epsilon^{196}\text{Pt}$	2 SE <sup>b</sup>
<b>North Chile A</b>	59 %						
10.03.2015		1.45	0.22	0.35	0.04	0.18	0.04
10.03.2015		1.29	0.21	0.30	0.04	0.18	0.04
07.05.2015		1.36	0.19	0.36	0.05	0.23	0.04
07.05.2015		0.71	0.19	0.36	0.05	0.21	0.04
08.05.2015		0.73	0.20	0.28	0.04	0.20	0.04
08.05.2015		1.12	0.18	0.35	0.03	0.20	0.03
15.12.2015		1.06	0.22	0.34	0.04	0.24	0.03
15.12.2015		0.67	0.18	0.35	0.04	0.17	0.03
15.12.2015		1.31	0.19	0.32	0.04	0.20	0.03
16.12.2015		0.54	0.18	0.36	0.04	0.21	0.03
<i>Mean (n = 10)</i>		<i>1.02</i>		<i>0.34</i>		<i>0.20</i>	
<i>2 SD</i>		<i>0.67</i>		<i>0.06</i>		<i>0.04</i>	
<b>North Chile B</b>	51 %						
07.05.2015		0.79	0.13	0.13	0.04	0.09	0.03
07.05.2015		1.34	0.14	0.14	0.04	0.07	0.03
<i>Mean (n = 2)</i>		<i>1.07</i>		<i>0.14</i>		<i>0.08</i>	
<b>North Chile C</b>	68 %						
15.12.2015		1.27	0.19	0.27	0.05	0.15	0.03
15.12.2015		0.22	0.17	0.24	0.04	0.18	0.04
15.12.2015		0.57	0.20	0.26	0.04	0.18	0.04
16.12.2015		1.01	0.17	0.22	0.04	0.12	0.03
16.12.2015		1.23	0.18	0.25	0.05	0.17	0.04
16.12.2015		1.50	0.21	0.19	0.04	0.15	0.03
<i>Mean (n = 6)</i>		<i>0.97</i>		<i>0.24</i>		<i>0.16</i>	
<i>2 SD</i>		<i>0.96</i>		<i>0.06</i>		<i>0.05</i>	
<b>North Chile D</b>	69 %						
29.06.2016		0.82	0.18	0.23	0.06	0.15	0.04
<b>External Reproducibility based on North Chile A, B, C and D:</b>							
Mean (n = 19)		1.00		0.28		0.17	
2 SD		0.73		0.15		0.09	

<sup>a</sup> Yield after column chemistry for each aliquot of North Chile. <sup>b</sup> Internal 2 standard error (SE) of each measurement.

### A.3.3. IVB iron meteorites

The Pt isotope compositions for the IVB irons Santa Clara and Tawallah Valley show positive offsets relative to the terrestrial standard for all three ratios (Table 7). In particular,  $\epsilon^{192}\text{Pt}$  varies between the two samples, with  $\epsilon^{192}\text{Pt}$  of  $15.36 \pm 0.71$  for Santa Clara, and  $7.37 \pm 0.32$  for Tawallah Valley. Platinum isotope differences between samples from the same iron meteorite groups have been attributed to the effects of GCR irradiation in space (Kruijjer et al., 2013, Kruijjer et al., 2014, Wittig et al., 2013). For example, neutron capture by  $^{195}\text{Pt}$  creates excess  $^{196}\text{Pt}$ . Furthermore, the magnitude of the offsets induced by GCR irradiation is related to both exposure time in space and the depth of a sample below the surface of a meteoroid (Leya and Masarik 2013). Large effects are also generated on  $\epsilon^{192}\text{Pt}$ , because  $^{191}\text{Ir}$  captures a neutron and subsequently  $\beta$ -decays to  $^{192}\text{Pt}$  (Leya and Masarik 2013). A similar reaction creates  $^{194}\text{Pt}$  from  $^{193}\text{Ir}$ . The Ir/Pt ratio of a sample is therefore important, particularly to the amount of  $^{192}\text{Pt}$  produced (Fig. 5a). North Chile has an Ir/Pt ratio of 0.16 (Wasson et al., 2007) and Pt isotope data fit well to GCR trends modelled with this value (Fig. 5). The Ir/Pt ratios of the IVBs are  $0.73 \pm 0.05$  for Santa Clara, and  $0.57 \pm 0.04$  for Tawallah Valley (ratios and 1SD uncertainties calculated from Campbell and Humayun 2005; these uncertainties are represented by grey areas on Fig. 5). Data for the IVBs, shown with those from previous studies for the same meteorites, fall within uncertainty of the modelled neutron capture trends for the stated Ir/Pt ratios (Leya and Masarik 2013; Fig. 5) and this supports the conclusion that Pt isotopes vary in iron meteorites as a result of exposure to GCR.

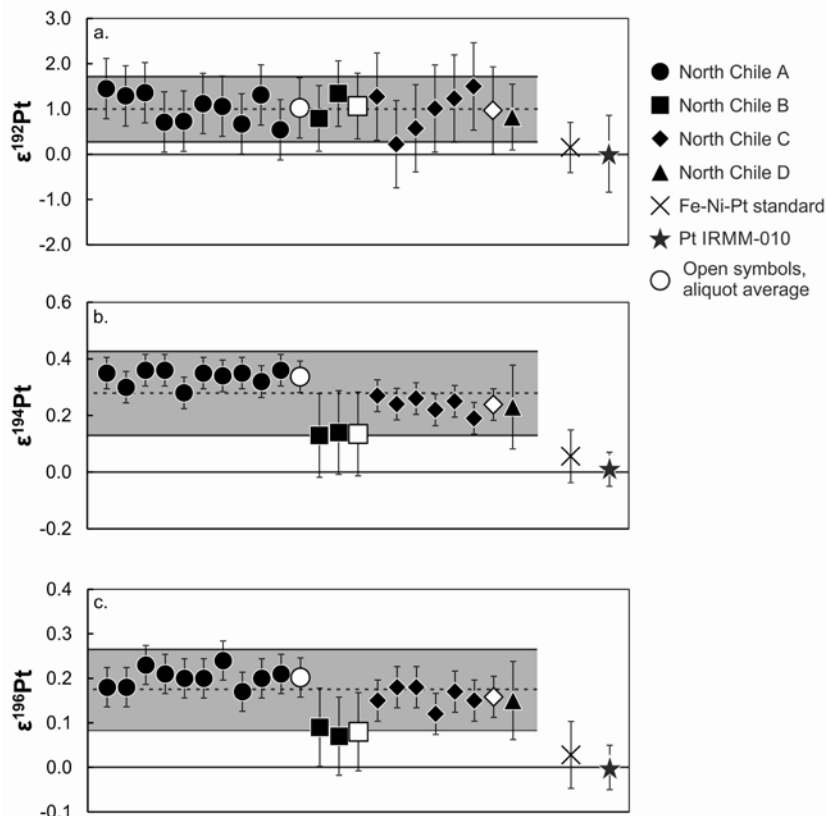


**Figure A.4.** The Pt isotope composition of four different aliquots from North Chile, an Fe-Ni powder doped with Pt SRM 3140, and the pure Pt standard IRMM-010: (a)  $\epsilon^{192}\text{Pt}$ , (b)  $\epsilon^{194}\text{Pt}$  and (c)  $\epsilon^{196}\text{Pt}$ . The averages for the Fe-Ni-Pt standard passed through our column procedure and IRMM-010 both yield ratios that are within uncertainty of the terrestrial value. The dashed line and grey band represent the mean and 2 SD of all 19 measurements of North Chile. Open symbols represent the average of each aliquot. Uncertainties (2 SD) for North Chile A and C are based on those aliquots (individual measurements and aliquot average; Table 5). Uncertainties (2 SD) for the Fe-Ni-Pt standard and IRMM-010 are calculated using those datasets (Table 6). All other uncertainties are based on the overall 2 SD for North Chile ( $n = 19$ ).

Both Tawallah Valley and Santa Clara were sampled from a similar location in the meteorite as by Kruijer et al., (2013). Results from the two studies overlap for  $\epsilon^{194}\text{Pt}$  and  $\epsilon^{196}\text{Pt}$  for both samples, within uncertainty (Fig. 5b). However, our new  $\epsilon^{192}\text{Pt}$  data for Santa Clara do not agree well with Kruijer et al., (2013; Fig. 5a), with a difference of at least 3.5  $\epsilon$  between the two datasets. There are two possible reasons for this. First, the dataset of Kruijer et al., (2013) is subject to large corrections for peak tailing of Ir onto Pt. These authors state that corrections of between  $\sim 2$  and 15  $\epsilon$  were applied to  $\epsilon^{192}\text{Pt}$ , while the size of the correction to individual samples is not given. Kruijer et al., (2013) estimate their  $\epsilon^{192}\text{Pt}$  uncertainty after peak tailing correction to 2.2  $\epsilon$ , nevertheless the need to apply such large corrections may have contributed to the discrepancy between our two datasets. Second, GCR-induced effects change with sample depth and hence across a sample on a cm-scale (i.e., at the hand-specimen size). In a meteoroid with a pre-atmospheric radius of 60 cm and Ir/Pt = 0.73, the isotopic shift on  $\epsilon^{192}\text{Pt}$  is predicted to be as much as 1.2  $\epsilon$  per cm in the outer portions of the body (Leya and Masarik 2013). Thus, a difference of  $\sim 3$  cm between sampling locations may be enough to generate the discrepancy observed on  $\epsilon^{192}\text{Pt}$ . Additionally, because of the smaller shifts induced on  $\epsilon^{194}\text{Pt}$  and  $\epsilon^{196}\text{Pt}$ , no concomitant effects would be detectable for these isotopes at the level of uncertainty.

The samples analysed here were also measured by Wittig et al., (2013; Fig. 5). It is not known how our sampling locations relate to theirs and we make comparisons with caution. Our results for Tawallah Valley and Santa Clara agree well for the  $\epsilon^{192}\text{Pt}$  and  $\epsilon^{194}\text{Pt}$  data, given the expected GCR variations on a

**Table A.6.** Platinum isotope data for the Pt standard IRMM-010 and an Fe-Ni standard doped with Pt SRM 3140 and passed through our column procedure.

	$\epsilon^{192}\text{Pt}$	2 SE a	$\epsilon^{194}\text{Pt}$	2 SE a	$\epsilon^{196}\text{Pt}$	2 SE a
<b>Fe-Ni-Pt Standard</b>						
Fe-Ni-Pt Std 01	0.54	0.13	0.11	0.05	0.09	0.04
Fe-Ni-Pt Std 02	-0.09	0.12	0.08	0.03	0.02	0.03
Fe-Ni-Pt Std 03	-0.14	0.17	0.03	0.06	0.01	0.04
Fe-Ni-Pt Std 04	0.27	0.15	-0.01	0.05	-0.01	0.03
Fe-Ni-Pt Std 05	0.16	0.20	0.07	0.05	0.03	0.04
Mean	0.15		0.06		0.03	
2 SD	0.56		0.09		0.08	
<b>IRMM-010</b>						
IRMM-010-01	-0.60	0.25	-0.02	0.05	0.00	0.03
IRMM-010-02	0.09	0.21	0.04	0.05	0.03	0.04
IRMM-010-03	-0.01	0.17	0.03	0.05	-0.04	0.04
IRMM-010-04	-0.45	0.22	-0.03	0.05	-0.03	0.04
IRMM-010-05	0.82	0.25	0.04	0.04	0.02	0.04
IRMM-010-06	0.35	0.18	-0.01	0.06	0.00	0.04
IRMM-010-07	0.35	0.19	0.05	0.06	-0.04	0.04
IRMM-010-08	0.08	0.19	-0.01	0.05	-0.01	0.03
IRMM-010-09	-0.25	0.25	0.05	0.05	0.02	0.04
IRMM-010-10	-0.24	0.23	-0.01	0.04	0.02	0.03
IRMM-010 Mean	0.01		0.01		0.00	
2 SD	0.85		0.06		0.05	

a Internal 2 standard error (SE) of each measurement.

local scale. However, our  $\epsilon^{196}\text{Pt}$  values are consistently  $\sim 0.4 \epsilon$  higher than those from Wittig et al., (2013; Fig. 5). Since our  $\epsilon^{196}\text{Pt}$  data correlate well with  $\epsilon^{192}\text{Pt}$ , fit the predictions of Leya and Masarik (2013) well, and are in good agreement with those of Kruijer et al., (2013), we are confident that our values are representative of the samples analysed.

#### A.4. Conclusions

This study presents a new analytical method for the separation of Pt and Pd from iron meteorite samples and the determination of Pt isotopes by MC-ICP-MS. The method is tested using three iron meteorites and a terrestrial standard. After dissolution, a two-stage column procedure utilising strong anion resin is employed. In the first stage, Pt is separated from major matrix constituents, including Fe and Ni. This stage also allows the isolation and collection of Pd, which can yield information complimentary to Pt for a range of geological questions. The second stage separates Pt from Ir, which can cause peak tailing interferences during mass spectrometry. Reduction of Ir with ascorbic acid before the column procedure exploits the weak affinity of  $\text{Ir}^{3+}$  for strong anion exchangers, and allows separation of Pt from Ir. Finally, Os, which generates isobaric interferences on Pt isotopes, can be volatilised using perchloric acid. Platinum yields for this procedure are typically 50 – 70 %, and blanks are in the range 0.1 – 0.3 ng per 0.3 g sample.

The reproducibility of our method is assessed using the IIAB iron meteorite North Chile. Repeat analyses of multiple aliquots of this material indicate that the uncertainty of our technique is 0.73 for  $\epsilon^{192}\text{Pt}$ , 0.15 for  $\epsilon^{194}\text{Pt}$  and 0.09 for  $\epsilon^{196}\text{Pt}$  (n=19). An iron-nickel powder doped with Pt SRM 3140 and passed through our column procedure yields results that are within uncertainty of 0 for all ratios, indicating that our new

**Table A.7.** Platinum isotope ratios for the IVB iron meteorites Santa Clara and Tawallah Valley.

		Date	$\epsilon^{192}\text{Pt}$	2 SE <sup>a</sup>	$\epsilon^{194}\text{Pt}$	2 SE <sup>a</sup>	$\epsilon^{196}\text{Pt}$	2 SE <sup>a</sup>
<b>Santa Clara</b>								
Santa Clara	01	01.09.14	15.95	0.19	0.65	0.05	0.36	0.03
Santa Clara	02	01.09.14	15.17	0.23	0.52	0.05	0.34	0.04
Santa Clara	03	03.09.14	15.14	0.20	0.70	0.05	0.41	0.03
Santa Clara	04	03.09.14	15.09	0.21	0.70	0.06	0.40	0.04
Santa Clara	05 <sup>b</sup>	29.06.16	15.44	0.20	0.60	0.04	0.38	0.03
Santa Clara mean (n = 5)			15.36		0.63		0.38	
2 SD			0.71		0.15		0.06	
<b>Tawallah Valley</b>								
Tawallah Valley	01	01.09.14	7.33	0.19	0.41	0.05	0.25	0.04
Tawallah Valley	02	03.09.14	7.16	0.21	0.25	0.05	0.22	0.05
Tawallah Valley	03	03.09.14	7.41	0.18	0.34	0.05	0.19	0.03
Tawallah Valley	04	03.09.14	7.32	0.19	0.46	0.05	0.27	0.04
Tawallah Valley	05 <sup>b</sup>	12.11.16	7.60	0.15	0.37	0.04	0.27	0.04
Tawallah Valley mean (n = 5)			7.37		0.36		0.24	
2 SD			0.32		0.16		0.07	

<sup>a</sup> Internal 2 standard error (SE) of each measurement. <sup>b</sup> Data obtained on a different aliquot of the same digestion solution processed over the separation procedure.



technique is accurate within the limit of our uncertainties. Data for the IVB iron meteorites Santa Clara and Tawallah Valley generally compare well with those of Kruijer et al., (2013), but  $\epsilon^{196}\text{Pt}$  values are significantly different to those reported by Wittig et al., (2013). The data fit to modelled trends for neutron capture, and support that Pt isotope variations in iron meteorites are a result of variable exposure to galactic cosmic ray irradiation.

## A.5. Acknowledgements

This work was supported by the European Research Council under the European Union's Seventh Framework Programme (FP7/2007–2013)/ERC Grant agreement n°[279779]. We wish to thank David Cook, Manuela Fehr and Thomas Kruijer for their helpful discussions during this study. We also wish to thank the editor and two anonymous reviewers for their comments on this manuscript.

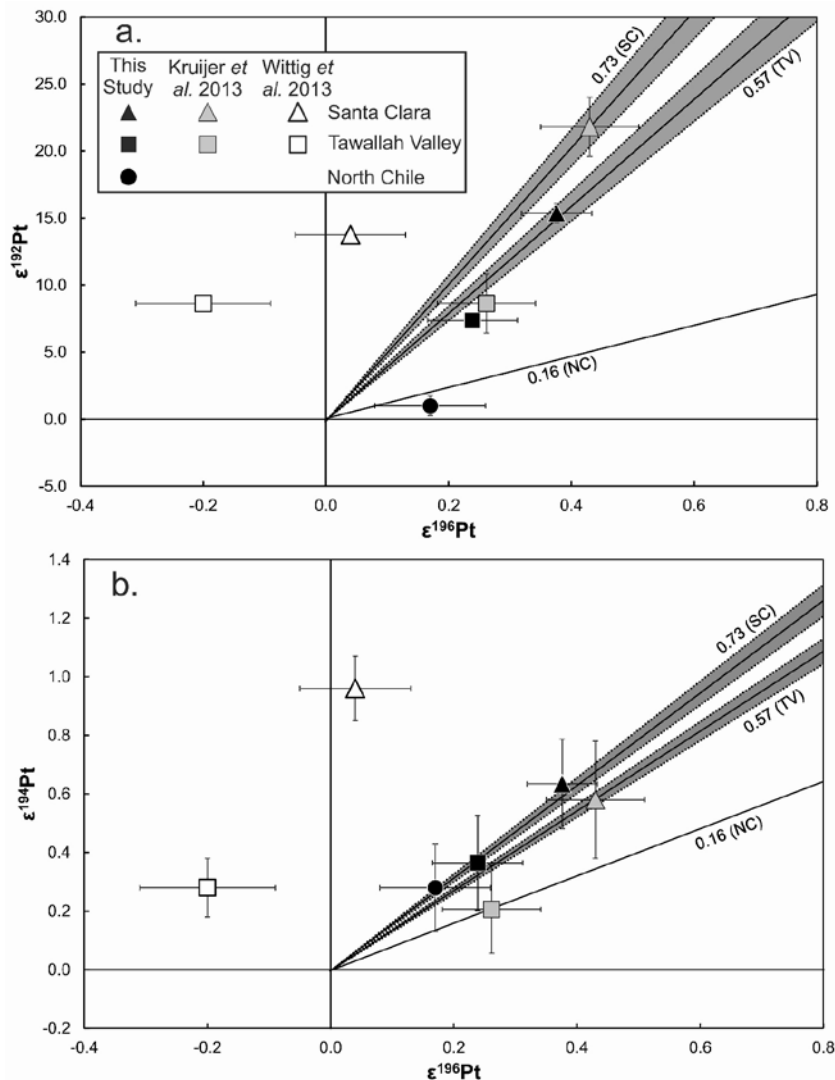


**Figure A.5.** The  $\epsilon^{192}\text{Pt}$  (a) and  $\epsilon^{194}\text{Pt}$  (b) isotope composition shown relative to  $\epsilon^{196}\text{Pt}$  for the IVB iron meteorites Santa Clara (SC) and Tawallah Valley (TV), and the IIAB North Chile (NC). Data from other studies for the same IVB meteorites are from Kruijer et al., (2013) and Wittig et al., (2013). The solid lines illustrate the expected GCR trends from Leya and Masarik (2013) calculated with an exposure time of 1200 Ma and Ir/Pt suitable for each sample. Numbers on the slopes show the Ir/Pt ratio for the respective meteorite: North Chile from Wasson et al., (2007); Tawallah Valley and Santa Clara from Campbell and Humayun (2005). The grey bands represent the uncertainty of the measurements of Campbell and Humayun (2005). Uncertainties (this study) are the 2 SD calculated for each sample from repeat analyses.

## References

- Akram W., Schönbächler M., Sprung P. and Vogel N. (2013) Zirconium—Hafnium isotope evidence from meteorites for the decoupled synthesis of light and heavy neutron-rich nuclei. *The Astrophysical Journal* **777**, 169.
- Akram W., Schönbächler M., Bisterzo S. and Gallino R. (2015) Zirconium isotope evidence for the heterogeneous distribution of s-process materials in the solar system. *Geochimica et Cosmochimica Acta* **165**, 484-500.
- Anbar A.D., Papanastassiou D.A. and Wasserburg G.J. (1997) Determination of iridium in natural waters by clean chemical extraction and negative thermal ionization mass spectrometry. *Analytical Chemistry* **69**, 2444-2450.
- Berglund M. and Wieser M.E. (2011) Isotopic compositions of the elements 2009 (IUPAC Technical Report). *Pure and Applied Chemistry* **83**, 397-410.
- Bisterzo S., Gallino R., Straniero O., Cristallo S. and Käppeler F. (2011) The s-process in low-metallicity stars – II. Interpretation of high-resolution spectroscopic observations with asymptotic giant branch models. *Monthly Notices of the Royal Astronomical Society* **418**, 284-319.
- Burkhardt C., Kleine T., Dauphas N. and Wieler R. (2012) Origin of isotopic heterogeneity in the solar nebula by thermal processing and mixing of nebular dust. *Earth and Planetary Science Letters* **357–358**, 298-307.
- Campbell A.J. and Humayun M. (2005) Compositions of group IVB iron meteorites and their parent melt. *Geochimica et Cosmochimica Acta* **69**, 4733-4744.
- Cotton F.A., Wilkinson G., Murillo C.A. and Bochmann M. (1999) *Advanced Inorganic Chemistry*. John Wiley & Sons, Inc.
- Creech J.B., Baker J.A., Handler M.R., Schiller M. and Bizzarro M. (2013) Platinum stable isotope ratio measurements by double-spike multiple collector ICPMS. *Journal of Analytical Atomic Spectrometry* **28**, 853-865.
- Creech J.B., Baker J.A., Handler M.R. and Bizzarro M. (2014) Platinum stable isotope analysis of geological standard reference materials by double-spike MC-ICPMS. *Chemical Geology* **363**, 293-300.
- Creech J.B., Baker J.A., Handler M.R., Lorand J.P., Storey M., Wainwright A.N., Luguët A., Moynier F. and Bizzarro M. (2017) Late accretion history of the terrestrial planets inferred from platinum stable isotopes. *Geochemical Perspectives Letters* **3**, 94-104.
- Dauphas N., Davis A.M., Marty B. and Reisberg L. (2004) The cosmic molybdenum–ruthenium isotope correlation. *Earth and Planetary Science Letters* **226**, 465-475.
- Ek M., Hunt A.C. and Schönbachler M. (2017) A new method for high-precision palladium isotope analyses of iron meteorites and other metal samples. *Journal of Analytical Atomic Spectrometry* **32**, 647-656.
- Fischer-Gödde M., Burkhardt C., Kruijjer T.S. and Kleine T. (2015) Ru isotope heterogeneity in the solar protoplanetary disk. *Geochimica et Cosmochimica Acta* **168**, 151-171.
- Fischer-Gödde M. and Kleine T. (2017) Ruthenium isotopic evidence for an inner Solar System origin of the late veneer. *Nature* **541**, 525-527.
- Gros M., Lorand J.-P. and Luguët A. (2002) Analysis of platinum group elements and gold in geological materials using NiS fire assay and Te coprecipitation; the NiS dissolution step revisited. *Chemical Geology* **185**, 179-190.
- Kleine T., Mezger K., Palme H., Scherer E. and Münker C. (2005) Early core formation in asteroids and late accretion of chondrite parent bodies: Evidence from  $^{182}\text{Hf}$ - $^{182}\text{W}$  in CAIs, metal-rich chondrites, and iron meteorites. *Geochimica et Cosmochimica Acta* **69**, 5805-5818.
- Kraus K.A. and Nelson F. (1956) Anion-exchange studies of the fission products. *Proceedings of the 1<sup>st</sup> UN Conference on Peaceful Uses of Atomic Energy* **7**, 113-125.
- Kruijjer T.S., Fischer-Gödde M., Kleine T., Sprung P., Leya I. and Wieler R. (2013) Neutron capture on Pt isotopes in iron meteorites and the Hf–W chronology of core formation in planetesimals. *Earth and Planetary Science Letters* **361**, 162-172.
- Kruijjer T.S., Touboul M., Fischer-Gödde M., Bermingham K.R., Walker R.J. and Kleine T. (2014) Protracted core formation and rapid accretion of protoplanets. *Science* **344**, 1150-1154.

- Leya I. and Masarik J. (2013) Thermal neutron capture effects in radioactive and stable nuclide systems. *Meteoritics and Planetary Science* **48**, 665-685.
- Leya I., Wieler R. and Halliday A.N. (2000) Cosmic-ray production of tungsten isotopes in lunar samples and meteorites and its implications for Hf–W cosmochemistry. *Earth and Planetary Science Letters* **175**, 1-12.
- Lodders K. (2003) Solar system abundances and condensation temperatures of the elements. *The Astrophysical Journal* **591**, 1220-1247.
- Markowski A., Leya I., Quitté G., Ammon K., Halliday A.N. and Wieler R. (2006) Correlated helium-3 and tungsten isotopes in iron meteorites: Quantitative cosmogenic corrections and planetesimal formation times. *Earth and Planetary Science Letters* **250**, 104-115.
- Masarik J. (1997) Contribution of neutron-capture reactions to observed tungsten isotopic ratios. *Earth and Planetary Science Letters* **152**, 181-185.
- Matthes M., Fischer-Gödde M., Kruijer T.S., Leya I. and Kleine T. (2015) Pd–Ag chronometry of iron meteorites: Correction of neutron capture-effects and application to the cooling history of differentiated protoplanets. *Geochimica et Cosmochimica Acta* **169**, 45-62.
- Mayer B., Wittig N., Humayun M. and Leya I. (2015) Palladium isotopic evidence for nucleosynthetic and cosmogenic isotope anomalies in ivb iron meteorites. *The Astrophysical Journal* **809**, 180-187.
- Pearson D.G. and Woodland S.J. (2000) Solvent extraction/anion exchange separation and determination of PGEs (Os, Ir, Pt, Pd, Ru) and Re–Os isotopes in geological samples by isotope dilution ICP-MS. *Chemical Geology* **165**, 87-107.
- Peters S.T.M., Münker C., Wombacher F. and Elfers B.-M. (2015) Precise determination of low abundance isotopes ( $^{174}\text{Hf}$ ,  $^{180}\text{W}$  and  $^{190}\text{Pt}$ ) in terrestrial materials and meteorites using multiple collector ICP-MS equipped with  $10^{12} \Omega$  Faraday amplifiers. *Chemical Geology* **413**, 132-145.
- Rehkamper M. and Halliday A.N. (1997) Development and application of new ion-exchange techniques for the separation of the platinum group and other siderophile elements from geological samples. *Talanta* **44**, 663-672.
- Ren M., Sun Y., Wang C.Y. and Sun S. (2016) Determination of platinum-group elements in geological samples by isotope dilution-inductively coupled plasma-mass spectrometry combined with sulfide fire assay preconcentration. *Geostandards and Geoanalytical Research* **40**, 67-83.
- Schönbächler M. and Fehr M. A. (2014) 'Basics of Ion Exchange Chromatography for Selected Geological Applications', in Holland H.D and Turekian, K.K. (Eds.), *Treatise on Geochemistry*, 2<sup>nd</sup> ed., Elsevier, Oxford, pp. 123-146.
- Song C. and Zhang J. (2008) 'Electrocatalytic Oxygen Reduction Reaction', in Zhang, J. (Ed.), *PEM Fuel Cell Electrocatalysts and Catalyst Layers: Fundamentals and Applications*, Springer London, London, pp. 89-134.
- Sprung P., Scherer E.E., Upadhyay D., Leya I. and Mezger K. (2010) Non-nucleosynthetic heterogeneity in non-radiogenic stable Hf isotopes: Implications for early solar system chronology. *Earth and Planetary Science Letters* **295**, 1-11.
- Thirlwall M. F. (2002) Multicollector ICP-MS analysis of Pb isotopes using a  $^{207}\text{Pb}$ – $^{204}\text{Pb}$  double spike demonstrates up to 400 ppm/amu systematic errors in Tl-normalization. *Chemical Geology* **184**, 255-279.
- Trinquier A., Elliott T., Ulfbeck D., Coath C., Krot A. N. and Bizzarro M. (2009) Origin of nucleosynthetic isotope heterogeneity in the solar protoplanetary disk. *Science* **324**, 374-376.
- Vanhala H.A.T. and Boss A.P. (2002) Injection of radioactivities into the forming solar system. *The Astrophysical Journal* **575**, 1144.
- Walker R.J. (2012) Evidence for homogeneous distribution of osmium in the protosolar nebula. *Earth and Planetary Science Letters* **351**–352, 36-44.
- Wasson J. T., Huber H. and Malvin D. J. (2007) Formation of IIAB iron meteorites. *Geochimica et Cosmochimica Acta* **71**, 760-781.
- Wittig N., Humayun M., Brandon A.D., Huang S. and Leya I. (2013) Coupled W–Os–Pt isotope systematics in IVB iron meteorites: In situ neutron dosimetry for W isotope chronology. *Earth and Planetary Science Letters* **361**, 152-161.

Wolff Briche C.S.J., Held A., Berglund M., De Bièvre P. and Taylor P.D.P. (2002) Measurement of the isotopic composition and atomic weight of an isotopic reference material of platinum, IRMM-010. *Analytica Chimica Acta* **460**, 41-47.

# Appendix B

**Table B.1.** Palladium isotope composition of iron meteorites analysed in this study for  $^{108}\text{Pd}/^{105}\text{Pd}$  and  $^{110}\text{Pd}/^{105}\text{Pd}$  internal normalisations.

Group	Sample	n <sup>a</sup>	Internally normalised to $^{108}\text{Pd}/^{106}\text{Pd}$				Internally normalised to $^{110}\text{Pd}/^{105}\text{Pd}$			
			$\epsilon^{102}\text{Pd}^b$	$\epsilon^{104}\text{Pd}^b$	$\epsilon^{105}\text{Pd}^b$	$\epsilon^{110}\text{Pd}^b$	$\epsilon^{102}\text{Pd}^b$	$\epsilon^{104}\text{Pd}^b$	$\epsilon^{106}\text{Pd}^b$	$\epsilon^{108}\text{Pd}^b$
External reproducibility <sup>c</sup>			0.00 ± 1.35	0.00 ± 0.27	0.00 ± 0.18	0.00 ± 0.29	0.00 ± 1.24	0.00 ± 0.23	0.00 ± 0.13	0.00 ± 0.16
IAB	Caddo County	4	0.85 ± 0.89	0.10 ± 0.13	0.01 ± 0.09	-0.09 ± 0.23	0.78 ± 1.02	0.07 ± 0.18	0.01 ± 0.07	0.05 ± 0.11
	Canyon Diablo	3	0.17 ± 0.78	-0.05 ± 0.15	0.00 ± 0.11	-0.09 ± 0.17	0.11 ± 0.71	-0.07 ± 0.13	0.02 ± 0.08	0.05 ± 0.09
	Cranbourne	4	-0.24 ± 0.67	0.02 ± 0.16	-0.09 ± 0.11	-0.03 ± 0.16	-0.11 ± 0.62	0.13 ± 0.11	0.08 ± 0.07	0.06 ± 0.08
	Edmonton KY	2	0.05 ± 0.95	0.01 ± 0.19	-0.07 ± 0.13	0.02 ± 0.21	0.17 ± 0.87	0.10 ± 0.16	0.05 ± 0.09	0.02 ± 0.11
	Magura	3	-0.16 ± 0.78	-0.07 ± 0.15	-0.03 ± 0.11	-0.02 ± 0.17	-0.12 ± 0.71	-0.03 ± 0.13	0.03 ± 0.08	0.03 ± 0.09
	Odessa	2	-0.13 ± 0.95	0.15 ± 0.19	-0.25 ± 0.13	0.28 ± 0.21	0.46 ± 0.87	0.51 ± 0.16	0.14 ± 0.09	-0.07 ± 0.11
	Toluca 1a	4	0.25 ± 0.72	0.01 ± 0.21	0.00 ± 0.07	-0.10 ± 0.14	0.19 ± 0.65	-0.01 ± 0.16	0.02 ± 0.05	0.06 ± 0.08
	Toluca 2a	4	0.14 ± 0.70	0.00 ± 0.13	0.06 ± 0.08	-0.10 ± 0.06	-0.02 ± 0.57	-0.10 ± 0.04	-0.03 ± 0.05	0.03 ± 0.03
	Toluca 2b	4	0.61 ± 0.50	0.08 ± 0.05	0.05 ± 0.01	-0.10 ± 0.15	0.48 ± 0.57	0.00 ± 0.07	-0.02 ± 0.02	0.04 ± 0.08
	Toluca 2c	4	0.45 ± 0.24	-0.03 ± 0.09	0.02 ± 0.05	0.05 ± 0.16	0.44 ± 0.31	-0.05 ± 0.11	-0.03 ± 0.03	-0.04 ± 0.09
	Toluca 2d	4	0.12 ± 0.27	-0.08 ± 0.13	-0.04 ± 0.11	0.02 ± 0.11	0.20 ± 0.16	-0.03 ± 0.03	0.03 ± 0.09	0.00 ± 0.06
	Toluca Mean	20	0.32 ± 0.30	0.00 ± 0.06	0.02 ± 0.04	-0.04 ± 0.07	0.26 ± 0.28	-0.04 ± 0.05	-0.01 ± 0.03	0.02 ± 0.04
IIAB	North Chile	2	-0.01 ± 0.95	0.17 ± 0.19	-0.02 ± 0.13	0.24 ± 0.21	0.18 ± 0.87	0.24 ± 0.16	-0.03 ± 0.09	-0.14 ± 0.11
	Sikhote Alin	2	0.30 ± 0.95	0.22 ± 0.19	-0.01 ± 0.13	0.23 ± 0.21	0.46 ± 0.87	0.28 ± 0.16	-0.04 ± 0.09	-0.14 ± 0.11
	Coahuila	3	0.03 ± 0.78	-0.08 ± 0.15	0.06 ± 0.11	0.02 ± 0.17	-0.04 ± 0.71	-0.14 ± 0.13	-0.05 ± 0.08	-0.04 ± 0.09
IID	Rodeo	5	0.20 ± 0.60	-0.38 ± 0.12	0.11 ± 0.08	0.25 ± 0.13	0.18 ± 0.55	-0.47 ± 0.10	-0.14 ± 0.06	-0.20 ± 0.07
	Carbo A	3	-0.35 ± 0.78	0.55 ± 0.15	-0.19 ± 0.11	0.86 ± 0.17	0.50 ± 0.71	0.96 ± 0.13	-0.02 ± 0.08	-0.45 ± 0.09
	Carbo J	3	-0.82 ± 0.78	1.10 ± 0.15	-0.31 ± 0.11	0.94 ± 0.17	0.27 ± 0.71	1.67 ± 0.13	0.05 ± 0.08	-0.45 ± 0.09
	Carbo Y	3	-0.14 ± 0.78	0.66 ± 0.15	-0.10 ± 0.11	0.75 ± 0.17	0.50 ± 0.71	0.94 ± 0.13	-0.07 ± 0.08	-0.41 ± 0.09
	Carbo G	3	0.02 ± 0.78	0.92 ± 0.15	-0.24 ± 0.11	0.91 ± 0.17	0.97 ± 0.71	1.39 ± 0.13	0.00 ± 0.08	-0.46 ± 0.09

*Continues on next page*

**Table B.1. Continued**

Group	Sample	n <sup>a</sup>	Internally normalised to <sup>108</sup> Pd/ <sup>106</sup> Pd				Internally normalised to <sup>110</sup> Pd/ <sup>105</sup> Pd			
			ε <sup>102</sup> Pd <sup>b</sup>	ε <sup>104</sup> Pd <sup>b</sup>	ε <sup>105</sup> Pd <sup>b</sup>	ε <sup>110</sup> Pd <sup>b</sup>	ε <sup>102</sup> Pd <sup>b</sup>	ε <sup>104</sup> Pd <sup>b</sup>	ε <sup>106</sup> Pd <sup>b</sup>	ε <sup>108</sup> Pd <sup>b</sup>
IIIAB	Boxhole	4	0.27 ± 0.67	0.36 ± 0.13	-0.01 ± 0.11	0.27 ± 0.15	0.45 ± 0.62	0.43 ± 0.19	-0.05 ± 0.07	-0.16 ± 0.08
	Thunda	1	-1.33 ± 1.35	-0.20 ± 0.27	0.08 ± 0.18	0.00 ± 0.29	-1.45 ± 1.24	-0.30 ± 0.23	-0.06 ± 0.13	-0.03 ± 0.16
	Cape York	1	-0.75 ± 1.35	-0.24 ± 0.27	-0.01 ± 0.18	0.50 ± 0.29	-0.42 ± 1.24	-0.13 ± 0.23	-0.09 ± 0.13	-0.30 ± 0.16
IVA	Gibeon 1a	4	0.23 ± 0.79	-0.09 ± 0.13	0.06 ± 0.09	0.01 ± 0.19	0.15 ± 0.80	-0.15 ± 0.11	-0.05 ± 0.07	-0.03 ± 0.11
	Gibeon 2a	4	-0.45 ± 0.67	-0.22 ± 0.16	-0.11 ± 0.14	0.18 ± 0.15	-0.15 ± 0.62	-0.05 ± 0.15	0.06 ± 0.11	-0.06 ± 0.08
	Gibeon 2b	4	-0.07 ± 0.67	-0.13 ± 0.13	0.07 ± 0.09	0.15 ± 0.30	-0.08 ± 0.62	-0.18 ± 0.11	-0.08 ± 0.07	-0.12 ± 0.19
	Gibeon 2c	4	-0.09 ± 0.73	0.01 ± 0.13	0.08 ± 0.09	0.15 ± 0.15	-0.13 ± 0.71	-0.06 ± 0.11	-0.10 ± 0.07	-0.12 ± 0.08
	Gibeon Mean	14	-0.10 ± 0.34	-0.11 ± 0.07	0.02 ± 0.05	0.12 ± 0.09	-0.05 ± 0.31	-0.11 ± 0.06	-0.04 ± 0.04	-0.08 ± 0.05
	Muonionalusta	6	0.18 ± 0.71	-0.12 ± 0.14	0.05 ± 0.14	0.00 ± 0.16	0.11 ± 0.52	-0.17 ± 0.11	-0.04 ± 0.09	-0.02 ± 0.07
IVB	Tawallah Valley	9	0.99 ± 0.65	-0.26 ± 0.11	0.08 ± 0.07	0.53 ± 0.10	1.19 ± 0.58	-0.25 ± 0.08	-0.17 ± 0.05	-0.35 ± 0.05
	Santa Clara	8	-0.28 ± 0.48	-0.07 ± 0.09	-0.02 ± 0.06	0.63 ± 0.10	0.14 ± 0.44	0.08 ± 0.08	-0.11 ± 0.05	-0.37 ± 0.06
	Tlacotepec	3	-0.92 ± 0.78	0.71 ± 0.15	-0.16 ± 0.11	0.86 ± 0.17	-0.12 ± 0.71	1.09 ± 0.13	-0.05 ± 0.08	-0.46 ± 0.09
	Hoba	4	-0.59 ± 0.67	-0.18 ± 0.13	0.05 ± 0.09	0.35 ± 0.15	-0.46 ± 0.62	-0.17 ± 0.11	-0.11 ± 0.07	-0.23 ± 0.08

<sup>a</sup> Numbers in sample names indicate different dissolutions. Letters after number indicate aliquot of dissolution. <sup>b</sup> Number of analyses. <sup>c</sup> Uncertainties were calculated using the method outlined in section 4.3.1. <sup>d</sup> Calculated as described in section 4.3.1.



# Acknowledgments

Like most kids, I used to fantasise about exploring distant planets and learning the secrets of the universe. To be honest this continued well into my teenage years when my friends and I, would talk about the latest episode of Stargate during our lunch breaks. Even with my childish optimism I could never have imagined that one day I would get to realise these dreams. Yet, for the past six years I have destroyed countless planets (small fragments of them anyway) all in the name of science in an attempt to unlock the secrets of the solar system. I am eternally grateful to my supervisor Maria Schönbächler for giving me this opportunity. You were always able to provide valuable advice whenever I ran into problems and to help me understand what my data was telling me. Alison Hunt was burdened with my day-to-day supervision and I cannot express my gratitude for everything she has done for me. From teaching me the basic of ion exchange chromatography to reading endless versions of this thesis, I apologise for my often atrocious spelling. For keeping the lab running and helping me with a range of technical issues I would like to thank Manuela Fehr, Colin Maden, Corey Archer, Urs Menet, Donat Niederer and Andreas Süssli. Britt Meyer and Michèle Tewlin deserve a special thanks for their all their help with various organisational issues, especially after my accident. Sharing an office with Florian, Uli, Michi, Thom and Eniko during all these years has been a pleasure. A big thank you to my external examiners, Mark Rehkämper and Maria Lugaro. Mark was co-author on the first scientific paper I ever read (almost a decade ago) and I very honoured you agreed to serve as my examiner. Maria Lugaro has answered many ignorant questions on nucleosynthesis and helped make this thesis much better.

This thesis represents a long journey that started somewhere in 2002 during Ms Gotts geography lessons. Stealing the comfy chairs before your lessons (and the lessons themselves) remain one of my favourite memories from my time in Shetland. I also owe a debt of gratitude to Mr Spence for encouraging me too believe in myself. I remember telling you that one day I would get a PhD! Here it is and it would not have been possible without your encouragement all those years ago. When I returned to Sweden I was lucky have another great geography teacher in Ingemar Sjöholm. The enthusiasm with which you taught was infectious and perhaps the main reason I wound up studying geology at university. I am sorry my TOK essay was so terrible, I hope you find this thesis more enjoyable to read. While at university, Johan Hogmalm took me under his wing and taught me more about analytical geochemistry than I could ever have learned in class. You showed me how much fun doing science could be and I hope we get to do it together again one day. Duck Mittlefehldt introduced me to cosmochemistry one scorching summer in Houston where I learned that everything really is much cooler in space.

Life is not all about work and during my time in Zurich I have been fortunate enough to have made many fantastic friends. For all the nights spent dancing on the roof, playing dress up and evenings spent pretending to be trees I would like to thank Thom, Mike, Diogo, Emily, Sam, Lisa, Funky, Brandi, My, Eniko, Matthias, Max, Alison, Dave, Laura, Yoann, Aline, Susan, Nienke and many more. You all helped make Zürich feel like home. I look forward to many birthdays, weddings and random meetings around the world in the next few decades. Mike and Thom also deserve a special thank you for helping me in



the aftermath of my failed entrance exam to the 27 club. I am also grateful for my old friends Mats, Mattias, Ardo and Joachim. I know I don't see you as often as I once did, or would like, but whenever we do meet it's like the years haven't passed at all - a sign of true friendship I think. The last year has in many ways been the best one yet and much (if not all) is because of Fanny. Thank you for making me a better person ("In the basket!") and thank you for being so wonderful (You too Dinah!). You make me so incredibly happy.

Finally, I would like to thank my family. The PhD life is full of challenges but for me none compared to being so far away from you for so long. I am very much (for better or worse) a sum of my parents, my mother Marta and my father Joakim. I inherited my technical flair from my father. Thank you for always encouraging me and for teaching me so much. You are still the smartest person I know. If my dad taught me how to think then my mother taught me love and compassion. You were always there for me when I needed you and always made me feel loved. Your can do attitude, even in the toughest of times, taught me that anything is possible with a little 'jävlar anamma' attitude. My wonderfully weird sisters (#DTS), Madole, Jenny and Maria, are proof that there are many different forms of intelligence. You are every bit as smart as me and don't ever forget that! I am immensely proud of all of you. My niece Jessica has grown up way too fast and is perhaps the smartest one of us all. Aim for the stars and don't forget I will always be around to help you get there. I look forward to seeing who little Natalie grows up to be. I have no doubt you will become a star in your own right. A final thank you to rest of my family, farmor, farfar, mormor, morfar, Anette and everyone else for all the small things throughout the years.

Jag älskar er alla.



# Curriculum Vitae

## **Pär Karl Mattias Ek**

Date of birth: August 11, 1988

Place of Birth: Svarträ, Sweden

Nationality: Swedish

## **Education**

- 2012 - 2017 **ETH Zürich: Doctoral student, Isotope Geo/Cosmochemistry**  
*Thesis: Palladium isotope cosmochemistry: Constraints on nebular and parent body processes.*
- 2010 - 2012 **Göteborgs Universitet: MSc in Earth Science**  
*Thesis: Fractionation processes in the thin layered alkali gabbroic Ringkallen Hill Gabbro of the Ulvö Gabbro complex.*
- 2007 - 2010 **Göteborgs Universitet: BSc in Earth Science**  
*Thesis: Fractionation of trace elements in the Rävsnö Ulvö gabbro, central Sweden.*
- 2004 - 2007 **Sven Eriksonsgymnasiet, Borås, Sweden**
- 2001 - 2004 **Baltasound Junior High School, Unst, Shetland, United Kingdom**

## **Employment and Internships**

- 2012 **Göteborgs Universitet: Interim Laboratory Manager**
- 2010 - 2012 **Göteborgs Universitet: Teaching Assistant**
- 2011 **Lunar and Planetary Science Institute: Summer Intern**